Preparation, Characterisation and Modification of Porous Carbon Monolithic Materials for Chromatographic and Electrochemical Applications

Ali Eltmimi

BSc, University of Baghdad, 1987
MSc, University College Dublin, 2004
MRSC GradICI
Student No. 55134971

Under supervision of Prof. Brett Paull

A thesis is submitted to Dublin City University for consideration for the degree of:

Doctor of Philosophy

Dublin City University
School of Chemical Sciences
August 2009

TO MY MOTHER; DECEASED FATHER AND BROTHER; WIFE AND MY WONDERFUL SONS, MONTADAR, HASSAN AL-MUJTABA & …….

"وما أوتيتم من العلم إلاّ قليلا" (الإسراء 85)
"knowledge, you (mankind) have been given only a little." Noble Quran
16 July, 621

Table of Contents

		Page
Chapter One	**Development of Monolithic Materials in Chromatography**	**1**
1.1	Monolithic stationary phases for chromatography	1
1.2	Classification of monolithic columns	4
1.2.1	Silica monolithic phases	4
1.2.1.1	HPLC applications of silica monoliths	9
1.2.2	Polymer monolithic phases	11
1.2.2.1	HPLC applications of polymer monoliths	12
1.2.3	Carbon monolithic phases	14
1.3	Modified monolithic materials	18
1.3.1	Preparation of gold nano/micro-particles	18
1.3.2	Applications of gold/ and silver nano/micro-particles	18
1.4	Techniques for characterisation of nano/micro structured materials	21
1.4.1	Scanning electron microscopy (SEM)	21
1.4.2	Energy-dispersive X-ray spectroscopy (EDX)	23
1.4.3	Surface area measurements (Brunauer, Emmett, Teller)	23
1.4.3.1	The adsorption isotherm	24
1.4.4	Dilatometry analysis	27
1.4.5	Porosimetry analysis	28
1.4.6	Dynamic mechanical analysis	29
1.4.7	Photon correlation spectroscopy	33
1.5	Conclusions	33
	References	35
Chapter Two	**Preparation and Characterisation of Porous Carbon Monolithic Columns for Chromatographic Applications**	**44**
2.1	Introduction	44
2.2	Experimental	47
2.2.1	Chemicals	47
2.2.2	Instrumentation and characterisation	47
2.2.3	Synthesis of the carbon monolithic rod	49
2.2.3.1	Pyrolysis of the precursor rods	50

2.2.3.2	Etching (removal of the silica particles)	50
2.2.3.3	Cladding/Housing the carbon rod and column fitting	50
2.2.4	Characterisation of the carbon monoliths	53
2.2.4.1	Scanning electron microscopy/ Energy-dispersive X-ray spectroscopy	53
2.2.4.2	BET surface area measurements	54
2.2.4.3	Dilatometry analysis	54
2.2.4.4	Thermal analysis	54
2.2.4.5	Mercury porosimetry	55
2.2.4.6	Dynamic mechanical analysis	55
2.2.4.7.	Characterisation of carbon/gold composite monoliths using infrared spectroscopy	55
2.2.4.8	Conductivity measurements of the carbon monoliths	56
2.2.4.9	Back pressure determinations	56
2.3	Results and Discussion	56
2.3.1	Synthesis and pyrolysis of silica-embedded precursor rods	56
2.3.2	Morphology of macro-porous carbon monoliths	61
2.3.2.1	SEM results	61
2.3.2.2	Energy-dispersive X-ray analysis	67
2.3.3	BET Surface area of carbon monoliths	68
2.3.4	Dilatometry analysis	77
2.3.5	Differential thermal analysis/ Thermo gravimetric analysis	83
2.3.6	Mercury porosimetry	84
2.3.7	Dynamic mechanical analysis	88
2.3.8	Infrared spectroscopy	91
2.3.9	Conductivity measurements of the carbon monoliths	92
2.3.10	Backpressure determination of the 1 and 5 µm templated carbon monolithic columns	95
2.3.11	Physical characterisation summary	96
2.4	Conclusions	97
	References	99

Chapter Three	**Gold and Silver Particles Modified Porous Carbon Monoliths**	**101**
3.1	Introduction	101
3.2	Experimental	102
3.2.1	Chemicals	102
3.2.2	Instrumentation	103
3.2.3	Production of gold modified carbon monolith using tetrachlorauric acid	103
3.2.3.1	Modification of carbon monoliths with tetrachlorauric acid by sample immersion	104
3.2.3.2	Modification of a carbon monolith (5 µm pore diameter), with tetrachlorauric acid by a re-circulation technique	104
3.2.3.3	Modification of a carbon monolith (5 µm pore diameter), with tetrachlorauric acid by manual injection of a tetrachlorauric acid/dextran mixture	104
3.2.3.4	Characterisation of carbon/gold composite monoliths using SEX/EDX	105
3.2.3.5	Quantitation of the gold content of the carbon/gold composite monoliths using inductively coupled plasma–optical emission spectroscopy (ICP-OES)	105
3.2.3.6	Characterisation of carbon/gold composite monolithic rod, **IM5**, by SEM before and after removal the gold particles following HNO_3 treatment	105
3.2.3.7	Characterisation of gold particle size in the effluent of modifying solutions for carbon monolith modification by dynamic light scattering (DLS)	106
3.2.4	Modification of carbon/gold composite monoliths with 6-mercaptohexanoic acid	106
3.2.4.1	Characterisation of carbon/gold composite monolith, **IM5**, by SEM before and after attachment of 6-mercaptohexanoic acid to the surface	106
3.2.5	Modification of carbon monoliths with gold paint	107

3.2.5.1	Characterisation of carbon monoliths modified with gold paint by SEM and HR-SEM	107
3.2.6	Modification of a carbon monolith with silver particles	107
3.2.6.1	Characterisation of the silver/carbon composite by SEM/EDX	108
3.2.7	Modification of carbon monolith with gold nano-particles (5 nm particle size)	108
3.2.7.1	Characterisation of carbon monolith modified with 5 nm gold nano-particles by HR-SEM	108
3.3	Results and discussion	108
3.3.1	Preparation and characterisation of carbon monoliths modified with gold nano/micro-particles	108
3.3.1.1	Modification of the carbon monoliths**, IM1**, and, **IM5**, with gold nano/micro-particles, and characterisation by SEM/EDX	108
3.3.1.2	Modification of the carbon monolith **RC5**, with gold nano/micro-particles, and characterisation by SEM	113
3.3.1.3	Modification of the carbon monolith with gold nano/micro-particles, **MI5**, and characterisation by SEM/EDX	116
3.3.1.4	Characterisation of gold content within carbon composite monoliths using inductively coupled plasma–optical emission spectroscopy	120
3.3.1.5	Measurement of gold particle size in the effluent modification solution for the preparation of the carbon/gold composite monolith **RC5**, by dynamic light scattering	124
3.3.2	Dynamic coating of 6-mercaptohexanoic acid onto the surface of carbon/gold composite monoliths, **IM5** and **RC5**.	126
3.3.3	Direct modification of carbon monoliths, **P1** to **P4**, with gold paint, and characterisation by SEM/EDX	132
3.3.4	Conductivity measurements of the carbon/gold composite monoliths	139
3.3.5	Modification of the carbon monoliths, with silver micro-particle, **S10**, and characterisation by SEM/EDX	142

3.3.6	Direct modification of the carbon monolith, with gold nano-particles (5 nm particle size), **Au5**, and characterisation by SEM/EDX	145
3.3.6.1	The UV analysis of gold nano-particle colloid solution	151
3.4	Conclusions	153
	References	154
Chapter Four	**Evaluation of Porous Porous Carbon Monolithic Columns**	**156**
4.1	Introduction	156
4.2	Experimental:	157
4.2.1	Chemicals	157
4.2.2	Instrumentation	158
4.2.3	Chromatographic characterisation	158
4.3	Results and discussion	159
4.3.1	Templated porous carbon monolithic columns	159
4.3.1.1	Chromatographic evaluation of 5 µm templated carbon monolithic column	159
4.3.1.2	RP-HPLC on 5 µm templated carbon monolithic column	160
4.3.1.3	NP-HPLC on 5 µm templated carbon monolithic column	163
4.3.1.4	Chromatographic evaluation of acid treated carbon monolithic column (5 µm pore diameter), using NP-HPLC	173
4.3.1.5	Study of the surface treatment of carbon monolithic columns on the NP retention of non-polar and polar solutes	178
4.3.1.6	Increased monolith length and pore size effects	180
4.3.1.7	Acid Surface treatment of 10 µm templated carbon monolithic column	183
4.3.1.8	Chromatographic evaluation of 1 µm templated carbon monolithic column by NP-HPLC	185
4.3.1.9	Acid Surface treatment for 1 µm templated monolithic column	187
4.3.2	Modified porous carbon monolithic columns	188
4.3.2.1	Gold nano/micro-particles modified carbon monolithic column	188
4.3.2.2	Backpressure measurements on the carbon/gold composite monolithic column modified with 6-mercaptohexanoic acid	189

4.3.2.3	Chromatographic evaluation of the carbon/gold composite monolithic column modified with 6-mercaptohexanoic acid	190
4.3.2.4	1 μm templated carbon monolithic column modified with gold nano/micro-particles	192
4.3.2.5	The effect of the column temperature on the retention	195
4.3.2.6	The effect of the column temperature on the retention of imidazole on 10 μm modified carbon monolithic column	201
4.4	Conclusions	205
	References	207
Future work chapter	**Electrochemical Properties of Porous Glassy Carbon Monolithic Electrodes**	**208**
5.1	Introduction	208
5.2	Experimental	209
5.2.1	Reagents and materials	209
5.2.2	Instrumentation	210
5.2.3	Electrochemical characterisation	210
5.2.4	Electrochemical Cell	210
5.2.5	Procedure	210
5.2.5.1	Cyclic voltammetry	210
5.2.5.2	Preparation of Au/PGCME	211
5.3	Results and discussion	211
5.3.1	Cyclic voltammetry of commercial glassy carbon electrode	211
5.3.2	Electrocatalytic reduction of ferricyanide on PGCME	212
5.3.3	Characterisation of Au/PGCME by SEM/EDX	216
5.3.4	Electrocatalytic oxidation of ferricyanide on Au/PGCME	218
5.4	Conclusions	221
	References	222
	General conclusions	223
	Poster presentation	225
	Submitted Work	228

Declaration

I hereby certify that this material, which I now submit for assessment on the programme of study leading to the award of

Doctor of Philosophy

is entirely my own work, that I have exercised reasonable care to ensure that the work is original, and does not to the best of my knowledge breach any law of copyright, and has not been taken from the work of others save and to the extent that such work has been cited and acknowledged within the text of my work.

Signed: _____ ID No.: _____

Date: _____

List of Abbreviations

IM1	The 1 μm templated carbon/gold composite monolith prepared by immersion technique
IM2	The 2 μm templated carbon/gold composite monolith prepared by immersion technique
IM5	The 5 μm templated carbon/gold composite monolith prepared by immersion technique
IM10	The 10 μm templated carbon/gold composite monolith prepared by immersion technique
RC5	The 5 μm templated carbon/gold composite monolith prepared by re-circulating technique
MI5	The 5 μm templated carbon/gold composite monolith prepared by manual injection technique
P1	The 1 μm templated carbon monolith modified with gold paint
P2	The 2 μm templated carbon monolith modified with gold paint
P5	The 5 μm templated carbon monolith modified with gold paint
P10	The 10 μm templated carbon monolith modified with gold paint
S10	The 10 μm templated carbon/silver composite monolith
Au5	The 5 μm templated carbon monolith attempted modified with gold nano-particle (5 nm particle size)
Au/PGCME	Gold modified porous glassy carbon monolithic electrode
Au-CME	Gold-modified glassy carbon electrode
Au-GC	Gold nano-particle modified glassy carbon
BDDT	Brunauer, Deming, Deming and Teller
BET	Brunauer, Emmett and Teller
BSA	Bovine serum albumin
CE	Capillary electrophoresis
CEC	Capillary electrochromatography

CTE	Coefficient of thermal expansion
CV	Cyclic voltammetry
DEGDMA	Diethlyleneglycol dimethacrylate
DLS	Dynamic light scattering
DMA	Dynamic mechanical analysis
DMTA	Dynamic mechanical thermal analyser
DTA/TGA	Differential thermal analysis/thermo gravimetric analysis
EDMA	Ethylene dimethacrylate
EDX	Energy-dispersive X-ray spectroscopy
EG	Exfoliated graphite
FT-IR	Fourier transform infrared
GC	Gas chromatography
GCB	Graphitised carbon black
GMA	Glycidyl methacrylate
HEA	Hydroxyethylacrylate
HETP	Height equivalent to the theoretical plate
HPLC	High performance liquid chromatography
HR-SEM	High-resolution scanning electron microscopy
IR	Infrared spectroscopy
ICP-OES	Inductively coupled plasma-optical emission spectrometer
ISEC	Inverse size-exclusion chromatography
LC	Liquid chromatography
μ-HPLC	Micro-high performance liquid chromatography
MPA	Mercaptopropionic acid
MS-FS	Monolithic silica column within fused silica capillaries
NP	Normal-phase
NP-HPLC	Normal-phase-high performance liquid chromatography
PCS	Photon correlation spectroscopy
PGC	Porous glassy carbon
PGCME	Porous glassy carbon monolithic electrode
PMMA	Poly(methyl methacrylate)
PSD	Pore size distribution

PTFE	Polytetrafluoroethylene
R/F	Resorcinol/formaldehyde
RP	Reversed phase
RP-HPLC	Reversed-phase high performance liquid chromatography
SEM	Scanning electron microscopy
SMB	Simulated moving bed
Tanδ	Damping factor
TEM	Transmission electron microscopy
Tg	Glass transition temperature
TMOS	Tetramethoxysilane
TRIM	Trimethylolpropane trimethacrylate
UHPLC	Ultra high performance liquid chromatography
XRD	X-ray diffraction

List of Figures

Figure 1.1	(a) Monolithic column based publications from 1993 to 2007 (b) Silica, polymer and carbon monolithic column publications from 1996 to 2007 using SciFinder Scholar, Version 2008, American Chemical Society.
Figure 1.2	SEM image of a porous monolithic silica rod prepared by polycondenstion. Reproduced from [28].
Figure 1.3	SEM image of a silica xerogel column. Scale bar 1 µm. Reproduced from [29].
Figure 1.4	SEM image of continuous monolithic silica prepared in a fused-silica capillary. Capillary diameter, 100 µm. Reproduced from [39].
Figure 1.5	SEM images of monolithic silica prepared in a mould (a) and in a 50-µm capillary (b). The bars denote 10 µm in (a) and 20 µm in (b). Reproduced from [40].
Figure 1.6	Schematic representation of the electron optics of SEM. Reproduced from [127].
Figure 1.7	The five types of adsorption isotherms, I to V, from the classification by Brunauer, Deming, Deming and Teller [129] (BDDT), together with Type VI, the stepped isotherm.
Figure 1.8	Applied stress (to) and the resultant strain (of) the material. Reproduced from [155].
Figure 1.9 (a)	The strain is in phase with the stress. Reproduced from [155].
Figure 1.9 (b)	The strain is 90° out of phase with the stress. Reproduced from [155].
Figure 1.9 (c)	The strain is in phase with the stress. Reproduced from [155].
Figure 1.10	Typical response from a DMA shows both modulus and Tanδ for PMMA. Reproduced from [155].
Figure 2.1	Formation of templated polymer material. Reproduced from [12].
Figure 2.2	Scheme illustrating the cladding and fitting procedures for the carbon monolithic column.
Figure 2.3	Optical 10 x microscope image of a 5 µm templated carbon monolithic rod clad within heat treated Teflon sheath with an epoxy exterior sealing layer for housing within a PEEK column.
Figure 2.4	Typical glue encased carbon monolithic column.

Figure 2.5	Optical 10 x microscope image of an epoxy resin clad 1 µm templated carbon monolith.
Figure 2.6	Optical 10 x microscope image of an epoxy resin clad 10 µm templated carbon monolith.
Figure 2.7	Photograph of a 90 x 4 mm glassy carbon monolith, with inset showing 4 x microscope image of homogenous surface.
Figure 2.8	TEM image of non-uniform silica particles (2µm in particle size).
Figure 2.9	SEM images of the silica particles: (a) 1µm; (b) 2µm; (c) 5µm and (d) 10µm particle sizes.
Figure 2.10	SEM images of the carbon/silica composite materials (a) 1 µm (b) 2 µm (c) 5 µm and (d) 10 µm (silica particle size) before HF treatment and removal of the silica particles.
Figure 2.11	SEM images of the carbon monolithic structures (a) 1 µm (b) 2 µm (c) 5 µm and (d) 10 µm (macro-pores) after HF treatment and removal of the silica particles.
Figure 2.12	HR-SEM images of the macro-pore carbon monolithic structures (a) 1.5-2 µm (b) 4.5-6 µm in size.
Figure 2.13	HR-SEM images of the meso-porous carbon monolithic structures (a) 7-14 nm (b) 7-40 nm.
Figure 2.14	HR-SEM image of the glassy carbon surface morphology of the 5 µm templated monolith.
Figure 2.15	EDX spectrum of the carbon monolith (10 µm macro-pores) before pyrolysis and removal of the silica particles and iron catalyst.
Figure 2.16	EDX spectrum of the carbon monolith (10 µm macro-pores) after pyrolysis and removal of the silica particles and iron catalyst.
Figure 2.17	BET adsorption isotherm and pore size distribution of 1 µm silica particles exhibiting a Type 1 isotherm.
Figure 2.18	BET adsorption isotherm and pore size distribution of 2 µm silica particles exhibiting a Type 1 isotherm.
Figure 2.19	BET adsorption isotherm and pore size distribution of 1 µm carbon-silica monolith before pyrolysis exhibiting a Type 4 isotherm.
Figure 2.20	BET adsorption isotherm and pore size distribution of 2 µm carbon-silica monolith before pyrolysis exhibiting a Type 1 isotherm.

Figure 2.21	BET adsorption isotherm and pore size distribution of 5 µm carbon monolith before pyrolysis exhibiting a Type 4 isotherm.
Figure 2.22	BET adsorption isotherm and pore size distribution of 10 µm carbon monolith before pyrolysis exhibiting a Type 4 isotherm.
Figure 2.23	BET adsorption isotherm and pore size distribution of 1 µm carbon monolith after pyrolysis exhibiting a Type 4 isotherm.
Figure 2.24	BET adsorption isotherm and pore size distribution of 2 µm carbon monolith after pyrolysis exhibiting a Type 4 isotherm.
Figure 2.25	BET adsorption isotherm and pore size distribution of 5 µm carbon monolith after pyrolysis exhibiting a Type 4 isotherm.
Figure 2.26	BET adsorption isotherm and pore size distribution of 10 µm carbon monolith after pyrolysis exhibiting a Type 4 isotherm.
Figure 2.27	Dilatometry profile of the 1 µm silica-particle templated monolithic rod subjected to a temperature-programmed pyrolysis cycle.
Figure 2.28	Dilatometry profile of the 2 µm silica-particle templated monolithic rod subjected to a temperature-programmed pyrolysis cycle.
Figure 2.29	Dilatometry profile of the 5 µm silica-particle templated monolithic rod subjected to a temperature-programmed pyrolysis cycle.
Figure 2.30	Dilatometry profile of the 10 µm silica-particle templated monolithic rod subjected to a temperature-programmed pyrolysis cycle.
Figure 2.31	Thermogravimetric curve of the 1 µm carbon-silica sample during the pyrolysis under flowing nitrogen.
Figure 2.32	Pore size distribution of carbon monolith 1µm (macro-pores) before pyrolysis and removal of the silica particles.
Figure 2.33	Pore size distribution of carbon monolith 1µm (macro-pores) after pyrolysis and removal of the silica particles.
Figure 2.34	Pore number fraction of pores for carbon monolith 1µm (macro-pores) after pyrolysis.
Figure 2.35	Temperature dependence of the Tanδ for 5 µm macro-porous carbon monolithic sample run from -150 to 180 ^{o}C.
Figure 2.36	Temperature dependence of the Tanδ for 5 µm macro-porous carbon monolithic sample run from -150 to 250 ^{o}C.
Figure 2.37	Temperature dependence of the Tanδ for 10 µm macro-porous carbon monolithic sample.

Figure 2.38	IR spectrum of the porous carbon monolith (5 µm pore diameter).
Figure 2.39	Flow through backpressure for the (left) 5 µm and (right) 1 µm & 5 µm carbon monolithic columns in various solvents. (right) Water only.
Figure 3.1	SEM image of the carbon monolith modified with gold nano/micro-particles, **IM1**, produced by monolith immersion technique.
Figure 3.2	SEM images of the carbon monolith modified with gold nano/micro-particles (a) before immersion and (b) after immersion of carbon monolithic rod, **IM5**, in tetrachlorauric acid solution.
Figure 3.3	EDX spectrum of the carbon/gold composite monolith **IM5**.
Figure 3.4	SEM image of the carbon monolith modified with gold nano/micro-particles by re-circulation of tetrachlorauric acid solution through a carbon monolith, **RC5**.
Figure 3.5	EDX spectrum of the carbon/gold composite monolith **RC5**.
Figure 3.6	Scheme illustrating the formation attempt of the gold sponge within the carbon monolithic structure.
Figure 3.7	SEM image of a carbon monolith modified with gold nano/micro-particles by manual injection of tetrachlorauric acid/dextran mixture into the clad carbon monolithic rod, **MI5**.
Figure 3.8	EDX spectrum of the carbon/gold composite monolith **MI5**.
Figure 3.9	SEM image of the carbon/gold composite monolith **IM5**, (a) before, and (b) after removal of the gold particles through extraction with HNO_3.
Figure 3.10	ICP-OES calibration curve for the gold standards (blank subtracted values).
Figure 3.11	Particle size distribution within the tetrachlorauric acid aqueous solution following passage of through carbon monolithic column, **RC5**.
Figure 3.12	Typical correlogram of gold containing large nano/micro-particles in aqueous solution (~ 400 nm) modified carbon monolithic column, **RC5**.
Figure 3.13	SEM image of the carbon/gold composite monolith, **IM5**, after the attachment of 6 mercaptohexanoic acid.

Figure 3.14	EDX spectrum of the carbon/gold composite monolith, **IM5**, after modification with 6 mercaptohexanoic acid.
Figure 3.15	EDX spectrum of the carbon/gold composite monolith, **RC5**, after modification with 6 mercaptohexanoic acid.
Figure 3.16	(a) SEM image (left), and (b) EDX spectrum (right) of the carbon monolith (1 µm pore diameter) modified with gold paint, **P1**.
Figure 3.17	(a) SEM image (left), and (b) EDX spectrum (right) of the carbon monolith (2 µm pore diameter) modified with gold paint, **P2**.
Figure 3.18	(a) HR-SEM image (left), and (b) EDX spectrum (right) of the carbon monolith (5 µm pore diameter) modified with gold paint, **P5**.
Figure 3.19	(a) SEM image (left), and (b) EDX spectrum (right) of the carbon monolith (10 µm pore diameter) modified with gold paint, **P10**.
Figure 3.20	HR-SEM images of the carbon monolith (5 µm pore diameter) modified with gold paint, **P5**, at magnification of (a) 20 k, (b) 130 k, (c) 200 k and (d) 400 k.
Figure 3.21	SEM image of the carbon/silver composite monolith, **S10**.
Figure 3.22	EDX spectrum of the carbon/silver composite monolith, **S10**.
Figure 3.23	HR-SEM image of the carbon monolith (5 µm pore diameter) after the modification attempt with gold nano-particles (5 nm particle size).
Figure 3.24	HR-SEM image of the meso-porous carbon monolith (5 µm pore diameter) following attempted modification with gold nano-particles (5 nm particle size), (a) at magnification 9 k. (b) at magnification 18 k.
Figure 3.25	The results of EDX analysis of the carbon monolith (5 µm pore diameter) following attempted modification with gold nano-particles (5 nm particle size) prepared by immersion in colloid gold suspension for 48 h.
Figure 3.26	The UV spectra of the gold nano-particle colloid suspension (5 nm particle size) (a) before, and (b) after modifying the carbon monolithic rod (5 µm pore diameter).
Figure 4.1	Typical 5 µm templated glassy carbon monolithic rod (50 x 6 mm i.d.) housed in PEEK tubing.

Figure 4.2	Overlaid chromatograms of toluene, ethylbenzene and butylbenzene (500 µg/mL standard concentration). Column: glassy carbon monolith 5 µm pore size (50 x 6 mm i.d.). Mobile phase: 100% methanol, flow rate: 1.0 mL/min and UV detection: 270 nm.
Figure 4.3	Chromatograms of toluene (500 µg/mL and 100 µg/mL standard concentration). Column: glassy carbon monolith, 5 µm pore size (50 x 6 mm i.d.). Mobile phase: 100% acetonitrile, flow rate: 1.0 mL/min and UV detection: 270 nm.
Figure 4.4	Chromatogram of a toluene (1 µg/mL standard concentration). Column: glassy carbon monolith 5 µm pore size. Mobile phase: hexane, flow rate: 0.7 mL/min and UV detection: 270 nm.
Figure 4.5	Chromatogram of an ethylbenzene (1 µg/mL standard concentration). Column: glassy carbon monolith, 5 µm pore size (50 x 6 mm i.d.). Mobile phase: hexane, flow rate: 0.7 mL/min and UV detection: 270 nm.
Figure 4.6	Chromatogram of a butylbenzene (1 µg/mL standard concentration). Column: glassy carbon monolith, 5 µm pore size(50 x 6 mm i.d.). Mobile phase: hexane, flow rate: 0.7 mL/min and UV detection: 270 nm.
Figure 4.7	Chromatogram of a toluene-ethylbenzene-butylbenzene mixture (1 µg/mL standard concentration). Column: glassy carbon monolith, 5 µm pore size(50 x 6 mm i.d.). Mobile phase: hexane, flow rate: 0.7 mL/min and UV detection: 270 nm.
Figure 4.8	Overlaid chromatograms of toluene and alkylbenzenes mixture (1 µg/mL) in hexane on a 5 µm templated glassy carbon monolithic column (50 x 6 mm i.d.) using hexane as mobile phase, flow rate was 0.7 mL/min and UV detection was performed at 270 nm.
Figure 4.9	Overlaid chromatograms of alkylbenzenes (toluene, ethylbenzene and butylbenzene) (1 µg/mL) in hexane on a 5 µm templated glassy carbon monolithic column (50 x 6 mm i.d.) using hexane as mobile phase, flow rate was 0.7 mL/min and UV detection was performed at 270 nm.

Figure 4.10	Elution profile of alkylbenzenes mixture (1 µg/mL) in pentane on a 5 µm templated glassy carbon monolithic column (50 x 6 mm i.d.) using pentane as mobile phase, flow rate was 0.7 mL/min and UV detection was performed at 270 nm.
Figure 4.11	Overlaid chromatograms of individual alkylbenzene standards and alkylbenzenes mixture (1 µg/mL) in 100% pentane on a 5 µm templated glassy carbon monolithic column (50 x 6 mm i.d.).
Figure 4.12	Typical 5 µm macro-porous carbon monolithic column (30 x 6 mm i.d).
Figure 4.13	Chromatogram of butylbenzene (100 µg/mL) on a 5 µm templated acid washed glassy carbon monolithic column (30 x 6 mm i.d.) using 100% pentane as mobile phase, flow rate was 1 mL/min and UV detection was performed at 254 nm.
Figure 4.14	Partial separation of butylbenzene and acetophenone (100 µg/mL) in hexane on a 30 x 6 mm i.d. 5µm templated acid washed glassy carbon monolithic column using hexane as mobile phase, flow rate was 1 mL/min and UV detection was performed at 254 nm.
Figure 4.15	Partial separation of butylbenzene and nitrobenzene (100 µg/mL) in hexane on a 5µm templated acid washed glassy carbon monolithic column (30 x 6 mm i.d.) using hexane as the mobile phase, flow rate was 1 mL/min and UV detection was performed at 254 nm.
Figure 4.16	The dependence of *k* on surface treatment on a 5 µm templated glassy carbon monolithic column (30 x 6 mm i.d.) treated with mineral acids.
Figure 4.17	The typical image of the carbon monolithic column (1 µm pore diameter), 75 x 6 mm i.d encased within epoxy resin.
Figure 4.18	Overlaid chromatograms of 50 µg/mL of hexane, butylbenzene, acetophenone and nitrobenzene on a 10 µm templated glassy carbon monolithic column (75 x 6 mm i.d.) using hexane as mobile phase, flow rate of 1 mL/min and UV detection was performed at 254 nm.
Figure 4.19	Overlaid chromatograms of nitrobenzene (50 µg/mL) on a 10 µm templated glassy carbon monolithic column (75 x 6 mm i.d.).

Figure 4.20	Chromatograms of nitrobenzene (50 µg/mL) before and (100 µg/mL) after acid treatment of the a 10 µm templated glassy carbon monolithic column (75 x 6 mm i.d.) with sulphuric and nitric acid. Mobile phase: hexane, flow rate of 1 mL/min and UV detection was performed at 254 nm.
Figure 4.21	The typical image of the 1 µm templated carbon monolithic column (73 x 4 mm i.d.) encased within epoxy resin.
Figure 4.22	Chromatograms of butylbenzene (50 µg/mL) and acetophenone (50 µg/mL) on a 1 µm templated glassy carbon monolithic column (73 x 4 mm i.d.). Mobile phase: hexane, flow rate of 0.5 mL/min and UV detection was performed at 254 nm.
Figure 4.23	Elution profile of acetophenone (50 µg/mL) on a 1 µm templated glassy carbon monolithic column (73 x 4 mm i.d.) before and after acid treatment. Mobile phase: hexane, flow rate was 0.5 mL/min and UV detection was performed at 254 nm.
Figure 4.24	The dependence of backpressure of the carbon/gold composite monolithic column (5 µm pore diameter) on flow rate in various solvents.
Figure 4.25	Retention of imidazole (1 µg/mL) (prepared in1 m*M* acetate buffer) on a gold-mercaptohexanoic acid modified 5 µm templated glassy carbon monolithic column (30 x 6 mm i.d). Mobile phase: 1 m*M* acetate buffer, flow rate was 1 mL/min and UV detection was performed at 280 nm.
Figure 4.26	Chromatogram of imidazole (50 µg/mL) on a gold-mercaptohexanoic acid modified 1 µm templated glassy carbon monolithic column (73 x 4 mm i.d.) using 1 m*M* of acetate buffer (pH 5.71) as the eluent, flow rate was 1 mL/min and UV detection was performed at 280 nm.
Figure 4.27	Chromatogram of histidine (50 µg/mL) on a gold-mercaptohexanoic acid modified 1 µm templated glassy carbon monolithic column (73 x 4 mm i.d.) using 1 m*M* of acetate buffer (pH 5.71) as the eluent, flow rate was 1 mL/min and UV detection was performed at 280 nm.

Figure 4.28	Chromatograms showing the influence of temperature on retention of imidazole. Column: gold-mercaptohexanoic acid modified 1 μm templated glassy carbon monolithic column (73 x 4 mm i.d.) over 15 to 60 ^{o}C using a 1 m*M* acetate buffer (pH 5.71) as the eluent, flow rate was 1 mL/min and UV detection was performed at 211 nm.
Figure 4.29	The retention dependence on column temperature for imidazole on a gold-mercaptohexanoic acid modified 1 μm templated glassy carbon monolithic column (73 x 4 mm i.d.).
Figure 4.30	The efficiency (*N*) dependence on column temperature for imidazole on a gold-mercaptohexanoic acid modified 10 μm templated glassy carbon monolithic column (73 x 4 mm i.d.).
Figure 4.31	Elution profile for resorcinol on a carbon/gold composite monolith (1 μm pore size) modified with 6-mercaprohexanoic acid mercaptohexanoic acid using a 1 m*M* acetate buffer (pH 5.71) as the eluent, flow rate was 1 mL/min and UV detection was performed at 211 nm.
Figure 4.32	The retention dependence on column temperature for resorcinol on a gold-mercaptohexanoic acid modified 1 μm templated glassy carbon monolithic column (73 x 4 mm i.d.).
Figure 4.33	The increase of retention of imidazole on a gold-mercaptohexanoic acid modified 10 μm templated glassy carbon monolithic column (75 x 6 mm i.d.) over 20 to 60 ^{o}C.
Figure 4.34	The retention dependence on column temperature of of imidazole on a gold-mercaptohexanoic acid modified 10 μm templated glassy carbon monolithic column (75 x 6 mm i.d.).
Figure 4.35	Elution profile for resorcinol on a carbon/gold composite monolith (10 μm pore size) modified with 6-mercaprohexanoic acid mercaptohexanoic acid using 1 m*M* of acetate buffer (pH 5.71) as the eluent, flow rate was 1 mL/min and UV detection was performed at 211 nm.
Figure 4.36	The retention dependence on column temperature for resorcinol on a gold-mercaptohexanoic acid modified 10 μm templated glassy carbon monolithic column (75 x 6 mm i.d.).

Figure 5.1	(a) Typical PGC monolithic rod, (b) Typical PGCME electrode.
Figure 5.2	Cyclic voltammogram of 10 m*M* $Fe(CN)_6^{3-}$ on a commercial 1 mm glassy carbon in PEEK. Scan rate: 20 mV/s.
Figure 5.3	(Left) Cyclic voltammograms on a (a) bare glassy carbon electrode and (b) on an Au/glassy carbon electrode, in 0.1 *M* phosphate buffer solution at at 100 mV/s. (Right) HR-SEM image of the Au/GCE surface. Reproduced from [13].
Figure 5.4	Cyclic voltammogram on a bare 5 µm templated PGCME in 1 *M* KCl, at scan rate of 20 mV/s.
Figure 5.5	Cyclic voltammetry on a 10 µm templated PGCME in the presence of ferricyanide (1 *M* KCl), at a scan rate of 20 mV/s.
Figure 5.6	Cyclic voltammetry on a 5 µm templated PGCME in the presence of ferricyanide (1 *M* KCl), at a scan rate of 20 mV/s.
Figure 5.7	SEM image of the surface of the Au/PGCME.
Figure 5.8	EDX spectrum of the surface of the Au/PGCME.
Figure 5.9	Cyclic voltammograms of (a) Au/glassy carbon electrode in the absence and (b) in the presence of of nitrite ions. (c) bare glassy carbon electrode in the presence of 1×10^{-4} *M* NO_2^- in 0.2 *M* acetate buffer solution at 100 mV/s. Reproduced from [13].
Figure 5.10	Cyclic voltammogram of 5 µm modified Au/PGCME in the absence of ferricyanide (1 M KCl), at 20 mV/s.
Figure 5.11	Cyclic voltammetry on a 5 µm templated Au/PGCME, in the presence of ferricyanide (1 *M* KCl), at a scan rate of 20 mV/s.

List of Tables

Table 2.1	Standard deviation and relative standard deviation of silica particles.
Table 2.2	Surface area and pore volumes measurements of the silica particles and carbon monoliths, before and after pyrolysis.
Table 2.3	Resistance measurements for the glassy carbon; 1, 2, 5, and 10 µm (pore diameter) templated carbon monoliths and graphite.
Table 2.4	Electrical conductivity calculated for the glassy carbon; 1, 2, 5, and 10 µm (pore diameter) templated carbon monoliths and graphite.
Table 2.5	Surface area, pore volume, shrinkage, weight loss, pore size and conductivity measurements of the carbon monoliths after pyrolysis and removal of the silica particles.
Table 3.1	The results of EDX for the carbon/gold composite monolith, **IM5.**
Table 3.2	The results of EDX for the carbon/gold composite monolith, **RC5.**
Table 3.3	Intensities of the gold standards and unknown samples.
Table 3.4	The results of the gold micro-particle parameters measurements after modification of carbon monolithic column, **RC5.**
Table 3.5	The results of EDX for of **IM5** and **RC5** modified with 6 mercaptohexanoic acid.
Table 3.6	The results of EDX for of **P1**, **P2**, **P5** and **P10.**
Table 3.7	Resistance measurements for the modified carbon/gold composite monoliths, **IM5** and **P5**.
Table 3.8	Conductivity measurements of the carbon monoliths, carbon/gold composite monoliths, glassy carbon, **IM5** and **P5**.
Table 3.9	The results of EDX for the carbon/silver composite monolith, **S10.**
Table 3.10	The results of EDX for the carbon monolith (5 µm pore diameter) modified with gold nano-particles (5 nm particle size).
Table 3.11	Element : Carbon ratio of the metal/carbon composite monoliths.
Table 4.1	Retention, retention factor and efficiency data for a range of alkylbenzenes on 5 µm templated glassy carbon monolithic column (50 x 6 mm i.d.) using a hexane as the mobile phase.

Table 4.2	Retention, efficiency, peak symmetry, resolution and selectivity data for butylbenzene and acetophenone on an acid washed templated glassy carbon monolithic column, (30 x 6 mm i.d.), 5 μm pore size.
Table 4.3	Retention, efficiency, peak symmetry, resolution and selectivity data for butylbenzene and nitrobenzene on a 5 μm templated acid washed glassy carbon monolithic column, 30 x 6 mm i.d.
Table 4.4	Functional group present on the surface of the carbon monolith.
Table 4.5	Retention factor values for test solutes on a 5 μm glassy carbon monolith (30 x 6 mm i.d.) following surface modification with mineral acids.
Table 4.6	Retention factor values for nitrobenzene on an encased glassy carbon monolithic column (10 μm pore size).
Table 4.7	The dependence of retention on temperature for imidazole on the weak cation exchange modified monolith.
Table 4.8	The dependence of efficiency on temperature for imidazole on a mercaptohexanoic acid modified gold/carbon monolith.
Table 4.9	Surface area and pore volume measurements of the carbon monoliths after pyrolysis.
Table 4.10	The dependence of A_s and T_f on pore diameter of 1 and 5 μm carbon monolithic columns.
Table 4.11	The dependence of retention on temperature for imidazole on the weak cation exchange modified monolith.

List of Equations

Eq. 1.1	Surface area (A) of the solid.
Eq. 2.1	The percentage decrease of weight, $WL(\%)$, from weight of sample before (W_{raw}) and after (W_{carb}) carbonisation.
Eq. 2.2	The percentage reductions in dimensions $RD(\%)$ after carbonisation.
Eq. 2.3	The cross sectional area.
Eq. 2.4	The resistivity of a sample.
Eq. 2.5	Conductivity σ (*sigma*), of the sample.
Eq. 4.1	The retention factor, k.

Publication

1. "Preparation, characterisation and modification of glassy carbon based monolithic rods for chromatographic applications".

Ali H.Eltmimi, Aran Rafferty, Pavel N. Nesterenko, John P.Hanrahan, Leon Barron and Brett Paull, *Journal of Materials Chemistry,* 200X, XXX, XXX-XXX.

List of Oral Presentations

1. Talk on 11-13 Jun 2008 at the 60th Irish Universities Chemistry Research Colloquium, University College Cork, Cork, Ireland. Titled: "Preparation and Characterisation of Carbon Monolithic Phases for Chromatographic Applications".
Ali Eltmimi, Aran Rafferty, Pavel N. Nesterenko, John P.Hanrahan, Leon Barron and Brett Paull

2. Talk on 21-23 July 2008 at the Analytical Research Forum 2008, University of Hull, Hull, UK. Titled: "Preparation, Characterisation and Modification of Carbon Monolithic Phases for Chromatographic Applications".
Ali Eltmimi, Aran Rafferty, Pavel N. Nesterenko, John P.Hanrahan, Leon Barron and Brett Paull

3. Talk on 02-05 December 2008 at the 33rd International Symposium on High Performance Liquid Phase Separations and Related Techniques, Kyoto University, Kyoto, Japan. Titled: "Modified Carbon Monolithic Columns for Chromatographic Applications".
Ali Eltmimi, Aran Rafferty, Pavel N. Nesterenko, John P.Hanrahan, Leon Barron and Brett Paull

List of Poster Presentations

1. "Carbon Monolithic Materials for Chromatographic Application".
Ali Eltmimi, Aran Rafferty, Pavel N. Nesterenko, John P.Hanrahan, Leon Barron and Brett Paull
4th Biennial Conference on Analytical Sciences in Ireland, 11-12 April, 2006, Dublin Institute of Technology, Dublin, Ireland.

2. "Carbon Monolithic Materials for Chromatographic Application".
Ali Eltmimi, Aran Rafferty, Pavel N. Nesterenko, John P.Hanrahan, Leon Barron and Brett Paull
Analytical Research Forum 2006, 17-19 July, 2006, University College Cork, Cork, Ireland.

3. "Carbon Monoliths Modified with Gold and Silver Nanoparticles as Stationary Phases for Chromatographic Applications".
Ali Eltmimi, Aran Rafferty, Pavel N. Nesterenko, John P.Hanrahan, Leon Barron and Brett Paull
31st International Symposium on High Performance Liquid Phase Separations and Related Techniques, 17-21 June, 2007, International Convention Centre, Ghent, Belgum.

4. "Modified Graphitised-Carbon Monolithic Columns for Chromatographic Applications".
Ali Eltmimi, Aran Rafferty, Pavel N. Nesterenko, John P.Hanrahan, Leon Barron and Brett Paull
Analytical Research Forum 2007, 16-18 July, 2007, University of Strathclyde, Glasgow, UK.

5. "Gold Modified Carbon Monolithic Columns for Chromatographic Applications".
Ali Eltmimi, Aran Rafferty, Pavel N. Nesterenko, John P.Hanrahan, Leon Barron and Brett Paull
21st International Ion Chromatography Symposium, 21-24 September, 2009, Grand Hotel Malahide, Dublin, Ireland.

List of Honours and Awards

1. Winner of a travel grant from the Royal Society of Chemistry to present my poster at the 31st International Symposium on High Performance Liquid Phase Separations and Related Techniques on 17-21 June, 2007, Ghent, Belgium. Titled: "Carbon Monoliths Modified with Gold and Silver Nanoparticles as Stationary Phases for Chromatographic Applications".
http://www.rsc.org/ScienceAndTechnology/Funding/OverseasConference/index.asp.

2. Winner of the Top Poster Prize (from 111 posters) at the Analytical Research Forum 2007, 16-18 July, 2007, University of Strathclyde, Glasgow, UK. Titled: "Modified Graphitised-Carbon Monolithic Columns for Chromatographic Applications".

3. Winner of a travel grant (from ~ 500 delegates) from the Society for Chromatographic Sciences to present my talk at the 33rd International Symposium on High Performance Liquid Phase Separations and Related Techniques, 02-05 December, 2008, Kyoto University, Kyoto, Japan. . Titled: "Modified Carbon Monolithic Columns for Chromatographic Applications".
http://anchem.mc.kyoto-u.ac.jp/hplc2008kyoto/index.html.

Acknowledgements

Thank Allah

Many people are responsible for my completion of this project. First and foremost, I am pleased to acknowledge the marvellous guidance of the director of this research, Professor Brett Paull.

Special thanks to Dr Aran Rafferty, Deptartment of Chemistry, Trinity College Dublin for his excellent supervision in regard to the characterisation of the carbon monolith materials.

My thanks are extended to the following: my co/supervisor Professor Pavel Nesterenko, ACROSS-Australian Centre for Research on Separation Science, School of Chemical Sciences, University of Tasmania, Australia; Dr Leon Barron, Dr. Silvija ABELE, and to all members in our such a great research group; the Chemical Services Unit in the School of Chemical Sciences especially Dr Brendan Twamley, Veronica Dobbyn, Damien McGuirk, Maurice Burke, Ambrose May in the store for their help and assistance and to Science Foundation of Ireland (SFI) for the grant. A big thank you to Dr Ekaterina Nesterenko for her kind help and great assistance during the writing up of my thesis. Also, great thanks to Ms Julie McArthur at the School of Chemical Sciences office for her fabulous co-operation during my course. Great thanks to Dr Dermot Brougham and his research group in lab XG 36, particularly Dr Jacek Stolarczyk and Ms Sarah Clarke for using the Zetasizer technique to characterise the particle size of my samples. Also special thanks to Mr Liam Domican, chief technical officer, Mr Jim Barry, senior technical officer and Mr Cian Merne, senior technical officer at the School of Manufacturing and Mechanical Engineering for great help in fabrication of the carbon monolithic columns. Also a big thank you to Dr Mohammed Al-Amiry, UK for his valuable guides during my MSc studies and the beginning of PhD course.

I also would like to thank my family (mother, sisters and brothers) in Iraq; my family here in Ireland (in particular my father in-law Dr Hassan Al-Alak and Said Malek Al-Alak) and my relatives there in Iraq (especially Dr Abd Alzahra'a Al-Alak and Said Salem Al-Alak) for their kind help in continuing my education to post-graduate level. Also great thanks to my friends: Mustafa Ramadhan (Ireland), Mohammed Al-Sa'adi (Yemen), and all my friends in Iraq, (Said Mohammed Witwit, Khaleel Ibrahim, Saeed Mahmoud and Muhsin Ali (Baghdad)), Said Ahmed Al-

Awadi and Ali Faisal (Al-Diwaniyah), Ahmed Add Al-Razzaq (Al-Basrah), Qusai Abid Assim, Dr Majid Jari and Said Hassan Jassim (Al-Kufa) for their encouragement and honest friendship. Great thanks for my real friend Kamil Jabbar for our special and exceptional brotherhood and for his very kind, actual and moral support to me during my studies. Kamil is considered to be a real brother to me.

Above all, I would like to thank my great father and lovely brother Abbass (Abu Haider) for their support and encouragement in this work, unfortunately, they did not live to see me complete it and all the other people who made this possible in my ten years as an exile from home.

Ali Eltmimi

Abstract

Chromatographic column technology in HPLC is an ever-growing field. One area in column technology that has captivated attention in recent years is the use of monolithic columns. Monolithic stationary phases for use in liquid chromatography possess unique characteristics, the most significant of which is a relatively high flow through porosity leading to low column pressure drops, with the potential for use with elevated flow rates leading to faster separations. Silica-based monolithic columns are the most popular phases currently for small molecule separations, although organic polymer-based monoliths have also been studies extensively.

Within this thesis the preparation of carbon monoliths of varying flow through porosity for potential chromatographic and electrochemical applications is described. Carbon based monoliths can provide excellent chemical and thermal stability, surpassing those of silica. Unlike alternative materials, carbon monoliths have the advantage of being resistant to swelling and hydrolysis.

Carbon monolithic rods produced within this work were characterised using diverse techniques such as SEM/EDX, BET, dilatometry, conductivity & backpressure determination and investigated for chromatographic application. Surface modification of the resultant carbon monoliths with gold nano-particles and nano-layers was carried out for further modification with thiol based affinity and exchange chemistries.

Retention on the carbon monolithic phases was investigated using reversed- and normal-phase high performance liquid chromatography. Preliminary separations of mixtures of hydrophobic molecules (alkylbenzenes) on a short 5 µm pore sized glassy carbon monolithic column were carried out using a mobile phase of 100% hexane (or pentane), flow rate 0.7 ml/min, UV detection 270 nm. The backpressure for the monolithic phase was 2 bar. Also, preliminary separations of mixtures of hydrophilic molecules (caffeine, theophylline and benzoic acid) using various concentrations of acetonitrile as a mobile phase were investigated on the same column. Furthermore, preliminary separations of mixtures of butylbenzene–acetophenone, and butylbenzene-nitrobenzene, respectively, on a same column column were also carried out using a mobile phase of 100% hexane (or pentane), flow rate 1 ml/min, UV detection 254 nm, with an injection volume 15 µL. The backpressure for the monolithic phase ranged between 5 and 8 bar.

To improve retention, surface modification (conditioning) of the glassy carbon monolith was performed using 0.5 and 2 *M* solutions of sulphuric acid, followed by a similar strength solution of 50:50 sulphuric:nitric acid. Following such conditioning the retention factors for the mixture of butylbenzene and nitrobenzenene were significantly increased under normal phase conditions, indicating increased surface polarity on the glassy carbon monolith.

The formation of metallic monolithic structures within the actual larger flow through pores (5-10 μm) of the carbon rods was also studied, leading to the formation of novel gold modified carbon monolithic phases. The carbon/gold composite monolithic columns were further modified with mercaptohexanoic acid and evaluated for retention characteristics in ion exchange chromatography. Imidazole (1 μg/mL) was injected onto the 5 μm pore sized gold modified glassy carbon monolithic column and was shown to be retained through ion-exchange chromatography using a 1 m*M* acetate buffer mobile phase (pH 3.96) at a flow rate of 1 mL/min, with UV detection at 280 nm. The column backpressure was 24 bar.

Carbon monoliths have the advantage of being conductive materials and were therefore also investigated as electrode materials for electrochemical analysis. Electrochemical measurements obtained on the porous glassy carbon monolithic electrode and gold modified porous glassy carbon monolithic electrode showed a more reproducible response relative to the standard glassy carbon electrode. The electrode was investigated using cyclic voltammetry following electrochemically induced oxidation to impart hydrophilicity. Cyclic voltammetry was investigated using a solution containing $K_3Fe(CN)_6$ and KCl between -0.2 and +1.1 V. The scan rate used for the above characterisations was 20–100 mV/s.

CHAPTER ONE

Development of Monolithic Materials in Chromatography

Porous monolithic materials have found many uses in various fields of science, catalysis [1-6], filtration [7-9], electrochemistry [10-12], and separation sciences [13-15].

Such monolithic materials have been prepared in various forms for chromatographic applications since the 1970s, including in the shape of discs, stacked layers, rolled sheets, sponges, irregular chunks, tubes, and cylinders [16]. An extensive range of materials have been used to prepare these novel monolithic forms, such as natural polymers (cellulose), synthetic polymers (porous styrene-, methacrylate-, and acrylamide-based polymers), and inorganic materials (silica). Significant attention has been paid to the applications and specific fluidic and surface properties of this range of monolithic materials.

Separation of different compounds in liquid chromatography (LC) is usually achieved using micro-particle packed columns (1 to 10 μm), which provide large surface areas to interact with the solutes from within the mobile phase. Despite the dominant use of packed columns historically, a new range of monolithic materials have been recently introduced as chromatographic separation medium offering alternative chromatographic performance and selectivity [13-15].

1.1. Monolithic stationary phases for chromatography

In chromatography band broadening occurs due to,

1. The presence of multiple flow paths of different length and velocity
2. Slow equilibration between phases, especially in nm-size pores
3. Solute diffusion in the mobile phase

The use of smaller particles (1-3 μm) in particle packed columns reduces the contribution of factors 1 and 2 to overall band broadening, leading to faster equilibration and narrower bands, and as result, higher efficiency (*N*). However, the

main disadvantage of this approach is a high pressure drop which is inversely proportional to the particle diameter squared. Monolithic columns, having a total porosity of about 80%, show much lower backpressures in comparison to packed particle-based columns, with a porosity of about 65%. Thus, due to higher porosity, monolithic columns are considered to be compatible with high flow rates. The use of such micro-particle packed columns, which generate such ultra high backpressures, require special instrumentation (so-called ultra high performance liquid chromatography-UHPLC) and often high temperatures.

Monolithic columns on the other hand can potentially provide chromatographic performance close to that of UHPLC using common instrumentation. A monolithic column can be defined as a column consisting of one single porous rod that has single interconnected skeletons and interconnected flow paths. The first monolithic columns introduced were initially organic polymer-based [17].

The main features of monolithic columns are,

1. The continuous one-piece structure, which does not require frits to maintain its structure and provides high mechanical stability.
2. A high porosity which provides high permeability.
3. A small skeleton and presence of large through-pores allowing use of high flow rates, which can result in faster separation capability.

Possessing the above characteristics, monolithic materials can therefore be applied to high *N* and high speed separations, often beyond the limit of particle packed columns, and have been utilised as high performance miniaturised columns [18] for high performance liquid chromatography (HPLC) and phases within microfluidic chips [19]**.** For example, as a new stationary phase in the shape of a flat "membrane", Tennikova *et al.,* [20] developed a new thin monolithic disk technology suitable for the separation of proteins and based upon a polymer monolith. The novel concept of such short monolithic rigid disks has been both theoretically [21-23] and practically [20], [24] employed.

The following charts show how interest in monolithic technologies has grown tremendously since early 1990's (Figure 1.1).

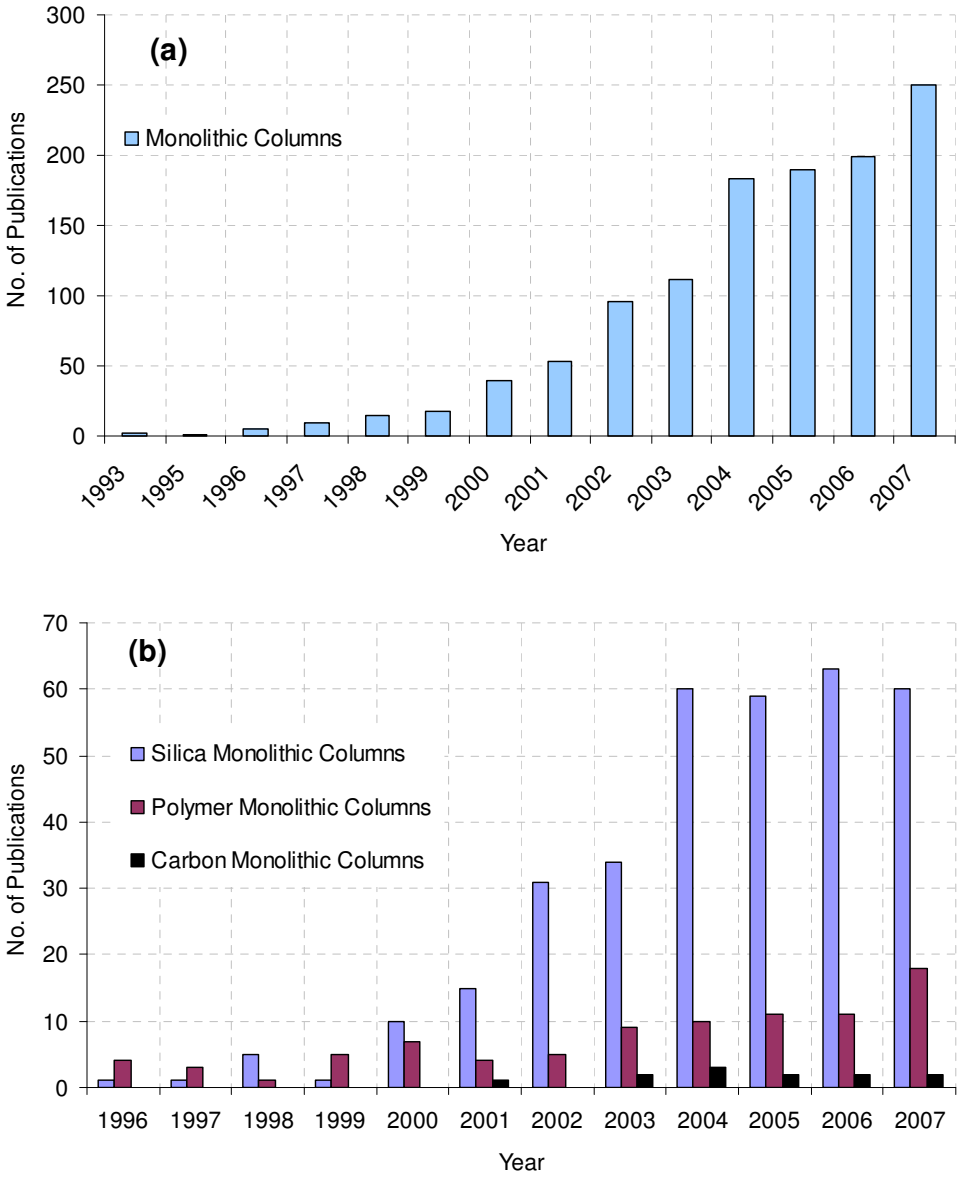

Figure 1.1. (a) Monolithic column based publications from 1993 to 2007 (b) Silica, polymer and carbon monolithic column publications from 1996 to 2007 using SciFinder Scholar, Version 2008, American Chemical Society.

1.2. Classification of monolithic columns

Organic polymers (polymethacrylate, polystyrenes or polyacrylamides-based) and inorganic polymers (silica, zirconia, titania) have been used to produce monolithic columns for chromatography. Accordingly, monolithic columns can be divided into two categories: inorganic-based (often silica based) monolithic columns and organic polymer-based monolithic columns. Legido-Quigley *et al.,* [25] reported a review on the chemistry and most recent applications of these various types of monoliths, as alternatives to traditional packed columns, for use in both capillary electrochromatography (CEC) and micro-high performance liquid chromatography (μ-HPLC).

As an alternative to the above main classes of monolithic columns, carbon monoliths have the potential to be ideal phases for chromatography, plus additional uses as catalyst supports, adsorbents and porous electrodes under continuous flow conditions.

1.2.1. Silica monolithic phases

One of the earliest attempts to produce monolithic silica phases was in the late 1970s, when the first continuous porous silica-based foam was reported by Pretorious *et al.*, [26] as a chromatographic support for gas chromatography (GC). In 1991, a technique for the production of porous silica monoliths by the hydrolysis and gelation of alkoxysilane solution containing poly(sodium styrenesulfonate) was described by Nakanishi and Soga [27], and used for HPLC applications. Problems in processing restricted more developments until 1996, where silica monoliths prepared by Minakuchi *et al.,* [28] exhibited a very narrow distribution of pores with biporous structure and high permeability making them ideal phases for further chromatographic application. The SEM image in Figure 1.2 shows the porous silica monolithic structure prepared by Minakuchi *et al.* [28]. This porous silica monolithic rod prepared (83 mm long) showed a slight tailing and lower performance for small molecules, despite producing 8000 theoretical plates with a HETP of 10 μm.

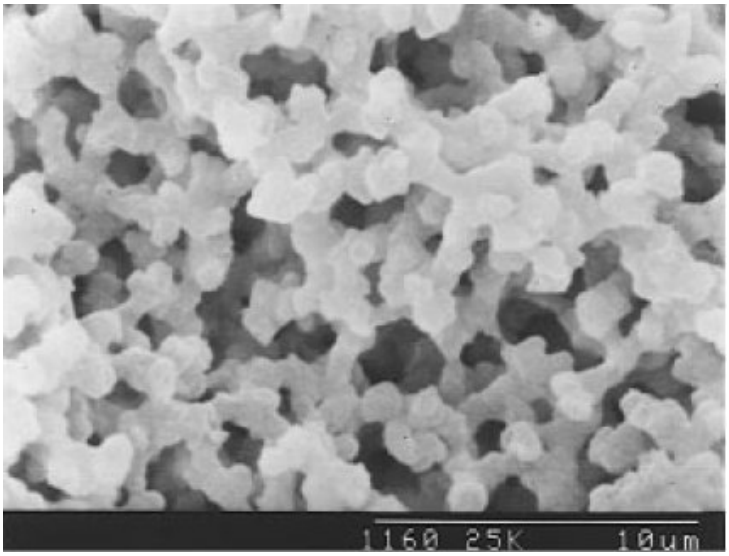

Figure 1.2. SEM image of a porous monolithic silica rod prepared by polycondenstion. Reproduced from [28].

An alternative technique for the production of silica-based monoliths for HPLC was reported by Fields [29] in 1996, whereby a silica xerogel column was synthesised inside a 130 mm x 0.32 mm i.d. fused silica tube using a potassium silicate solution and further derivatised with dimethyloctadecylchlorosilane. This column was investigated using ethyl benzoate and naphthalene with on-line UV detection. However, this column was neither homogeneous nor efficient (5000 plates per meter). The xerogel morphology prepared by Fields *et al.*, [29] showed heterogeneity, despite exhibiting reasonable chromatographic efficiency. The resultant structure of the column was irregular, as a consequence, a wide distribution of flow paths and mean diffusional distances were obtained. The total column efficiency should significantly improve by producing a structure with narrower distributions. The column capacity can be improved by either coating the column with polysiloxane film or coating a porous silica layer as developed and reported by Guo and Colon [30] for HPLC. Additional improvement of more homogeneous structures is an essential to provide even higher efficiency performance. Scanning electron microscopy (SEM) images of the xerogel (Figure 1.3) showed a continuous structure which was bonded to the fused silica column wall through attachment to surface silanols.

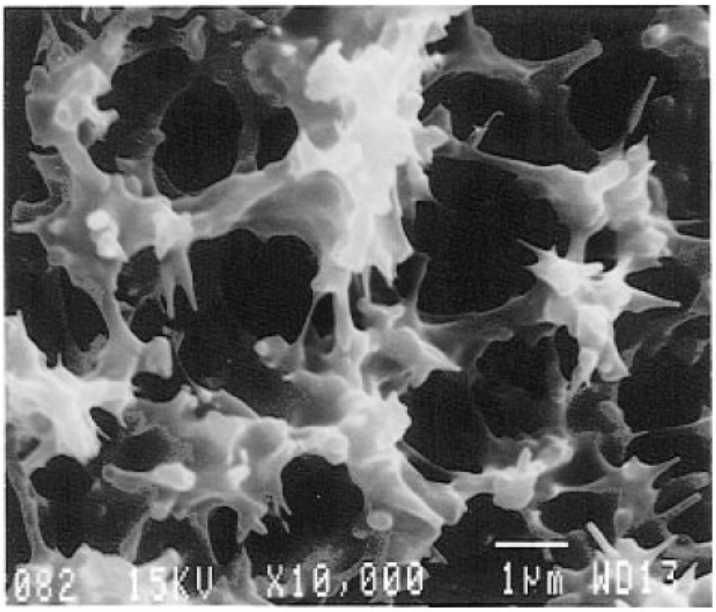

Figure 1.3. SEM image of a silica xerogel column. Scale bar 1 μm. Reproduced from [29].

Inorganic silica-based monoliths can also be prepared via sol-gel techniques [31-36]. However, reduction (shrinkage) of the whole silica structure results from this type of preparation, which takes place in a mould. When a mould of 6 and 9 mm i.d. is used, the diameters of products are ca. 4.6 or 7 mm, respectively. To fabricate a column for HPLC, the resulting silica monoliths should be covered with polytetrafluoroethylene (PTFE) tubing or with a PEEK resin. Column length cannot be longer than 15 cm, as such single long and straight monoliths cannot be readily prepared with the sol-gel technique.

The preparation of monolithic silica column within fused silica capillaries (MS-FS) is relatively straight forward compared to the preparation in a mould and subsequent column fabrication. However, in order to prevent shrinkage of the silica skeleton, the silica network structure has to be bonded to the capillary wall.

Typical preparation conditions for MS-FS columns are as follows [37-38]: tetramethoxysilane (TMOS) is added to a solution of poly(ethylene glycol) and urea in acetic acid and stirred at freezing point (0 ^{o}C) for a set period of time. The fused-silica capillary is treated with a solution of NaOH at elevated temperature for a number of hours in advance, before the resultant homogeneous solution is charged into the capillary and allowed to react at elevated temperature. Within 2 h, gelation

occurs and the gel is subsequently aged overnight at the same temperature. To complete meso-pore formation with ammonia generated by the hydrolysis of urea, the monolithic silica column is treated at higher temperature, e.g. 3 h at 120 ^{o}C [32], followed by washing with water and methanol. Then, the column is dried followed by further heat-treatment, e.g., 330 ^{o}C for 25 h, resulting in decomposition of organic moieties in the capillary. In terms of pressure drop and column efficiency, monolithic columns prepared under the above conditions showed reproducibility of about ±15% and could be used without retaining frits in CEC and in HPLC.

In 2000, Ishizuka *et al.*, [39] prepared a continuous silica gel network using an approach similar to that described above, and produced a highly efficient column (128,000 plates/m) for CEC with large through pores. The SEM image shown in Figure 1.4 shows a typical monolith from Ishizuka's work as formed inside a 100 μm capillary.

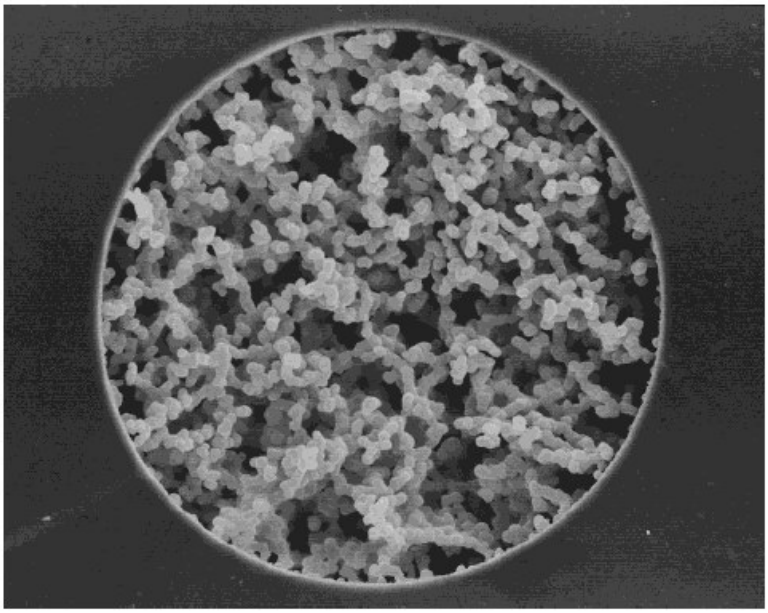

Figure 1.4. SEM image of continuous monolithic silica prepared in a fused-silica capillary. Capillary diameter, 100 μm. Reproduced from [39].

SEM images of monolithic silica columns prepared for HPLC application, shown in Figure 1.5, illustrate that both the silica skeletons and the through-pores are continuous [40]. When monolithic silica columns are prepared in a fused silica capillary, the silica network structure has to be bonded to the capillary wall (Figure 1.5 (b)). These silica monoliths can be used as a separation stationary phase directly after preparation or as a reversed phase (RP) substrate after alkyl modification. The

porosity of monolithic silica columns is much greater than that of a typical 3-10 μm particle-packed column. The major difference is seen in interstitial porosities, 65–70% for monolithic silica prepared in a mould and higher than 80% for those prepared in a capillary, compared to 40% for a modern standard 3-5 μm particle-packed column.

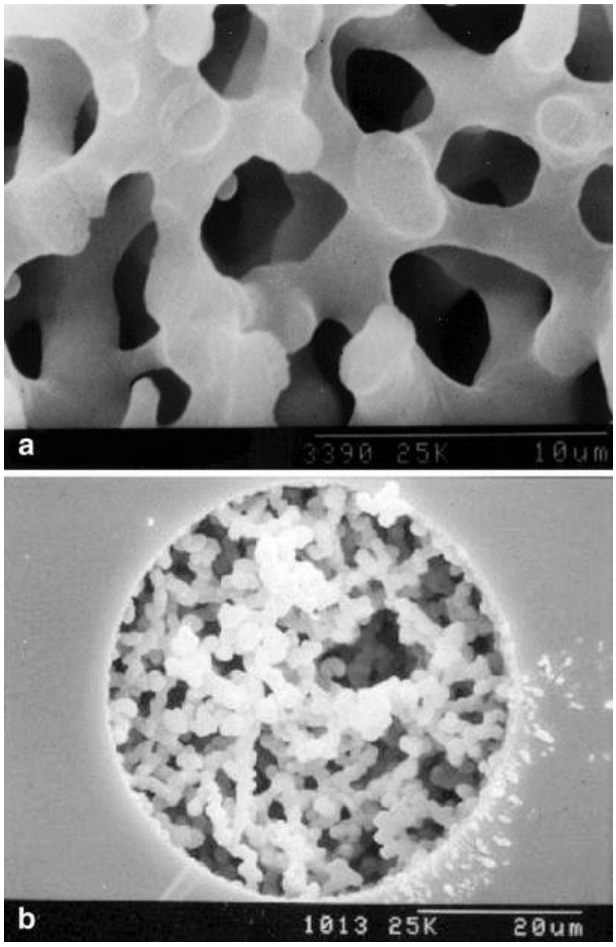

Figure 1.5. SEM images of monolithic silica prepared in a mould (a) and in a 50-μm capillary (b). The bars denote 10 μm in (a) and 20 μm in (b). Reproduced from [40].

Silica-based monoliths have now become commercially available for use in HPLC (Merck Chromolith phases). Based on the Nakanishi and co-worker's original process, silica-based monolithic HPLC columns designed specifically for rapid chromatographic analysis became available from Merck KGaA in 2000 [41-42].

1.2.1.1. HPLC applications of silica monoliths

Monolithic silica columns have been used extensively for different chromatographic applications. For example, Schulte and Dingenen [43] examined for the first time a new type of monolithic silica sorbent for the separation of a diastereomeric drug intermediate. They indicated that the low pressure drop of the monolithic silica in combination with it's high efficiency, even at high flow-rates, allowed the operation of simulated moving bed (SMB) systems at linear velocities of up to 2400 cm h^{-1}. Due to the short diffusion length inside the pore system, adsorption at high flow-rates was not affected and therefore a linear scale-up of all flow-rates up to the maximum system pressure drop was possible. On the other hand selectivity and saturation capacity were comparable to particulate silica.

Spoof and Meriluoto [44] investigated Chromolith RP-18 silica column for rapid separations of microcystins and nodularin with a short total analysis time of just 4.3 min. A complete separation for most toxin analogues was achieved using the Chromolith column compared to that of the amide C_{16} reference column [44]. For comparison, the total analysis time seen in commonly used chromatographic systems for microcystins was 45–60 min. [45-46].

Vallano *et al.,* [47] determined levels of cyclooxygenase II inhibitors in human plasma using the same Chromolith RP silica phase. The Chromolith showed significant reductions in analysis times (up to five-fold) and acceptable column to column reproducibility and ruggedness after nearly 1600 injections of plasma extracts.

Rocheleau *et al.,* [48] compared Chromolith RP-18 columns with different types of conventional HPLC columns and silica particle-based packings, with a combination of mobile phases to achieve the separation of all the impurities of a synthetic taxane. Garrido *et al.,* [49] used the same RP monolithic columns (Chromolith) for the fast separation of chlorophylls *a* and *b* and their demetallated and dephytylated derivatives. Examples of the application of this method to the analysis of these compounds in senescent leaves, ripening fruits and a microalga were studied.

Sugrue *et al.,* [50] used an ion exchange functionalised monolithic silica column for the efficient separation of alkaline earth and transition metal cations in monolithic ion chromatography. O'Riordain *et. al*. [51] and Nesterenko *et al.,* [52],

also used monolithic RP-silica columns dynamically modified with *N*-(dodecyl-*N*,*N*-dimethylammonio)undecanoate as a zwitterionic stationary phase for the efficient separation of inorganic anions and metal cations. The coated silica monolithic columns with *N*-dodecyl-*N*,*N*-(dimethylammonio)undecanoate showed impressive selectivity and *N* values of 29,000 N/m for a 2.5 cm column and 42,000 N/m for the 10 cm monolithic column, under same elution conditions.

For affinity chromatography application, Mallik *et al.*, [53] used a silica monolith (100 x 4.6 mm i.d.) containing immobilised human serum albumin as an alternative to silica particle columns containing the same protein for chiral separations and also as standards for determination of the protein content of the monoliths. This column achieved good *N* with acceptable backpressure under high flow rates, thus, it could be used in other affinity applications that require high flow rates, such as ultrafast immunoextractions or rapid chromatographic immunoassays [54].

As an application for an inverse size exclusion chromatography (ISEC), Thommes *et al.*, [55] successfully prepared and characterised *n*-octadecyl monolithic silica rods for the separation of polymer standards of poly(styrene). This silica monolith showed a type IV isotherm response and revealed a hysteresis loop indicative of pore condensation. Also revealed were a bimodal structure consisted of macro-pores (1800 nm pore diameter) and a meso-pore (10 nm pore diameter).

However, despite the above variety of chromatographic applications, the major obstacle to a wider use of silica-based monolithic columns is their limited resistance to hydrolysis, which restricts their operation to a relatively narrow pH range.

1.2.2. Polymer monolithic phases

At the early stages of production of organic monolithic phases, in 1967, Kubin *et al.,* [17] prepared a continuous polymer matrix for chromatographic separations in size-exclusion mode using a redox free-radical initiating system. The procedure was carried out by polymerisation of 100 mL of 22% aqueous solution of a 2-hydroxyethylmethacrylate containing 0.2% ethylene dimethylacrylate in a 25 mm i.d. glass tube for 24 h at room temperature. The spongy elastic gel was then removed from the tube and heated in water to extract the unreacted compounds. The

prepared rod (22 cm long) was soft and highly swollen and drawn by vacuum in a column and used for the separation of water-soluble polymers.

Later, open pore polyurethane foams were prepared in-situ within the confines of large chromatographic columns [56-57] with various lengths and diameters, which could be readily filled because of the low viscosity of the precursor reagent. The polyurethane structure which was used to prepare the foams adhered tightly to the interior walls of the columns, thus preventing channelling along the support-column wall interface. Another benefit from this foam was that the porosity, density, surface area and flow characteristics could be controlled by varying reaction conditions. This material could be used as a gas-solid, gas-liquid, liquid-liquid and thin layer chromatographic support and the chemical stationary phases could be added either by incorporation with the reactants or by a solution method after the support was formed.

Polyurethane foams prepared by Kubin *et al.,* [17] were capable of being applied to some low pressure separations but exhibited poor permeability. Hileman *et al.,* [58] produced polyurethane foams for HPLC and GC from a mixture containing 4,4'-diphenylmethanediisocyanate and a polyol in various proportions, dissolved in an isodensity solvent composed of 60:40 toluene-carbon tetrachloride mixture. This mixture was transferred into a column tube, sealed, and polymerised at room temperature. The polymerisation reaction was initiated by the tertiary amine functionalities of the polyol component and continued for 18 h upon continuous tumbling which prevented settling of the polymer and eliminated channelling. Once the reaction was finished, the solvent was removed from the pores of the monolith by a nitrogen flush and the column conditioned at 100 ^{o}C for 24 h. However, this monolith exhibited significant solvent instability. One year later, for a LC application, Lynn *et al.,* [59] also used polyurethane monoliths. The columns resisted pressures of up 10 MPa, above which the monolith was detached from the wall and compacted. A backpressure of only 0.2 MPa at a flow rate of 4 mL/min through a 100 x 0.2 cm i.d. column was measured using isopropanol/heptane as a mobile phase indicating good permeability of the monolith for liquids. However, this polyurethane monolith did swell significantly in dimethylformamide.

In 1989, Hjerten *et al.,* [60] prepared continuous polymer beds based upon condensed spongy gels. Such spongy gels and foams found limited application in fast HPLC because they were unable to resist the pressures related to high flow rates [61].

However, this limitation in the spongy gels was resolved by Svec and Frechet [62] when they utilised macro-porous polymer monoliths, structurally more rigid to be applied as efficient stationary phase for HPLC and widely used since for all types of chromatographic separations.

These monolithic polymer materials were prepared using a simple moulding process carried out by polymerisation of a mixture that typically contains monomers, initiator, and porogenic solvent.

These small diameter synthetic polymer monoliths have a substantial advantage in terms of the simplicity of their preparation, as various monomers are available and also various functional groups, which can be covalently bonded onto their surface [63].

However, disadvantages of these early columns, included performance (*N*) of the organic based monoliths for HPLC, which was relatively poor compared to standard HPLC, as most organic chromatographic materials do not match the mechanical strength of typical chromatographic silicas. Some organic monoliths also showed excessive swelling when typical HPLC solvents were used.

1.2.2.1. HPLC applications of polymer monoliths

Applications of polymer monolithic materials have been demonstrated in the chromatographic separation of biological compounds and synthetic polymers, electrochromatography, gas chromatography, enzyme immobilization, and in advanced detection systems.

In the literature, a variety of organic polymer-based monoliths have been evaluated under micro-liquid chromatography conditions [64-66]. Peters *et al.,* [67] reported that rigid macro-porous polymer monoliths possess a number of unique properties compared to their more traditional corresponding macro-porous silica. Petro *et al.,* [68-69] used polymer monolithic columns (50 x 8 mm long) based upon modified poly(glycidyl methacrylate-co-ethylene dimethacrylate) or poly(styrene-*co*-divinylbenzene) rods, for the separation of styrene oligomers and polymers using HPLC. Excellent separations were obtained using a solvent gradient composed of water, methanol, or acetonitrile and increasing amounts of tetrahydrofuran. Xie *et al.,* [70] attempted to separate five proteins in less than 20 seconds using a (4.6 mm i.d.) analytical HPLC organic monolith based on a poly(styrene-*co*-divinylbezene)

polymer. However, the separation was not achieved, apparently due to a lack of selectivity of the styrene stationary phase [70]. Janco *et al.,* [71] used a small monolithic poly(styrene-*co*-divinylbenzene) column, (50 x 4.6 mm i.d.), for the rapid and efficient HPLC separation of polystyrenes, poly(methyl methacrylates), poly(vinyl acetates), and polybutadienes. The separation process involved precipitation of the macro-molecules on the macro-porous monolithic column followed by progressive elution utilising a gradient mobile phase.

An anion-exchange supermacro-porous monolithic column, based on a poly *N*,*N*-dimethylaminoethyl methacrylate grafted monolith was used for the separation and quantification of bovine serum albumin (BSA). Elution was performed with a 1.5 *M* NaCl running buffer. [72]. Zhang *et al.,* [73] analysed the derivatives of aspartate and glutamate by HPLC with fluorescence detection, with monolithic micro-extraction using a poly(acrylamide–vinylpyridine– N,N′-methylene bisacrylamide) monolithic column.

For affinity chromatography, Pan *et al.,* [74] prepared two different monolithic capillary columns by polymerisation of glycidyl methacrylate (GMA) as a monomer and trimethylolpropane trimethacrylate (TRIM) and ethylene dimethacrylate (EDMA) as cross-linkers, respectively. Characterisation of those columns showed that the rod prepared with GMA and TRIM proved to be mechanically more stable than that prepared with GMA and EDMA.

In 2007, Beiler *et al.*, [75] prepared a hydrophilic polymer monolithic column by co-polymerising diethlyleneglycol dimethacrylate (DEGDMA) and 2-hydroxyethylacrylate (HEA) in selected solvents. They also studied the effect of addition of HEA to the DEGDMA/solvent system on the flow characteristics and the porous structure of the resulting monoliths, as well as the utility of such monolithic HPLC columns for the separation of nucleic and amino acids from proteins. Recently, Urban and Jandera [76] published a review on the characterisation and chromatographic applications of polymethacrylate monolithic stationary phases in capillary liquid chromatography, including reversed phase (RP), hydrophobic and hydrophilic interactions, ion-exchange and ion chromatography modes. Separations using immobilised enzymes and sample pre-treatment were also reviewed.

In addition to the number of uses documented for these materials, they also show promise as novel stationary phases in a variety of less common formats such as membranes, capillaries, and media for lab-on-chip devices.

1.2.3. Carbon monolithic phases

Non-graphitised carbon monoliths combine glassy and ceramic properties, are resistant to high temperatures and chemical attack, and impermeable to gases and liquids. Glassy carbon is a composite which consists of unstructured carbon and one or more additional materials, which often result in additional specific properties and chracteristics.

Meso/macro-porous carbon monoliths have great significance in a variety of scientific fields, having the potential to be candidate materials for catalyst support [77], adsorbent applications [78], energy storage [79-80] and electrode materials [10-12]. Such materials have relatively high specific surface areas, large pore volumes, good mechanical stability and chemical inertness. Therefore, synthesis of meso-porous carbons, with a narrow pore size distribution, is currently receiving considerable attention.

One of the main advantages of carbon phases for chromatographic application is that unlike silica-based rods, they are resistant to hydrolysis and can be applied over a wide pH range. Although polymer columns could also overcome this limitation, the swelling of polymer beds in the presence of organic solvents results in poor hydraulic performance. The use of activated carbon adsorbents has long been suggested to solve both of these stability problems, but early results obtained with various kinds of activated carbons were poor as a result of the combination of a weaker than expected mechanical strength, a wide pore-size distribution, and a highly impure surface. Carbon monoliths however, can provide good chemical and thermal stability, and being conductive materials, could also be suitable for potential use in electromodulated liquid chromatography [81].

As early as 1976, Colin *et al.,* [82] demonstrated some attractive properties of graphitised carbon in liquid chromatography. Unfortunately, graphitised carbon black supports showed extremely poor mechanical stability, so were unsuitable for routine chromatographic work. To overcome this limitation, several attempts were carried out to treat graphitised carbon black. The best method was achieved by heating the graphitised carbon black at 900°C in a stream of nitrogen [82]. Later, several groups made other significant contributions [83-93]. Gilbert *et al.,* [87] prepared glassy carbon particles for GC and HPLC by soaking porous silica beads with a phenolic resin, pyrolysing the resin under inert atmosphere, and dissolving the

silica with an alkali. Improved performance was obtained by graphitising the porous glassy carbon. This product is still commercially available. Graphitic carbon is a conductive crystalline material made up of smooth graphene sheets. Its unique structure and physicochemical properties cause carbon-based adsorbents to exhibit a retention mechanism that is completely different from that of conventional RP packing materials [91]. This property enables carbon columns to resolve structurally similar compounds, such as geometric isomers (e.g., anthracene and phenanthrene) and many diastereoisomers [92-93].

For the production of meso-porous carbon monoliths, Yang *et al.*, [94] prepared meso-porous silica monoliths through sol gel process and used it as a hard template. The silica monolith was then impregnated with sucrose solution in the presence of sulphuric acid and dried at 50 ^{o}C. The sample was pyrolysed at 950 ^{o}C under N_2 atmosphere, as a result, a significant shrinkage was observed. Finally, the meso-porous carbon monolith was formed after treatment of the resultant carbon-silica monolith with an aqueous solution of HF acid (10%) and removal of the silica template. Hydrofluoric acid has the ability to dissolve metal oxides and this is the bases of many applications such as glass etching. Hydrofluoric acid attacks glass and silica surfaces by reaction with SiO_2 to form gaseous or water soluble silicon fluorides. This etching process was carried out as follows:

$$SiO_2\ (s) + 4\ HF\ (aq) \rightarrow SiF_4\ (g) + 2\ H_2O\ (l)$$
$$SiO_2\ (s) + 6\ HF\ (aq) \rightarrow H_2SiF_6\ (aq) + 2\ H_2O\ (l)$$

Han *et al.*, [95] used different conditions and procedure and prepared carbon monolith by dissolving methylated β-cyclodextrin in an aqueous sulphuric acid solution followed by the addition of a tetramethyl orthosilicate under stirring. The gel was aged for a long period of time followed by carbonisation at 900 °C with flowing nitrogen. The carbon/silica composite monolith was then treated with HF (5%) solution to remove the silica template. The carbon monolith was prepared in different sizes.

Taguchi *et al.,* [96] described the preparation of monolithic carbon possessing a hierarchical bimodal meso- and macro-porosity. Lee *et al.,* [97] also reported the fabrication of carbon phases with bimodal pores, designated as ‘meso-nano-C’ using a corresponding silica template. In 2005, Tonanon *et al.,* [98] prepared a macro-

porous carbon monolith without template, using ultrasonic irradiation. The procedure was carried out by mixing resorcinol/formaldehyde (RF) aqueous solutions in the presence of sodium carbonate as a basic catalyst. During the gelation at temperature of 35 ^{o}C, the ultrasonic wave was applied into the RF solution to increase the reaction rate and yields of products then stopped when it was close to the gelation time. Next, the RF solution was transferred into the cylindrical glass tube followed by aging for a week at 75^{o}C. The solvent was then replaced by 1-butanol and then, the RF sonogels were freeze-dried at -10 ^{o}C for number of hours to form freeze dried macro-porous RF sonogel monoliths. As a result this was pyrolysed at 750 ^{o}C under flowing nitrogen gas, causing low shrinkage to the macro-porous structure.

Bimodal meso-porous carbon monoliths with high mechanical strength were also prepared by Shi *et al.*, [99], again using silica as a template. The hierarchical structured monolith was prepared with a narrow pore size distribution and full interconnected porosity. Also using a silica template, Xu *et al.,* [100] synthesised a carbon monolith with a trimodal porous structure of macro/macro/meso-pores. For this work, the template was filled with a mixture of styrene and divinylbenzene, using dodecanol as the porogenic solvent. The carbon monolith was formed after the polymerisation and pyrolysis of the polymer-silica composite, followed by removal of the silica template using NaOH solution (1.0 mol/L).

Lu *et al.,* [101] reported a new method for the preparation of hierarchically structured carbon monoliths. The procedure involved mixing of a calcined SBA-15 (mixture of pluronic surfactant P123 as structure-directing agent and tetraethoxysilane as silica source) and furfuryl alcohol as a carbon precursor. The resultant powder was mixed with NaCl as a salt template and then pressed into cylindrical rods in a stainless steel dye followed by carbonisation of the mixture. Carbon monoliths were then formed by dissolving the NaCl and removal of the silica with (~ 10%) HF treatment or 1*M* NaOH aqueous solution.

Alvarez and Fuertes [102] prepared a carbon monolith by immersing a macro/meso-porous silica monolith in a solution of paratoluene sulfonic acid, drying and mixing with furfuryl alcohol as a carbon precursor. The mixture was carbonised, followed by removal of the silica template with (~ 48%) HF treatment.

Most recently, Siyasukh *et al.*, [103] successfully prepared a hierarchical carbon monolith by mixing resorcinol with sodium carbonate as a catalyst, and formaldehyde using deionised water as a solvent. The resultant

resorcinol/formaldehyde (RF) solution was filled into an ultrasonic reactor glass tube and then irradiated by ultrasonicwave and transferred into a cylindrical glass tube, where an RF gel was formed. After aging for 3 days at 75 ^{o}C, the gel was removed from the tube, washed with water and dried. The interconnected macro-porous carbon monolith was then obtained by either carbonisation of the dried gel in a quartz tube reactor or by CO_2 activation via flowing of CO_2 at 50 mL/min and heating in the same reactor.

1.3. Modified monolithic materials

1.3.1. Preparation of gold nano/micro-particles

Metallic nano/micro-particles have been known to find numerous uses in various fields, particularly in electrochemical [104-105] and biological applications [106-108].

Gold nano/micro-particles are used extensively in research due to their unique optical, electronic, and molecular properties, with applications in a wide selection of areas, including in the synthesis of novel materials such as gold modified carbon monoliths, which are described in this thesis (see Chapter 3), electronics and nanotechnology [109-110]**.**

For the preparation of colloidal gold (although more advanced and specific methods are also available), nano-particles are produced in a liquid by reduction of tetrachloroauric acid ($HAuCl_4$). The procedure involves dissolving $HAuCl_4$, stirring the aqueous solution rapidly while adding a reducing agent. As a result, Au^{3+} ions are reduced to neutral gold atoms and as more and more of these gold atoms form, the solution becomes supersaturated, and gold gradually starts to precipitate in the form of sub-nanometer particles, acting as precipitation nuclei. The rest of the gold atoms that form begin to cluster to the existing particles, and these particles will be reasonably uniform in size if the solution is stirred vigorously. To prevent the particles from aggregating, some sort of stabilising agent that binds to the nano-particle surface is usually added such as citrate for example. They can also be functionalised with various organic ligands to create organic-inorganic hybrids with advanced functionality [111].

1.3.2. Applications of gold/ and silver nano/micro-particles

As mentioned above, gold nano/micro-particles are being a widely used in various fields. For instance, for the electrochemical immobilisation/adsorption of haemoglobin, Zhang *et al.,* [104] modified a glassy carbon electrode with gold nano-particles. Gold nano-particles can significantly support electron transfer between hemoglobin and the modified glassy carbon electrode, acting as a bridge of electron transfer without using an electron mediator.

Applications of gold nano-particles, commonly reported in the literature, involve modifying glassy carbon electrodes to be used for electrochemical analyses. Casella *et al.,* [105] modified a glassy carbon electrode with gold micro-particles, characterised by SEM, and then applied the modified carbon electrode as an electrochemical sensor for the detection of carbohydrates in flow injection and HPLC. Also, Goyal *et al.*, [112] used gold nano-particles to modify an indium tin oxide electrode for the simultaneous determination of dopamine and serotonin. Barrosse-Antle *et al.*, [113] chemically deposited gold micro-particles onto glassy carbon micro-spheres and studied the mechanical stability of the gold micro-particles during the anodic stripping voltammetric detection of varying concentrations of mercury.

Gold nano-particles have also been extensively used in biological applications. Voltammetric sensors based on gold nano-particles have received considerable attention due to their high stability, electrocatalytic capability and biocompatibility [106-108]. For example, Elyacoubi *et al.,* [114] modified nano-porous silica based magnetic micro-particles with gold to support the immobilisation of the enzyme horseradish peroxidase. The enzyme modified gold micro-particles were retained onto the surface of a solid carbon paste electrode with the help of a permanent magnet.

Recently, Dai *et al.*, [115] reported a number of methods to increase the water-solubility, biocompatibility and biostability of gold nano-particles for application of bioconjugated gold nano-particles for cancer biomarker detection and cell imaging. The researchers reported a bioconjugation study using the surface-modified gold nano-particles for different antibodies and DNA probes.

As is well known, thiol compounds are organic compounds similar to the alcohols and phenols but containing a sulphur atom in place of the oxygen atom. The thiol group (-SH) plays an important role in many biological systems [116]. Thiols

are the most commonly used ligands to bind to noble metal substrates such as gold surfaces.

Using the thiol-gold selectivity in an electrochemical application, Cui *et al.,* [117] successfully attached 3-mercaptopropionic acid (MPA) on a gold nano-particle modified glassy carbon (GNP-GC) electrode to investigate the determination of Cu(II). Under developed conditions, the MPA modified electrode produced a voltammetric response linearly proportional to the Cu(II) concentration from 0.1 μg/1 to 100 μg/L, with a detection limit of 3.2 ng/L. This method was successfully applied to the determination of Cu(II) in tap water [117].

More recently, Dai *et al.,* [118] developed a method to replace an ionic surfactant layer on a gold nanorod surface with a more stable thiol ligand**.** The gold nanorods were first loaded into porous ionic exchange polymer beads. Then, the trapped gold nanorods were loaded with a bifunctional thiol ligand inside the polymer beads leading the successful surface modification of the gold nanorods with a thiol ligand protecting layer. This process was termed a 'place exchange' reaction.

Silver particles are also commonly used for the modification of a wide range of materials, in particular carbon materials. To study the concentration effect of silver on the modification process of glassy carbon surface, the immersion time, and the presence of oxygen in silver nitrate solution, Dekanski *et al.,* [119] modified a glassy carbon electrode with silver nitrate using a simple immersion technique, whereby the glassy carbon was immersed in an aqueous solution of silver nitrate. The results showed that electrode was successfully modified with silver particles, which were reduced on the glassy carbon surface to their elemental state. However, the silver particles were not deposited the surface uniformly. Also, the electrochemical evaluations showed that the voltammogram obtained from the silver electrode were similar to that of silver modified glassy carbon electrode. The determination of silver content which was deposited on the glassy carbon electrode was mainly dependent on the pre-treatment of the electrode before its immersion.

Further developments have been reported in the metal nano-particles field, such as employing core-shell nano-particles (structured nano-particles that consist of a core of one material and a coating (shell) of another material). Kaiser *et al.*, [120] reported an interesting method for purifying breathing air using a carbon-based monolith structure saturated with silver and triethylenediamine, in which the monolith structure is saturated by a multiple step process. The method of

impregnation results in a carbon-based monolith structure that purifies nuclear, biological, or chemical contaminants under conditions of high flow rate and low pressure drop.

Bacic-Vukcevic *et al.,* [121-122] deposited silver particles onto a sample of carbon monoliths and studied the rate of silver deposition on these monoliths as a function of immersion time (silver nitrate concentration 75 mg/dm^3), as well as a function of concentration of silver nitrate solution (25, 50, 75, 100, 125 mg/dm^3). The concentration of silver in solution was determined using atomic absorption spectrometry.

Kucharczyk *et al.*, [123] reported that a partial substitution of lanthanum with silver in $LaMnO_3$ and deposited the complex onto a monolithic metal support, which improved the catalytic activity in the oxidation of CH_4 and CO.

For the incorporation of inorganic nano-particles into carbon monoliths, Jaroniec *et al.*, [124] prepared a silver-containing carbon substrate using a silver-containing meso-porous silica monolith as a hard template (MS-Ag) and impregnating the meso-porous silica monolith (MS) with oxalic acid which was used as a catalyst. This impregnation was carried out by immersing the MS monolith in an ethanol solution of oxalic acid for 10 min. To evaporate the ethanol, the impregnated template was then dried at 90 for 2 h °C. Next, the oxalic acid-treated MS monolith was impregnated with a resorcinol/crotonaldehyde mixture for 30 min. the resultant composite sample was heated at 60 °C for 0.5 h then at 120 °C for 10 h. The actual polymerisation was performed at 200 °C for 5 h. The resultant sample was pyrolysed at 900 ^{o}C at 2 ^{o}C/min for 2 h under nitrogen flowing. The silica template was removed following HF treatment (15%). The resultant meso-porous carbon monolith was washed with butanol, hexane, and distilled water and dried in an oven at 80 °C for 12 h.

1.4. Techniques for characterisation of nano/micro structured materials

1.4.1. Scanning electron microscopy (SEM)

One of the key techniques for characterisation of nano/micro structured materials such as described above is SEM. The use of SEM for morphological investigation of monolithic materials is often reported, including carbon monoliths [85], [87], [125-126]. SEM is a type of electron microscopy that images the sample

surface by scanning it with a high-energy beam of electrons which interact with the atoms that make up the sample producing signals which contain information about the sample's surface topography and composition. A beam of electrons generated from an electron gun is accelerated down the electron column and this electron beam is shaped and focused as a spot onto the sample by electromagnetic lenses and apertures. During the process, a scan generator scans the beam of electrons across the sample surface and the incident electrons interact with the sample. As a result, electrons are collected by one of the detectors building up an image of the sample on the monitor. There are a number of key components within the SEM (Figure 1.6):

1. The electron source (tungsten, tantalum or lanthanum hexaboride filame), where the electron beam is formed and the source is housed within the gun assembly.
2. The objective aperture which limits the solid angle surrounded by the beam providing a more consistent beam of electrons onto the sample. It also reduces the spot size and, thus improves resolution.
3. The objective lens, which focuses the beam onto the surface of the sample (Figure 1.6).
4. The working distance, this is the distance between the objective lens and the sample. For high resolution imaging, the working distance is typically short. For imaging a wider area of the sample, a longer working distance can be used.

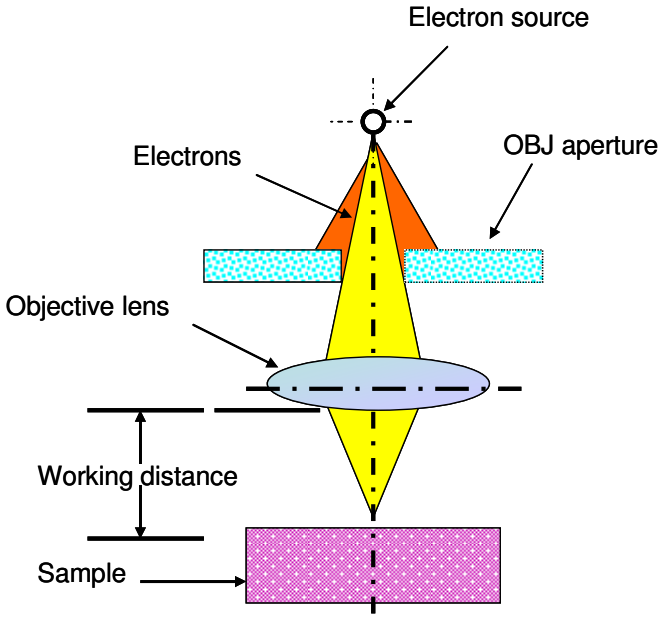

Figure 1.6. Schematic representation of the electron optics of SEM. Reproduced from [127].

1.4.2. Energy-dispersive X-ray spectroscopy (EDX)

Energy-dispersive X-ray spectroscopy (EDX) is an analytical technique used for the chemical characterisation of a sample by interactions between electromagnetic radiation and matter, analysing X-rays emitted by the matter in response to being hit with charged particles. As a result, EDX detects the presence of elements in a selected volume of a sample, providing qualitative and quantative information. X-ray emission originates from the decay of electronically highly excited states of sample, resulting from a primary excitation (excitation by electrons) and secondary or fluorescence excitation (by photons) [128]. Series of X-ray spectral lines with discrete frequencies, characteristic of the emitting atom are generated. Each element has a unique atomic structure resulting in X-rays that are characteristic for each element.

1.4.3. Surface area measurements (Brunauer, Emmett, Teller)

A variety of materials, including monolithic substrates have been characterised by measuring BET nitrogen adsorption/desorption isotherms, to determine the surface area and the pore volume/size distribution. A Type II isotherm is usually typical of physical adsorption of gases by non-porous solids [129]. It is possible to obtain a value of the monolayer capacity of a sample from the Type II isotherm of a given gas on a particular sample, which can be used to calculate the specific surface of the solid sample. The monolayer capacity is defined as the amount of adsorbate which can be completely filled, single molecular layer (monolayer) on the surface of the sample (1 g) unit mass. So the surface area (A) of 1 g of the solid can be expressed by the simple equation,

$$A = n_m a_m L \qquad \text{Eq. 1.1}$$

where a_m is the average area occupied by a mole of adsorbate in the completed monolayer and L is the Avogadro constant, n_m being expressed in moles of adsorbate per gram of adsorbent.

It is necessary to understand the Type II isotherm in quantitative terms in order to obtain the monolayer capacity from the isotherm. For this reason, a number of theories have been developed. The most useful theory in relation to surface area determination, was that of Brunauer, Emmett and Teller (BET) [129].

The BET treatment is based on a kinetic model of the adsorption process carried out by Langmuir [130], in which the surface of the solid was regarded as a selection of adsorption sites. A state of dynamic equilibrium was suggested in which the rate at which molecules arriving from the gas phase and condensing on to bare sites is equal to the rate at which molecules evaporate from occupied sites. The BET isotherm describes the amount of gas adsorbed on the surface of the sample, as a function of the pressure of the gas in equilibrium with the surface.

1.4.3.1. The adsorption isotherm

To explain the adsorption process, when a solid sample is exposed in a closed space to a gas or vapour at some definite pressure, the sample begins to adsorb the gas by an increase in the weight of the sample and a decrease in the pressure of the gas [129]. After a time the pressure becomes constant at the value, *p*, and respectively the weight stops to increase any further. The amount of gas thus adsorbed can be calculated from the fall in pressure by application of the gas laws, if the volumes of the vessel and of the solid are known. The majority of isotherms which result from physical adsorption may conveniently be grouped into five classes. The five types, I to V, arise from the classification originally proposed by Brunauer, Deming, Deming and Teller (BDDT) [129]. The essential features of these isotherms are indicated in Figure 1.7. The Type I isotherm is typical of micro-porous solids and chemisorption isotherms (classification of adsorption characterised by a strong interaction between an adsorbate and a substrate surface). Type I isotherms are characterised by a long flat branch which is nearly or quite horizontal and which in some instances cuts the line $P/Po = 1$ sharply but in others gives a "tail" as in Figure 1.7. Type I isotherms are less common than those of Type II or IV. Type II is exhibited by finely divided non-porous solids. The point at which the linear portion begins was termed by Emmet and Brunauer [129] "point B" and was taken by them to indicate the completion of the monolayer; the adsorption at point B, was thus equal to the monolayer capacity. Type III and type V are typical of vapour adsorption (i.e. water vapour on hydrophobic materials). Type III isotherms are characterised by their being convex to the pressure axis. This suggests that the adsorption is co-operative in nature: the more molecules that are already adsorbed, the easier it for further molecules to become adsorbed. Type IV isotherms resemble isotherms of Type II in

having a point of inflection at the low pressure end, but instead of approaching the line *P/Po* = 1 asymptotically (Figure 1.7) they turn towards the pressure axis again, giving a branch HJ which is nearly (or quite) horizontal. Type IV isotherms are quite common, and are found especially amongst the xerogels such as silica and ferric oxide [129]. The isotherms of Type IV and Type V have a hysteresis loop generated by the capillary condensation of the adsorbate in the meso-pores of the solid, the lower branch of which shows measurements obtained by progressive addition of gas to the system, and the upper branch by progressive withdrawal. Hysteresis effects are likely to appear in isotherms of the other types also. Finally, the rare type VI step-like isotherm is shown by nitrogen adsorbed on carbon.

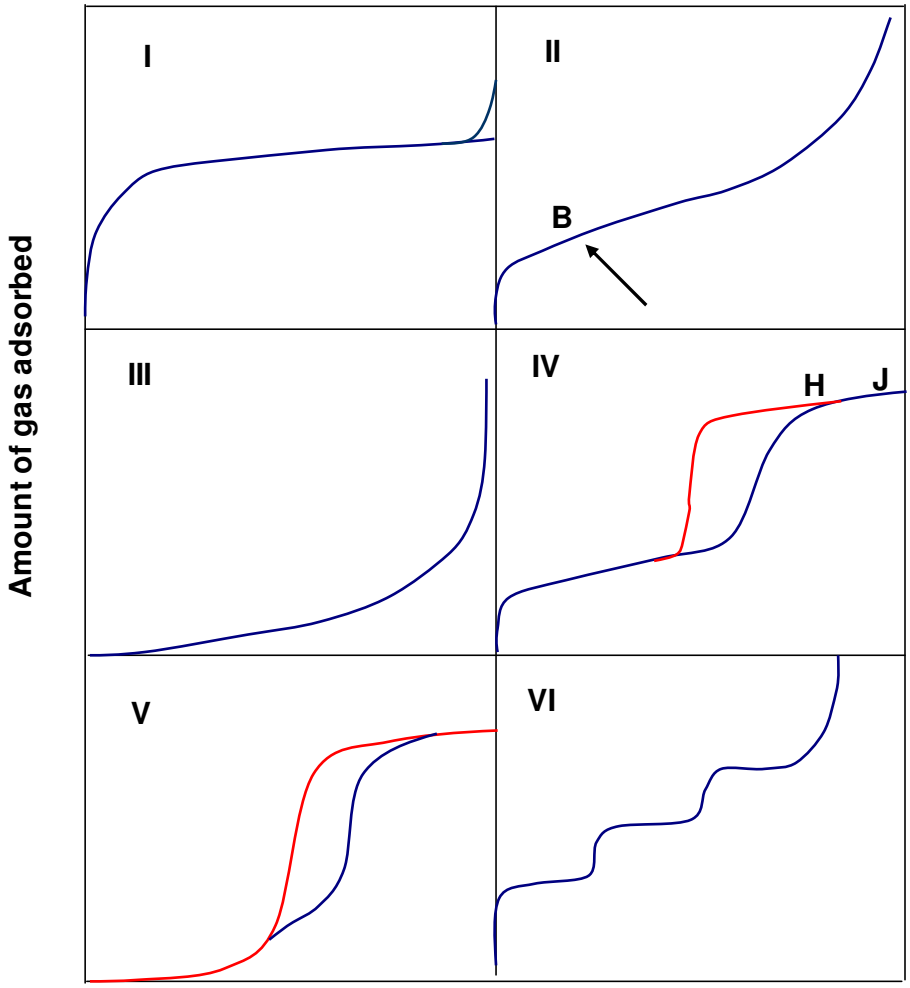

Figure 1.7. The five types of adsorption isotherms, I to V, from the classification by Brunauer, Deming, Deming and Teller [129] (BDDT), together with Type VI, the stepped isotherm.

1.4.4. Dilatometry analysis

The influence of temperature on the dimensional changes of materials is determined using dilatometry. With this technique, length or volume changes upon subjecting materials to heat treatment are detected.

Dilatometers have a wide range of applications, such as in the production of metallic alloys, compressed and sintered refractory compounds, glasses, ceramic products, composite materials, plastics, etc. [131-134]. It is based on the thermal expansion of the sample during the pyrolysis and as a consequence, measuring the shrinkage taken place after pyrolysis of the sample. The thermal expansion coefficient, α, of the sample is defined as the rate of change of sample volume (which presents as a change in height of sample since the cross sectional area in the dilatometer is constant) with respect to the change in temperature.

In-depth studies of the behaviour of materials during pyrolysis using dilatometry analysis have been carried out [27], [33], [36], [135-141]. Park *et al.*, [142] investigated the behaviour of the silica spheres during pyrolysis and reported that the comparison between the initial sphere average size and the derived pore size revealed a 23% to 36% difference, due to the shrinkage of the silica spheres when the meso-porous SiC ceramics obtained were annealed at 1000 $^{\circ}$C.

Dilatometry was also used to characterise the porous ceramics produced by Wang *et al.,* [143]. Using silica spheres with diameters less than 500 nm Wang *et al.*, found that about 25–30% shrinkage of the structure occurred after calcination and little shrinkage occurred when silica spheres with diameters greater than 500 nm were used.

Iacono *et al.*, [144] prepared and examined the glassy carbon during the pyrolysis. The glassy carbon was prepared by heating bis-ortho-diynylarene (BODA) monomers to form poly naphthalene networks at 1000 ^{o}C. Dilatometry was used to determine the linear coefficient of thermal expansion of various BODA-derived glassy carbon. Different glassy carbon-based systems ranging from 3.20 to 6.92 x 10^{-6} $^{o}C^{-1}$over 20–1000 ^{o}C gave similar linear coefficient of thermal expansion. Carbonisation of polynaphthalene networks to 1500 ^{o}C caused an increase in short-range order. The linear coefficient of thermal expansion was observed between 2.85–2.93 x 10^{-6} $^{o}C^{-1}$ over 20–1000 ^{o}C for such thermal cycling. The yields of the glassy

carbon during pyrolysis can be optimised via the carbonisation mechanism which can be obtained also by the dilatometry.

Finally, dilatometric analysis for monolithic silica and carbon aerogels was reported by Gross and Fricke [145]. Thermal expansion of silica aerogels and carbon aerogels was recorded from 30-130°C and from 1-1000 °C, respectively. A partially irreversible shrinkage took place for the silica aerogels sample during the pyrolysis caused by the condensation reactions and by the pyrolysis of carbon aerogel samples in temperature range 1050 to 2100 ^{o}C. The linear thermal expansion of silica aerogels was recorded as (4 x 10^{-7} K^{-1}) higher than that of vitreous silica. However, thermal expansion coefficients of carbon aerogels was recorded at room temperature as (10^{-6} K^{-1}). Heating the carbon aerogels to 1000 ^{o}C caused increasing it's thermal expansion to (3.5-8) × 10^{-6} K^{-1} at 1000°C.

1.4.5. Porosimetry analysis

Another significant technique used for the characterisation of various types of porous materials, including monolithic materials, in terms of pore size distributions (PSD) and porosity is porosimetry. Porosity is one of the most important geometrical quantities for describing textile materials as it influences some important physical and mechanical properties [146-148]. For instance, pore size distribution in a fibrous material mainly that of intra-yarn pores, affects moisture uptake, thermal insulation, filtering properties, wettability, softness, tactile and other properties [149-150].

There are several methods of testing porosity and the relevant quantities such as pore size, pore size distribution, pore diameter, etc [151-152]. Mercury intrusion porosimetry is based upon the application of an external pressure to force mercury into pores against the opposing force of the liquid's surface tension, allowing pore size to be determined. The gas pressure begins at zero since the technique is usually carried out under vacuum.

In HPLC, Urban *et al.*, [153] prepared polymethacrylate capillary columns with different porous properties. The pore size distribution of the pores was determined with ISEC and compared with that obtained using mercury-intrusion porosimetry. Mercury-porosimetry was used to measure the entire range of pore sizes and provided physical information on the monoliths prepared, while ISEC was only appropriate for determining the size of meso-pores in the swollen monoliths. The

mercury-intrusion-porosimetry technique covered the range of flow-through pore sizes and meso-pores down to 4 nm [153].

Lu *et al.*, [154] prepared a carbon monolith by mixing furfuryl alcohol with 1,3,5-trimethylbenzene, containing oxalic acid as a catalyst. The mixture was impregnated within a silica monolith. Pyrolysis of the carbon precursor rod was performed at 850 ^{o}C under argon. The carbon monolith was them formed after removal of the silica template following HF treatment (25–40%). The pore size of the carbon monolith produced was characterised by mercury intrusion porosimetry and showed a distribution of pores larger than 50 nm.

Recently, Xu *et al.*, [100] prepared a carbon monolith by polymerisation reaction of styrene as a monomer and divinylbenzene as a crosslinker in the presence of dodecanol as a porogenic solvent and 2,2-azobis (isobutyronitrile) as an initiator. The mixture was then impregnated into a silica monolith, initially prepared as a template, filling the voids of the silica phase. Polymerisation was carried out at 343 K for 6 h, and then the polymer-silica composite monolith was pyrolysed at 1173 K for 5 h under inert atmosphere. The silica template was then removed by a 1.0 mol/L NaOH treatment and the carbon monolith was produced. The pore size distribution of the resultant carbon monoliths were characterised using mercury intrusion porosity and showed a bimodal macro-pore size distribution of 2.5 μm with pore volume of 6.4 cm^3/g.

1.4.6. Dynamic mechanical analysis

Dynamic mechanical analysis (DMA) is usually used for examining the viscoelastic nature of materials such as glassy and polymer materials. The measured frequency is dependent upon the nature of the transition from high modulus materials, such as glassy phases to low modulus materials, such as rubbers [155]. The modulus is expressed as the ratio of stress to strain for the elastic materials. The degree of dependence is particular to the transition type. The glass transition temperature (Tg) is highly dependent on frequency, while melting is frequency independent. DMA can also determine sub- Tg transitions, like beta (β) relaxation, which is observed at low temperatures and gamma (γ) relaxations, which are observed at very low temperatures and can occasionally be detected in materials.

Tg is a key property for any material, and can be easily examined by DMA. This technique gives very useful information about sample relaxations through the damping factor (Tanδ) vs temperature data. Tanδ is related to the amount of energy a sample can store. The temperature of the sample can be changed during the measurement, therefore, DMA is frequently called a dynamic mechanical thermal analyser (DMTA). To calculate the stiffness of the sample under stress, applied stress and the resultant strain are used (Figure 1.8).

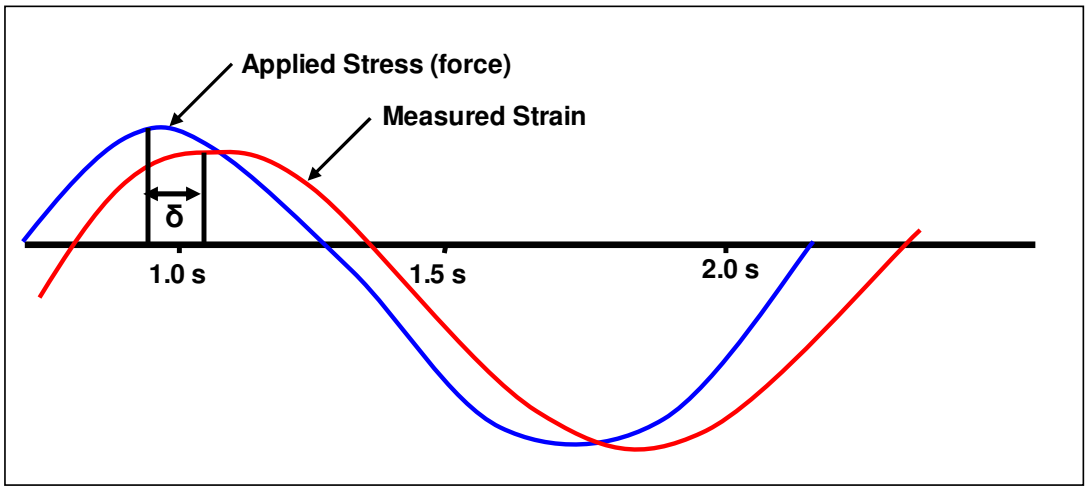

Figure 1.8. Applied stress (to) and the resultant strain (of) the material. Reproduced from [155].

To determine Tanδ, the phase lag between the two (or δ) is usually used. The sample is classified as elastic when the strain is in phase with the stress (δ = 0°) (Figure 1.9 a).

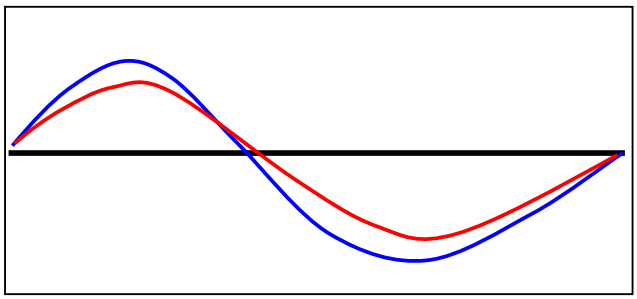

Figure 1.9 (a). The strain is in phase with the stress. Reproduced from [155].

The material is classified as viscous when the strain is out of phase with the stress by 90° (δ = 90°). Large damping properties can be shown by these materials (Figure 1.9 b).

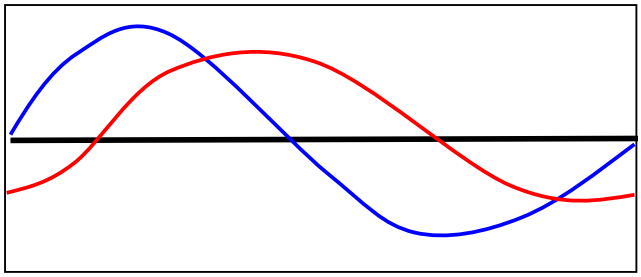

Figure 1.9 (b). The strain is 90° out of phase with the stress. Reproduced from [155].

However, when (δ = 0°-90°), the material will be classified as viscoelastic, polymers in general show this kind of properties (Figure 1.9 c).

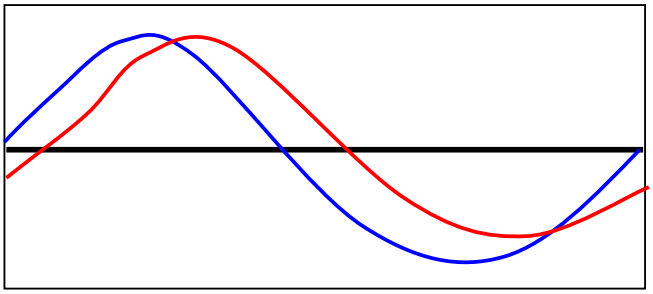

Figure 1.9 (c). The strain is out of phase by $0^o < \delta < 90^o$ with the stress. Reproduced from [155].

Tan δ will be low for the elastic materials and high for viscous materials as the stress and strain are related as a function of time, as there is a phase difference between the two in viscous materials. Both modulus and Tanδ for poly(methyl methacrylate) (PMMA) (acrylic glass) can be shown from a typical DMA response (Figure 1.10). The modulus decreases (the sample becomes less stiff), and the Tanδ goes through a peak (the molecular reorganisation of the relaxation induces less elastic action) as the sample goes through its Tg. The statistics give information on sample stiffness, the location of the glass transition temperature, its frequency dependence, and other viscoelastic properties [155].

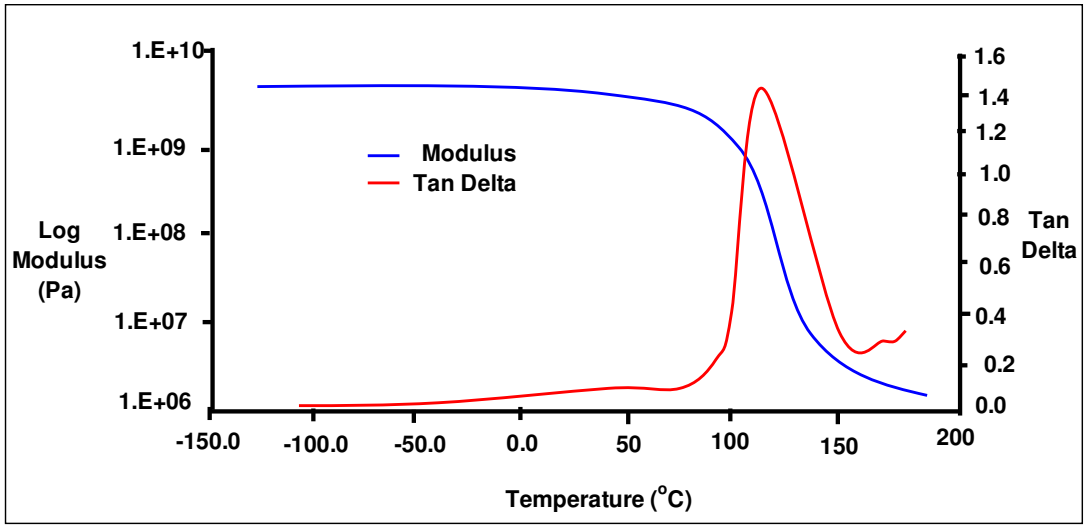

Figure 1.10. Typical response from a DMA shows both modulus and Tanδ for PMMA. Reproduced from [155].

DMA has been used to characterise the thermal and mechanical properties of carbon nanotubes [156-158], epoxy resins [159-162], carbon nano-particles [163] and also proteins [164]. Using thermomechanical analysis, Khandare *et al.,* [165] measured Tg of mesophase pitches prepared by careful heat treatment of a commercially available petroleum pitch. The glass transition as observed in the coefficient of thermal expansion (CTE) vs *T* curve for the mesophase pitches was found to be very significant and reproducible. This significant transition consistently occurred for all the samples at around 90% of the softening point temperature. The behaviour was found to be reproducible within +2% for all the samples ranging from 100% isotropic to 100% mesophase. The method of identifying the glass transition temperature as the peak of the CTE curve is an accepted technique [165]. Ku *et al.,* [166] used DMA to characterise in-situ the structure of airborne carbon nano-fibres in real-time. Zhou *et al.*, [167] used DMA to evaluate the effect of the inorganic K^{-10} montmorillonite clay on the thermal and mechanical performance of conventional carbon fiber reinforced composites.

1.4.7. Photon correlation spectroscopy

Photon correlation spectroscopy (PCS) or dynamic light scattering (DLS) is used for the size measurement of nano-particles, typically in the sub-micron range. The time-dependent variation in the intensity of light scattered by colloidal particles in suspension is measured using this technique [168]. Colloidal suspensions have been studied extensively by PCS [169-170] since 1964, the date of the emergence of the modern PSC technique [171-172]. Particles in suspension cause scattering of a low intensity laser beam. Fast changes in backscattered intensity around a mean value are caused by the diffusion of particles [173]. By measuring the rate of changes in the scattered laser light, the particle size is determined using PCS. Depending on the particle size, the time scale of the variation in the scattered laser light will be variable [168]. The particle size is given as the diameter from PCS analysis when the particles measured are spherical. From PCS, information is given on the average hydrodynamic diameter and width of distribution, called the polydispersity index (PDI). The PCS is a non-destructive technique and an average particle size in a range of 0.6-6000 nm can be measured in -situ [174].

1.5. Conclusions

Porous monolithic materials are widely used in different scientific fields, including electrochemistry, catalysis, adsorption or various modes of chromatography. Monolithic phases represent a very important development in column technology for the separation sciences. Decreasing analysis time through low column backpressures and allowing for the use of high flow rates, thus, faster transfer kinetics are the main advantages of these columns. Monolithic columns are mainly classified into polymer- and silica-based, the latter being the most popular monolithic columns in use. The organic columns can be prepared using organic polymers such as polymethacrylates or polystyrenes, and the inorganic species can be prepared from inorganic polymers, such as silica, titania or zirconia. Less attention to-date has been applied to carbon monolithic materials, particularly for separation science.

Various techniques can be used to characterise these new range of monolithic materials and a number of them have been briefly described in this Chapter. Many of these advanced techniques have been used to characterise the novel porous carbon

monolithic rods reported in this thesis, including some unique carbon/gold and carbon/silver composite monoliths. Such techniques include SEM/EDX for the examination of surface morphology, BET to determine the surface area, dilatometry to study the influence of hydrolysis on these monoliths, and mercury porosimetry to investigate the pore size distribution etc.

Based on the analysis of up-to-date literature sources, the aim of this project was the development and characterisation of novel monolithic stationary phases based on carbon and gold modified carbon, for chromatographic and electrochemical applications, As the advantage of these materials in chromatography are resistance to hydrolysis and the absence of swelling in various organic solvents unlike, e.g., silica or polymer-based monoliths.

Also the large surface area and pore volume allow these novel carbon-based monolithic materials to be potentially applied in electrochemistry.

References

1. G. Groppi, E. Tronconi, *Chem. Eng. Sci.*, 52 (1997) 3521.
2. A. A. Klinghoffer, R. L. Cerro, M. A. Abraham, *Catal. Today*, 40 (1998) 59.
3. G. Groppi, E. Tronconi, *Chem. Eng. Sci.*, 55 (2000) 2161.
4. Z.R. Ismagilov, R.A. Shkrabina, S.A. Yashnik, N.V. Shikina, I.P. Andrievskaya, S.R. Khairulin, V.A. Ushakov, J.A. Moulijn, I.V. Babich, *Catal. Today*, 69 (2001) 351.
5. H. Jung, W. L. Yoon, H. Lee, J. S. Park, J. S. Shin, H. Lab, J. D. Lee, *J. Power Sources*, 124 (2003) 76.
6. P. Wu, X. Li, S. Ji, B. Lang, F. Habimana, C. Li, *Catal. Today,* xxx (2009) xxx, Article in press.
7. H. Zheng, J. M. Keith, *Catal. Today*, 98 (2004) 403.
8. M. Hamidipour, F. Larachi, Z. Ring, *Chem. Eng. Sci*., 62 (2007) 5538.
9. M. Hamidipour, F. Larachi, *Chem. Eng. Sci.,* xxx (2009) xxx, Article in press.
10. M. Opallo, J. Kukulka-Walkiewicz, *Electrochim. Acta*, 46 (2001) 4235.
11. I. Nischang, G. Chen, U. Tallarek, *J. Chromatogr., A*, 1109 (2006) 32.
12. Y. Zhao, M. Zheng, J. Cao, X. Ke, J. Liu, Y. Chen, J. Tao, *Mater. Lett.*, 62 (2008) 548.
13. D. Josic, A. Buchacher, A. Jungbauer, *J. Chromatogr., B,* 752 (2001) 191.
14. P. Krajnc, N. Leber, D. Stefanec, S. Kontrec, A. Podgornik, *J. Chromatogr., A,* 1065 (2005) 69.
15. J. Randon, S. Huguet, A. Piram, G. Puy, C. Demesmay, J. Rocca, *J. Chromatogr., A,* 1109 (2006) 19.
16. F. Svec, T.B. Tennikova, Z. Deyl, *Monolithic Materials: Preparation, Properties and Applications.* Amsterdam: Elsevier Science, 1st edition (2003).
17. Kubin, M., Spacek, P., Chromecek, R., *Coll. Czechosl. Chem. Commun.,* 32 (1967) 3881.
18. K. Ralla, F. Anton, T. Scheper, C. Kasper, *J. Chromatogr., A,* 1216 (2009) 2671.
19 H. Bjorkman, C. Ericson, S. Hjerten, K. Hjort, *Sensor and Actuators B: Chemical*, 79 (2001) 71.
20. T. B. Tennikova, F. Svec, B. G. Belenkii, *J. Liq. Chromatogr.*, 13 (1990) 63.
21. T. B. Tennikova, F. Svec, *J. Chromatogr.*, 646 (1993) 279.
22. B. G. Belenkii, A. M. Podkladenko, O. I. Kurenbin, V. G. Maltsev, D. G.

Nasledov, S. A. Trushin, *J. Chromatogr.*, 645 (1993) 1.

23. N. I. Dubinina, O. I. Kurenbin, T. B. Tennikova, *J. Chromatogr., A,* 753 (1996) 217.
24. T. B. Tennikova, M. Bleha, F. Svec, T. V. Almazova, B. G. Belenkii, *J. Chromatogr.*, 555 (1991) 97.
25. C. Legido-Quigley, N.Marlin, V. Melin, A. Manz, N. W. Smith, *Electrophoresis*, 24 (2003) 917.
26. V. Pretorious, J. C. Davidtz, D. H. Desty*, J. High Resolut. Chromatogr. Chromatogr. Commun.,* 2 (1979) 583.
27. K. Nakanishi, N. Soga, *J. Am. Ceram. Soc.,* 74 (1991) 2518.
28. H. Minakuchi, K. Nakanishi, N. Soga, N. Ishizuka, N. Tanaka, *Anal. Chem*., 68 (1996) 3498.
29. S. M. Fields, *Anal. Chem.*, 68 (1996) 2709.
30. Y. Guo, L. A. Colon, *Anal. Chem.*, 67 (1995) 2511.
31. K. Nakanishi, *J. Porous Mater.*, 4 (1997) 67.
32. K. Nakanishi, H. Shikata, N. Ishizuka, N. Koheiya, N. Soga, *J. High Resolut. Chromatogr.*, 23 (2000) 106.
33. N. Tanaka, H. Nagayama, , H. kobayashi, T. Ikegami, K. Hosoya, N. Ishizuka, H. Minakuchi, K. Nakanishi, K. Cabrera, D. Lubda, *J. High Resolut. Chromatogr.*, 23 (2000) 111.
34. F. Rabel, K. Cabrera, D. Lubda, *Int. Lab. News*, 01/02 (2001) 23.
35. K. Cabrera, K. Sinz, D. Cunningham, *Int. Lab. News*, 02 (2001) 12.
36. K. Cabrera, D. Lubda, H.-M. Eggenweiler, H. Minakuchi, K. Nakanishi, *J. High Resolut. Chromatogr.*, 23 (2000) 93.
37. N. Ishzuka, H. Kobayashi, H. Minakuchi, K. Nakanishi, K. Hirao, K. Hosoya, T. Ikegami, N. Tanaka, *J. Chromatogr., A,* 960 (2002) 85.
38. M. Motokawa, H. Kobayashi, N. Ishizuka, H. Minakuchi, K. Nakanishi, H. Jinnai, K. Hosoya, T. Ikegami, N. Tanaka, *J. Chromatogr., A,* 961 (2002) 53.
39. N. Ishizuka, H. Minakuchi, K. Nakanishi, N. Soga, H. Nagayama, K. Hosoya, N. Tanaka, *Anal. Chem.,* 72 (2000) 1275.
40. N. Tanaka, H. Kobayashi, *Anal. Bioanal. Chem.*, 376 (2003) 298.
41. K. Nakanishi, N. Soga, *Inorganic Porous Materials and Process for Making*

Same. U.S. Patent 5,624,875 (1997).

42. K. Cabera, D. Lubda, H. M. Eggenweiler, H. Minakuchi, K. Nakanishi, *J. High Resolut. Chromatogr.,* 23 (2000) 93.
43. M. Schulte, J. Dingenen, *J. Chromatogr., A,* 923 (2001) 17.
44. L. Spoof, J. Meriluoto, *J. Chromatogr., A,* 947 (2002) 237.
45. L. A. Lawton, C. Edwards, G. A. Codd, *Analyst (London),* 119 (1994) 1525.
46. L. Spoof, K. Karlsson, J. Meriluoto., *J. Chromatogr., A,* 909 (2001) 225.
47. P. T. Vallano, R. S. Mazenko, E. J. Woolf, B. K. Matuszewski, *J. Chromatogr., B,* 779 (2002) 249.
48. M. J. Rocheleau, C. Jean, J. Bolduc, D. Carazzato, *J. Pharm. Biomed. Anal.*, 31 (2003) 191.
49. J. L. Garridoa, F. Rodriguezb, E. Campana, M. Zapata, *J. Chromatogr., A*, 994 (2003) 85.
50. E. Sugrue, P. N. Nesterenko, B. Paull, *Anal. Chim. Acta*, 553 (2005) 27.
51. C. O'Riordain, L. Barron, E. Nesterenko, P. N. Nesterenko, B. Paull, *J. Chromatogr., A,* 1109 (2006) 111.
52. E. P. Nesterenko, P. N. Nesterenko, B. Paull, *J. Chromatogr., A,* 1213 (2008) 62.
53. R. Mallik, D. S. Hage, *J. Pharm. Biomed. Anal*., 46 (2008) 820.
54. T. Jiang, R. Mallik, D.S. Hage, *Anal. Chem.*, 77 (2005) 2362.
55. M. Thommes, R. Skudas, K.K. Unger, D. Lubda, J. Chromatogr., A, 1191 (2008) 57.
56. W. D. Ross, R. T. Jefferson, *J. Chromatogr. Sci.*, 8 (1970) 386.
57. H. Schnecko, O. Bieber, *Chromatographia*, 4 (1971) 109.
58. F. D. Hileman, R. E. Seivers, G. G. Hess, W. D. Ross, *Anal. Chem*., 45 (1973) 1126.
59. T. R. Lynn, D. R. Rushneck, A. R. Cooper, *J. Chromatogr. Sci.*, (1974) 76.
60. S. Hjerten, J. Liao, R. Zhang, *J Chromatogr.,* 473 (1989) 273.
61. I. Mihelic, T. Koloini, A. Podgornik, A. Strancar, *J. High Resolut. Chromatogr.,* 23 (2000) 39.
62. F. Svec, J. M. J. Frechet, *Anal. Chem*., 64 (1992) 820.
63. A. Maruska, O. Kornysova, *J. Biochem. Biophys. Methods*, 59 (2004) 1.
64. Y. M. Li, J. L. Liao, K. Nakazato, J. Mohammad, L. Terenius, S. Hjerten, *Anal.*

Biochem., 223 (1994) 153.

65. S. Xie, F. Svec, J. M. J. Frechet, *J. Chromatogr., A,* 775 (1997) 65.
66. S. A. Rodriguez, L. A. Colon, *Chem. Mater.,* 11 (1999) 754.
67. E. C. Peters, F. Svec, J. M. J. Frechet, *Adv. Mater.*, 11 (1999) No. 14.
68. M. Petro, F. Svec, I. Gitsov, J. M. J. Frechet, *Anal. Chem.*, 68 (1996) 315.
69. M. Petro, F. Svec, I. Gitsov, J. M. J. Frechet, *J. Chromatogr., A,* 752 (1996) 59.
70. S. Xie, R. W. Allington, F. Svec, J. M. J. Frechet, *J. Chromatogr., A,* 865 (1999) 169.
71. M. Janco, D. Sykora, F. Svec, J. M. J. Frechet, J. Schweer, R. Holm, *J. Polym. Sci., A*, 38 (2000) 2767.
72. I. N. Savina, I. Y. Galaev, B. Mattiasson, *J. Chromatogr., A*, 1092 (2005) 199.
73. H. J. Zhang, J. S. Li, H. Wang, Y. Q. Feng, *Anal. Bioanal. Chem.*, 386 (2006) 2035.
74. Z. Pan, H. Zou, W. Mo, X. Huang, R. Wu, *Anal. Chim. Acta*, 466 (2002) 141.
75. B. Beiler, A. Safrany, *Rad. Phys. Chem.,* 76 (2007) 1351.
76. J. Urban, P. Jandera, *J. Sep. Sci.,* 31 (2008) 2521.
77. E. Garcia-Bordeje, F. Kapteijn, J.A. Moulijn, *Carbon*, 40 (2002) 1079.
78. C. Liang, S. Dai, G. Guiochon, *Anal. Chem.,* 75 (2003) 4904.
79. D. Lozano-Castello , D. Cazorla-Amoros , A. Linares-Solano , D.F. Quinn, *Carbon*, 40 (2002) 2817.
80. M. Jorda-Beneyto, D. Lozano-Castello, F. Suarez-Garcıa, D. Cazorla-Amoros, A. Linares-Solano, *Micropor. Mesopor. Mater.*, 112 (2008) 235.
81. R. F. Antrim, R. A. Scherrer, A. M. Yacynych, *Anal. Chim. Acta*, 164 (1984) 283.
82. H. Colin, C. Eon, G. Guiochon, *J. Chromatogr.,* 122 (1976) 223.
83. K. K. Unger, P. Roumeliotis, H. Mueller, H. Gotz, *J. Chromatogr.,* 202 (1980) 3.
84. Z. J. Plzak, F. P. Donsek, J. Jansta, *J. Chromatogr.,* 148 (1978) 5308.
85. P. Ciccioli, R. Tappa, A. Di Corcia, A. Liberti, *J. Chromatogr.*, 206 (1981) 35.
86. J. H. Knox, M. T. Gilbert, *U.K. Patent* 2,035,282 (1978).
87. M. T. Gilbert, J. H. Knox, B. Kaur, *Chromatographia.,* 16 (1982) 138.
88. J. H. Knox, B. Kaur, G. R. Millward, *J. Chromatogr.,* 352 (1986) 3.
89. P. T. Jackson, P. W. Carr, *J. Chromatogr., A,* 958 (2002) 121.
90. A. P. Schellinger, Y. Mao, P. W. Carr, *Anal. Bioanal. Chem.,* 373 (2002) 587.

91. H. Colin, P. Jandera, G. Guiochon, *Chromatographia* ,15 (1982) 133.
92. P. Ross, R. E. Majors, *LC-GC*, 18 (2000) 14.
93. H. Colin, A. Siouffi, G. Guiochon, *Anal. Chem.,* 51 (1979) 1661.
94. H. Yang, Q. Shi, X. Liu, S. Xie, D. Jiang, F. Zhang, C. Yu, B. Tu, D. Zhao, *Chem. Commun.,* (2002) 2842.
95. B. H. Han, W. Zhou, A. Sayari, *J. Am. Chem. Soc.,* 125 (2003) 3444.
96. A. Taguchi, J. H. Smatt, M. Linden, *Adv. Mater*., 15 (2003) 1209.
97. J. Lee, J. Kim, T. Hyeon, *Chem, Commun.,* 1 (2003) 1138.
98. N. Tonanon, A. Siyasukh, Y. Wareenin, T. Charinpanitkul, W. Tanthapanichakoon, H. Nishihara, S. Mukai, H. Tamon, *Carbon*, 43 (2005) 2808.
99. Z. G. Shi, Y. Q. Feng, L. Xu, S. L. Da, Y. Liu, *Mater. Chem. Phys.*, 97 (2006) 472.
100. L. Xu, Z. G. Shi, Y. Q. Feng, *Micropor. Mesopor. Mater.,* 115 (2008) 618.
101. A. H. Lu, W. Li, W. Schmidt, F. Schuth, *Micropor. Mesopor. Mater.*, 95 (2006) 187.
102. S. Alvarez, A. B. Fuertes, *Mater. Let.*, 61 (2007) 2378.
103. A. Siyasukh, P. Maneeprom, S. Larpkiattaworn, N. Tonanon, W. Tanthapanichakoon, H. Tamon, T. Charinpanitkul, *Carbon*, 46 (2008) 1309.
104. L. Zhang, X. Jiang, E. Wang, S. Dong, *Biosens. Bioelectr.,*, 21 (2005) 337.
105. I. Casella, A. Destradis, E. Desimoni, *Analyst*, 121 (1996) 249.
106. S. Trasatti, O.A. Petrii, *Pure Appl. Chem.,* 63 (1991) 711.
107. X. Dai, R.G. Compton, *Anal. Sci.,* 22 (2006) 567.
108. C. M. Welch, R. G. Compton, *Anal. Bioanal. Chem.,* 384 (2006) 601.
109. P. Mulvaney, *The beauty and elegance of Nanocrystals*, Ph.D. thesis, University of Melbourne, Melbourne, Australia, 2004.
110. C. N. R. Rao, G. U. Kulkarni, P. J. Thomasa, P. P. Edwards, *Chem. Soc. Rev.*, 29 (2000) 27.
111. V. R. Reddy, "*Gold Nanoparticles: Synthesis and Applications*", (2006) 1791, and references therein.
112. R. N. Goyal, V. K. Gupta, M. Oyama, N. Bachheti, *Talanta* **72** (2007) 976.
113. L. E. Barrosse-Antle, L. Xiao, G. G. Wildgoose, R. Baron, C. G. Salter, A.Crossley, R. G. Compton, *New J. Chem.*, 31 (2007) 2071.
114. A. Elyacoubi, S. I. M. Zayed, B. Blankert, J. M. Kauffmann, *Electroanalysis*, 18

(2006) 345.

115. Q. Dai, J. Coutts, X. Liu, L. Austin, Q. Huo, Gold Nanoparticle Bioconjugates for Biomolecular Imaging and Detection, *University of Central Florida, US*, Chapter 3 (2008) 256.
116. A. I. Busev, L. I. Teternikov, M. M. Buzlanova, E. D. Kashparova, L. M. Rozdestvensky,P. Nenning, *Talanta*, 23 (1976) 433.
117. Y. Cui, C. Yang, W. Zeng, O. Munetaka , W. Pu, Y. Zheng, J. Zhang, *Anal. Let.,* 40 (2007) 2151.
118. Q. Dai, J. Coutts, J. Zou, Q. Huo, *Chem. Commun*., (2008) 2858.
119. A. Dekanski, J. Stevanovi, R. Stevanovi, V. M. Jovanovi, *Carbon*, 39 (2001) 1207.
120. M. Kaiser, P. M. Michalakos, G. Seminara, J. R. Regalbuto, US Patent 20040259729 (2004).
121. M. Bacic-Vukcevic, A. Udovicic, Z. Lausevic, A. Peric-Grujic, M. Lausevic, *Mater. Sci. Forum,* 518 (2006) 217.
122. M. Bacic-Vukcevic, A. Kalijadis, S. Dimitrijevic-Brankovic, Z. Lausevic, M. Lausevic, *Sci. Technol. Adv. Mater*., 9 (2008) 015006.
123. B. Kucharczyk, W. Tylus, *App. Catal., A*, 335 (2008) 28.
124. M. Jaroniec, J. Choma, J. Gorka, A. Zawislak, *Chem. Mater.,* 20 (2008) 1069.
125. G. Y. Onyestyak, K. Laszlo, L. V. C. Rees, *Helv. Chim. Acta*, 87 (2004) 1888.
126. J. M. Gatica, J. M. Rodríguez-Izquierdo, D. Sanchez, T. Chafik, S. Harti, H. Zaitan, H. Vidal, *C. R. Chimie*, 9 (2006) 1215.
127. C. Jones, *Hitachi S-3000N VP SEM, Hitachi High Technologies.*
128 R. Jenkins, R. Manne, R. Robin, C. Senemaud, *Nomenclature*, 63 (1991) 735.
129. S. J. Gregg, K. S. W. Sing, *Adsorption, surface area, and porosity*, London , New York : Academic Press, 2nd edition (1982).
130. M. D. Bubba, C.A. Arias, H. Brix, *Water Res.*, 37 (2003) 3390.
131. H. Lehmann, R. Gatzke, *Dilatometrie and differential thermal analysis for the evaluation of processes*, 1956.
132. A. B. Pippard, *The of element OF Classical Thermodynamics* Cambridge University press, Cambridge (England), 1968.
133. T. H. K. Barron, *Generalized theory of thermal expansion of solids* ASM, 1998.
134. M. Paganelli, *Am. Ceram. Soc. Bull*, 81 (11) (2002) 25.

135. K. Nakanishi, H. Minakuchi, N. Soga, N. Tanaka, *J. Sol-Gel Sci. Tech.,* 8 (1997) 547.
136. H. Minakuchi, K. Nakanishi, N. Soga, N. Ishizuka, N. Tanaka, *J. Chromatogr., A*, 762 (1997) 135.
137. T. H. Ko, W. S. Kuo, Y. H. Chang, *J. App. Polym. Sci.*, 81 (2000) 1084.
138. M. Al-Bokari, D. Cherrak, G. Guiochon, *J. Chromatogr., A*, 975 (2002) 275.
139. F. Leinweber, D. Lubda, K. Cabrera, U. Tallarek, *Anal. Chem.,* 74 (2002) 2470.
140. E. S. M. Lutz, M. E. Markling, C. M. Masimirembwa, *J. Chromatogr., B*, 780 (2002) 205.
141. K. Cabrera, G. Wieland, D. Lubda, K. Nakanishi, N. Soga, H. Minakuchi, K. Unger, *Trends Anal. Chem.,* 17 (1998) 50.
142. K. H. Park, I. K. Sung, D. P. Kim, *J. Mater. Chem.*, 14 (2004) 3436.
143. H.Wang, X. D. Li, J. S. Yu, D. P. Kim, *J. Mater. Chem.,*14 (2004) 1383.
144. S. T. Iacono, M. W. Perpall, P. G. Wapner, W. P. Hoffman, D. W. Smith Jr., *Carbon*, 45 (2007) 931.
145. J. Gross, J. Fricke, *J. Non-Cryst. Solids*, 186 (1995) 301.
146. B. Neckar, S. Ibrahim, *Structural Theory of Fibrous Assemblies and Yarns*, Technical University of Liberec, Czech Republic, 2003.
147. J.W.S. Hearle, P. Grosberg, S. Backer, *Structural Mechanics of Fibers*, Yarns, and Fabrics Volume 1, Wiley-Interscience, 1969.
148. J.W.S. Hearle, J.J. Thwaites and J. Amirbayat, *Mechanics of Flexible Fibre Assemblies, Sijthoff & Nordhoff*, Alpen an der Rijn, The Netherlands, Germantown, Maryland, U.S.A., 1980.
149. B. Neckar, *The Mechanical Structure Modeling of Staple Yarn*, Vlakna a Textil, 7. (2000) 82.
150. L.M. Vas. V. Nagy. P. Nagy. A. Lazar. L. Devenyi, *Comparative Testing of Spun Yarns Manufactured from Polyester Fibers of Different Cross Sections*. Budapest, In-Tech-Ed (2002).
151. M. Raheel ed., *Modern Textile Characterization Methods*, Marcel Dekker, Inc. New York, (1996).
152. B.P. Saville, *Physical Testing of Textiles*, Woodhead, New York, (2003).
153. J. Urban, S. Eeltink, P. Jandera, P. J. Schoenmakers, *J. Chromatogr., A*, 1182

(2008) 161.

154. A.-H. Lu, J.-H. Smatt, S. Backlund, M. Linden, *Micropor. Mesopor. Mater.*, 72 (2004) 59.

155. TTInf_DMA, Triton Technology**,** Nottinghamshire, United Kingdom, www.triton-technology.co.uk

156. A. J. Gu, G. Z. Liang, D. Liang, M. Ni, *Polym. Adv. Technol*,. 18 (2007) 835.

157. S. Kanagaraj, R. M. Guedes, M. S. A. Oliveira, J. A. O. Simoes, *J. Nanosci. Nanotech.*, 8 (2008) 4008.

158. C. U. Lee, M. D. Dadmun, *J. Polym. Sci.: Part B: Polym. Phys.*, 46 (2008) 1747.

159. Y. Zhou, F. Pervin, L. Lewis, S. Jeelani, *Mater. Sci. Eng. A*, 452–453 (2007) 657.

160. M. Costa, M. Rezende, J. de Paiva, E. Botelho, *Polym.-Plas. Tech. Eng*., 45 (2006) 1143.

161. Y. Zhou, F. Pervin, S. Jeelani, *J Mater. Sci*., 42 (2007) 7544.

162. J. Gu, G. Wu, X. Zhao, *Polym. Comp*., (2009) 232.

163. M. Barankin1, Y. Creyghton, A. Schmidt-Ott, *J. Nanopar. Res.*, 8 (2006) 511.

164. J. Carpenter, D. Katayama, L. Liu, W. Chonkaew, K. Menard, *J. Therm. Ana. Calor.*, 95 (2009) 881.

165. P. Khandare, J. W. Zondlo, A. S. Pavlovic, *Carbon*, 34 (1996) 663.

166. B. K. Ku, M. S. Emery, A. D. Maynard, M. Stolzenburg, P. H. McMurry, *Nanotechnology*,17 (2006) 3613.

167. Y. Zhou, F. Pervin, V. Rangari, S. Jeelani, *J. Mater. Process. Tech.*, 191 (2007) 347.

168. http://www.malvern.com/. Accessed 11 May, 2009.

169. H. Z. Cummins, E. R. Pike, in *Photon Correlation and Light-Beating Spectroscopy*, Plenum Press: New York, 1974.

170. R. Pecora, ed., in *Dynamic Light Scattering, Applications of Photon Correlation Spectroscopy*, Plenum Press: New York, 1985.

171. R. Pecora, *J. Chem. Phys.*, 40(6) (1964) 1604.

172. H. Z. Cummins, Y. Yeh, N. Knable, *Phys. Rev. Lett.*, 12(6) (1964) 150.

173. S. Ghosh, The preparation of magnetic nano-particle assemblies for biomedical applications, Ph.D. thesis, Dublin City University, Dublin, Ireland, 2006.

174. J. B. Berne, R. Pecora, in *Dynamic Light Scattering*, Dover Publications Inc.: New York, USA, 2000.

CHAPTER TWO

Preparation and Characterisation of Porous Carbon Monolithic Columns for Chromatographic Applications

2.1. Introduction

Porous monolithic columns have many advantageous characteristics compared to traditional particle packed columns which allow them to be utilised in various modes of LC [1-2]. The most significant of these characteristics is a relatively high flow through porosity, leading to a low column pressure drop, with the possibility for use with various flow rates leading to faster separations. Hierarchical porous materials containing both interconnected macro-porous and meso-porous structures have enhanced properties compared with single-sized pore materials due to increased mass transport through the material and maintenance of a specific surface area on the level of fine pore systems [3-4].

The first attempts toward the production of monolithic columns were based on polyurethane foams, made by Ross and Jefferson in GC [5]. The columns were prepared by polymerisation in-situ (i.e. directly in the tube) and successfully tested for the separation of a range of hydrocarbon mixtures (for example, alkanes C_6-C_9). The idea was then extended to LC as early as 1974 by Hansen and Sievers [6], who prepared porous polyurethane monolithic columns by polymerisation in-situ of toluene-carbon tetrachloride solutions of a polyol and an isocyanate. In 1991, a significant progress in the preparation of monolithic silica rods was reported [7-8], and the first rod column via phase separation was prepared by polymerisation of tetramethoxysilane in the presence of poly(ethylene oxide). The development of meso-pores with a narrow pore size distribution in the silica skeleton was achieved through hydrothermal treatment of this silica rod with ammonium hydroxide. Since this pioneering work, silica-based monolithic columns have become one of the most popular phases currently applied to small molecule separations, although organic polymer-based monoliths have also been extensively studied. Recently, other alternatives to silica materials for the preparation of monolithic columns have been

investigated, including zirconia [9-10], hafnia [10], titania [11] and carbon monoliths [12]. These materials and corresponding columns have better hydrolytical and thermal stability properties compared to silica, but at the same time, in the case of zirconia and hafnia, they are more reactive.

Carbon monoliths combine all the advantages of inorganic oxides and organic polymers, whilst also being resistant to swelling and hydrolysis. Additionally, being a conductive material, porous glassy carbon (PGC) is potentially suitable for use in electromodulated LC [13].

Various authors have recently reported the preparation of carbon monolithic structures: carbon monoliths were synthesised from isotropic fibers [14] and as carbon aerogels [15-16]. Mareche *et al.,* [17] proposed a new kind of porous monoliths prepared using exfoliated graphite (EG) as a starting material. The EG material was compressed into adjustable shapes and the porosity and density of carbon block was shown to be dependent upon the compression rate.

The idea of using spherical particles as templates for the preparation of monolithic rods of dimensions and physical stability suitable for chromatographic application was first generated in 1966 by John Knox, who proposed an "inverse column" in which the stationary phase structure had the same shape as the mobile phase (gas phase) in the particle packed column [18]. In Knox's opinion such a structure could be made "by filling a column with beads of some low melting point substance, fusing the points of contact, filling the gas space with a thermosetting resin, and, after curing, melting out the original beads".

A PGC packing materials was prepared for GC and HPLC with density of 2.20 g/cm^3 and a range of surface area from 20 to 400 m^2/g [19]. These materials were prepared by immersing porous silica particles (template) with a phenol-formaldehyde resin mixture, pyrolysing the resin under inert atmosphere (argon), and dissolving the silica with an alkali. Better performance was obtained by graphitising the porous glassy carbon at a high temperature in the range 2000-2800 ^{o}C. Some *n*-alkanes and alkyl benzenes were successfully separated on this PGC column for GC. Phenols and methyl benzenes were also successfully separated on the same column for HPLC. This PGC column was shown to be stronger than graphitised carbon black (GCB) which showed very poor mechanical stability. Also the peak symmetry using PGC column was better, and it was found to be easier to prepare this type of phase compared to GCB.

Carbon monoliths were prepared by soaking a macro/meso-porous silica monolith as a template in a paratoluene sulfonic acid solution [20]. Then, the template was filled with furfuryl alcohol which was polymerised at 80 ^{o}C for 15 h. The pyrolysis was carried out at 800 °C under N_2 for 1 h. The silica template was then removed by HF treatment leaving the carbon monolith. They show a high surface area (1860 m^2/g) with a large porosity made up of large pore volume (1.9 cm^3/g) and meso-pores with size centred at around 3.4 nm.

Also, a carbon monolith was prepared for catalysis and separation applications with a tri-modal porous structure of macro/macro/meso-porous by nano casting inorganic silica as a template [21]. In this method, a mixture of styrene and divinylbenzene in the presence of initiator and porogenic reagent (dodecanol) was filled into the void space of the silica monolithic template.

The use of template particles, in particular silica based, for the preparation of ordered nano- and micro-structured carbon materials has been the topic of much attention in recent years in the production of so-called 'inverse opals'. For example, Zakhidov *et al.,* [22] synthesised carbon inverse opals by infiltrating silica opal plates with a phenolic resin. They cured the resin at low temperature, pyrolysed the resin then removed the silica with aqueous HF. They also reported that the X-ray diffraction indicated an amorphous structure consistent with a glassy carbon. Further work followed in this area [23-26], and most recently Guan *et al.,* [27] in 2007 synthesised carbon micro-particle arrays with different particle morphologies from phenolic resin using a similar inverse opal templating process.

Recently, Liang *et al.,* [12] reported on the preparation of a monolithic carbon-based column for LC. For this, 10 μm silica particles were suspended in ethanol, and then the copolymer of a resorcinol/iron(III) complex and formaldehyde was prepared within the silica suspension. The mixture was aged, polymerised and dried, followed by pyrolysis. The silica template was removed by HF treatment leaving the carbon monolithic rod. Examination of the surface morphology of the carbon monolith revealed macro-pores with diameters between 5 and 10 μm and a developed surface area of 163 m^2/g. Efficient separations of *n*-alkylbenzenes were achieved with dichloromethane and methanol as the mobile phase, with 1% *n*-hexane as an additive [12].

In this Chapter, a detailed examination of the synthesis, and subsequent physical characterisation of carbon monolithic rods with different macro-pore size,

prepared using an adapted and optimised templating procedure based on that proposed by Liang *et al.,* [12] is presented. Synthetic carbon rods of up to 10 cm in length were produced using a simple thermally initiated process, based upon pyrolysing a cast rod made of a copolymer of a 25:75 phenol resin mixed with formaldehyde in the presence of silica particles (1, 2, 5 & 10 µm in particle size, respectively). These rods were comprehensively physically characterised using various techniques such as SEM/EDX, BET, dilatometry, conductivity and backpressure measurement, and then clad using a variety of methods to ensure elimination of all housing voids to enable later chromatographic evaluation.

2.2. Experimental

2.2.1. Chemicals

Resorcinol (99%), formaldehyde (37 wt % aqueous solution), ethanol, toluene (99.9%), ethylbenzene (99.9+%), butylbenzene (99.9%), hydrofluoric acid (38-40%), gold (III) chloride 99.99% and 6-mercaptohexanoic acid 90 % were obtained from Sigma-Aldrich (Gillingham, UK). 1-Butanol and ferric chloride (99%) were obtained from Riedel-de Haen, Seelze (Hannover, Germany). Nucleosil 5 and 10 µm silica particles were obtained from Macherey- Nagel (Düren, Germany) and 1 and 2 µm silica particles were obtained from Glantreo Ltd., (The Rubicon Centre, CIT Campus, Bishopstown, Ireland). Araldite epoxy glue was obtained from Bostik Findley Limited (Stafford, UK). Reagent water was obtained from a Millipore Milli-Q water purification unit (Millipore, Bedford, MA, USA) and was 18.2 MΩ or better. All chemicals were used as received from the manufacturers.

2.2.2. Instrumentation and characterisation

To characterise the (1, 2, 5 and 10 µm pore size) carbon monolith structures, BET (characterisation of specific surface area and pore volume), mercury porosimetry (characterisation of pore size distribution), dilatometry (characterisation of dimensional change of carbon rod as a function of temperature), DTA/TGA (characterisation of thermal behaviour and weight loss), and SEM/EDX and TEM (characterisation of surface morphology) were employed. The carbon monolithic rods were then sealed into short chromatographic columns and evaluated for flow-

through porosity and back-pressure profiles, and later for retention selectivity for a range of test solutes, and ruggedness over extended use.

A GFL water bath, model 1013 (Laborgerätebörse GmbH, Burladingen, Germany) was used to prepare the matrix carbon rod. An EHRET thermovacuum oven (Ehret Labor- und Pharmatechnik GmbH & Co. KG, Emmendingen, Germany) was used to complete the polymerisation of the precursor carbon rod. For the pyrolysis of the rod, a benchtop alumina tube furnace, model GSL1300X (MTI Corporation, Richmond, USA) was used. Optical microscope images for the carbon monolithic rods were obtained using a synchronized microscope model SVM340 (LabSmith, Livermore, CA, USA). The surface morphology of the carbon monoliths was examined using scanning electron microscopy/ energy-dispersive X-ray spectroscopy (SEM/EDX) systems, models S-3000N VP and S-3400N VP and ultra high resolution cold field emission scanning electron microscopy, model S-5500 (Hitachi, Oxford, UK) and transmission electron microscopy (TEM) system, model H-9500 (Hitachi, Krefeld, Germany). Inductively coupled plasma - optical emission spectrometer (ICP-OES), model Liberty 220 series (Varian, Palo Alto, USA) was used for the quantitative analysis of gold. A Brunauer-Emmett-Teller (BET) analyser, model 2375 (Micromeritics Gemini Ltd., Georgia, USA) was used to measure the specific surface area and pore volume with a nitrogen adsorption/desorption technique. Dilatometric analysis was carried out using a programmable horizontal pushrod dilatometer, model Dil 402-E (Netzsch Ltd., Emmendingen, Germany) to study the effect of the pyrolysis on the carbon monoliths. Thermal analysis was carried out using differential thermal analysis/thermo gravimetric analysis (DTA/TGA), model STA 1500 (Stanton Redcroft Ltd., London, UK). Additionally, pore size distribution of the carbon monoliths was characterised by mercury porosimetry, model Autoscan 33 (Quantachrome Ltd., Hook, UK) with a nominal measurement range of 3.2 nm to 5 μm over a range of pressure from atmospheric to 2275 bar.

Stiffness and damping properties of the carbon monoliths were obtained using a Triton dynamic mechanical analyser, model Tritec 2000 (Triton Technology, Nottingham, UK). Infrared spectra of the carbon monolith were recorded in the solid state as 1 – 2 % KBr (potassium bromide) disks using an FT–IR spectrometer, model Paragon 1000 (Perkin-Elmer, Massachusetts, USA). The back pressure was determined using an HPLC pump, model Waters 510 (Waters Corporation, Milford, USA)

by encasing the carbon monolithic rods within a Chromolith RP-18e monolithic guard cartridge, 10 mm in length (Merck KGaA, Darmstadt, Germany). Electrical conductivity of the carbon monoliths was measured using a clamp voltmeter, model ISO-TECH$_{ICM\ 3090}$ ((RS Components Pty Ltd, Smithfield, Australia).

2.2.3. Synthesis of the carbon monolith rod

A modified procedure [12] was followed for synthesis of the carbon monolithic rods. A 1 g portion of silica particles (either 1, 2, 5 or 10 µm diameter), was dispersed in 1.5 g of 1-butanol and sonicated for 1 h. A 0.18 g portion of ferric chloride followed by addition of 0.367 g of resorcinol were then slurried in the silica suspension and dissolved by gentle shaking. The colloid solution turned dark immediately after the addition of resorcinol, indicating the fast formation of a resorcinol/Fe(III) complex. A 0.3 g portion of an ice cold, 37 % formaldehyde solution in water was introduced into the mixture in one step with further gentle agitation. The mixture was kept in an ice-water bath for 1 h with constant stirring. After removal from the ice-water bath, the mixture was slowly transferred into 7 mm i.d. glass tubes which were capped when full. These tubes were then placed in a 90 °C water bath. The mixture polymerised into a solid rod inside the glass tube. The rod detached from the tube wall due to shrinking caused by polymerisation. The polymer rods were aged in the glass tube overnight in the water bath. Crack-free phenolic resin/silica rods were then removed from the glass tubes and kept within a fumehood for 72 h to slowly evaporate the majority of residual solvent. Finally, the rods were thoroughly dried in a vacuum oven at 80 °C overnight and further cured at 135 °C for 4 h to ensure complete polymerisation. The general scheme for the preparation of monolithic rods based on synthetic carbon is shown in Figure 2.1.

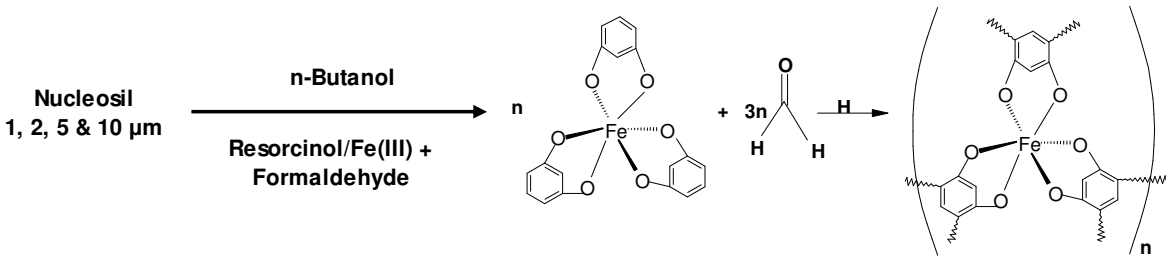

Figure 2.1. Formation of templated polymer material. Reproduced from [12].

2.2.3.1. Pyrolysis of the precursor rods

A benchtop alumina tube furnace purged with N_2 gas was employed to pyrolyse the rods. The temperature was first ramped from room temperature to 800 °C at 2.5 °C/min, and then held at 800 °C for 2 h, to ensure complete carbonisation. A second ramp took place from 800 to 1250 °C at 10 °C/min. The temperature was kept constant at 1250 °C for 1 h. Then the furnace was allowed to cool naturally to room temperature.

2.2.3.2. Etching (removal of the silica particles)

The silica particles and the iron catalyst were removed by etching the carbon-silica composite monoliths in concentrated hydrofluoric acid (38-40%) for 3 h (6 h only for the 10 µm templated carbon-silica composite monolith) and washed away with copious amounts of distillated water. The porous carbon rod obtained was thoroughly dried under vacuum at 80 °C.

2.2.3.3. Cladding/Housing the carbon rod and column fitting

Cladding/Housing the carbon monoliths was carried out using two different approaches. In the first approach, the carbon monolithic rod was clad according to the procedure similar to that described by Liang *et al.,* [28]. Briefly, the initial range of monolithic carbon rods was clad in heat-shrinkable PTFE tubing by heating to 340 °C.

Encased carbon rods were then sealed (making sure all air pockets were eliminated) into short PEEK HPLC columns (typically 30 x 6 mm i.d.) with Araldite epoxy resin adhesive (Figure 2.2).

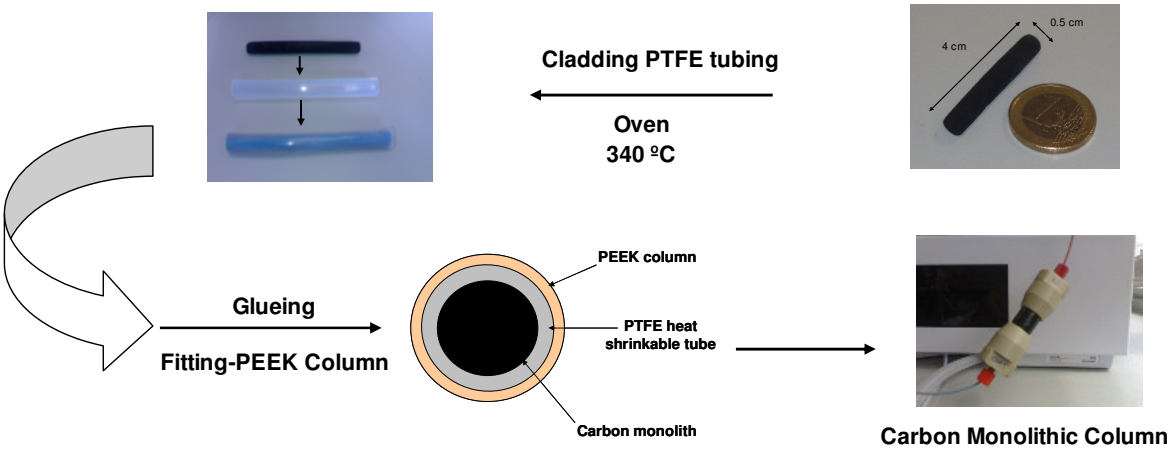

Figure 2.2. Scheme illustrating the cladding and fitting procedures for the carbon monolithic column.

A microscopic image of a cross section of a typical monolith housed with heat shrinkable Teflon and epoxy resin is shown in Figure 2.3.

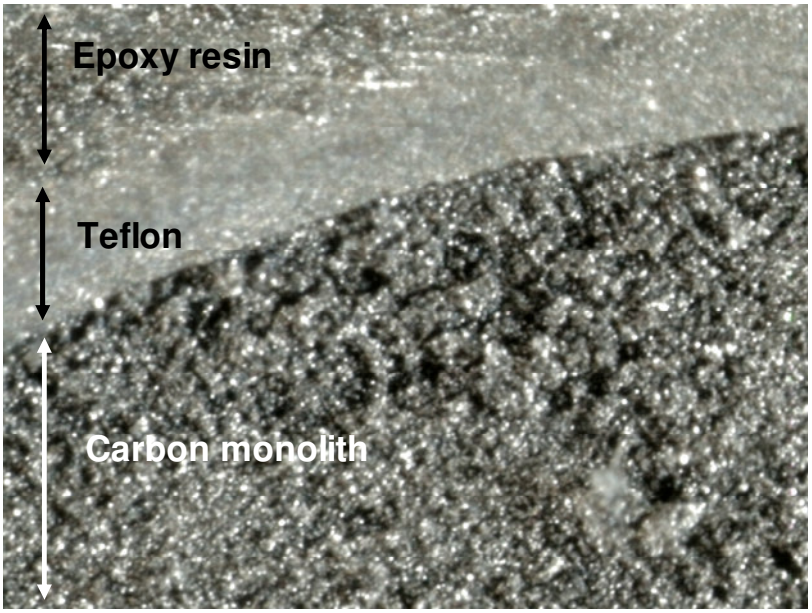

Figure 2.3. Optical 10 x microscope image of a 5 µm templated carbon monolithic rod clad within heat treated Teflon sheath with an epoxy exterior sealing layer for housing within a PEEK column.

The second cladding approach carried out, involved the carbon monolithic rods (1 and 10 µm macro-pores) being completely encased directly within epoxy resin of ~ 0.5 cm thickness, into which chromatographic tubing connections were sealed directly interfacing with the end of the monolithic rod. A typical glue encased carbon monolithic column is shown in Figure 2.4.

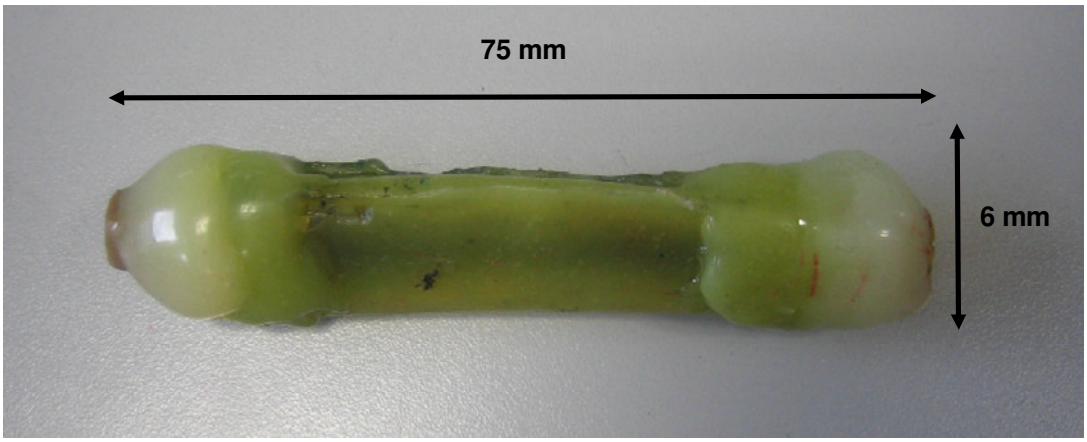

Figure 2.4. Typical glue encased carbon monolithic column.

Cross sections of glue encased carbon monolithic columns (1 µm and 10 µm macro-pore) are shown in Figures 2.5 and 2.6, respectively.

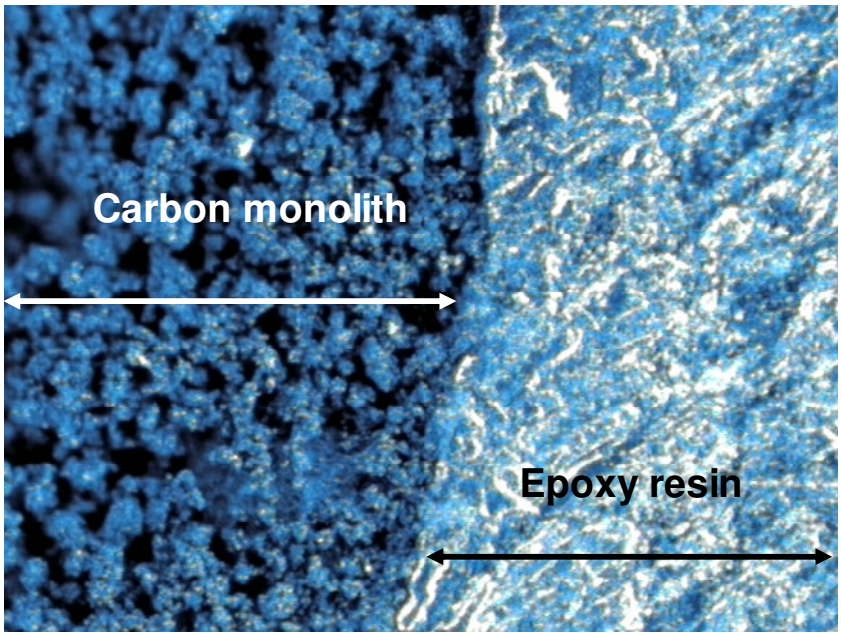

Figure 2.5. Optical 10 x microscope image of an epoxy resin clad 1 µm templated carbon monolith.

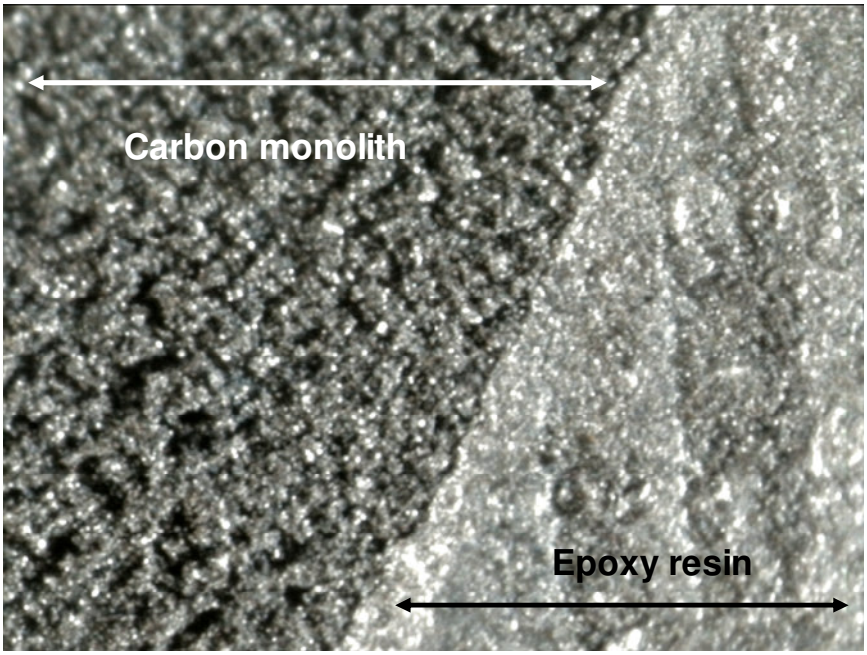

Figure 2.6. Optical 10 x microscope image of an epoxy resin clad 10 µm templated carbon monolith.

Both approaches proved successful with microscopic evaluation confirming complete elimination of voids along the monolithic edge (Figures 2.3 and 2.5). Both cladding techniques were subjected to applied column backpressures of up to 23 bar without obvious signs of stress induced voids.

The above careful control of monolith preparation, pyrolysis and cladding conditions resulted in the ability to produce carbon monoliths of up to 10 cm in length without obvious internal and surface fissures or cracks.

2.2.4. Characterisation of the carbon monoliths

2.2.4.1. Scanning electron microscopy/ Energy-dispersive X-ray spectroscopy

The surface morphology of the carbon monoliths was examined by SEM. For the best obtainable resolution imaging, a high accelerating voltage of 20 keV and a typically short analytical working distance at 7.0–7.4 mm were used. Magnification at 2.5-10 k and objective aperture No 3 were used, suitable for both imaging and analysis. It is necessary that the sample should be conductive before viewing by the SEM otherwise it would require coating with a thin layer of gold using the sputter

coater. However, the carbon monolithic samples were inherently conductive and therefore did not require sputter coating. To study the internal structure (cross section) of the monoliths, the samples were cut into small pieces and then the clean carbon monolith sample glued onto a metallic conductive disk and placed into the SEM chamber. The elements present in a selected area of the SEM image was detected by the EDX system providing qualitative information about the monolith composition.

2.2.4.2. BET surface area measurements

Specific surface area and pore volume was measured using a BET analyser. Typically, 0.05 g (~ 1 cm in length) of carbon monolith was heated at 150 °C and degassed for 90 min with pure Ar gas. Subsequently, upon loading into the sample chamber, the surface area of porous carbon monolith was calculated from the volume of N_2 gas adsorbed onto the surface of the monolith at liquid nitrogen temperature (-196 ^{o}C) in a flow-through cell followed by desorption. The nitrogen gas will fill the small pores first measuring the surface area at ~ 0.4 relative pressure (P/Po). Then the nitrogen gas will start filling the large pores measuring the pore volume.

2.2.4.3. Dilatometry analysis

Dilatometrric analysis was carried out using the dilatometer under flowing N_2 (250 mL/min). Cylindrical samples (approximately 7 mm diameter x 5 mm length) were used. The sample was placed inside the furnace (dilatometer) and a heating profile was applied with heating rates in accordance with the pyrolysis profile described in Section 2.2.3.1. The sample length then was measured and the percentage of shrinkage was determined.

2.2.4.4. Thermal analysis

DTA/TGA was carried out under flowing nitrogen to determine the weight gain or loss of carbon monoliths due to gas release or absorption as a function of temperature. Platinum crucibles containing 20 mg of sample, and 20 mg of alumina as a reference, were employed with heating rates in accordance with the pyrolysis profile described in Section 2.2.3.1.

2.2.4.5. Mercury porosimetry

Mercury porosimetry was used for investigating the porous structure of the carbon monolith samples with a nominal measurement range of 3 nm to 5.3 μm over a range of pressure from atmospheric to 33,000 psi. In this method, Hg is forced into the pores of a dry monolith sample (~ 0.1 g), and the volume of mercury is determined very accurately by weight difference at each applied pressure.

First, an accurate weight of the empty Hg cell assembly must be obtained. During the run, mercury initially fills the large pores of the sample under low pressure but (at this pressure) the mercury does not yet enter the reference cell's internal void. A stable increase of pressure is then initiated. At a specific higher pressure corresponding to the exterior pore size, mercury then enters the internal void of the cell and the small pores of the carbon monolith.

2.2.4.6. Dynamic mechanical analysis

Dynamic mechanical analysis (DMA) was carried out by applying a varying force to the monolith and the resultant displacement of the sample measured. The stiffness was determined and Tan δ (the ratio of the loss component to the storage component) was calculated. It was possible to determine the damping properties of the monolith by measuring the phase lag in the displacement compared to the applied force. Tan δ is plotted against temperature and glass transitions are usually observed as a peak. Using the Triton DMA system with sample tubes held in a single cantilevered bending mode, 5 μm macro-porous carbon monolithic samples were run from -150 to 180 ^{o}C and to 250 ^{o}C and 10 μm macro-porous carbon monolithic sample was run from -150 to 250 ^{o}C. About 10 mg of each sample was weighed into a material pocket before being mounted into the DMA in single cantilever bending geometry.

2.2.4.7. Characterisation of carbon monolith using infrared spectroscopy

The infrared spectrum of the porous glassy carbon monolith measured in the solid state (KBr disks). A homogeneous carbon monolith and potassium bromide mixture was prepared by mixing and grinding a small amount of a dried potassium

bromide in a mortar and with a 1 to 2 % of carbon monolith to a fine powder. The IR disk was then prepared, inserted into the IR sample holder and analysed.

2.2.4.8. Conductivity measurements of the carbon monoliths

Electrical conductivity or specific conductivity of the carbon monoliths was measured using a digital voltmeter to determine the monolith's ability to conduct an electric current. The resistance was first measured by the voltmeter for each monolith sample (~ 10 mm in length, 5 mm in i.d.) and the conductivity was then calculated.

2.2.4.9. Back pressure determinations

The back pressure was determined using an HPLC pump. Carbon monolithic rods (1 and 5 μm pore diameters) of dimensions 10 x 6 mm i.d. were encased separately within monolithic guard cartridges 10 mm in length. The net pressure drop over the column was calculated by subtracting the system tubing pressure drop from the total recorded pressure drop.

2.3. Results and Discussion

2.3.1. Synthesis and pyrolysis of silica-embedded precursor rods

Within this study, the carbon monolithic rods were prepared in various lengths and diameters, including 73 x 4 mm i.d. for 1 μm pore-sized, 70 x 6 mm i.d. for 2 μm pore-sized, 50 x 6 mm i.d., 55 x 6 mm i.d. and 30 x 6 mm i.d. for 5 μm pore sized and 75 x 6 mm i.d. for 10 μm pore-sized. Visible microscopy of the monolith surface showed a smooth homogenous surface structure along the complete length of the monolithic rod (Figure 2.7).

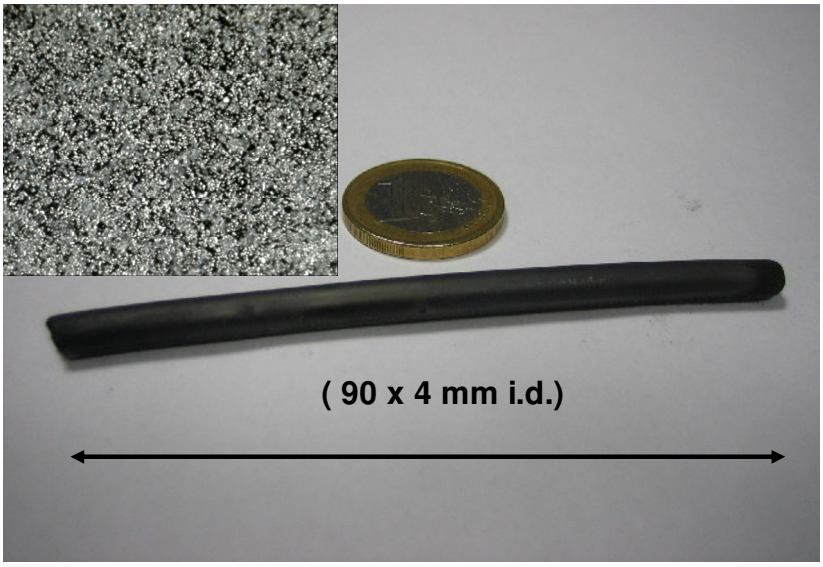

Figure 2.7. Photograph of a 90 x 4 mm glassy carbon monolith, with inset showing 4 x microscope image of homogenous surface.

A range of silica particles (1, 2, 5 and 10 µm in particle size) were used as described in Section 2.2.3. The pore size distribution of the silica particles was determined by mercury porosimetry and SEM. As is common for commercial sources of silica particles, TEM image of the 2 µm macro-porous silica particles (Figure 2.8) and SEM images of the silica particles (Figures 2.9 (a) 1 µm, (b) 2 µm, (c) 5 µm and (d) 10 µm particle size) did not show perfect uniformity.

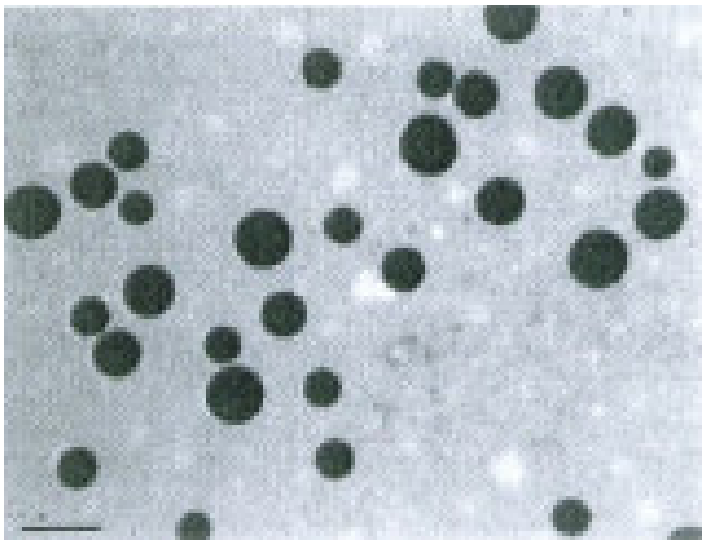

Figure 2.8. TEM image of non-uniform silica particles (2µm in particle size).

The range of silica particles used with the various particle sizes determined is shown in Table 2.1 with standard deviation and relative standard deviation of silica particles shown. A range of particle size between 0.995-1.57 μm for the 1 μm maco-porous silica particles, 1.36-2.10 μm for the 2 μm maco-porous silica particles, 1.74-5.04 μm for the 5 μm maco-porous silica particles and 7.89-12.41 μm for the 10 μm maco-porous silica particles, could be estimated from SEM observations for the silica particles used.

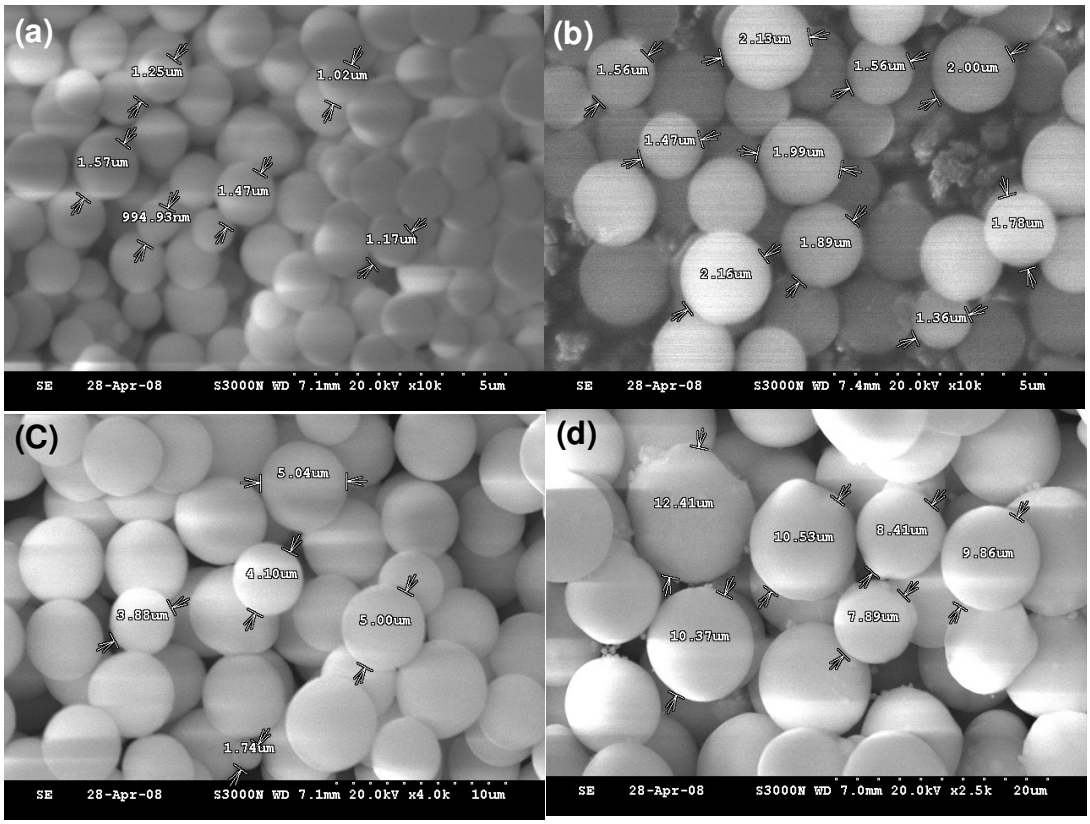

Figure 2.9. SEM images of the silica particles: (a) 1μm, (b) 2μm, (c) 5μm and (d) 10μm particle sizes.

Table 2.1. Standard deviation and relative standard deviation of silica particles.

	1 µm	**2 µm**	**5 µm**	**10 µm**
Average Diameter (µm)	1.25 (n = 6)	1.82 (n = 9)	3.95 (n = 5)	9.91 (n = 6)
Standard Deviation (SD)	0.23	0.29	1.34	1.62
Relative Standard Deviation (RSD)	18.83%	16.07%	33.95%	16.38%

Elimination of cracks and the development of the mesopore structure are the two main issues in the preparation of the carbon monolith. Formation of cracks is the most common problem associated with this procedure. For instance, set up the sonication time for 15 min led to crack the carbon rod, therefore, the time was increased and the silica particles was dispersed in 1-butanol and sonicated for 1 h. Also the 80% ethanol was not the suitable solvent to produce a carbon rod strong enough to overcome the cracks so the solvent was replaced by 1-butanol. In addition, the stirring time after the addition of the formaldehyde into the resorcinol-iron complex within the silica suspension, was set for 10 min according to literature [12], this time was extended to 1 h to ensure achieving a good mixing between the polymer components and thus a homogenous precursor rod free of cracks. The drying procedure is the most important in the production of large pieces of crack-free, porous monoliths. One day drying was not enough to obtain a crack-free carbon rod so the time was extended to 72 h. All the main steps of the synthesis procedure which could potentially cause cracking of the rod have been carried out very carefully and under gentle conditions, as each step has the potential to cause interior pressure causing the cracking of the rod.

The first challenge is the ageing and drying of the silica/phenolic resin wet rod. The rod is aged overnight (16 h) at 90 °C after the formation of the phenolic resin and the silica particles are agglomerated within a rod in a glass tube during this step. An interior pressure gradient develops during this step, caused by the butanol

molecules leaving the resin. Aging allows the phenolic resin compose a highly cross-linked bulk polymer that is strong enough to overcome this pressure. The aging temperature is set below the boiling point of butanol to prevent the formation of bubbles inside the rod. A strong adhesion of the silica particles to the phenolic resin caused by the hydrogen bonds between silanol groups on the silica surface and hydroxyl groups in the polymer matrix renders the whole rod rigid and strong. Inside a fumehood, the aged wet rod was then dried slowly, at room temperature for three days. These gentle drying conditions avoid cracking of the precursor rod.

The pyrolysis of the dry precursor rod is the second challenge in the synthesis of the crack-free carbon monolith. The heating profile was applied as in the literature [12] and found to be ideal for the production of crack-free carbon monoliths. This heating profile was involved two heating ramps. Large amounts of water vapor, carbon monoxide, and hydrogen are generated by the carbonisation of phenolic resin. These gases must be evacuated to avoid their expansion, which also causes interior pressure gradients within the rod. When the heating rate is controlled and kept at 2.5 °C/min up to 800 °C, the formation of gas is slow enough to ensure that the gases diffuse out of the polymer matrix without cracking the rod. Then, increasing the heating rate to 10 °C/min and heating proceeds to 1250 °C was safe enough to complete the carbonisation of the phenolic resin and to form the crack-free carbon monolith.

Shrinking and/or thermal expansion are the two other important possible reasons behind cracking. The pores between graphite strips can have any shape and size because the voids between graphite strips cannot be controlled. An overall shrinking was observed during pyrolysis of the silica precursor rod. The resin is located in the voids between the silica particles and is turned to pure carbon during the carbonisation process. Consequently, the shrinking caused by carbonisation is localised within the voids between the silica particles. Hence, the localised shrinking has two positive effects on the preparation of the porous carbon monolith:

1. It provides space for the thermal expansion of the pyrolysed carbon (note that the linear thermal expansion coefficient of fused silica is 0.36×10^{-6} K^{-1} at 1000 K, that of graphite is 30×10^{-6} K^{-1}) [29].
2. It contributes to improvement of the connecting gaps between the silica particles. This second effect contributes significantly to the development of the connectivity of the macro-pores that result from the removal of the silica particles.

The cladding procedure was the last challenge and was carried out by casing the carbon monolithic rod in a piece of heat-shrinkable PTFE tubing. The temperature was set for 340 ^{o}C and the procedure took 5-6 min. Initial time was set on 10 min led to crack the Teflon tubing, there the time was decreased and found a 5-6 min to be the optimum time. When the temperature of the heated tube was dropped, the PTFE tube was shrinked over the carbon rod. To avoid the cracking of the rod, the hot PTFE tube allowed for a slow cooling.

2.3.2. Morphology of macro-porous carbon

2.3.2.1. SEM results

As described in Section 2.2.4.1, SEM analysis was carried out on a cross-section of the carbon monolithic samples (1, 2, 5 and 10 μm pore diameter) at an accelerating voltage of 20 keV. To study the internal structure of the monoliths, the samples were cut into small pieces and then the clean carbon monolith sample glued onto a metallic conductive disk and placed into the SEM chamber. Both sides of the samples were inspected. SEM images of the 1, 2, 5 and 10 μm macro-porous carbon/silica composite monolith structures as shown in Figure 2.10 showing how the silica particles are held within the polymer before the pyrolysis and removal of the silica particles by HF treatment. The silica particles are not closely packed in the dry precursor rod as shown in Figure 2.10 because these particles do not have an identical volumes and diameters due to the non-uniformity and heterogeneity. The ideal scenario is to have a close-packed structure where silica particles (of identical volume and diameter) are arranged in a tight, locked-in structure. In this case, the silica particles are not free to move. SEM images for the carbon/silica composite monolithic samples used a high accelerating voltage at 20 keV for the best obtainable resolution imaging and typically a short analytical working distance at 8.0–13.1 mm was used.

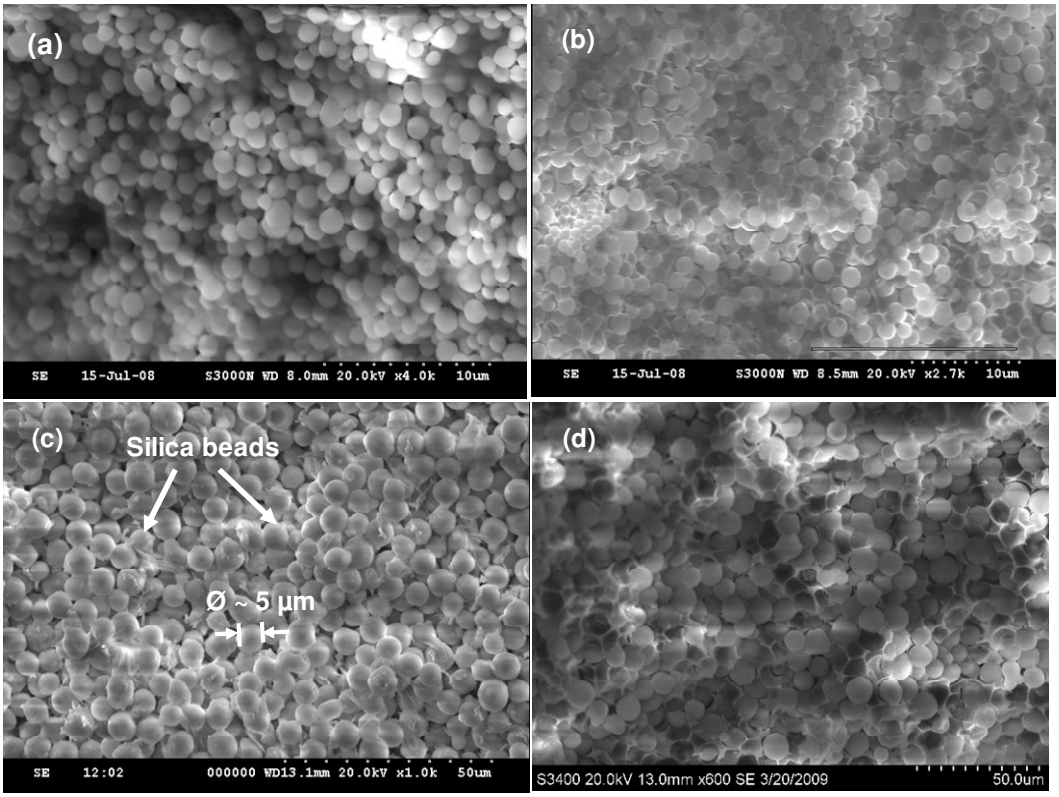

Figure 2.10. SEM images of the carbon/silica composite materials (a) 1 µm (b) 2 µm (c) 5 µm and (d) 10 µm (silica particle size) before HF treatment and removal of the silica particles.

Magnification at 4.0 k was used for the 1 µm templated carbon/silica composite monolith, 2.7 k was used for the 2 µm templated carbon/silica composite monolith, 1.0 k was used for the 5 µm templated carbon/silica composite monolith and 600 was used for the 10 µm templated carbon/silica composite monolith.

SEM images in Figure 2.11 show the 1, 2, 5 and 10 µm macro-porous carbon monolithic structures after removal of the silica particles following the pyrolysis and HF treatment. The SEM analysis revealed an interconnected rigid bimodal porous structure involving macro-pores and meso-pores and verified the quantitative removal of the embedded silica particles. For chromatographic applications, a good monolith requires a bimodal porous structure with suitable surface area [7-8]. The large flow-through channels corresponded to the dimensions of the silica gel template used.

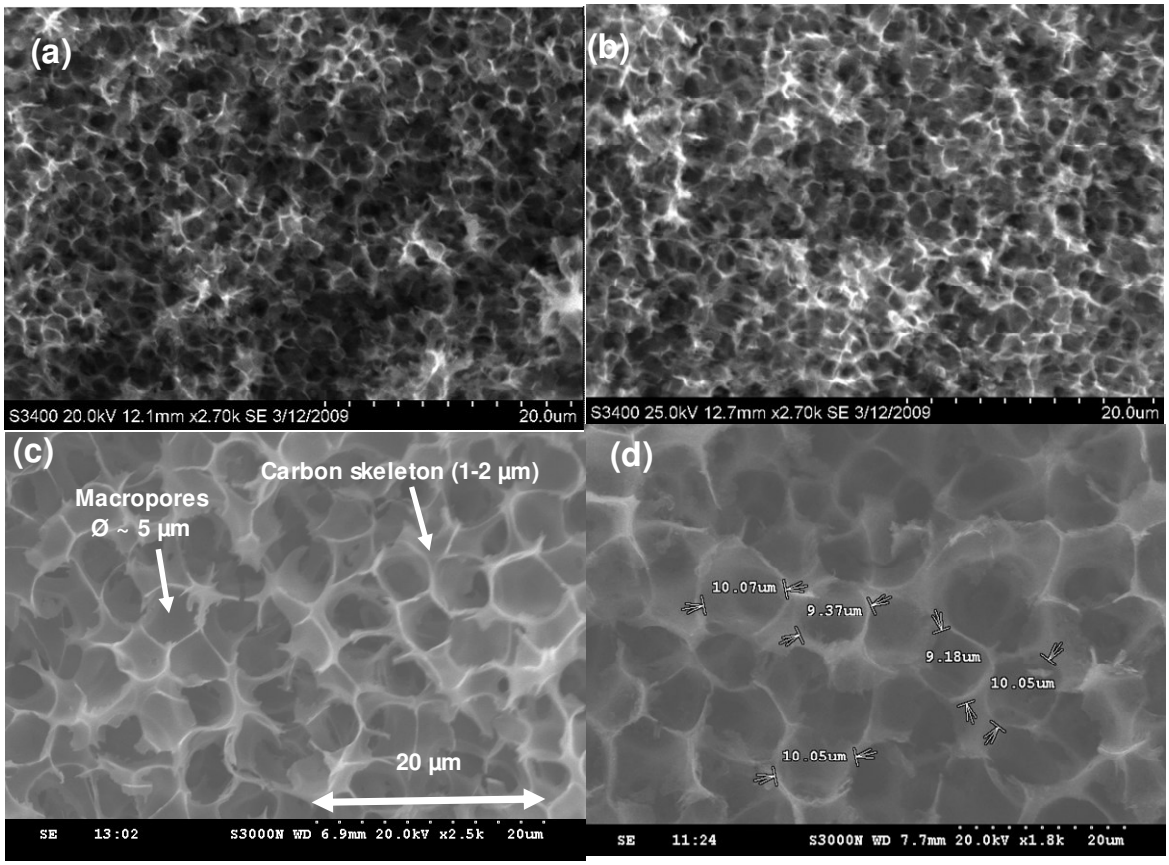

Figure 2.11. SEM images of the carbon monolithic structures (a) 1 µm (b) 2 µm (c) 5 µm and (d) 10 µm (macro-pores) after HF treatment and removal of the silica particles.

The SEM analysis also showed the dimensions of the continuous carbon skeleton to be in the range of 1-2 µm after the pyrolysis and removal of the silica particles (Figure 2.11 (c)). A high accelerating voltage at 20-25 keV, an analytical working distance at 6.9–12.7 mm, and magnification at 1.8-2.7 k were used for best resolution imaging and analysis.

As was demonstrated by Nakanishi and co-workers [7-8], and mentioned above, a suitable monolithic structure for chromatography has a bimodal porous structure comprising macro-pores and meso-pores. The macro-pore (Figure 2.12) network affords a low hydraulic resistance within the column. The flow-through channels within the monolith offer a more regular shape than those around the particles of a conventional bed. Accordingly, band dispersion resulting from eddy

diffusion is reduced within monolithic columns. To produce regular flow-through channels within the carbon monolith, narrow size distribution silica particles were used.

Meso-pores (Figure 2.13) can be generated within the skeleton of the monolith. HR-SEM was used to image the smooth glassy carbon surface morphology. The presence of isolated meso-pores in the carbon skeleton of the order 10-20 nm were clearly present (Figure 2.14).

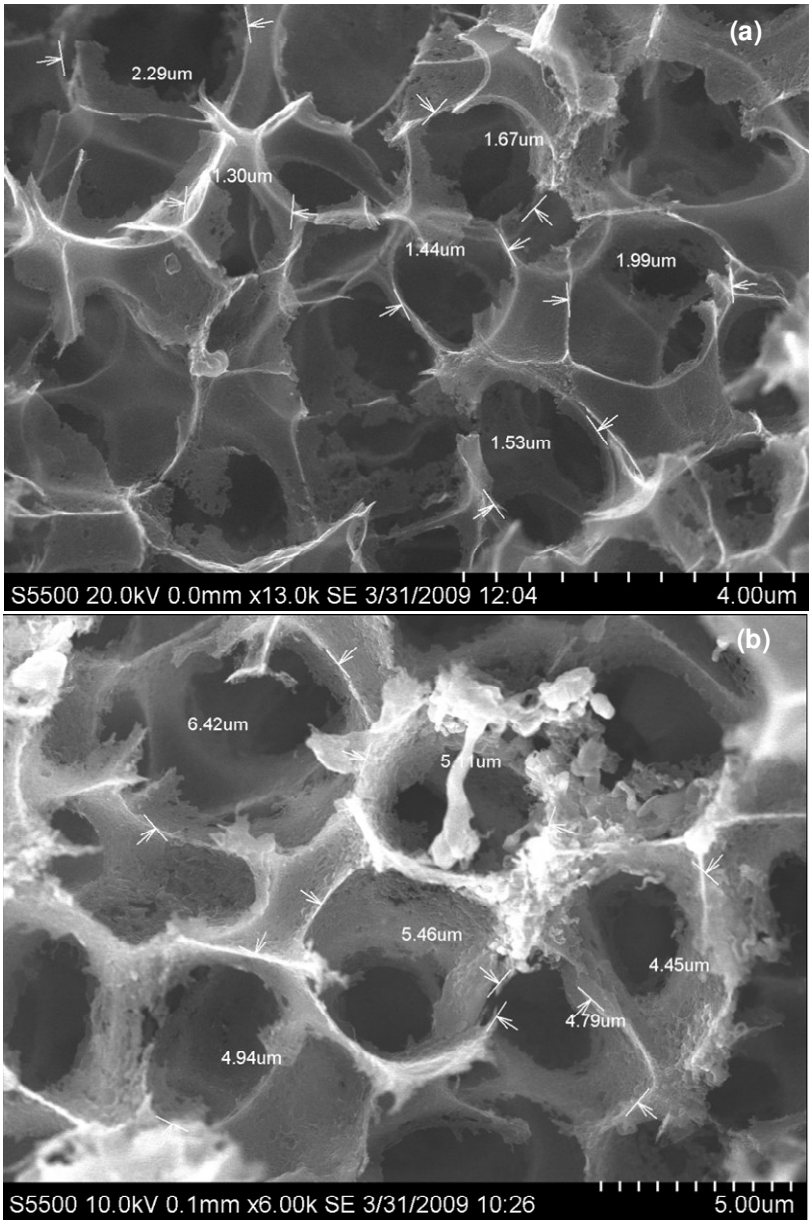

Figure 2.12. HR-SEM images of the macro-pore carbon monolithic structures (a) 1.5-2 μm (b) 4.5-6 μm in size.

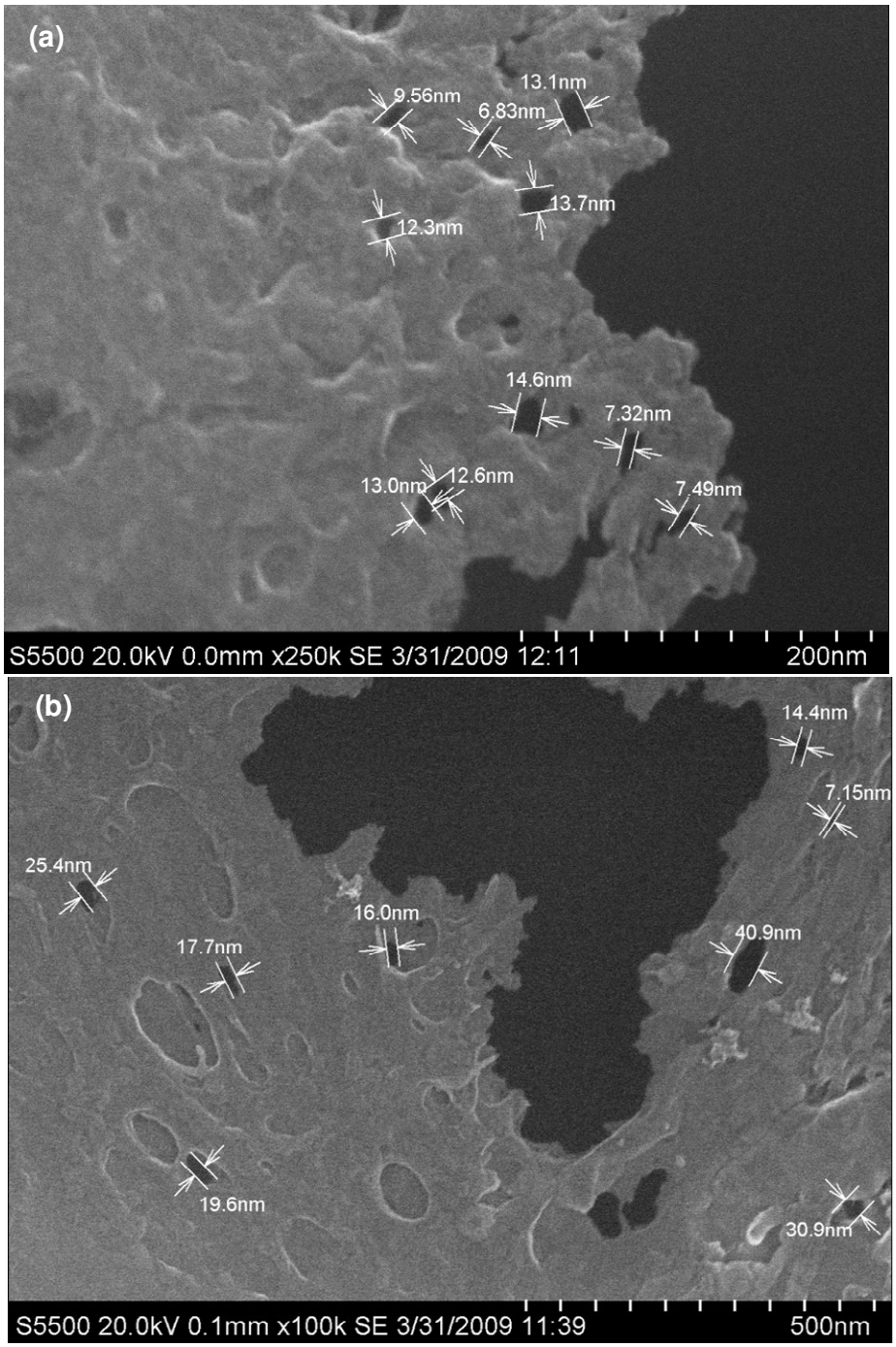

Figure 2.13. HR-SEM images of the meso-porous carbon monolithic structures (a) 7-14 nm (b) 7-40 nm.

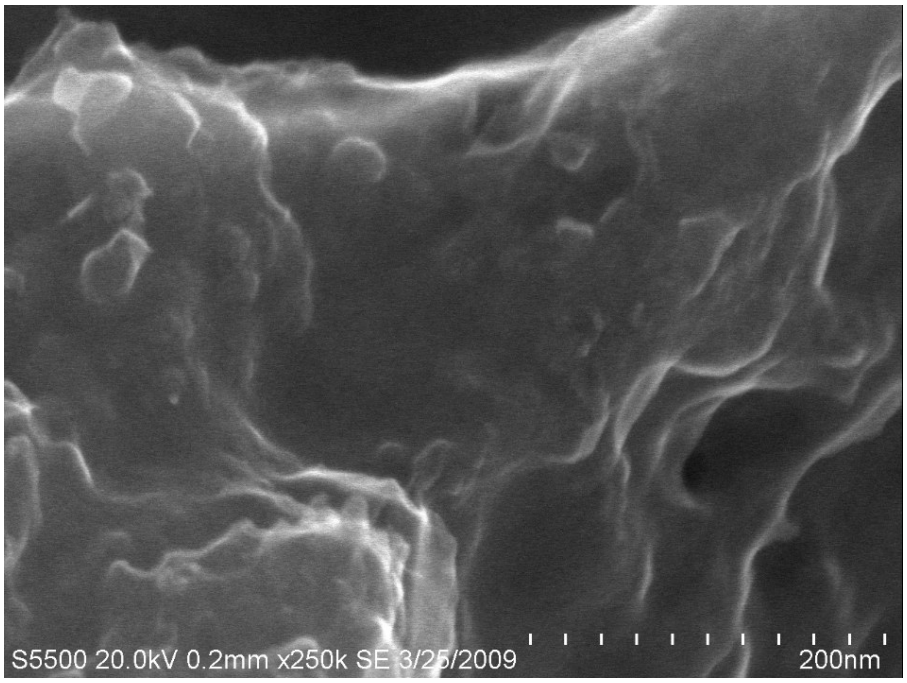

Figure 2.14. HR-SEM image of the glassy carbon surface morphology of the 5 μm templated monolith.

Knox *et al.,* [30] prepared a predominately micro-porous glassy carbon by pyrolysis of phenolic resins which has been proved (by earlier researchers) to be not ideal as a chromatographic stationary phase. The micro-pores, although contributing to the surface area, where also identified as possibly causing band broadening and severe tailing in the elution peak, and poor column efficiency. Thus, carbon material with such micro-pores has been shown to exhibit poor LC performance [12]. Knox and his co-workers [30-31] eliminated most of the micro-pores in glassy carbon through graphitisation**.** However, graphitisation must be carried out at temperature of ~ 2400 ^{o}C or higher. Such a high temperature treatment will drastically diminish the meso-porosity of the glassy carbon, so the graphitised carbon rod may no longer have a sufficient surface area to achieve separations. To retain meso-porous carbon, catalytic graphitisation is often used which has the potential to yield a product with a high graphite index at a relatively low temperature.

The meso-porosity of the carbon monoliths produced here was developed by in-situ catalytic graphitisation. The polymer prepared was a complex of Fe, resulting from the polycondensation of the resorcinol/Fe(III) complex. The Fe(III) ions are

reduced to Fe atoms catalysing the crystallisation of glassy carbon during pyrolysis. This crystallisation of the micro-porous glassy carbon forms graphite strips within the carbon matrix. The glassy carbon turns into graphite strips during graphitisation and becomes denser causing an increase in the meso-porous volume.

2.3.2.2. Energy-dispersive X-ray analysis

The elements present in selected regions of the monolithic carbon samples were detected by EDX analysis providing qualitative information about the monolith composition. EDX analysis carried out on cross sections of the carbon monolithic samples (1, 2, 5 and 10 µm macro-pores) provided evidence that the silica was totally removed from the carbon rod after treatment in concentrated HF. Figure 2.15 shows the elemental distribution of C, Si, Cl, Fe and O within a section removed from a monolithic rod (10 µm macro-pores) before pyrolysis and silica removal, the corresponding SEM for which is shown as Figure 2.10 (d).

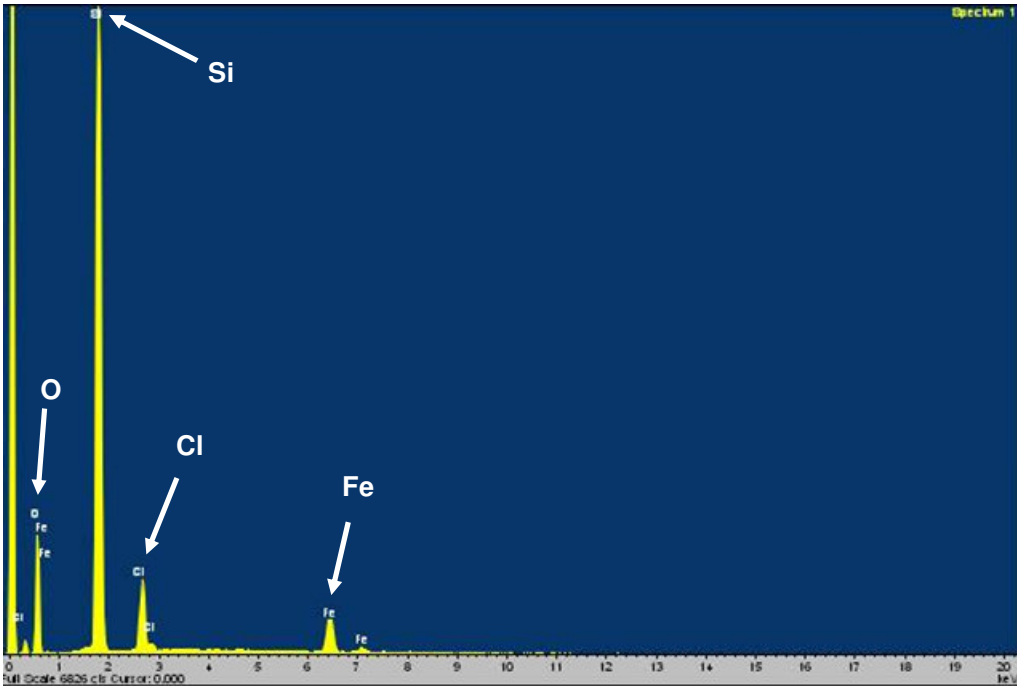

Figure 2.15. EDX spectrum of the carbon monolith (10 µm macro-pores) before pyrolysis and removal of the silica particles and iron catalyst.

The elemental distribution of C of the corresponding SEM (Figure 2.11 (d)) of the section removed from the beam centre of the monolithic rod (10 µm macro-pores) are shown in Figure 2.16.

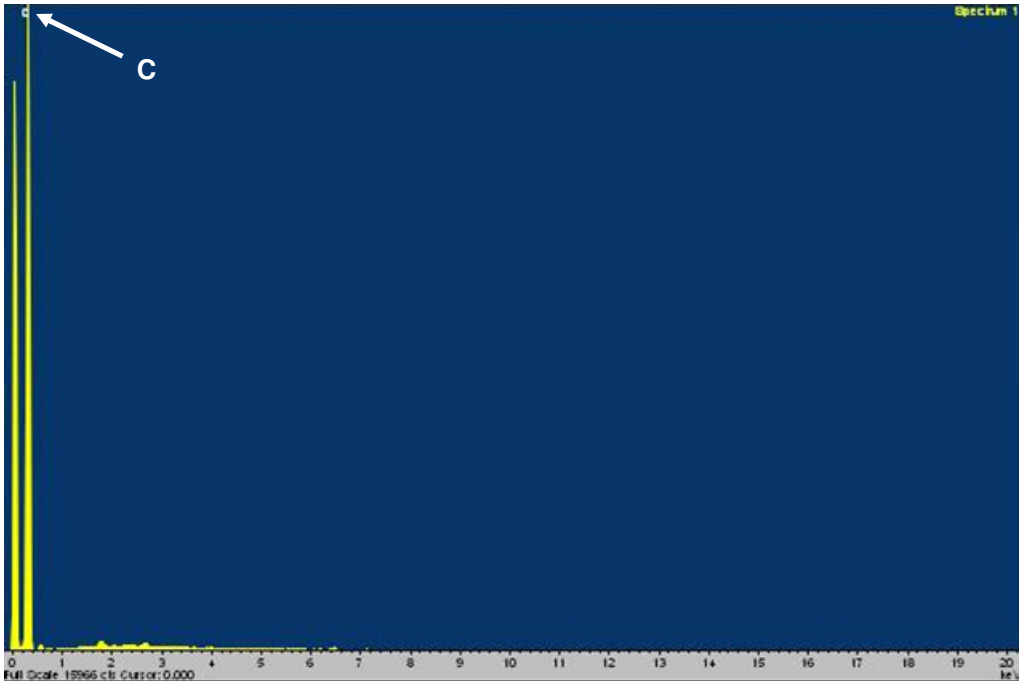

Figure 2.16. EDX spectrum of the carbon monolith (10 µm macro-pores) after pyrolysis and removal of the silica particles and iron catalyst.

2.3.3. BET Surface area of carbon monoliths

The meso-porosity of the carbon monoliths was further examined by measuring BET nitrogen adsorption/desorption isotherms. BET surface area analysis was employed to investigate characteristics of the monoliths before and after pyrolysis. The starting silica particles themselves were also characterised. The support surface area of silica particles (1, 2, 5 and 10 µm particle size) was typically in the range of about 300-900 m^2 g^{-1} as follows, 934, 616, 359 and 339 m^2/g, respectively, with a pore diameter 48, 50, 50 and 100 Å, respectively. Table 2.2 shows the measured surface areas and pore volumes of the silica particles and produced monoliths investigated in this study.

Table 2.2. Surface area and pore volumes measurements of the silica particles and carbon monoliths, before and after pyrolysis.

SiO_2 particle size (μm)	Surface area (SiO_2) (m^2/g)	Monolith before pyrolysis (m^2/g)	Monolith after pyrolysis (m^2/g)	Pore vol (cm^3/g) before pyrolysis	Pore vol (cm^3/g) after pyrolysis
1	934	315	178	0.34	0.23
2	616	235	154	0.23	0.23
5	359	196	85	0.30	0.095
10	339	195	125	0.57	0.32

In general, it can be seen from column 2 of Table 2.2, that the surface area of the silica particles decreases as the particle size and the internal pore size of these particles increases. The 1 μm silica exhibited a surface area of 934 m^2/g, indicative of a highly porous material and the 2 μm silica exhibited a surface area of 616 m^2/g. The silica particles (1 and 2 μm particle size) exhibited a classic Type 1 isotherm (Figures 2.17 and 2.18), respectively, indicative of micro-porous materials. The curve rises very steeply at first as the micro-pores are filled and as progressively larger micro-pores fill in order of increasing size. The curve then becomes a horizontal line as the majority of the pores have been filled and there is very little room for further adsorption. A final rise is observed close to unity and this is accompanied by hysteresis, as saturation is approached and bulk condensation begins to occur. The pore volume distribution of the1 μm silica peaked at 2.1 nm (Figure 2.17).

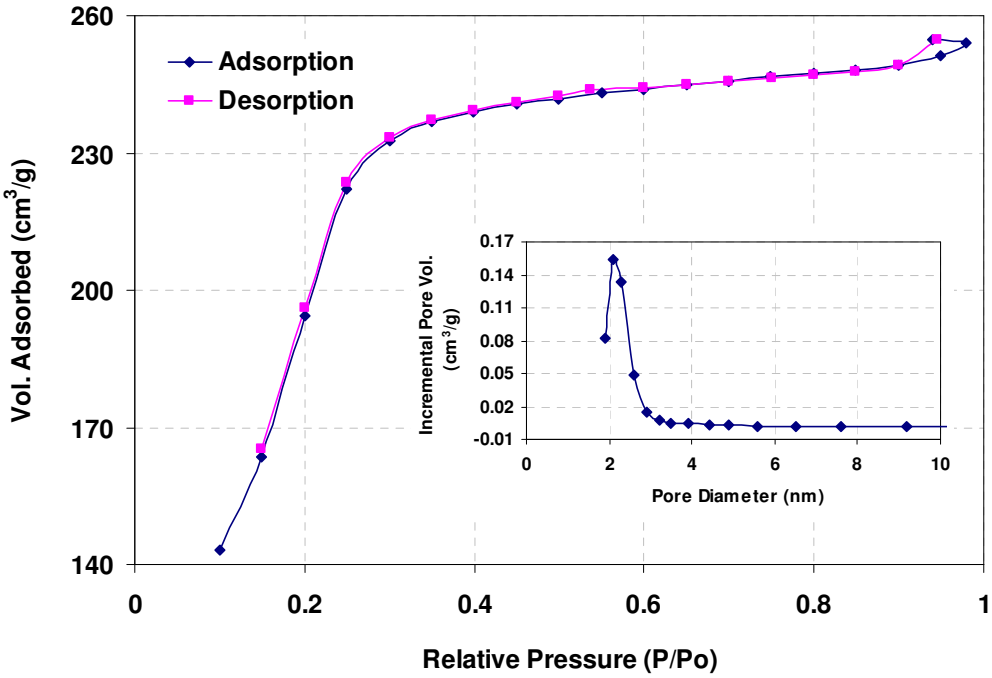

Figure 2.17. BET adsorption isotherm and pore size distribution of 1 µm silica particles exhibiting a Type 1 isotherm.

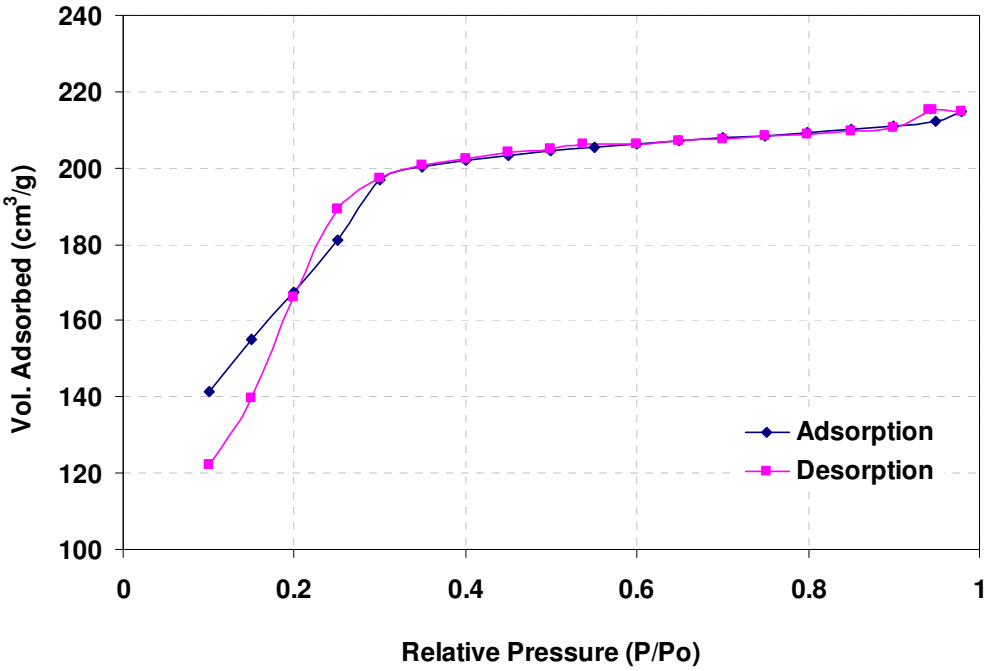

Figure 2.18. BET adsorption isotherm and pore size distribution of 2 µm silica particles exhibiting a Type 1 isotherm.

In terms of the monolithic carbon-silica samples, lower surface areas when compared to the silica particles were observed. For the 1 µm carbon-silica monolith before pyrolysis a surface area of 315 m^2/g was recorded (Figure 2.19). The surface area is made up of the phenolic resin element and the silica element of the composite. It is taken that the phenolic resin is non-porous at this stage and that the surface area is attributed to the internal porosity inside the silica particles. In this case it may be expected that this monolithic sample would show very similar characteristics to the 1 µm particle size sample. In fact, a Type 4 isotherm, commonly associated with the presence of meso-porosity, was observed (Figure 2.19).

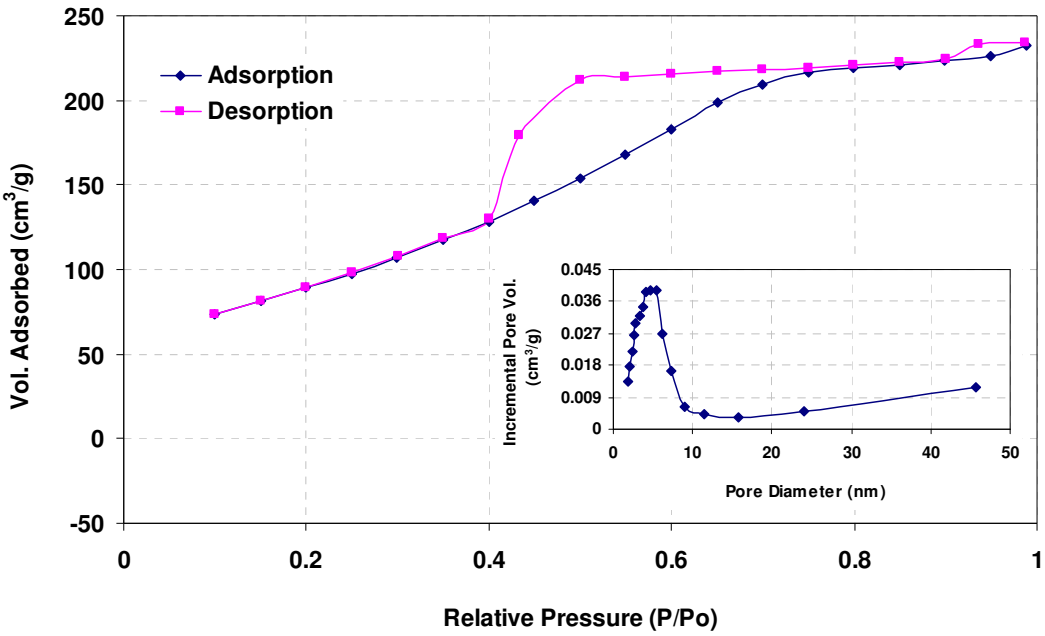

Figure 2.19. BET adsorption isotherm and pore size distribution of 1 µm carbon-silica monolith before pyrolysis exhibiting a Type 4 isotherm.

Capillary condensation gave rise to a hysteresis loop at medium pressures. A hysteresis loop was also observed close to unity, similar to that observed for the 1 µm silica particles sample. A peak was observed for pores between 2-9 nm. Presumably, this is the same porosity as was found for the silica particles sample. In this sample however, there is a distinct uptake in volume absorbed beyond 15 nm and this continues to rise to 45 nm and beyond. This could perhaps be attributed to pores formed by the contact points between silica particles which were not completely filled by phenolic resin. Following pyrolysis and HF treatment, the surface area of

the sample with 1 µm (macro-pore size) dropped to 178 m^2/g. This further drop was due to the removal of the porous silica particles which were responsible for the high surface area prior to pyrolysis, thus, leaving a skeleton of large pores (approximately 1 µm). Such large pores are beyond the measurement range of the BET.

In terms of the 2 µm monolithic carbon-silica sample, a lower surface area when compared to the 2 µm silica particles was observed. For the 2 µm carbon-silica monolith before pyrolysis a surface area of 235 m^2/g was recorded made up of the phenolic resin element and the silica element of the composite (Figure 2.20). The surface area is attributed to the internal porosity inside the silica particles and it is taken that the phenolic resin is non-porous at this stage as mentioned above in this Section. As expected, this monolithic sample would show very similar characteristics to the 2 µm particle size sample and a Type 1 isotherm was observed (Figure 2.20).

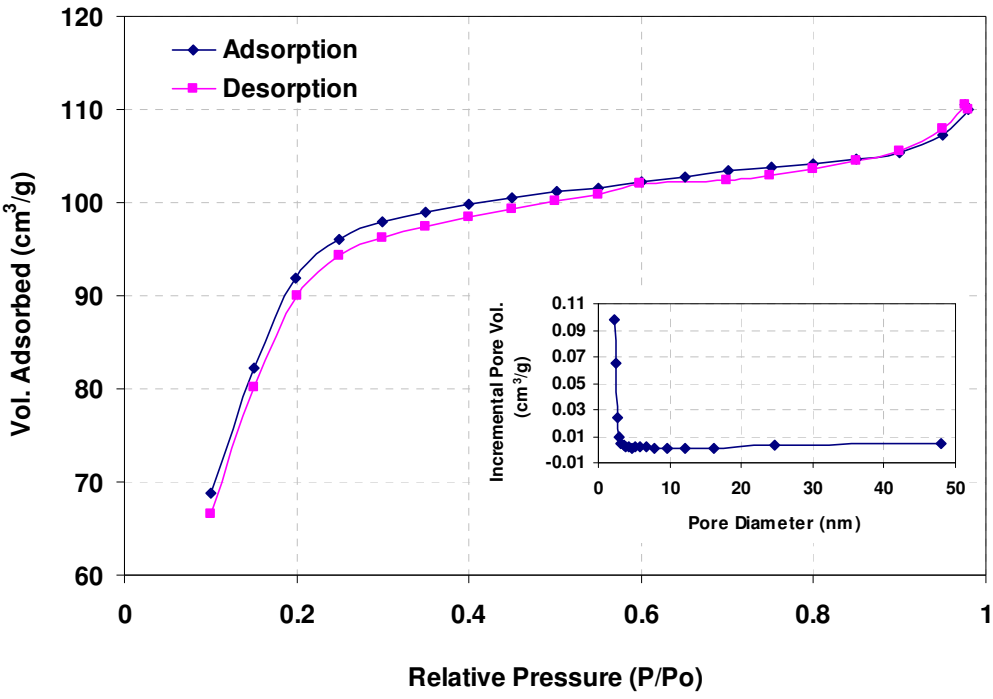

Figure 2.20. BET adsorption isotherm and pore size distribution of 2 µm carbon-silica monolith before pyrolysis exhibiting a Type 1 isotherm.

The 5 and 10 µm monolithic carbon-silica samples showed similar trends to the 1 µm monolithic carbon-silica sample and Type 4 isotherms were observed (Figures 2.21 and 2.22), respectively

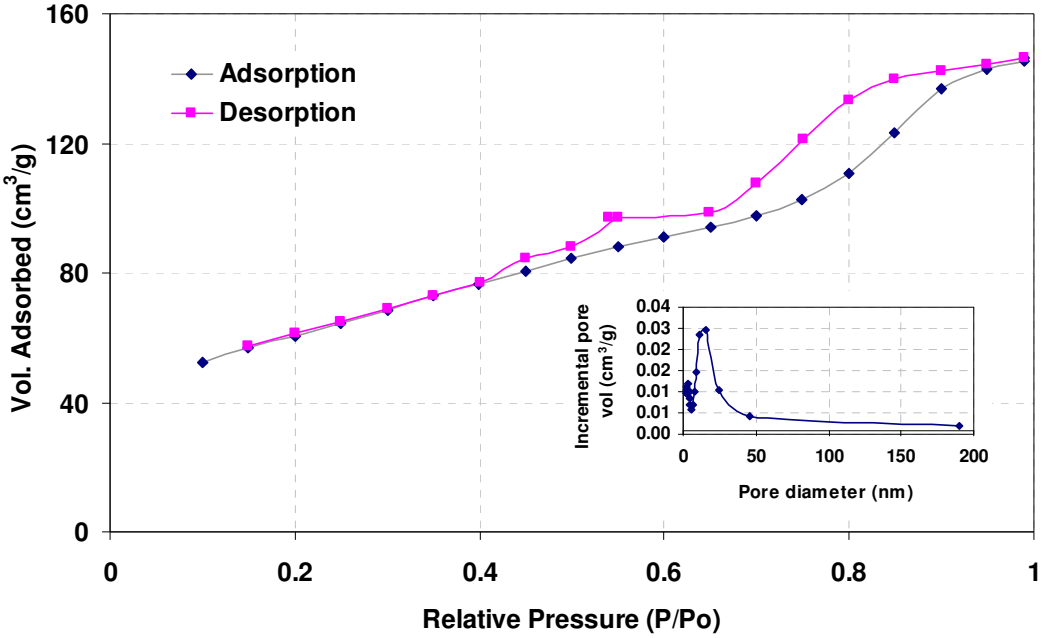

Figure 2.21. BET adsorption isotherm and pore size distribution of 5 µm carbon monolith before pyrolysis exhibiting a Type 4 isotherm.

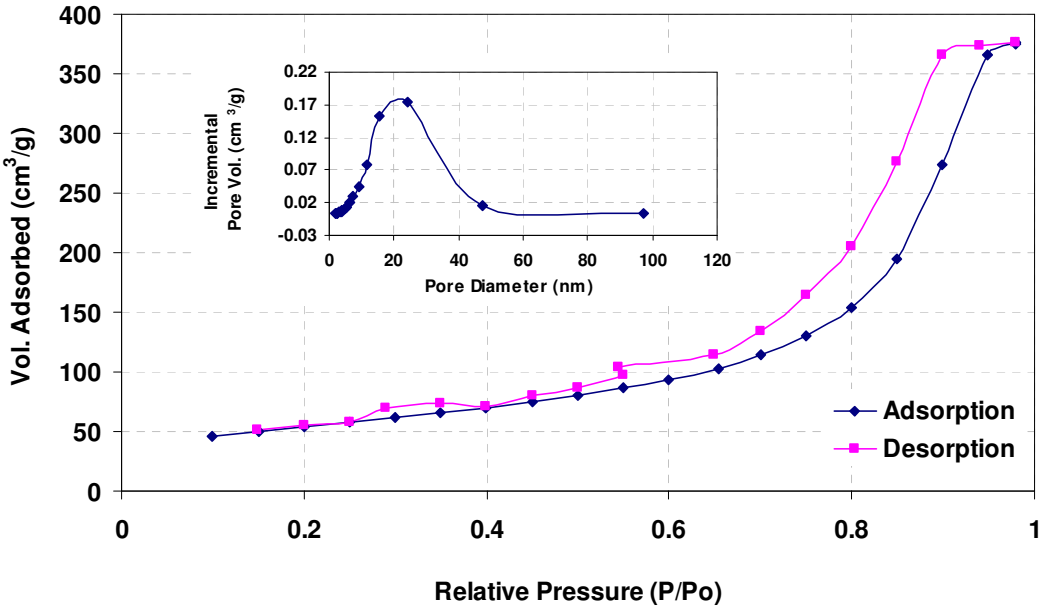

Figure 2.22. BET adsorption isotherm and pore size distribution of 10 µm carbon monolith before pyrolysis exhibiting a Type 4 isotherm.

The adsorption-desorption isotherms for the 1, 2, 5 and 10 μm (macro-pore size) carbon monoliths after pyrolysis and HF treatment were also Type 4, but in these cases hysteresis was exhibited from relative pressure 0.4 to unity, indicative of pores in the meso-range and beyond. Pores were shown to exist at high volumes below 15 nm but also up to 200 nm and further, beyond the range of the instrument. This was expected since pores of approximately 1 μm were expected following removal of the silica (Figures 2.23, 2.24, 2.25 and 2.26).

These carbon monoliths do not have the sharp condensation step that characterises a narrow pore size distribution. The meso-pores within the rod have a wide size distribution with irregular pore shapes. The specific surface area contributions of the meso-pores of the 1, 2, 5 and 10 μm monoliths were 315, 235, 196 and 195 m^2/g before pyrolysis and removal of the silica particles, and 178, 154, 85 and 125 m^2/g after the pyrolysis and removal of the silica template, respectively. The pore volumes of meso-pores derived from BET isotherms of the 1, 2, 5 and 10 μm monoliths were 0.34, 0.23, 0.30 and 0.57 cm^3/g before pyrolysis and removal of the silica particles, and 0.23, 0.23, 0.095 and 0.32 cm^3/g after the pyrolysis and removal of the silica template, respectively. The pore size distributions of meso-pores derived from BET isotherms of the 1, 2, 5 and 10 μm monoliths were 3.6, 2.5, 6.2 and 10.6 mL/g before pyrolysis and removal of the silica particles, and 6.5, 6.4, 7.0 and 8.9 mL/g after the pyrolysis and removal of the silica template, respectively. For comparison, the specific surface area contribution of the meso-pores in a 10 μm carbon monolith was 163 m^2/g and the volume of meso-pores derived from a BET isotherm derived in the same way was 0.52 cm^3/g after the pyrolysis and removal of the silica template [12].

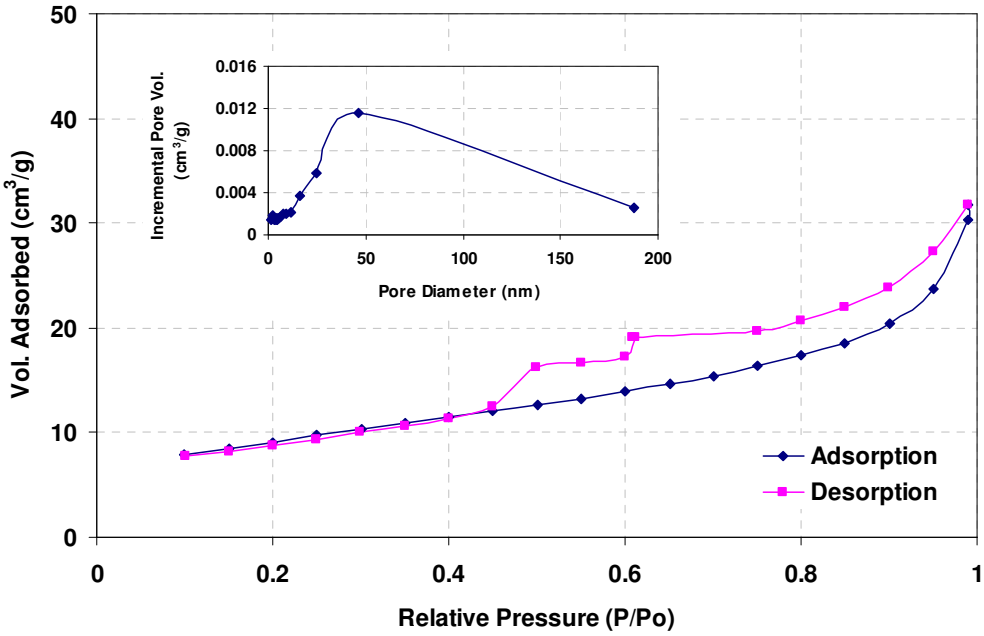

Figure 2.23. BET adsorption isotherm and pore size distribution of 1 µm carbon monolith after pyrolysis exhibiting a Type 4 isotherm.

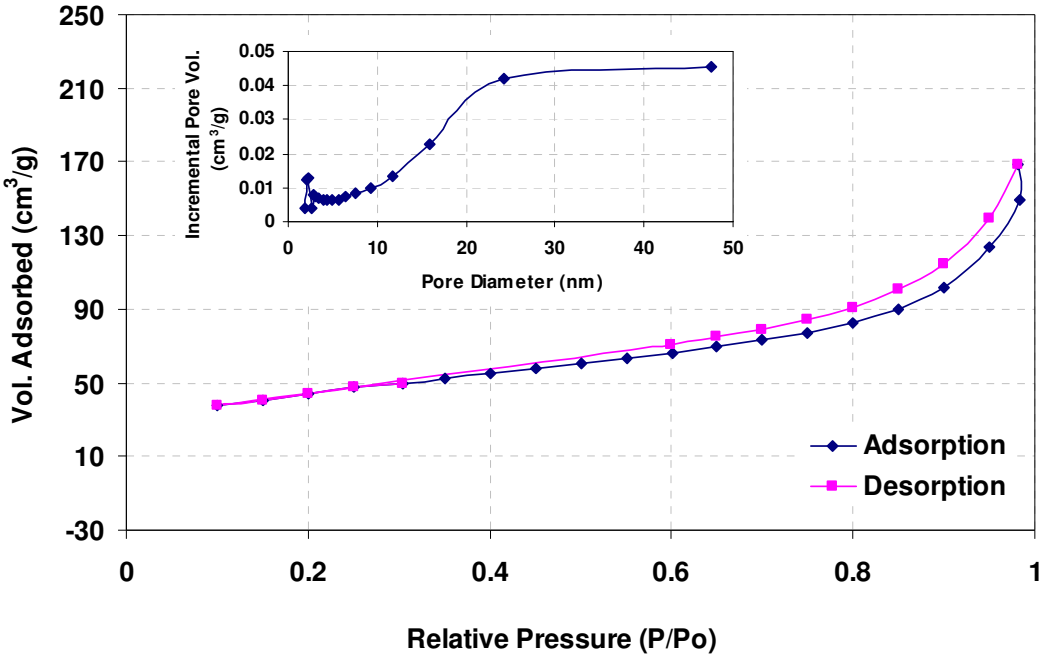

Figure 2.24. BET adsorption isotherm and pore size distribution of 2 µm carbon monolith after pyrolysis exhibiting a Type 4 isotherm.

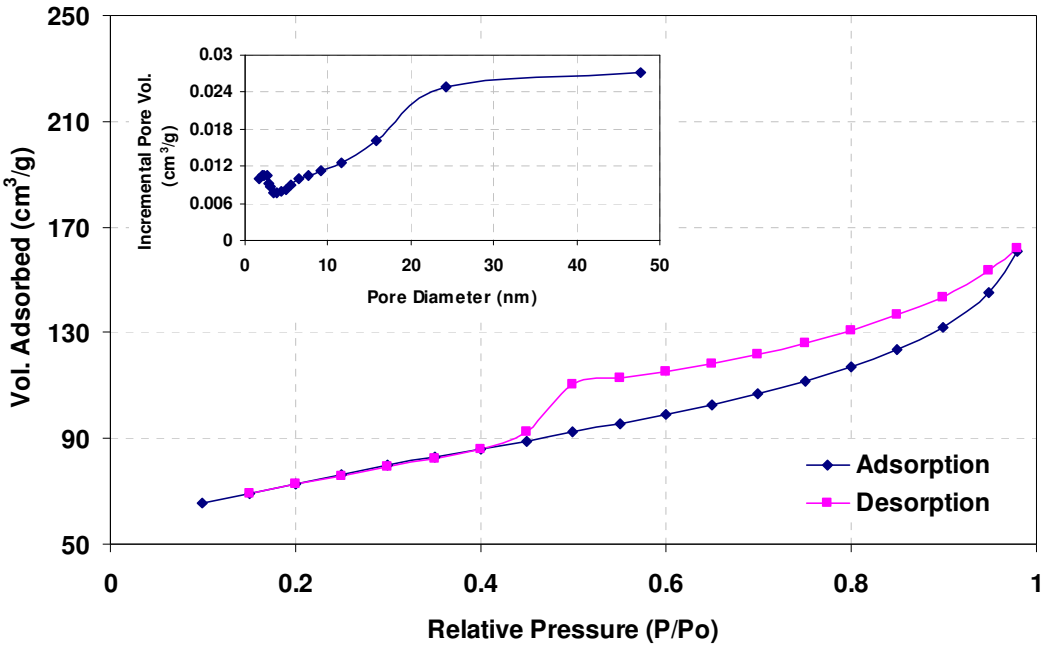

Figure 2.25. BET adsorption isotherm and pore size distribution of 5 µm carbon monolith after pyrolysis exhibiting a Type 4 isotherm.

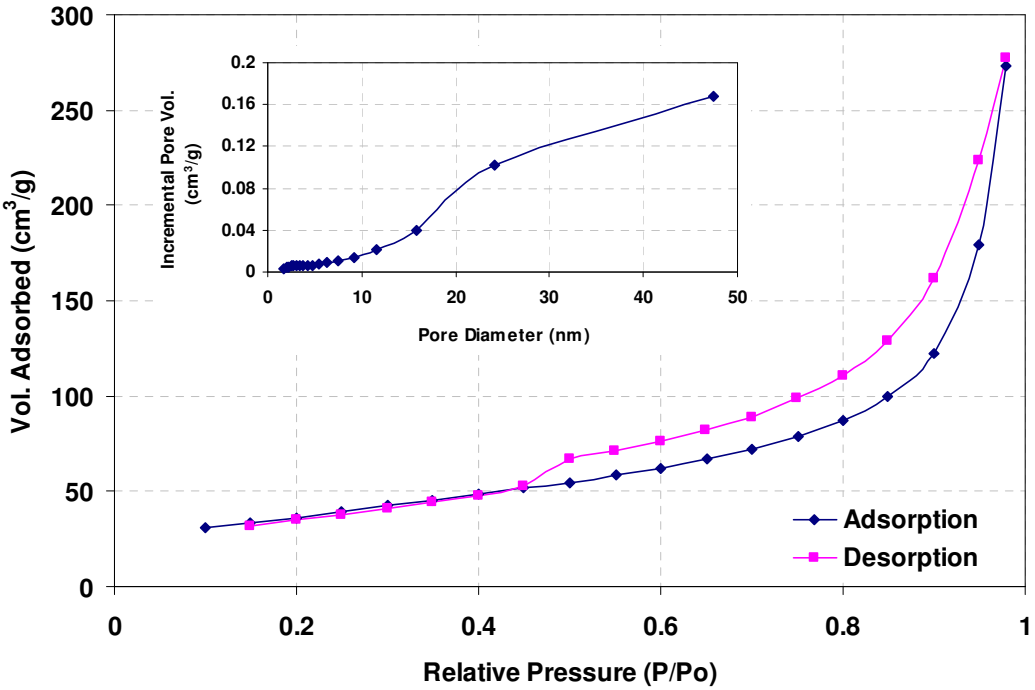

Figure 2.26. BET adsorption isotherm and pore size distribution of 10 µm carbon monolith after pyrolysis exhibiting a Type 4 isotherm.

The pore volume of the 10 μm sample after pyrolysis and removal of the silica particles was quite high (0.32 cm^3/g). After pyrolysis it would appear that a large quantity of these pores may still exist if the silica was not entirely removed during the HF treatment of for this sample. Perhaps there is a relationship between etch time and size of SiO_2 particle, i.e. the larger the particle the longer the etch time required.

However, the etch time was 3 h for the 1, 2 and 5 μm templated silica-carbon composite monoliths, while 6 h for the 10 μm templated silica-carbon composite monolith.

2.3.4. Dilatometry analysis

Dilatometry is a useful technique to investigate the shrinkage of the carbon monolith samples during a pyrolysis heating cycle. As described in Section 2.2.4.3, dilatometric analysis for the cylindrical (approximately 7 mm diameter x 5 mm length) 1, 2, 5 and 10 μm carbon monolithic samples was carried out using the dilatometer under flowing N_2 (250 cm^3/min). Each sample was placed inside the furnace and a heating profile was applied with heating rates in accordance with the pyrolysis profile described in Section 2.2.3.1. The shrinkages of the four monolithic 1 μm (Figure 2.27), 2 μm (Figure 2.28), 5 μm (Figure 2.29) and 10 μm (Figure 2.30) samples during pyrolysis were studied here. Shrinkage commenced at approximately 200 °C and was rapid up to approximately 800 °C. During this step a slow heating rate of 2.5 °C/min was used, to minimise the potential for thermal shock, rapid gas evolution and cracking. A plateau in the shrinkage occurs, coinciding with the 2 h isothermal hold at 800 °C. The shrinkage slows down as the structure is consolidated. After the isothermal hold the heating rate is increased to 10 °C/min and heating proceeds to 1250 °C. During this new heating phase, a second phase of rapid shrinkage was observed. The temperature was then held constant at 1250 °C for 1 h.

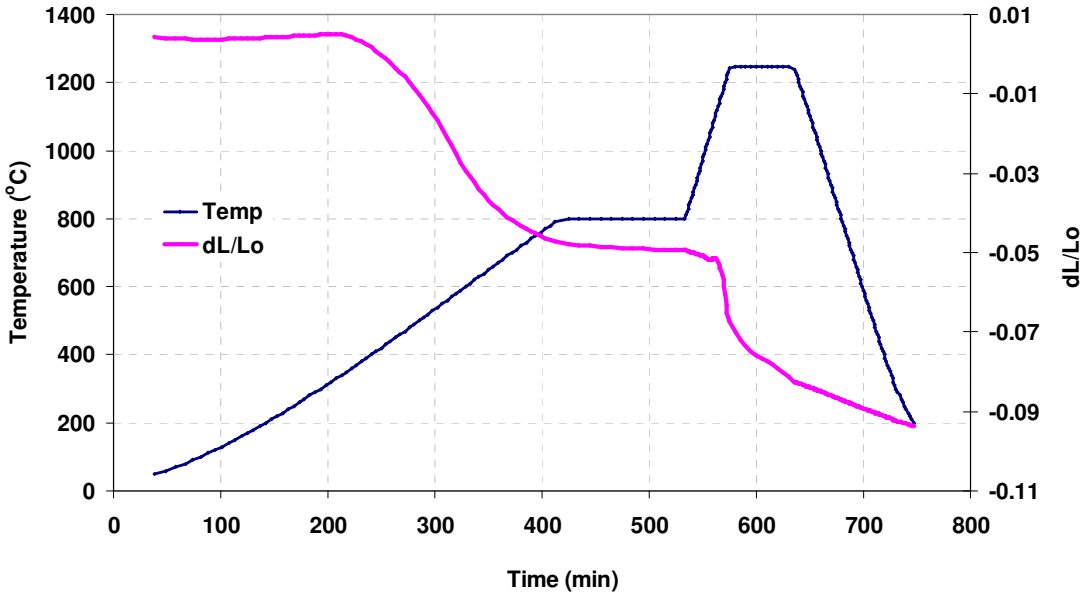

Figure 2.27. Dilatometry profile of the 1 μm silica-particle templated monolithic rod subjected to a temperature-programmed pyrolysis cycle.

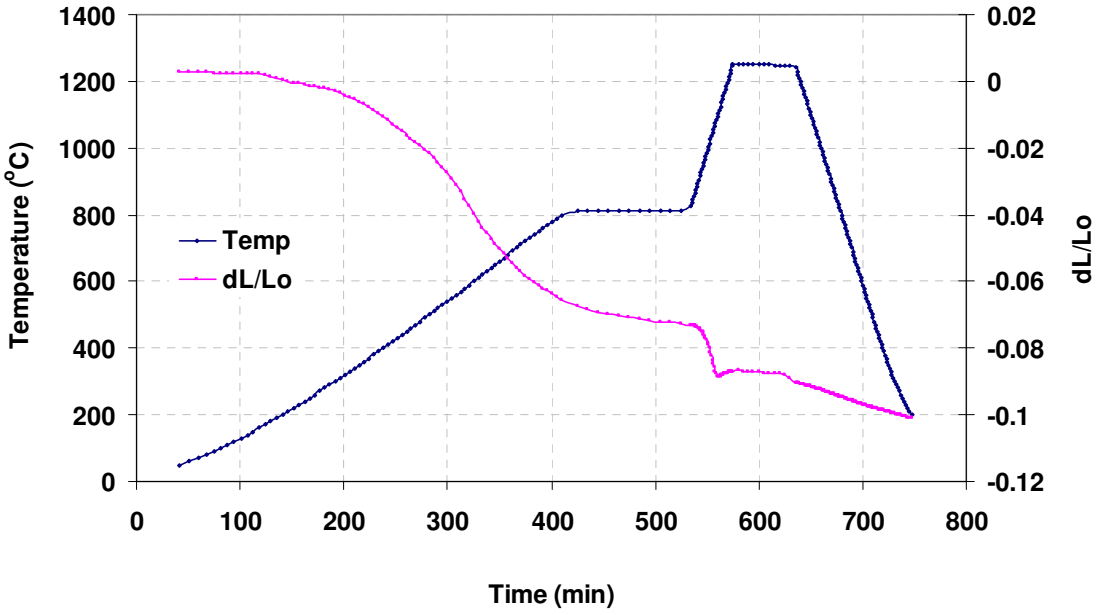

Figure 2.28. Dilatometry profile of the 2 μm silica-particle templated monolithic rod subjected to a temperature-programmed pyrolysis cycle.

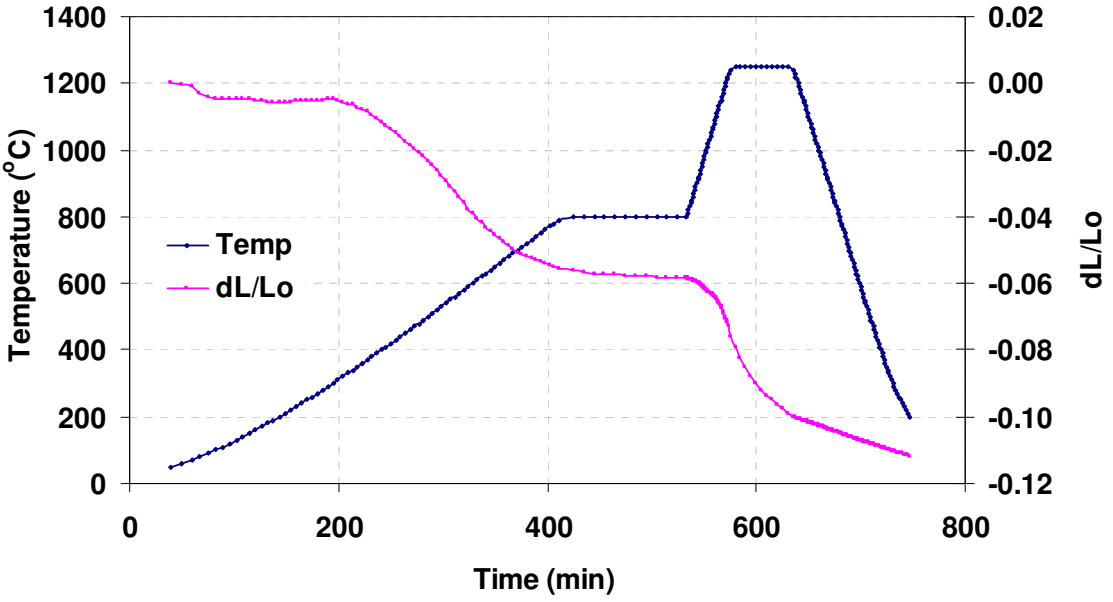

Figure 2.29. Dilatometry profile of the 5 μm silica-particle templated monolithic rod subjected to a temperature-programmed pyrolysis cycle.

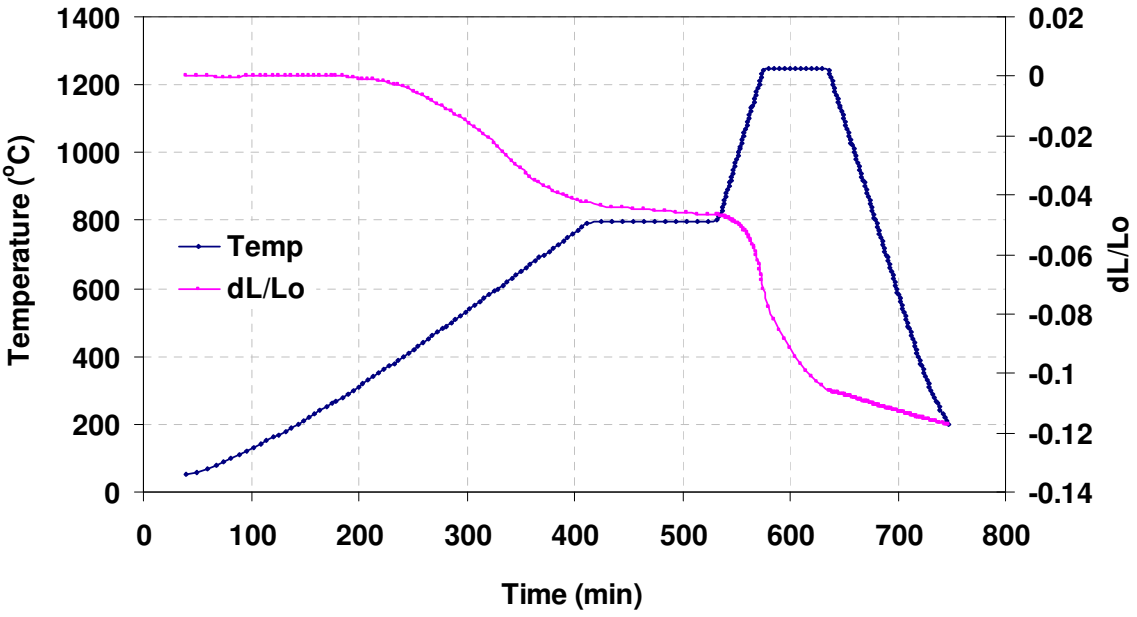

Figure 2.30. Dilatometry profile of the 10 μm silica-particle templated monolithic rod subjected to a temperature-programmed pyrolysis cycle.

The behaviour observed was different for the 1 and 2 µm samples compared to the 5 µm and 10 µm samples. For the 1 and 2 µm samples, a sharp shrinkage was observed during the 10 °C/min heating ramp to 1250 °C. During the isothermal hold at 1250 °C these sample curves tended to plateau out. The 5 and 10 µm samples exhibited a steady rapid shrinkage from 800 °C to the end of the isothermal hold at 1250 °C. All of the samples continued to contract, almost identically, during cooling. Shrinkage could be increased in proportion to the particle size of the silica used. Thus, the larger the particle size the larger the gaps between particles. The phenolic resin resides in these gaps, leading to a larger degree of particle re-arrangement for larger particle sizes. The shrinkage observed in Figures 2.27-2.30 can be partly attributed to carbonisation of the resin located between the silica particles. Further shrinkage can be attributed to the non-uniformity of silica particles. During the pyrolysis the silica particles will rearrange themselves and shift slightly until such time as they become locked in position. However, the overall shrinkage of the rods ranged from approximately 9 % to almost 13 %.

In theory, the approximate volume ratio of silica to phenolic resin was ~ 1.3, or in other words, the silica particles occupied 57% and the phenolic resin occupied 43% of the rod. The ideal scenario is to have a close-packed structure where silica particles (of identical volume and diameter) are arranged in a tight, locked-in structure as mentioned earlier in Section 2.3.2.1. In this case, the silica particles are not free to move. The phenolic resin occupies the voids between the beads. In practice, a perfectly ordered 3-dimensional structure is difficult to achieve, particularly due to the difficulty of sourcing silica particles of exact uniformity on the micron-scale. Another possible reason for high shrinkage could be non-uniform infiltration of phenolic resin into the void spaces between silica particles. Infiltration can be difficult to achieve and is dependent on the conditions used to mix the phenolic resin and silica particles (and achieve full wetting of the silicas), including the use of stirring or vacuum to force the resin into the voids. The viscosity of the resin solution is another variable which can determine the degree of infiltration. Wang *et al.,* [32] state that the smaller the particle sizes of the silica particles the greater the contact area per unit volume between the silica and the infiltrating resin. Ko *et al.,* [33] carried out an in-depth study of the behaviour of phenolic resin during pyrolysis. According to Ko *et al.,* volatiles such as H_2O, CO, CO_2, H_2 and other gases are removed during pyrolysis, leading to weight loss and shrinkage.

Significantly, Ko *et al.,* claim that 91% of the total gases evolved during pyrolysis occurred in the temperature range of 400 – 700 °C. Shrinkage of the phenolic resin increased linearly with temperature below 700 °C and was attributed to the rearrangement of the carbon structure. Above 1000 °C the shrinkage neared completion due to the packing and crosslinking of the glassy carbon structure. Total shrinkage of approximately 17 % was observed. However, Liang *et al.,* [12] surprisingly reported that no significant overall shrinking was observed during carbonisation of the silica embedded precursor rod.

Krzesinka and Zachariasz [34] studied the effect of pyrolysis temperature on the physical properties of monolithic carbons. Weight loss, i.e., the percentage decrease of weight of an initial sample observed during pyrolysis, *WL*(%), was calculated from weight of sample before (W_{raw}) and after (W_{carb}) carbonisation using a relation:

$$WL(\%) = \left(1 - \frac{w_{carb}}{w_{raw}}\right).100 \qquad \text{(Eq. 2.1)}$$

Here to calculate the percentage decrease of weight, *WL*(%) of the carbon/silica composite monoliths after pyrolysis and before removal of the silica template, the following calculations were used.

For 1µm carbon monolith $WL(\%) = \left(1 - \frac{0.305\ g}{0.480\ g}\right).100 = 36.5\%$

For 2µm carbon monolith $WL(\%) = \left(1 - \frac{0.3\ g}{0.5\ g}\right).100 = 40\%$

For 5µm carbon monolith $WL(\%) = \left(1 - \frac{0.2\ g}{0.3\ g}\right).100 = 33\%$

For 10µm carbon monolith: $WL(\%) = \left(1 - \frac{0.2\ g}{0.3\ g}\right).100 = 33\%$

However, as expected the percentage decrease of weight was dramatically increased after the HF treatment and removal of the silica template as shown below. Samples used in the percentage decrease of weight measurements before (above) and after (below) silica removal were taken from the same corresponding rods.

To calculate the percentage decrease of weight, *WL*(%), of the carbon monoliths after pyrolysis and removal of the silica template:

For 1µm carbon monolith $WL(\%) = \left(1 - \frac{0.045g}{0.387g}\right).100 = 88.4\%$

For 2µm carbon monolith $WL(\%) = \left(1 - \frac{0.039g}{0.451g}\right).100 = 91.4\%$

For 5µm carbon monolith $WL(\%) = \left(1 - \frac{0.029g}{0.351g}\right).100 = 91.7\%$

For 10µm carbon monolith: $WL(\%) = \left(1 - \frac{0.022g}{0.325g}\right).100 = 93.2\%$

Reductions in dimensions (*RD*) caused by heat-treatment (shrinkage) were determined along axial, radial and tangential directions in a sample using the following equation.

$$RD(\%) = \left(1 - \frac{D_{carb}}{D_{raw}}\right).100 \qquad \text{(Eq. 2.2)}$$

Where D_{raw} and D_{carb} denote dimensions of raw and carbonised samples, respectively. To calculate the percentage reductions in dimensions, *RD*(%) of the carbon monoliths after pyrolysis and before removal of the silica template:

For 1 µm carbon monolith: $RD(\%) = \left(1 - \frac{4.22mm}{4.73mm}\right).100 = 10.8\%$

For 2 µm carbon monolith: $RD(\%) = \left(1 - \frac{4.59mm}{5.05mm}\right).100 = 9.1\%$

For 5 µm carbon monolith: $RD(\%) = \left(1 - \frac{3.93mm}{4.54mm}\right).100 = 13.4\%$

For 10 µm carbon monolith: $RD(\%) = \left(1 - \frac{4.09mm}{4.63mm}\right).100 = 11.7\%$

2.3.5. Differential thermal analysis/ Thermo gravimetric analysis

DTA/TGA is a thermogravimetric technique for recording the difference in temperature between a substance and a reference material against either time or temperature as the two specimens are subjected to identical temperature regimes in an environment heated or cooled at a controlled rate. DTA/TGA was applied to determine the weight gain or loss of the carbon monoliths due to gas release or absorption as a function of temperature. Changes in the carbon monolith can be detected relative to the inert reference to be either exothermic or endothermic.

In the study conducted by Ko *et al.,* [33], a total weight loss of phenolic resin of > 35% was observed up to a temperature of 2400 °C. 94% of this weight loss occurred below 900 °C. Herein, DTA/TGA analysis was used to investigate thermal behaviour and weight loss of the 1 µm silica particles and also the 1 µm carbon-silica rod during the pyrolysis. For the silica particles sample, a weight loss of 7.4% was observed up to 1250 °C. This is expected since porous silica generally acts as a sponge for organics and contaminants. For the combined silica-carbon sample, a total weight loss of 50% was observed (Figure 2.31). For the carbon-silica sample, a small endothermic peak was observed at approximately 55 °C. A broad exothermic peak occurred between 240 °C and 400 °C. The blips observed at 800 °C and 1250 °C were artefacts created by the pyrolysis profile which contained isothermal dwell times at these temperatures.

Clearly, the weight loss is dramatic and is accompanied by a vigorous exothermic reaction, even at a heating rate of 2.5 °C/min. The instrument was not stable at heating rates lower than 2.5 ^{o}C/min. According to Ko *et al.,* [33], the condensation of polymer structures results in gas evolution and pore creation in the carbonised sample. Above 700 °C the effects of chemical densification is greater than the formation of pores. It can be seen from Figure 2.31 that at approximately 400 °C the bulk of the burn-off activity and associated weight loss has been completed. However, based on Figure 2.31, it would be reasonable to suggest that an even lower heating ramp rates than 2.5 °C/min in the region up to 400 °C could be beneficial, such is the volatility of the reaction in this region.

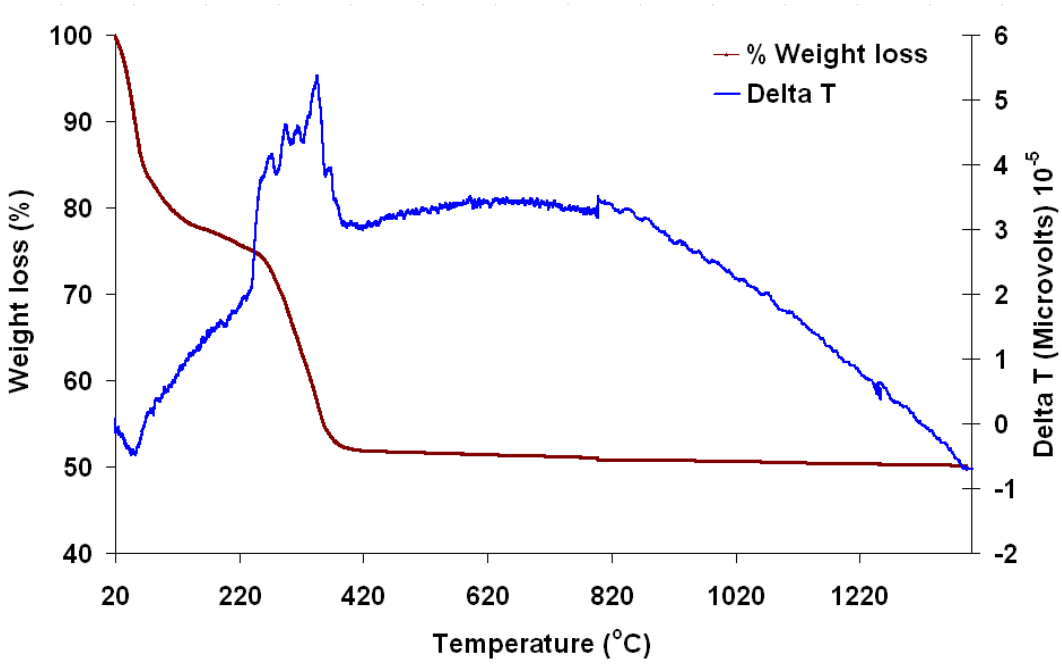

Figure 2.31. Thermogravimetric curve of the 1 µm carbon-silica sample during the pyrolysis under flowing nitrogen.

2.3.6. Mercury porosimetry

As described in Section 2.2.4.5, mercury porosimetry was used for investigating the porous structure of the carbon monolith samples by forcing the mercury into the pores of a dry monolith sample (~ 0.1 g), and the volume of mercury is determined very accurately at each applied pressure. An accurate weight of the empty mercury cell assembly was obtained first. Then, the mercury initially filled the large pores of the monolith sample under low pressure. At this pressure the mercury does not yet enter the reference cell's internal void. A stable increase of pressure is then started. Mercury then enters the internal void of the cell and the small pores of the carbon monolith at a specific higher pressure corresponding to the exterior pore size. The 1 µm silica particles were compacted to form a disc. This was done to minimise the possibility of silica particles being sucked into the mercury under vacuum. It also allowed for more direct comparison with the monolithic

samples. Silica particle powders behave differently under conditions of mercury filling in terms of filling of free space between particles.

In terms of the pore volume of the 1 µm silica particles, a large distribution peak was observed at approximately 500 nm. This was attributed to the spaces between the contact points of the 1 µm silica spheres. No other pores were observed for the volume distribution. However, a different picture emerged when the pore number fraction was taken into consideration. In this case, a very small peak was observed at 500 nm. However, a sharp rise was observed at approximately 30 nm and continued down to 6 nm, something that was entirely absent from the volume distribution. Clearly, large quantities of small pores exist, but these possess a low pore volume. It is believed that these pores correspond to the pores within the silica particles, as found earlier by BET. In the volume distribution, the presence of these small pores is being masked by a smaller number of large volume pores.

Porosimetry was then carried out on the carbon-silica (1µm) monolith before pyrolysis. The pore distribution of this sample is shown in Figure 2.32. This sample exhibited pores of approximately 250 nm.

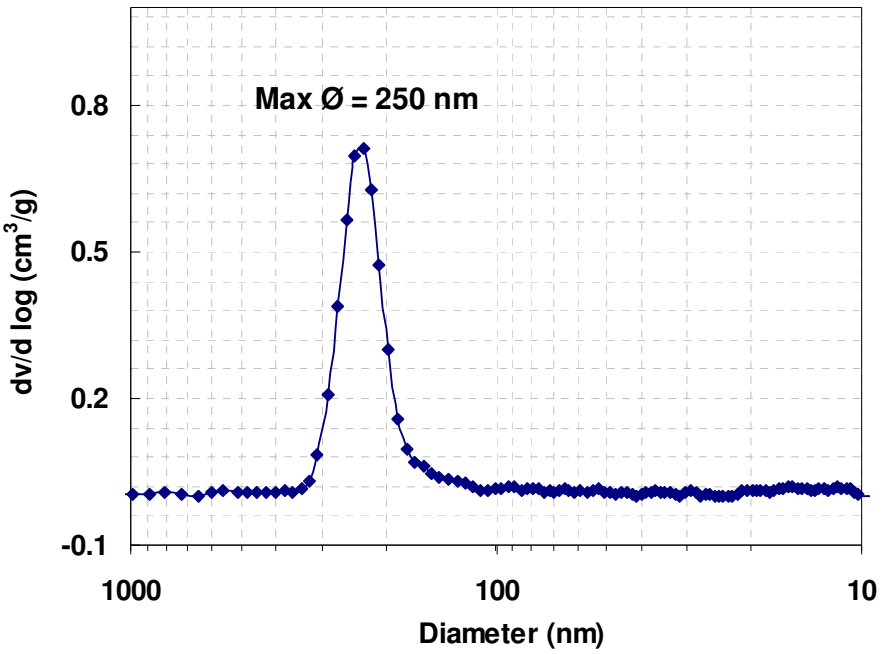

Figure 2.32. Pore size distribution of carbon monolith 1µm (macro-pores) before pyrolysis and removal of the silica particles.

This was somewhat unexpected, in that it may well have been reasonable to expect a result similar to the compacted 1µm silica particles disc discussed above, assuming that the phenolic resin was non-porous. The pore number fraction data revealed a minor peak at approximately 250 nm, but the main activity occurred at 6-7 nm and 10-20 nm. These latter two peaks are believed to correspond to the internal pores in the silica particles. Less clear was the presence of the large volumetric peak at 250 nm. There are a number of possible reasons for this as previously mentioned, including impartial infiltration of phenolic resin into the void spaces between silica particles, or too-high viscosity of the resin solution affecting degree of infiltration. Coating silica particles with resin will reduce the interparticle void space. The raw volume intruded for this sample was 1.234 cm^3/g as compared to 2.363 cm^3/g for the compacted silica particles, adding weight to this theory that the silicas are partially coated, and the spaces between silicas particles are partially filled.

Following pyrolysis and silica removal, the pore size distribution changes again, as shown in Figure 2.33.

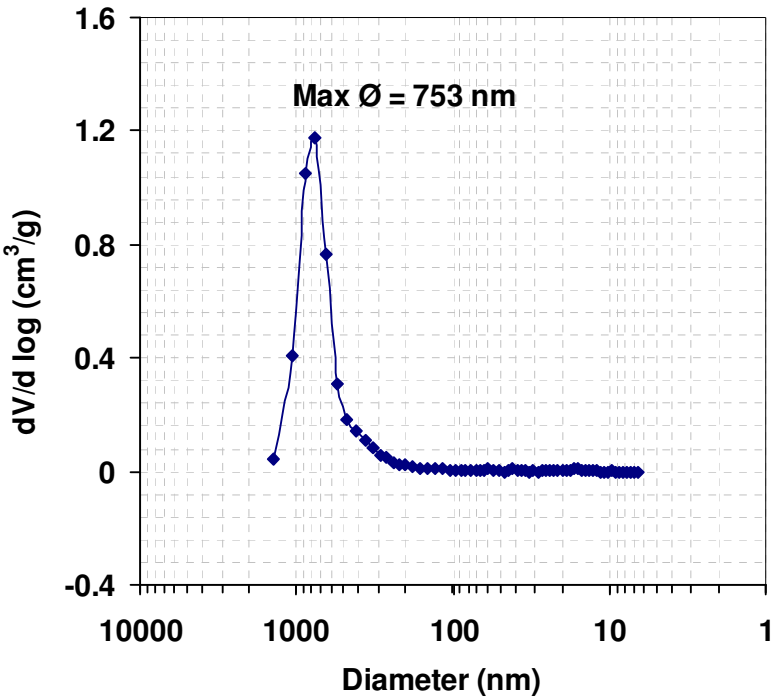

Figure 2.33. Pore size distribution of carbon monolith 1µm (macro-pores) after pyrolysis and removal of the silica particles.

As can be seen from Figure 2.33, the pore size distribution forms a sharp peak at approximately 800 nm. The raw volume intruded has increased to 3.15 mL/g, indicating the increase in pore size. The sharp peak found at 250 nm prior to pyrolysis (attributed to interparticle voids) is no longer in evidence; however the large peak at 800 nm does possess a tail which extends to approximately 150 nm. The large peak observed in Figure 2.33 ranges from 1200 nm to 500 nm, and this is believed due to the pores left by the removal of the 1 μm silica particles. The pores are expected to be less than 1 μm in diameter due to shrinkage during pyrolysis and before removal of the silica template, which was shown in Figure 2.27 to be approximately 10.8% for the sample made from 1 μm silica particles. Other variances are expected due to the imperfect particle size distribution of the silica particles, i.e. deviation of particles away from exactly 1 μm in diameter.

The pore number fraction data was examined. The pore number fraction is the number of pores in a narrow range of pore sizes relative to the total number of pores in the measurement range. The pore number fraction is found by dividing the number of pores in a small interval by the total number of pores. The resulting number represents the fractional amount of all the pores which are found in that particular interval. The calculation of pore number fraction is based on the assumptions that all pores are cylindrical and are of equal length. Pore number fraction is a dimensionless quantity. When the pore number fraction data was examined, it is clear that many other fine pores also exist in the pyrolysed sample (Figure 2.34).

The predominant pore size (in volume terms) are the pores remaining after the removal of the 1 μm silica particles. However, other pores also exist, ranging from 9 nm to approximately 70 nm. This phenomenon has been observed by other authors. For example, Wang *et al.,* [32] reported four types of pores in their final samples prepared using 10 μm template silica. These were macro-pores formed from the original silica spheres, macro-pores from the contact points of the spheres, meso-pores formed by silica diffusion into carbon and micro-pores formed by pyrolysis of phenol-formaldehyde resin. It is likely that the porosity found in the 1 μm monolith is due to the effects outlined above; however more work is needed to definitively prove or disprove this. However, the bulk density of the carbon monolith (2 μm macro-pores) before pyrolysis and removal of the silica particles was 0.87 g cm^{-3} and this dropped to 0.57 g/cm^3 after pyrolysis and removal of the silica particles. The

porosity of the carbon monolith (2 µm macro-pores) was calculated to be approximately 66%.

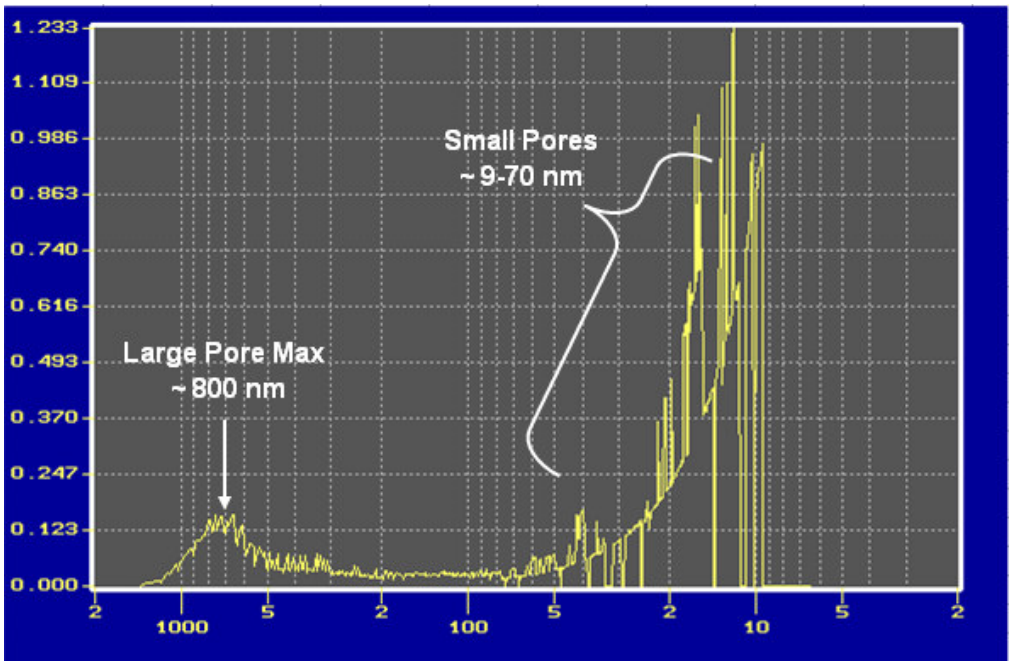

Figure 2.34. Pore number fraction of pores for carbon monolith 1µm (macro-pores) after pyrolysis.

2.3.7. Dynamic mechanical analysis

The stiffness and damping properties of carbon monoliths were measured using a dynamic mechanical analyser. The stiffness depends on the mechanical properties of the monoliths and their dimensions. Damping is expressed in terms of Tanδ and is related to the amount of energy a monolith can store. As mentioned in Section 2.2.4.6, a 5 µm macro-porous monolithic sample (Figure 2.35) was initially run from -150 to 180 ^{o}C. In this sample, there appears to be a relaxation centred around 0 ^{o}C.

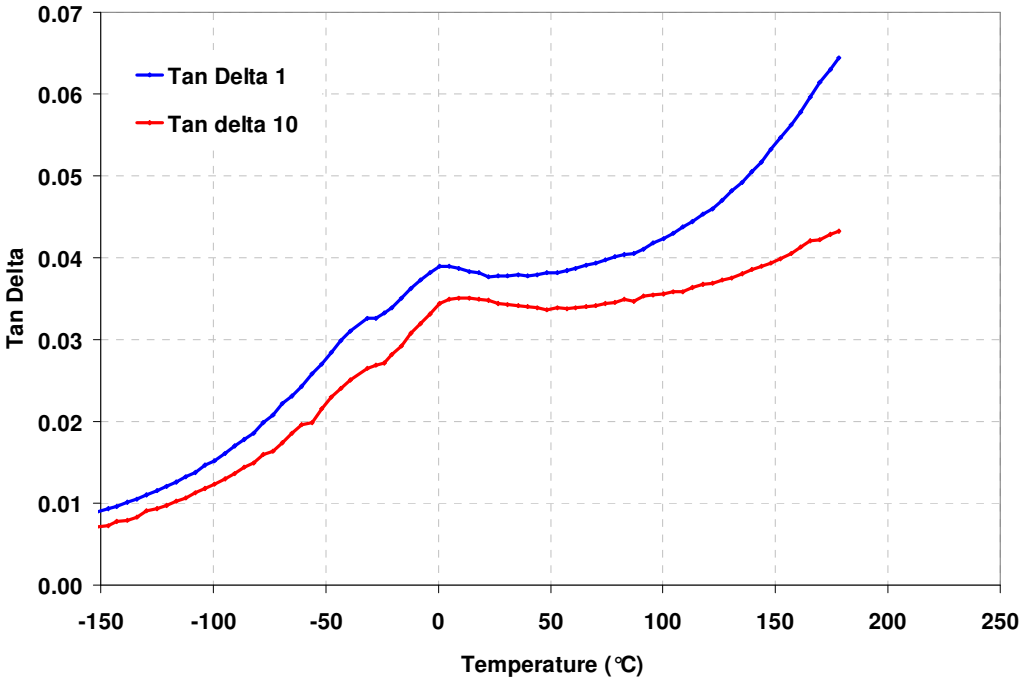

Figure 2.35. Temperature dependence of the Tanδ for 5 µm macro-porous carbon monolithic sample run from -150 to 180 ^{o}C.

However, following initial results further experiments were carried out to 250 ^{o}C on 5 µm (Figure 2.36) and 10 µm (Figure 2.37) macro-porous monolithic samples. The samples were run at two frequencies to check if the process was a relaxation event or not. The natural frequency represents an angular frequency, which is a scalar measure of rotation rate and expressed in radians per second [35]. If the process shows frequency dependence then the event is almost certainly a relaxation event. A relaxation in a material is an event where the conformation of the molecules, or ability of the molecules to move, changes. This kind of event is normally observed as a function of temperature but can also be observed as a function of frequency in the case of DMA. The main relaxation event of a material is the glass transition (Tg) but other, mainly, lower temperature transitions also exist such as β- and very low temperature such as γ-relaxations [35]. In these samples, there appears to be a β-relaxation centred around 0 ^{o}C and the glass transition temperature (Tg) of the glassy carbon monolith could be observed a significant event at high temperature between 200-250 ^{o}C (Figures 2.36 and Figure 2.37). The measurement of the glass transition

temperature of mesophase pitches in the literature was recorded in the same range [36].

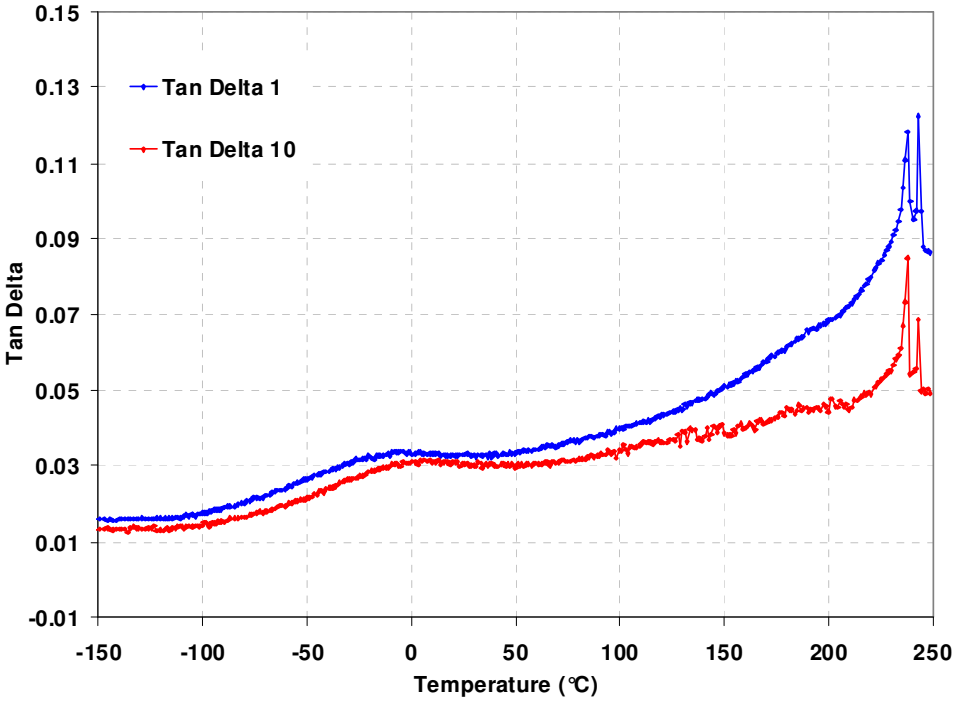

Figure 2.36. Temperature dependence of the Tanδ for 5 µm macro-porous carbon monolithic sample run from -150 to 250 °C.

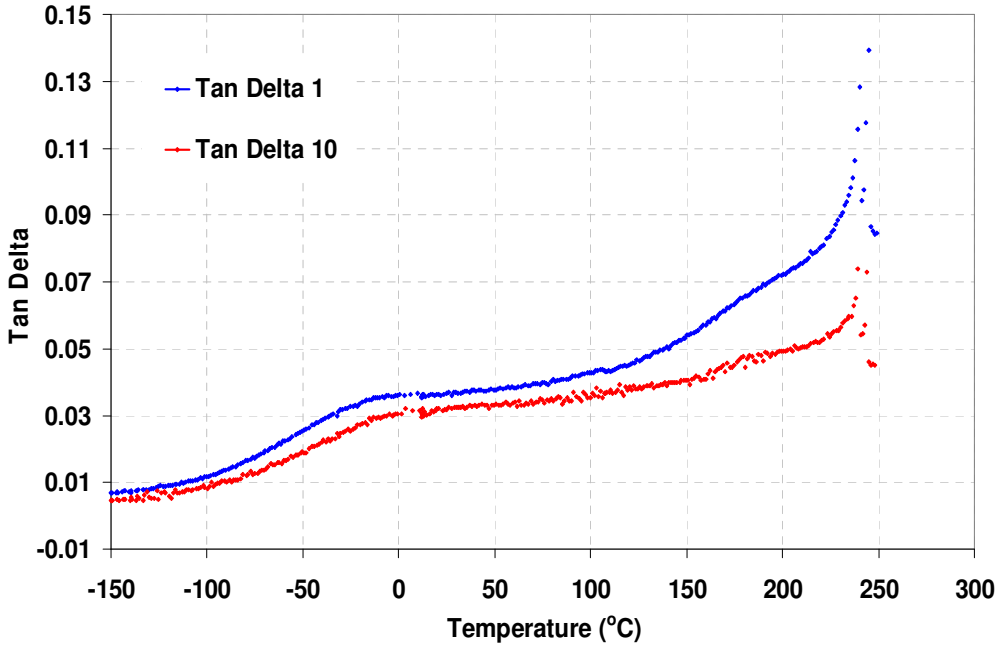

Figure 2.37. Temperature dependence of the Tanδ for 10 µm macro-porous carbon monolithic sample.

2.3.8. Infrared spectroscopy

One of the most common spectroscopic techniques used by organic and inorganic chemists is the infrared (IR) spectroscopy. As well known, IR is the absorption measurement of different IR frequencies by a sample positioned in the path of an IR beam, and determination of the chemical functional groups in the sample is the main goal of this spectroscopic analysis. Different functional groups absorb characteristic frequencies of IR radiation. A section of the electromagnetic spectrum having wavenumbers from roughly 13,000 to 10 cm^{-1}, or wavelengths from 0.78 to 1000 μm is covered by infrared radiation. It is bound by the red end of the visible region at high frequencies and the microwave region at low frequencies.

The infrared spectrum of the porous glassy carbon monolith was measured using KBr disks as mentioned in Section 2.2.4.7. A sample containing 1 to 2 % of carbon monolith was used and the IR spectrum was run.

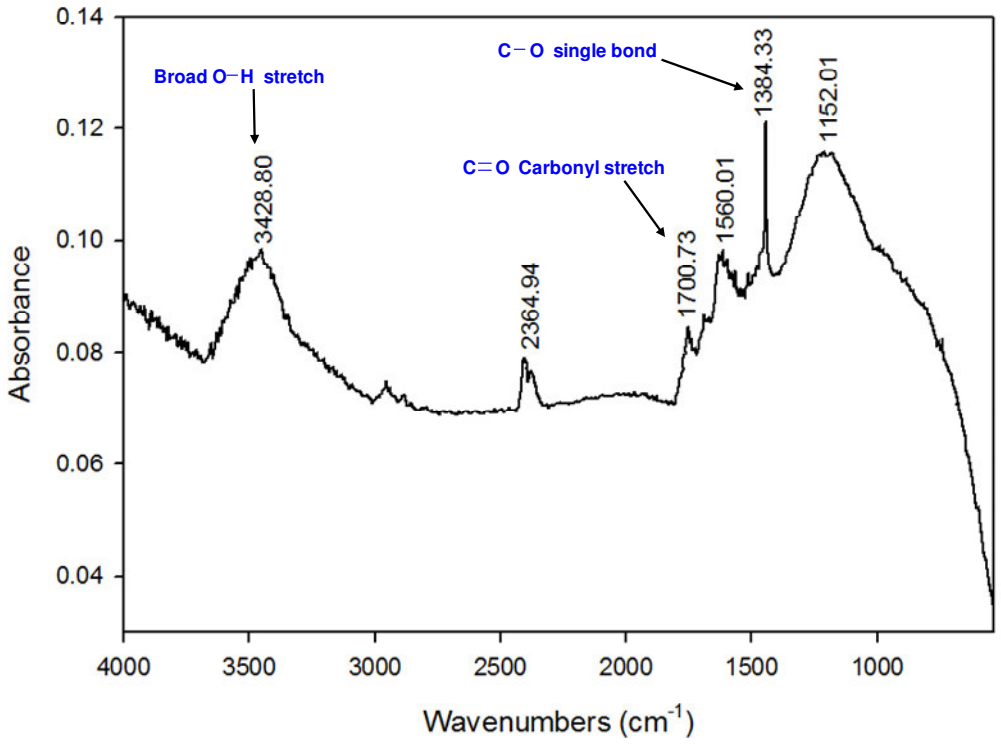

Figure 2.38. IR spectrum of the porous glassy carbon monolith (5 μm pore diameter).

The IR spectrum of the carbon monolith exhibited functional groups present on the surface of the glassy carbon (Figure 2.38). The spectrum of the carbon monolith showed a broad peak in the water region (3428) cm^{-1} and a small peak at 1700 cm^{-1}, assigned to the hydroxyl and carbonyl stretching vibration, respectively, and a strong peak at 1384 cm^{-1} assigned to carbonyl single bond.

2.3.9. Conductivity measurements of the carbon monoliths

Generally, carbon materials are good candidates for electrochemical analysis as a consequence of their relatively low cost, good electronic conductivity, high surface area and availability. One of the most sensitive kinetic electronic properties of materials is the electrical resistivity. It is dependent on many factors such as temperature, structure, crystalline lattice defects, impurities and their location etc. [37].

The electric current density is the amount of current flow passing through a unit area of the monolith. An idea of the current density is very helpful to understand the relationship between the surface area and resistivity for carbon monoliths.

The cross sectional area can be expressed as:

$$A = r^2 .\pi \qquad \text{Eq. 2.3}$$

where *A* is a cross sectional area measured in meter square (m^2). r is radius measured in meters (m) and π is mathematical constant.

The resistivity of a monolith can be expressed as:

$$\rho = \frac{RA}{L} \qquad \text{Eq. 2.4}$$

where *p* is the static resistivity measured in ohm-meters (Ω m), *R* is the electrical resistance of a uniform carbon monolithic specimens measured in ohms (Ω) using a clamp voltmeter and L is the length of the piece of carbon monolithic specimens measured in meters (m).

Electrical resistivity is also expressed as the inverse of the conductivity σ (*sigma*), of the monolith, or

$$\sigma = \frac{1}{p} \qquad \text{Eq. 2.5}$$

where σ is electrical conductivity. *R* will be highly affected by the surface area of the carbon monolithic samples at certain length and radius. The highest surface area, the lowest resistance and therefore, the highest conductance.

Barykin *et al.*, [38] studied the electrical conductivity of a glassy carbon electrode prepared at 1000 K, via carbonisation of a 30:70 mixture of cellulose and a synthetic resin. Higher electrical resistance of 0.18 ohm/cm was recorded after annealing the glassy carbon at 2600 K.

In comparison, for some elements, such as carbon in the form of graphite, electrical conductivity is anisotropic; it differs when measured in different directions. Graphite has a crystal structure of two dimensional layers of carbon atoms packed one above the other and each carbon in graphite is sp^2 hybridised. As the delocalised electrons are free to move within the layers, graphite is a good conductor of electricity. The conductivity is high only in the direction parallel to the layers and is low perpendicular to the layer. Thus, the electrical resistivity (ohm.m) of graphite is (parallel to c-axis = 4.1x10^-5) in the plane of the hexagonal layers of carbon atoms, but is (perpendicular to c-axis = 9.8x10^-6) perpendicular to those layers and is natural = 1.2x10^-6 [39].

For the glassy carbon [38],

$A = (0.0076)^2 . 3.14$

$A = 1.814 \times 10^{-4}\ m^2$

$p = 0.18\ (\Omega) . 1.814 \times 10^{-4}\ m^2/0.01\ m$

$p = 3.265 \times 10^{-3}\ \Omega m$

$\sigma = 1/3.265 \times 10^{-3}\ \Omega m$

$\sigma = 306\ Sm^{-1}$

The electrical conductivity of the carbon monoliths produced in this study was calculated. The highest pore diameter monolith (10 μm) was the least conductive and the lowest pore diameter monolith (1 μm) was the most conductive material.

Table 2.3. Resistance measurements for glassy carbon and 1, 2, 5, and 10 μm (pore diameter) templated carbon monoliths.

Carbon monolith (pore diameter, μm)	**Resistance (Ω)**	**Length (mm)**	**Inner Diameter (mm)**
Glassy carbon	0.18 (measured by Barykin *et al.,* [38].)	10	15.2
1	2.0	10	6
2	2.1	10	6
5	2.2	10	6
10	2.3	10	6

Calculations of the electrical conductivity of the 1, 2, 5, and 10 μm (pore diameter) templated carbon monoliths were as follows:

1 μm (pore diameter) templated carbon monolithic sample:

$A = (0.003)^2 . 3.14$

$A = 2.826 \times 10^{-5}\ m^2$

$p = 2.0\ (\Omega) . 2.826 \times 10^{-5}\ m^2/0.01\ m$

$p = 5.652 \times 10^{-3}\ \Omega m$

$\sigma = 1/5.652 \times 10^{-3}\ \Omega m$

$\sigma = 177\ Sm^{-1}$

The electrical conductivity measurement of the 2, 5 and 10 μm (pore diameter) templated carbon monoliths were calculated following the same calculations above. The results were as follows: $\sigma = 169\ Sm^{-1}$ (for 2 μm monolith), $\sigma = 161\ Sm^{-1}$ (for 5 μm monolith), $\sigma = 154\ Sm^{-1}$ (for 10 μm monolith).

Table 2.4 is showing the electrical conductivity of the monolith rods produced.

Table 2.4. Electrical conductivity calculated for the glassy carbon and 1, 2, 5, and 10 µm (pore diameter) templated carbon monoliths.

Carbon monolith (pore diameter (µm))	**Conductivity (σ), Sm^{-1}**
Glassy carbon	306
1	177
2	169
5	161
10	154

The glassy carbon showed the highest conductivity as it was more dense than the glassy carbon monoliths which consisting of an interconnected skeleton and have an internal voids making the monoliths conducting less than the dense glassy carbon. The amount of current flowing through 1 and 10 µm carbon monolithic samples will be different with a constant voltage**.** 1 µm carbon monolithic sample with high surface area (178 m^2/g) conducts more easily than the 10 µm carbon monolithic sample with lower surface area (125 m^2/g).

2.3.10. Backpressure determination of the 1 and 5 µm templated carbon monolithic columns

As detailed in Section 2.2.4.9, the backpressure was determined using an HPLC pump by encasing the carbon monolithic rods (1 and 5 µm pore diameters, 10 x 6 mm i.d.) separately within monolithic guard cartridge (10 mm in length) housings. The net pressure was calculated to be approximately 150 psi for carbon monolithic rods at a flow rate of 1 mL/min by subtracting the system tubing pressure drop from the total recorded pressure drop (Figure 2.39).

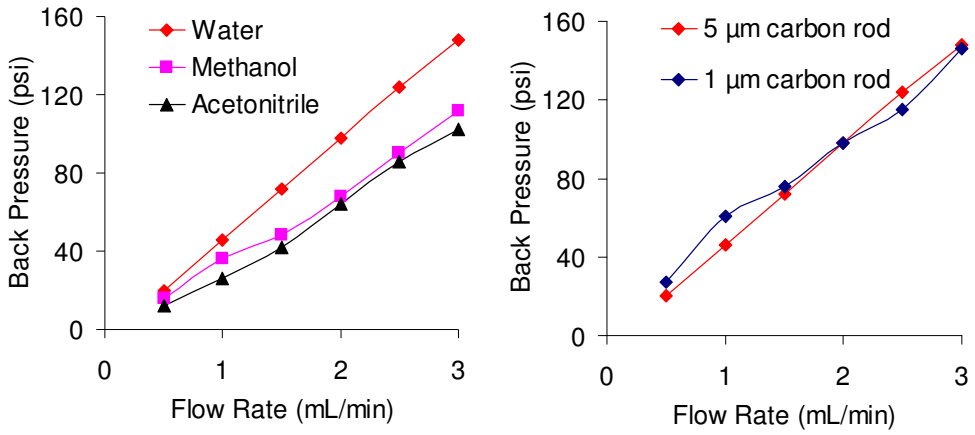

Figure 2.39. Flow through backpressure for the (left) 5 µm and (right) 1 µm & 5 µm carbon monolithic columns in various solvents. (right) Water only.

For comparison, particle-based conventional columns show a relatively high backpressure. As mentioned in Chapter 1, compared to packed particle-based columns, with a porosity of about 65%, monolithic columns, having a total porosity of about 80%, show much lower backpressures. Thus, due to higher porosity, monolithic columns are considered to be compatible with high flow rates. Also, due to a low backpressure, they bring less stress on the system, and absence of inlet bed setting, thus they have an increased reliability and lifetime [40].

2.3.11. Physical characterisation summary

Table 2.5 shows the variance analysis summary for the parameters such as surface area, shrinkage (%) during pyrolysis of the carbon monoliths, mercury porosimetry, percentage decrease of weight, *WL*(%) after pyrolysis and removal the silica template, pore size, conductivity and backpressure determination. For characterisation the pore size distribution using the mercury porosimetry, only the 1 µm templated carbon monolithic sample was characterisaed and used as a standard for the rest of the carbon monolithic samples (2, 5 and 10 µm).

Table 2.5. Surface area, pore volume, shrinkage, weight loss, pore size and conductivity measurements of the carbon monoliths after pyrolysis and removal of the silica particles.

	1 µm	2 µm	5 µm	10 µm
Surface area (m^2/g)	178	154	85	125
Pore volume (cm^3/g)	0.23	0.23	0.095	0.32
Shrinkage (%)	10.8	9.1	13.4	11.7
Percentage decrease of weight, *WL*(%),	88.4	91.4	91.7	93.2
Pore size (µm)	0.8	N/A	N/A	N/A
Conductivity (Sm^{-1})	177	169	161	154
Backpressure (psi)	149	N/A	153	N/A

2.4. Conclusions

Carbon monolithic rods with minimal silica residue were successfully prepared. These columns were made of a partially graphitised, pyrolysed phenolic resin. These monoliths were characterised using different techniques such as SEM/EDX, BET, dilatometry, mercury porosimetry, DTA/TGA, DMA, conductivity and backpressure determination. The carbon monoliths had a total surface area of 178 m^2/g (1 µm), 154 m^2/g (2 µm), 85 m^2/g (5 µm) and 125 m^2/g (10 µm) and with high porosity. The surface area of the carbon monoliths decreases as the pore size increases. However, the surface area of the carbon monolith (5 µm pore diameter) were lower than expected and lower than the monolith (10 µm pore diameter) potentially due to the non-homogeneous and non-uniform size of silica particles (5 µm particle size) used for the preparation of the original 5 µm templated silica-polymer mix, resulting in potential presence of internal voids when forming the rod and larger than expected overall porosity. The overall shrinkage of the carbon

monolithic rods during the pyrolysis at range approximately from 9 % to almost 13 % before removal of the silica template.

The pore size distribution of the carbon monolith was determined by mercury porosimetry. The pores were found to be less in diameter than the original silica particle size template used due to shrinkage during pyrolysis. For electrochemical analysis, the conductivity of the carbon monoliths was investigated. The highest pore size monolith (10 μm) with lower surface area was the least conductive, while the lowest pore size monolith (1 μm) with higher surface area was the most conductive material.

References

1. T. B. Tennikova, F. Svec, B.G. Belenkii, *J. Liq. Chromatogr.*, 13 (1990) 63.
2. B. Paull, P. N. Nesterenko, *Trends in Anal. Chem.*, 24 (2005) 295.
3. Z. Y. Yuan, B. L. Su, *J. Mater. Chem.*, 16 (2006) 663.
4. O. Sel, D. Kuang, M. Thommes, B. Smarsly, *Langmuir,* 22 (2006) 2311.
5. W. D. Ross, R. T. Jefferson, *J. Chromatogr. Sci*., 8 (1970) 386.
6. L. C. Hansen, R. E. Sievers, *J. Chromatogr. Sci*., 99 (1974) 123.
7. K. Nakanishi, N. Soga, *J. Am. Ceram. Soc*., 74 (1991) 2518.
8. K. Nakanishi, N. Soga, *J. Non-Cryst. Solids*, 139 (1992) 1.
9. J. Randon, S. Huguet, A. Piram, G. Puy, C. Demesmay, J. L. Rocca, *J. Chromatogr., A*, 1109 (2006) 19.
10. D. C. Hoth, J. G. Rivera, L. A. Colon, *J. Chromatogr., A*, 1079 (2005) 392.
11. V. Zizkovsky, R. Kucera, J. Klimes, J. Dohnal, *J. Chromatogr. A*, 1189 (2008) 83.
12. C. Liang, S. Dai, G. Guiochon, *Anal. Chem*., 75 (2003) 4904.
13. R.F. Antrim, R.A. Scherrer and A.M. Yacynych, *Anal. Chim. Acta*, 164 (1984) 283.
14. T. D. Burchell, J. W. Klett, M. R. Rogers, *Eurocarbon 98*, (1988) 671, Extended abstracts, Strasbourg (France).
15. X. Lu, R. Caps, J. Fricke, C. T. Alviso, R. W. Pekala,. *J. Non-Cryst Solids*, 188 (1995) 226.
16. S. Berthon, S. Escribano, P. Archard, *Eurocarbon* 98, (1988) 661, Extended abstracts, Strasbourg (France).
17. J. F. Mareche, D. Begin, G. Furdin, S. Puricelli, J. Pajak, A. Albiniak, M. Jasienko-Halat, T. Siemieniewska, *Carbon*, 39 (2001) 771.
18. J.H. Knox, *Anal.Chem.,* 38 (1966) 254.
19. M. T. Gilbert, J. H. Knox, B. Kaur, *Chromatographia*, 16 (1982) 138.
20. S. Alvarez, A. B. Fuertes, *Mater. Lett.*, 61 (2007) 2378.
21. L. Y. Xu, Z. G. Shi, Y. Q. Feng, *Micropor. Mesopor. Mater.*, 115 (2008) 618.
22. A.A. Zakhidov, R.H. Baughman, Z. Iqbal, C.X. Cui, I. Khayrullin, S.O. Dantas, I. Marti, V.G. Ralchenko, *Science*, 282 (1998) 897.
23. A.A. Zakhidov, I.I. Khayrullin, R.H. Baughman, Z. Iqbal, K. Yoshino, Y. Kawagishi, S. Tatsuhara, *Nanostruct. Mater.*, 12 (1999) 1089.

24. H. Kajii, H. Take and K. Yoshino, *Synthet. Met.*, 121 (2001) 1315.
25. H. Take, T. Matsumoto, S. Hiwatashi, T. Nakayama, K. Niihara and K. Yoshino, *Jpn. J. Appl. Phys. Pt. 1,* 43 (2004) 4453.
26. A.E. Aliev, S.B. Lee, R.H. Baughman, A.A. Zakhidov, *J. Luminesc.*, 125 (2007) 11.
27. G. Guan, K. Kusakabe, H. Ozono, M. Taneda, M. Uehara and H. Maeda, *J. Mater. Sci.*, 42 (2007) 10196.
28. C. Liang, S. Dai, G. Guiochon, *Chem. Commun*., 22 (2002) 2680.
29. R. Taylor, Thermal Expansion of Solids, *Cindas Data Series on Mater. Proper.*, Vol I-4 (1998), ASM International, Ohio (USA).
30. J. H. Knox, M. T. Gilbert, *U.K. Patent*, 2,035,282, 1978.
31. J. H. Knox, B. Kaur, G. R. Millward, *J. Chromatogr*., 352 (1986) 3.
32. H. Wang, X. Li, L. Y. Hong, D. P. Kim, *J Porous Mater.*, 13 (2006) 115.
33. T. H. Ko, W. S. Kuo, Y. H. Chang, *J. App. Poly. Sci.*, 81 (2001) 1084.
34. M. Krzesinka, J. Zachariasz*, J. Anal. Appl. Pyr.*, 80 (2007) 209.
35. TTInf_DMA, Triton Technology**,** Nottinghamshire, United Kingdom, www.triton-technology.co.uk
36. P. M. Khandare, J. W. Zondlo, A. S. Pavlovic, *Carbon*, 34 (1996) 663.
37. B. I. Stadnyk, V. P. Motalo, *Measurement Techniques*, 30 (1987) 608.
38. B. M. Barykin, E. G. Spiridonov, A. S. Tarabanov, *Khim. Tverdogo Topliva (USSR)*, 2 (1967) 116.
39. In American Institute of Physics Handbook, Powell, R.L. & Childs, G.E., 3rd edition, McGraw-Hill, New York, USA, 1972.
40. E. Haghedooren, L. Peeters, S. Dragovic, J. Hoogmartens, E. Adams, *Talanta*, 78 (2009) 665.

CHAPTER THREE

Gold and Silver Particle Modified Porous Carbon Monoliths

3.1. Introduction

Nano/Micro-particle based materials have unusual physicochemical properties and these properties facilitate various possible applications in many different areas. For this reason, they have attracted significant attention from many leading research groups and their applications in analytical chemistry has become of interest to the wider scientific community more generally [1].

Gold and silver nano/micro-particles display a wide range of characteristic effects in areas such as optical absorption, optical extinction and light scattering, surface plasmon resonance, surface-enhanced Raman scattering, and many aspects of electrochemistry, which make them excellent candidate materials for application in such fields as medical diagnostics, biological imaging, molecular recognition systems, catalysis, electronics and optoelectronic devices [2-14].

For example, in electrochemistry, Yang *et al.,* [15] electrochemically prepared gold micro-particles on the surface of glassy carbon electrodes and utilised them for the oxidation of formaldehyde. The surface of the gold micro-particle modified glassy carbon was characterised in-situ by fourier transform infrared (FTIR) spectroscopy, SEM and X-ray diffraction (XRD), and the SEM image of the modified-surface showed the presence of gold as small spherical particles, confirming that the distribution of the gold nano-particles on the glassy carbon electrode surface was uniform [15-16].

Nano-particles have also found application in the separation sciences. For instance, nano-particles were used as a pseudo-stationary phase in capillary electrophoresis (CE) [17-19]. Dodecanethiol monolayer-protected gold nano-particles were also investigated as stationary phases in GC [20-21]. Gross *et al.,* [20] successfully coated a thin film of monolayer-protected gold nano-particle (60 nm thick, 530 μm i.d.) within a 2 m capillary for GC. Gross *et al.,* [21] also modified a 1.3 m long, 100 μm x 100 μm square capillary column with dodecanethiol

monolayer-protected gold nano-particles for micro-GC for the separation of alkanes, alcohols, ketones, and aromatic compounds. In addition, a mixture of common hydrocarbons (benzene, toluene, *p*-xylene, and dimethylmethyl phosphonate) were separated on the same column in 2 s compared with a similar separation on an unmodified square capillary column using a micro-GC system requiring 50 s [21]. Templeton *et al.,* [14] also tested a thin monolayer-protected gold nano-particle film as an efficient stationary phase for GC. These studies showed that sufficient chemical selectivity could be achieved for different monolayer-protected gold nano-particle-based GC stationary phases, as a wide range of thiol-based organic ligands are readily available.

In the work described in the following chapter, the modification of the carbon monoliths with metallic nano/micro-particles for potential chromatographic application was investigated. Further modification of the resultant carbon/gold composite monoliths with thiol based chemistry (6-mercaptohexanoic acid) to produce weak cationic exchange composite monoliths is also presented. Physical characterisation carried out to investigate the morphology and the internal structure of the metallic modified carbon monoliths involved using SEM/EDX (surface morphology). The resultant gold and silver modified carbon monoliths were analysed for gold content using an inductively coupled plasma-optical emission spectrometer (ICP-OES). UV-Vis analysis was also carried out for the gold nano-particles (colloidal gold) before and after modifying the carbon monolith. Further characterisation was carried out based upon conductivity measurements.

3.2. Experimental

3.2.1. Chemicals

Gold (III) chloride (tetrachloroauric acid) (99.99%), gold colloid (concentration ~ 0.01% $HAuCl_4$), ~ 1 A_{520} units/mL, 3.0-5.5 nm mean particle size (mono-disperse), nitric acid (90%), hydrochloric acid (37%) and 6-mercaptohexanoic acid (90%) were obtained from Sigma-Aldrich, (Gillingham, UK). Dextran FP70 (Mr 65000-73000) research grade was obtained from SERVA Electrophoresis GmbH (Heidelberg, Germany). Gold paint was obtained from Glazura s. r. o. (Roudnice nad Labem, Czech Republic). Reagent water was obtained

from a Millipore Milli-Q water purification unit (Millipore, Bedford, MA, USA) and was 18.2 MΩ or better. All chemicals were used as received from the manufacturers.

3.2.2. Instrumentation

For the instrumentation used for the preparation and characterisation of the precursor carbon monolithic rods before the modification, see Section 2.2.2, Chapter 2.

For the heat treatment of the carbon/gold composite monoliths, a benchtop alumina tube furnace, model GSL1300X (MTI Corporation, Richmond, USA) was used. The surface morphology of the carbon/gold (or carbon/silver) composite monoliths was examined using SEM/EDX systems, models S-3000N VP and S-3400N VP and ultra high resolution cold field emission scanning electron microscopy, model S-5500 (Hitachi, Oxford, UK). An inductively coupled plasma - optical emission spectrometer (ICP-OES), model Liberty 220 series (Varian, Palo Alto, USA) was used for the quantitative analysis of gold and silver.

The back pressure of the carbon/gold composite monolithic columns modified with 6-mercaptohexanoic acid was investigated using an Agilent 1200 series high performance liquid chromatograph, incorporating a vacuum degasser, quaternary pump, ALS autosampler, thermostatted column compartment and UV-Vis detector. Data analysis was performed using Agilent chemstation programme, version B.02.01 (Agilent Technologies, USA).

The measurements of gold particle sizes within the effluent collected after modification of the carbon monoliths using solutions of tetrachlorauric acid, were carried out using a Malvern high performance particle sizer (Zetasizer), Nanoseries, model ZEN3600 (Malvern instruments limited, UK). Electrical resistance of the carbon/gold composite monolith was measured using a clamp voltmeter, model ISO-TECH$_{ICM\ 3090}$ (RS Components Pty Ltd, Smithfield, Australia).

3.2.3. Production of gold modified carbon monolith using tetrachlorauric acid

For the preparation of gold modified carbon monoliths, previously prepared carbon monolithic rods were used (see Section 2.2.3, Chapter 2). These matrix rods were prepared using various particle size silica (1, 2, 5 and 10 μm). The carbon/gold composite monoliths were prepared using three different procedures as follows:

3.2.3.1. Modification of carbon monoliths with tetrachlorauric acid by sample immersion

The carbon/gold composite monoliths **IM1, IM2, IM5** and **IM10** (1, 2, 5 and 10 µm pore diameter, respectively), were prepared following an adapted procedure reported by Dekanski *et al.,* [22]. The carbon monolithic rod was immersed in 100 m*M* tetrachloroauric acid (~ 0.026 g) (pH 1.8 aqueous solution) overnight (16 h), followed by drying for 24 h. The rods were then heated to 200 °C at 2.5 °C/min, and then held at 200 °C for a further 2 h. A second ramp took place from 200 to 700 °C at 5 °C/min. The temperature was kept constant at 700 °C for 20 min to remove impurities and check gold thermal stability. Then the furnace was allowed to cool naturally to room temperature.

3.2.3.2. Modification of a carbon monolith (5 µm pore diameter), with tetrachlorauric acid by a re-circulation technique

A carbon/gold composite monolith, **RC5** (5 µm pore diameter), 55 x 6 mm i.d.**,** was prepared by re-circulating of a 75 m*M* aqueous solution of tetrachlorauric acid (pH 1.8) through a carbon monolithic rod for 24 h at flow rate 2 mL/min using the peristaltic pump.

3.2.3.3. Modification of a carbon monolith (5 µm pore diameter), with tetrachlorauric acid by manual injection of a tetrachlorauric acid/dextran mixture

A carbon/gold composite monolith, **MI5** (5 µm pore diameter), 10 x 6 mm i.d.**,** was prepared using a carbon monolith as the 'mould' for the formation of gold micro-sponges within the large pores of the carbon monolith. This was attempted by manual injection of a mixture of gold chloride 10%, water 60% and dextran 30% through the monolithic carbon rod using a plastic syringe followed by flushing with nitrogen. The wet rod was dried in air for two days and heated to a temperature of 800 °C at 2.5 °C/min for 2.5 h under nitrogen.

3.2.3.4. Characterisation of carbon/gold composite monoliths using SEX/ED

The surface morphology and elemental analysis of gold modified carbon monoliths were examined by SEM/EDX. Monoliths **IM1** and **IM5** were characterised using the following SEM conditions: the accelerating voltage was set to 20 keV for both monoliths, the analytical WD was set to 8.7 for monolith **IM1** after the modification (see Section 2.3.2.1, Chapter 2 for bare carbon monolith analysed by SEM). For monolith **IM5**, WD was set to 6.9 mm before, and 8.7 mm after the modification. Both short working distances allow observation of the topography of the sample. Also, a small objective aperture was used for high resolution and improving the contrast of the final image. Magnification of 2.5 k was used. These conditions were suitable for both imaging and EDX.

Monolith **RC5** was characterised using the following SEM conditions: 20 keV accelerating voltage, 7.4 mm WD and 2.5 k magnification.

Monolith **MI5** was characterised using the following SEM conditions: an accelerating voltage of 20 keV, WD of 6.7 mm and a magnification of 2.5 k.

3.2.3.5. Quantitation of the gold content of the carbon/gold composite monoliths using inductively coupled plasma–optical emission spectroscopy (ICP-OES)

The carbon/gold composite monoliths, **IM1** (1 μm pore diameter), **IM5** (5 μm pore diameter) and **MI5** (5 μm pore diameter), were separately extracted in 10 mL concentrated HNO_3 to quantitatively remove the immobilised gold, then the gold containing solution was diluted to 10 % and analysed for gold content using ICP-OES. Gold standards were prepared (4, 6, 8 and 10 mg/L), injected and run individually onto the ICP-OES under optimised conditions.

3.2.3.6. Characterisation of carbon/gold composite monolithic rod, IM5, by SEM before and after removal the gold particles following HNO_3 treatment

The surface morphology of the gold modified carbon monolith, **IM5,** was examined by SEM and HR-SEM. Monolith **IM5,** was characterised before the removal the gold particles using the following SEM conditions: the accelerating voltage was set to 25 keV, the analytical WD was set to 13.9 and magnification of 2.70 k. After removal the gold particles, the surface morphology of monolith **IM5,**

was examined by HR-SEM using the following conditions: an accelerating voltage of 1.0 keV and magnification of 2.00 k.

3.2.3.7. Characterisation of gold particle size in the effluent of modifying solutions for carbon monolith modification by dynamic light scattering (DLS)

Measurements were carried out using a Malvern high performance particle sizer at 25 ^{o}C. Standard disposable cuvettes were used with outside dimensions (12.5 mm W x 12.5 mm D x 45 mm H). The column effluent, after modification of the carbon monolith **RC5,** with 75 m*M* aqueous solution of tetrachlorauric acid was collected and analysed. The aqueous sample was loaded into the sample chamber in the instrument. The sample temperature was kept constant with an internal heating system installed in the instrument. As a light source, a variable power (60 m*W*) standard helium-neon laser at wavelength 632.8 nm was used [23].

3.2.4. Modification of carbon/gold composite monoliths with 6-mercaptohexanoic acid

A Carbon/gold composite monolithic rod (5 µm pore diameter), 30 x 6 mm i.d., **IM5,** was modified with 10 m*M* of 6-mercaptohexanoic acid following the adapted procedure reported by Huo and Worden [24], by immersing the rod in 10 m*M* mercaptohexanoic acid overnight, followed by drying for 24 h at room temperature.

An alternative procedure to modify the carbon/gold composite monolithic column involved re-circulation of 20 m*M* of 6-mercaptohexanoic acid through the carbon/gold composite monolithic column (5 µm pore diameter), 55 x 6 mm i.d., **RC5,** at 0.1 mL/min for 48 h.

3.2.4.1. Characterisation of carbon/gold composite monolith, IM5, by SEM before and after attachment of 6-mercaptohexanoic acid to the surface

Monolith **IM5,** was characterised by SEM before and after attachment of 6-mercaptohexanoic acid to the surface. The conditions for the SEM before (see Section 3.2.3.4) and after the attachment were as following: accelerating voltage at 20 keV, magnification of 2.5 k and analytical WD was 7.4 mm.

3.2.5. Modification of carbon monoliths with gold paint

Carbon monolithic rods (1, 2, 5 and 10 µm pore diameter), 10 x 6 mm i.d. were modified with gold paint (12 % Au), (**P1, P2, P5** and **P10,** respectively). The procedure involved immersing each rod in diluted gold paint (1:10 dilution in trichloroethene) overnight. The rods were dried in a fumehood for 24 h followed by heat treatment using a high temperature vacuum horizontal tube furnace purged with N_2 gas. The temperature was first ramped from room temperature to 200 °C at a heating rate of 2.5 °C/min, and then held at 200 °C for 2 h. A second ramp took place from 200 to 700 °C at a heating rate of 5 °C/min. The temperature was kept constant at 700 °C for 20 min. Then the furnace was allowed to cool naturally to room temperature.

3.2.5.1. Characterisation of carbon monoliths modified with gold paint by SEM and HR-SEM

The resultant carbon monolithic rods modified with gold paint were characterised using SEM. An accelerating voltage of 20 keV for high resolution images, an analytical working distance at 11, 12.1 and 12.3 mm and magnification at 1.2, 1.6 and 3.0 k were used for the analysis of the carbon monoliths modified with gold paint, **P1**, **P2**, **P5** and **P10**. The monolith **P5,** was characterised by HR-SEM. HR-SEM conditions used were as follows, an accelerating voltage of 5-20 keV and magnification of 4-400 k.

3.2.6. Modification of a carbon monolith with silver particles

A carbon monolith (10 µm pore diameter), 10 x 6 mm i.d. modified with silver micro-particles, **S10,** was prepared following a procedure adapted from the work of Dekanski *et al.,* [22]. A piece of carbon monolithic rod was immersed in 0.1 M $AgNO_3$ aqueous solution in a small 5 mL glass vial, capped and left for a period of 24 h following by drying in fumehood for 48 h.

3.2.6.1. Characterisation of the silver/carbon composite by SEM/EDX

The carbon/silver composite monolith, **S10,** was characterised by SEM/EDX using an accelerating voltage of 20 keV, analytical working distance of 8.6 mm and magnification set to 1.0 k.

3.2.7. Modification of carbon monolith with gold nano-particles (5 nm particle size)

The procedure was carried out according to the adapted method reported by Dekanski *et al.,* [22]. The carbon monolithic rod was immersed in 2 ml of gold nano-particles (5 nm, ~ 0.01 % $HAuCl_4$) solution and kept in the fridge overnight followed by drying for 24 h at room temperature.

3.2.7.1. Characterisation of carbon monolith modified with 5 nm gold nano-particle by HR-SEM

The carbon monolith modified with directly gold nano-particle (5 nm particle size), **Au5,** was characterised using HR-SEM at an accelerating voltage of 10-20 keV and a magnification of 1.3-2.2 k.

3.3. Results and discussion

3.3.1. Preparation and characterisation of carbon monoliths modified with gold nano/micro-particles

3.3.1.1. Modification of the carbon monoliths, IM1, and, IM5, with gold nano/micro-particles, and characterisation by SEM/EDX

The modification of the glassy carbon surface in contact with aqueous solution of tetrachlorauric acid has been studied using SEM/EDX and Brunauer, Emmett and Teller (BET) surface analysis methods. The reduction of metallic gold, confirmed by SEM/EDX, affected the pore system resulting in a decrease of surface area and pore volume.

The first procedure for the production of a carbon/gold composite monolith was carried out by immersion of carbon monolithic rods into a tetrachlorauric acid solution as described in Section 3.2.3.1. The resultant carbon/gold composite

monoliths **IM1** and **IM5** are shown as an SEM images in Figures 3.1 and 3.2, respectively. The strategy followed here consisted of reducing the gold on the carbon monolithic surface at active sites, and the subsequent growth of the attached gold into nano/micro-particles. During gold nucleation and growth, gold was constantly available through immersing the carbon monolith in a tetrachlorauric acid solution overnight (~ 15 h). This effect, namely the surface induced spontaneous reduction of metals on the surface of the glassy carbon has been shown previously on glassy carbon. Dekanski *et al.* [22] modified a glassy carbon chemically using immersion technique and electrochemically using cyclic voltammetry. The immersion technique was carried out by immersion of the glassy carbon in silver nitrate solution and involved a process of spontaneous reduction of Ag^+ ions on the surface and near surface layers of glassy carbon. The reduction took place on active sites such as functional groups, present on the surface of glassy carbon. The reduction of Ag^+ ions began when glassy carbon was just immersed into the silver nitrate solution, allowed by surface and external electron donors. Inner electron donors were involved in the reduction of silver on subsurface layers due to the diffusion of Ag^+ ions through the pores of glassy carbon and into the near surface layers. The silver reduced in the pores of a glassy carbon and near surface layers and disabled further diffusion of electrolyte (Ag^+ ions) through the glassy carbon. Then the inner reduction of silver was stopped and the external continued on the surface of glassy carbon. Since silver is a great conductor, then external electron donors from the glassy carbon took some part in the reduction of Ag^+ ions.

Also, for electrochemical reduction of silver particles on the surface of glassy carbon electrode, the application showed that when this material was in contact with silver nitrate solution its electrochemical properties changed, as a result of spontaneous silver reduction on the surface of the material [22][25-26].

Examination of the modified carbon monoliths by SEM (Figures 3.1 and 3.2 (b)) revealed small spherical gold nano/micro-particles, homogenously distributed on the surface of the carbon monolith, formed by a surface reduction mechanism and displaying particle diameters in the range of 50-150 nm.

The results show that after the immersion of the carbon monolithic rod in tetrachlorauric acid solution for such time period (~ 15 h), the Au(III) ions were readily reduced on the surface of the carbon monolith to Au(0). The gold atoms were

immobilised, aggregated and presented as nano/micro-particles on the inner and outer surface layers of the carbon monolith.

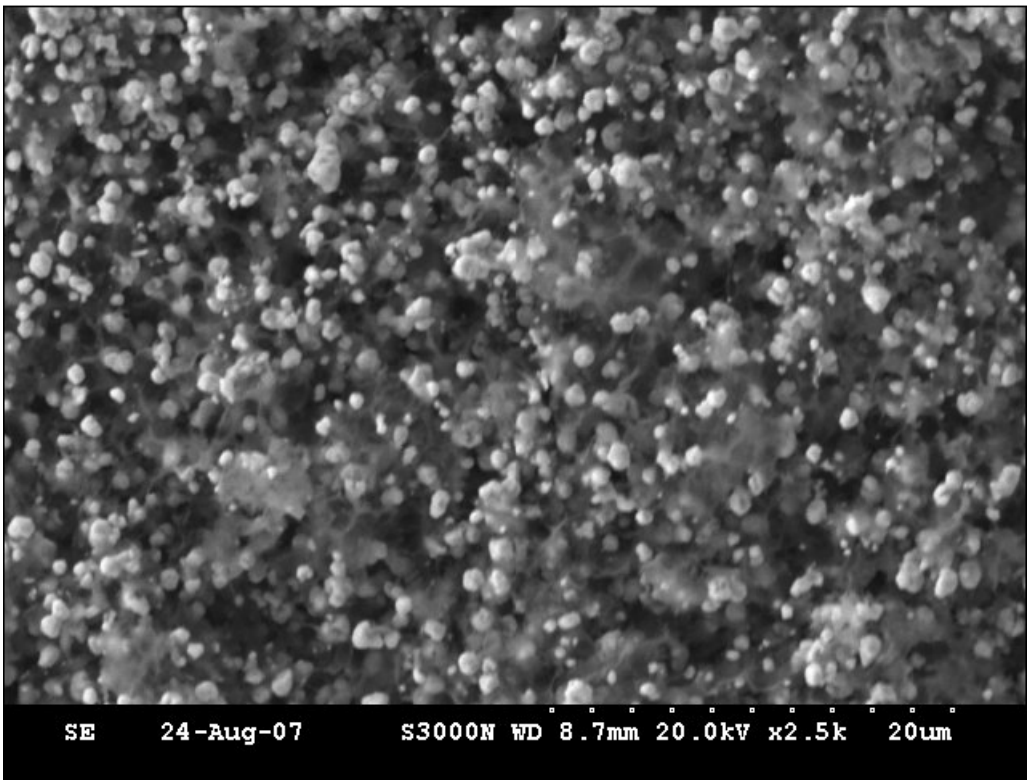

Figure 3.1. SEM image of the carbon monolith modified with gold nano/micro-particles, **IM1,** produced by monolith immersion technique.

It is expected that the nature of the bond is electrostatic not covalent, as there is no electron shared, the ion loses its charge and is incorporated into the surface of the monolithic glassy carbon. The reduction proceeds on active sites, i.e. functional groups formed on the surface of glassy carbon which is formed only on the sites of defects on the surface.

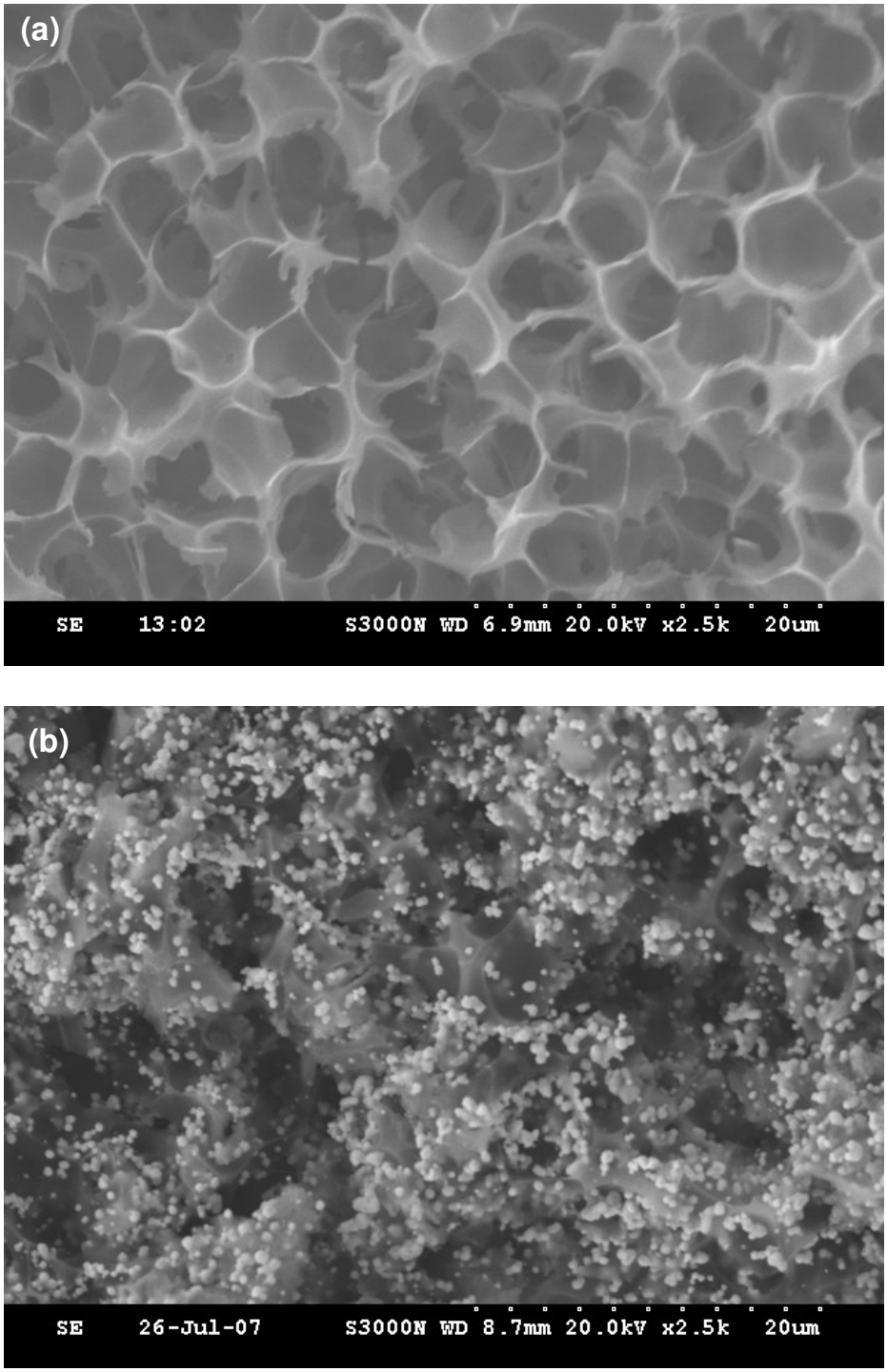

Figure 3.2. SEM images of the carbon monolith modified with gold nano/micro-particles (a) before immersion and (b) after immersion of carbon monolithic rod, **IM5**, in tetrachlorauric acid solution.

Evidence that functional groups were presented on the surface of the glassy carbon could be found by IR spectrum of the carbon monolith (see Figure 2.38, Chapter 2). This spectrum exhibited a carbonyl stretching vibration at 1700 cm^{-1}, a carbonyl single bond at 1384 cm^{-1} and hydroxyl group at 3428 cm^{-1}.

When such functional sites come in contact with oxygen from the air or solution, functional groups are formed on the glassy carbon surface by breaking the bonds between ordered graphite structures present in glassy carbon. The rate of gold modification is proportional with number of functional groups present on the glassy carbon surface. SEM image (Figure 3.2) showed considerable gold content on the surface. The active groups are donors of electrons, i.e. their oxidation enables the reduction of gold ions. During the overnight immersion of the monolithic glassy carbon, gold is reduced and grown significantly only on the sites where functional groups are present.

EDX analysis was carried out on a cross section of monolith **IM5**, which verified the particles were indeed gold. The EDX spectrum of **IM5,** shown in Figure 3.3, shows a number of strong gold peaks after the modification of the carbon monolithic rod (5 µm pore diameter). EDX spectrum (Figure 3.3) shows clearly the presence of the elements C and Au.

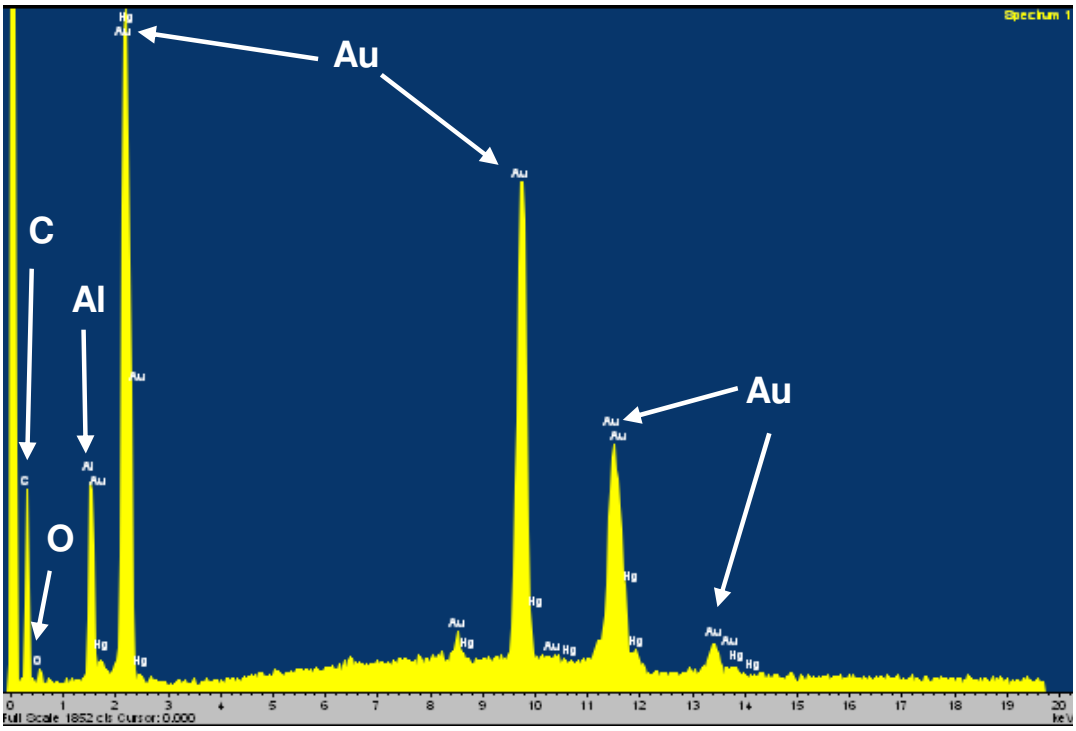

Figure 3.3. EDX spectrum of the carbon/gold composite monolith **IM5**.

The obtained EDX data for the carbon/gold composite monolith (5 µm pore diameter), **IM5**, is shown in Table 3.1.

Table 3.1. The results of EDX for the carbon/gold composite monolith, **IM5**.

Element : Carbon ratio	**IM5**
Au : C	1.3 : 1
Al : C	0.1 : 1
O : C	0.08 : 1

As shown in Table 3.1., the (element : carbon) ratio was considered, as the actual percentage of these elements on the surface cannot be measured accurately unless the surface of the monolith is polished and flat. However, a high gold:carbon ratio was recorded from the selected cross section of monolith **IM5,** indicating a very successful modification procedure through immersion. A very small amount of oxygen was detected in this cross section. Also a strong peak of aluminium was observed in the spectrum of the monolith **IM5,** (Figure 3.2). This was likely due to surface contamination, possibly caused by the furnace during the pyrolysis of the sample, as an alumina tube was used in this furnace.

3.3.1.2. Modification of the carbon monolith RC5, with gold nano/micro-particles, and characterisation by SEM

The second procedure for production of a carbon/gold composite monolith involved re-circulating a 75 m*M* aqueous solution of tetrachlorauric acid through a carbon monolith (5 µm pore diameter), for 24 h as described in Section 3.2.3.2. Reduction of gold at functional sites within the glassy carbon monolith took place, causing the orange-brown solution of the tetrachlorauric acid solution to become pale yellow after the modification process. Similar results were reported by Hostetler *et al.,* [27] and Brust *et al.,* [28]. Hostetler *et al.,* [27] prepared gold nano-particles by reduction of $AuCl_4^-$ using sodium borohydride in the presence of dodecanethiol. The orange-brown colour of the $AuCl_4^-$ aqueous solution in the presence of dodecanethiol became either very pale yellow or colourless within 5 min during the reduction process.

The resultant carbon/gold composite monolith, **RC5,** was characterised using SEM/EDX techniques and a typical SEM image (see Section 3.2.3.4 for the SEM conditions) is shown in Figure 3.4. As for monoliths prepared using the rod immersion modification technique, the SEM image of **RC5,** showed gold nano/micro-particles as small round-shaped particles size (average 400 nm) and indicated a homogenous distribution of the gold nano/micro-particles throughout the carbon monolithic structure.

The gold in the carbon/gold composite monolith, **RC5,** had lower surface coverage compared to monolith **IM5** achieved using monolith modification immersion technique.

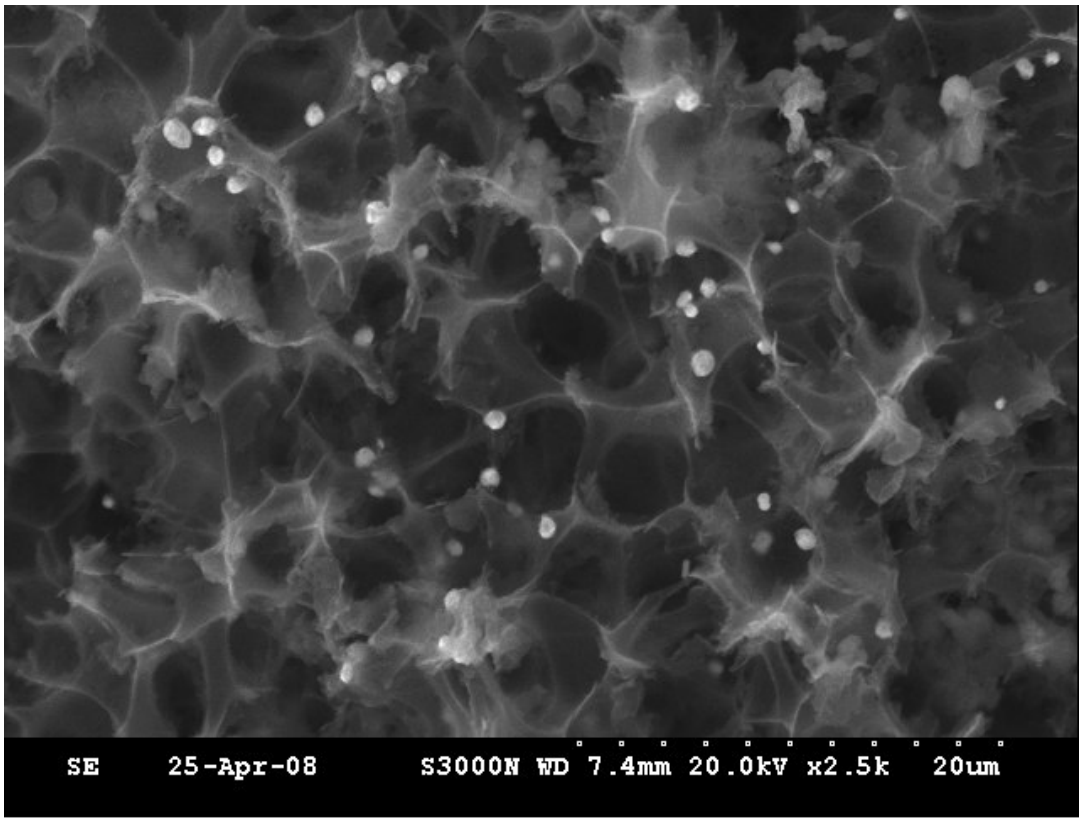

Figure 3.4. SEM image of the carbon monolith modified with gold nano/micro-particles by re-circulation of tetrachlorauric acid solution through a carbon monolith, **RC5**.

EDX analysis was carried out on a cross section of monolith **RC5**, which verified the particles were indeed gold. The EDX spectrum of **RC5,** shown in Figure

3.6, shows a number of weak gold peaks after the modification of the carbon monolithic column (5 µm pore diameter). EDX spectrum (Figure 3.5) shows clearly the presence of the elements C and Au only.

The EDX data for the carbon/gold composite monolith., **RC5,** is shown in Table 3.2.

Table 3.2. The results of EDX for the carbon/gold composite monolith, **RC5.**

Element : Carbon ratio	**RC5**
Au : C	0.2 : 1

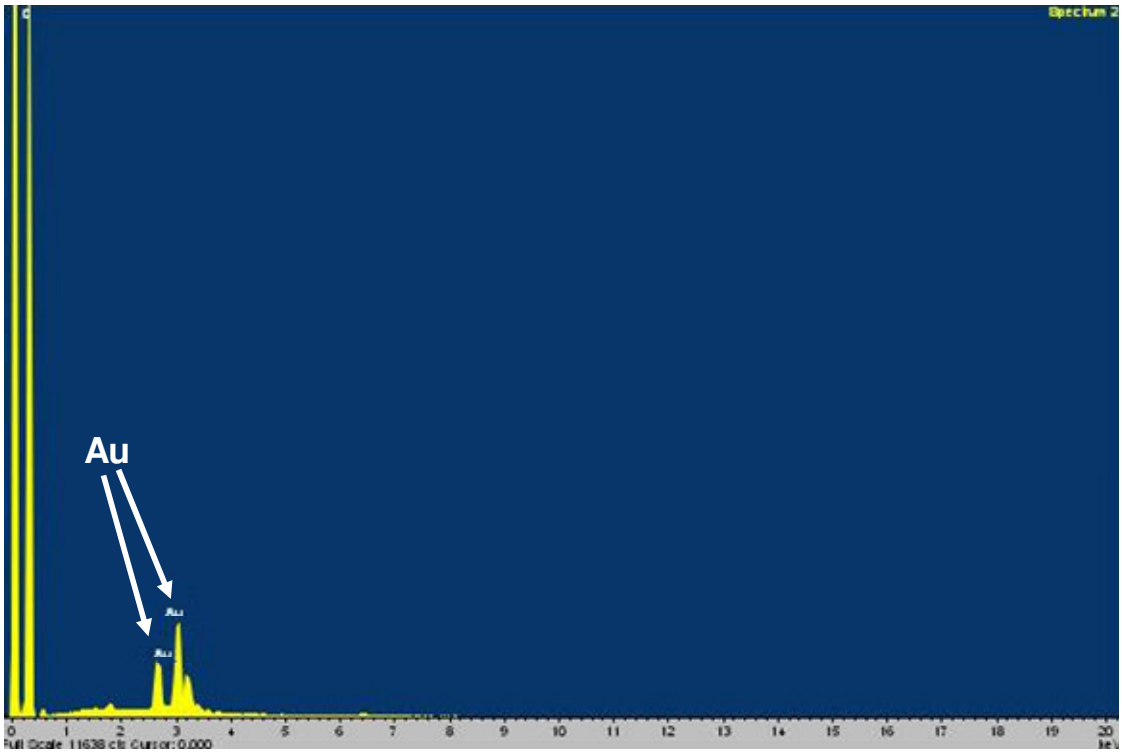

Figure 3.5. EDX spectrum of the carbon/gold composite monolith **RC5**.

As shown in Table 3.2., a low (gold : carbon) ratio was recorded from the selected cross section of monolith **RC5**, following the modification procedure based on the re-circulation technique.

Chromatographic evaluation of the above (55 x 6 mm i.d.) column is investigated in detail in Chapter 4. Once again this modification procedure proved

inferior in regard to the amount of gold nano/micro-particles on the modified carbon monolith, when compared with the procedure developed for monolith **IM5**.

3.3.1.3. Modification of the carbon monolith with gold nano/micro-particles, MI5, and characterisation by SEM/EDX

The third procedure for production of carbon/gold composite monoliths involved manual injection of a tetrachlorauric acid/dextran mixture into the clad carbon monolithic rod as described in Section 3.2.3.3.

The aim of this work was to form metallic monolithic structures within the actual larger pores (5-10 μm) of the carbon rods. Initial work followed the method of Walsh *et al.,* [29] for the production of gold and silver micro-sponges. In this work the carbon monolith itself was used as the 'mould' for the formation of the gold micro-sponges. Figure 3.6 shows the formation attempt of metallic monolithic structures within the actual larger pores (5-10 μm) of the carbon rods.

This modification procedure proved inferior in regard to the amount of gold nano/micro-particles on the modified carbon monolith, when compared with that achieved by the full immersion of the carbon monolithic rod in tetrachlorauric acid solution, **IM5**.

The resultant carbon/gold composite monolith **MI5,** was characterised using SEM/EDX techniques. SEM image of the resultant structure (Figure 3.7) shows the gold present as small and spherical micro-particles and not, as was hoped, as a sponge-like structure within the pores. The gold sponge did not form within the actual larger pores (5-10 μm) of the carbon rods and again site-specific surface reduction of gold occurred on the surface of carbon monolith instead.

EDX analysis was carried out on a cross section of monolith **MI5**. The EDX spectrum (Figure 3.8) showed the presence of C and Au. However, the gold peaks were considerably smaller than those shown in Figure 3.2 for the carbon/gold composite monolith **IM5,** obtained by immersion. In the case of **MI5,** only 10 % tetrachlorauric acid solution was mixed with dextran and used for the formation attempt of the gold sponge within the carbon monolithic structure, compared to the 100 % tetrachlorauric acid solution was used for the formation of **IM5**.

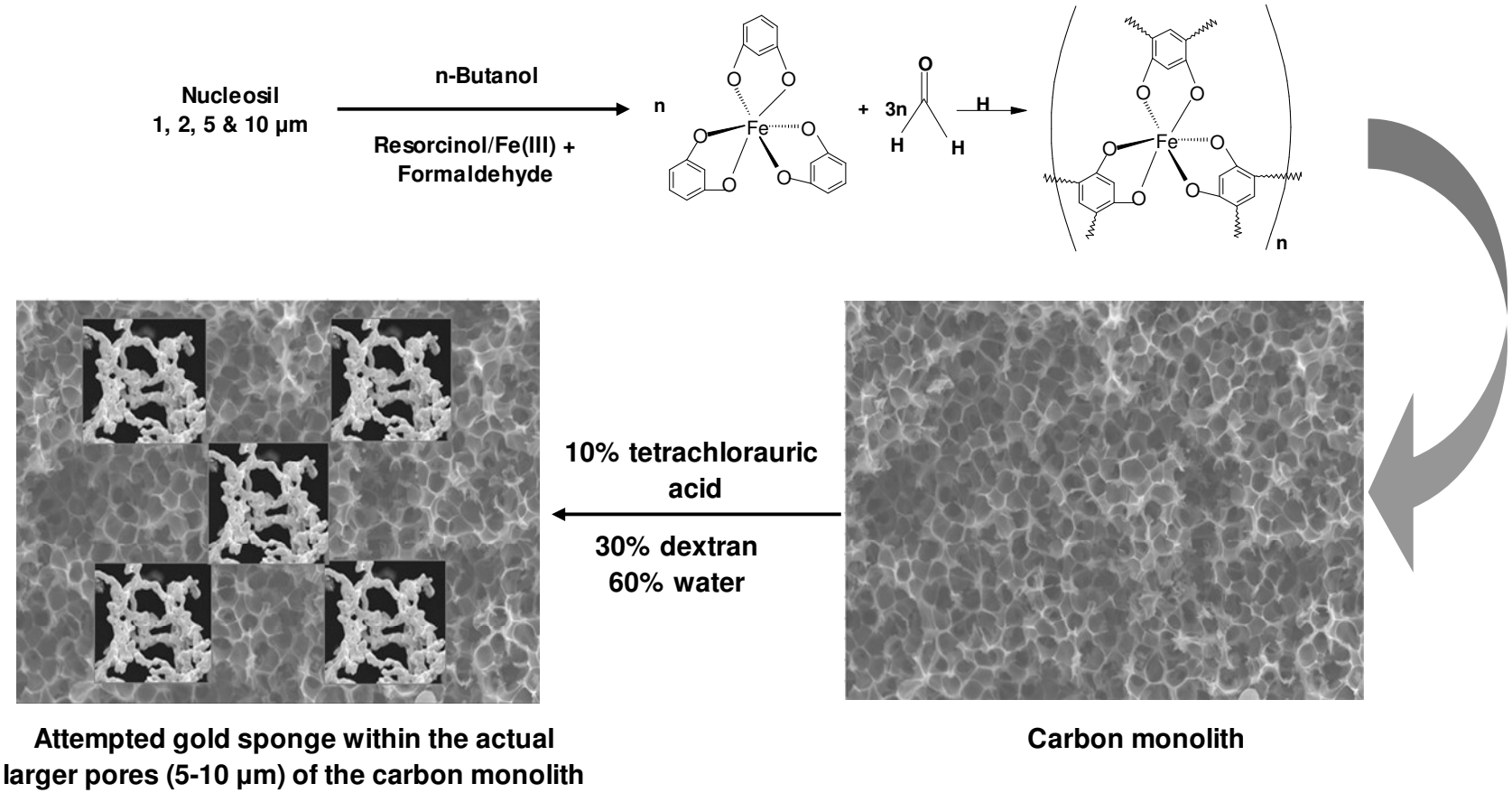

Figure 3.6. Scheme illustrating the formation attempt of the gold sponge within the carbon monolithic structure.

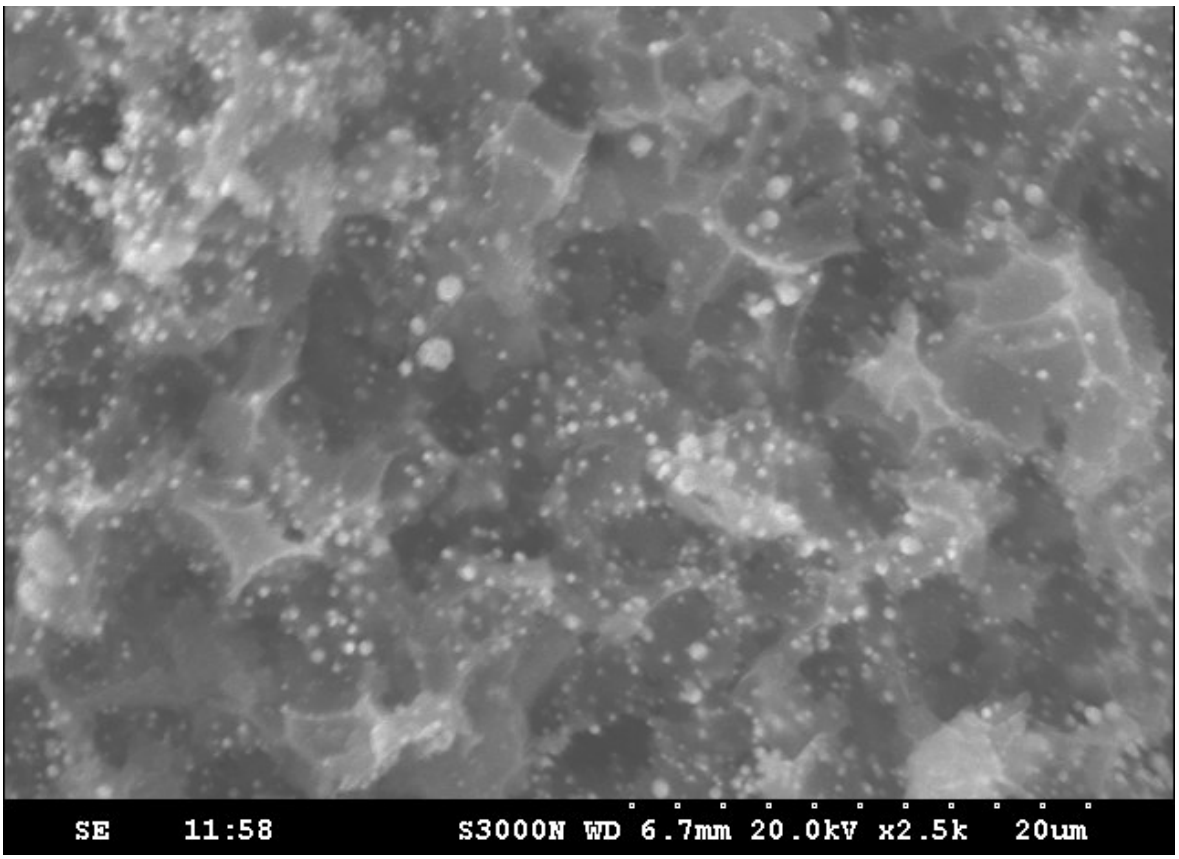

Figure 3.7. SEM image of a carbon monolith modified with gold nano/micro-particles by manual injection of tetrachlorauric acid/dextran mixture into the clad carbon monolithic rod, **MI5**.

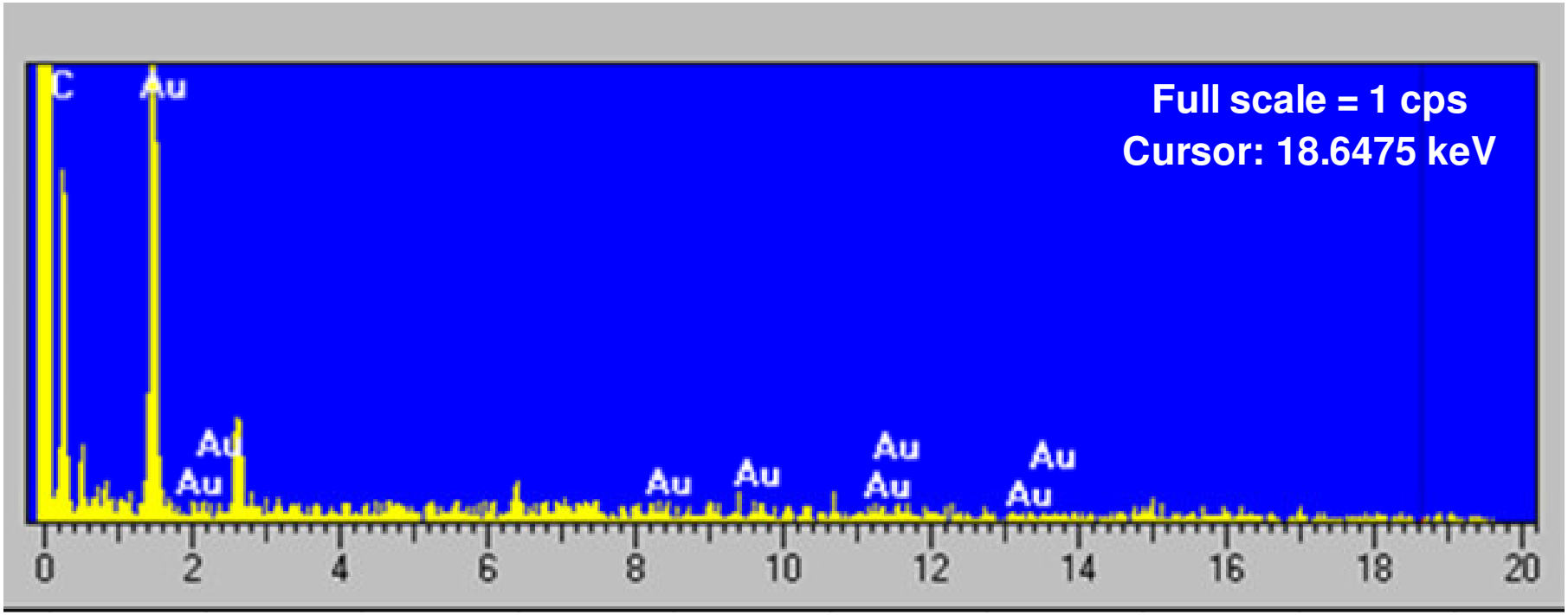

Figure 3.8. EDX spectrum of the carbon/gold composite monolith **MI5**.

3.3.1.4. Characterisation of gold content within carbon composite monoliths using inductively coupled plasma–optical emission spectroscopy

The carbon/gold composite monoliths **IM1** and **IM5,** were prepared by immersion of carbon monolithic rods into a tetrachlorauric acid solution as described in Section 3.2.3.1. Gold particles from composite monoliths **IM1** and **IM5,** were extracted/digested separately in 10 mL concentrated HNO_3 then diluted 10 fold and analysed for gold content using ICP-OES. The carbon/gold composite monolith **IM5,** was examined by SEM before the removal of the gold particles (Figure 3.9 (a)) and by HR-SEM after removal of the gold particles following HNO_3 treatment (Figure 3.9 (b)).

The four gold standards prepared were run individually on the ICP-OES under optimised conditions. The average intensity for each standard was obtained and the calibration curve in Figure 3.10 was constructed. Calibration data is fitted satisfactorily with a second order polynomial. Table 3.3 shows the intensities for different gold chloride standards.

Table 3.3. Intensities of the gold standards and unknown samples.

Concentration (mg/L)		Intensity	Minus blank intensity
Blank	0	1727	0
Std 1	4	44957	43230
Std 2	6	51909	50182
Std 3	8	61397	59670
Std 4	10	69406	67679
Unknown 1	Extracted gold from 1 μm templated carbon/gold composite monolith:	56246	54519
Unknown 2	Extracted gold from 5 μm templated carbon/gold composite monolith:	63207	61480

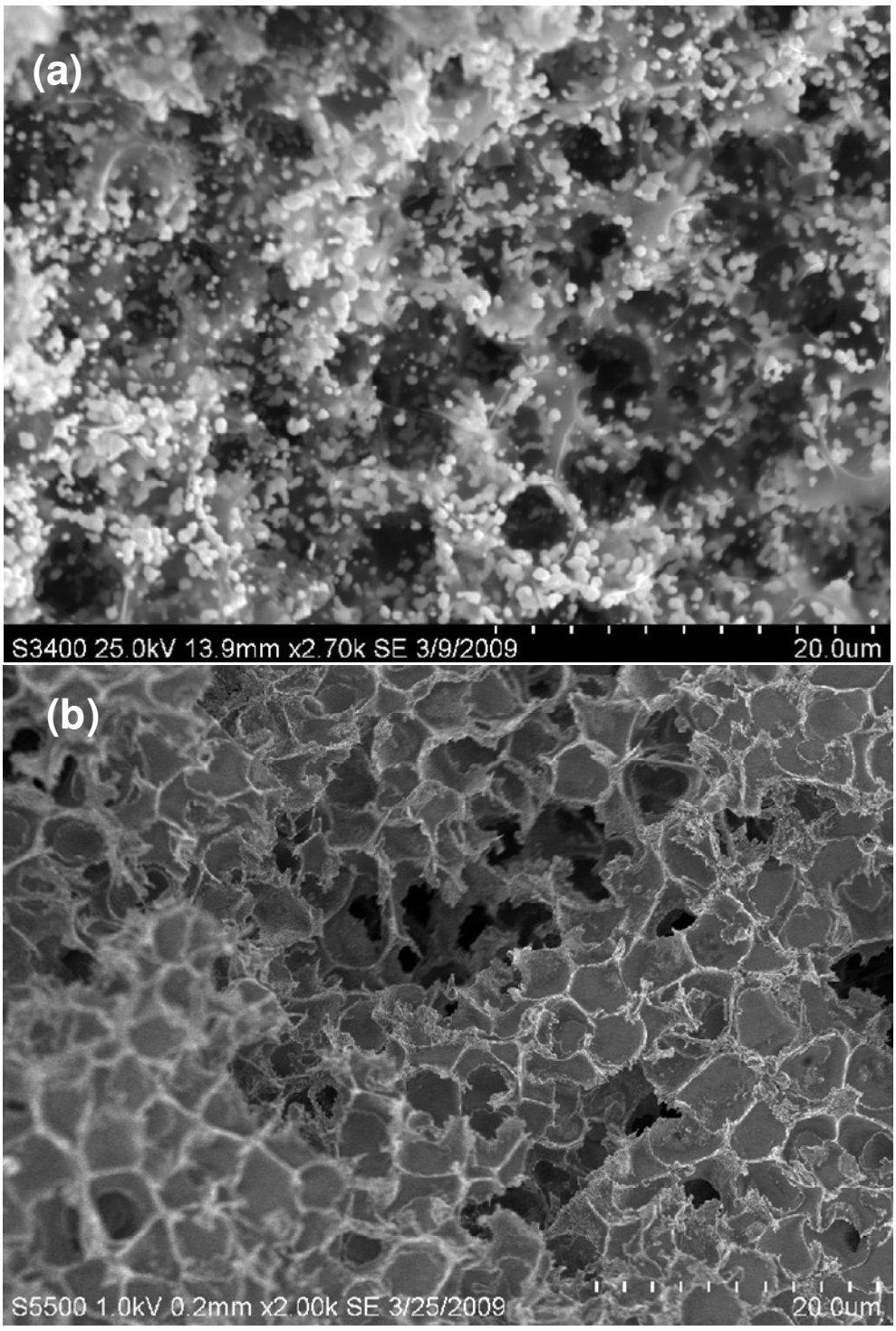

Figure 3.9. SEM image of the carbon/gold composite monolith **IM5,** (a) before, and (b) after removal of the gold particles through extraction with HNO_3.

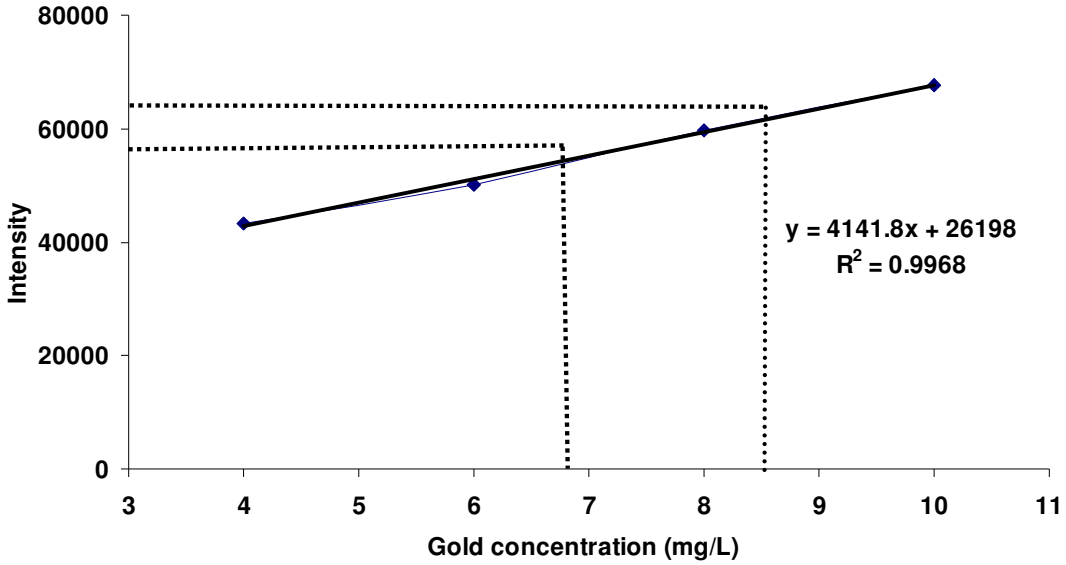

Figure 3.10. ICP-OES calibration curve for the gold standards (blank subtracted values).

The equation for the calibration curve is y = 4141.8x + 26198 and the R^2 value is 0.9968.

The percentage of gold in the carbon/gold composite monolith, **IM1**, was calculated in the following way:

54519 = 4141.8x + 26198

x = 6.84 mg/L in 10 % gold extraction solution

Taking the 1:10 dilution into account,

68.4 mg/L in original extract

0.684 mg Au in 10 ml of extract (HNO_3 volume which monolith was washed with to remove gold nano/micro-particles)

Original sample weight (carbon/gold composite monolith) = 0.0695 g

To determine the gold content and percentage in the carbon monolithic sample (69.5 mg):

0.684 mg/69.5 mg monolith x 100 = 0.98 % w/w Au (50 µM Au/g C) in the actual carbon/gold composite monolith.

The percentage of gold in the carbon/gold composite monolith **IM1 = 0.98 % w/w Au (50 µM Au/g C)**

The percentage of gold in the carbon/gold composite monolith, **IM5**, was calculated in the following way:

61480 = 4141.8x + 26198
x = 8.52 mg/L in 10 % gold extraction solution
Taking the 1:10 dilution into account,
85.2 mg/L in original extract
0.852 mg Au in 10 ml of extract (HNO_3 volume which monolith was washed with to remove gold nano/micro-particles)
Original sample weight (carbon/gold composite monolith) = 0.0581 g
To determine the gold content and percentage in the carbon monolithic sample (58.1 mg):
0.852 mg/58.1 mg monolith x 100 = 1.47 % w/w Au (75 µM Au/g C) in the actual carbon/gold composite monolith.
The percentage of gold in the carbon/gold composite monolith, **IM5 = 1.47 % w/w Au (75 µM Au/g C)**

The results indicated a 0.98 % and 1.47 % w/w Au/g C content for **IM1,** and **IM5**, respectively, using the modification method described in Section 3.2.3.1. This modification procedure proved superior in regard to the amount of gold nano/micro-particles modified carbon monolithic rod (5 µm pore diameter) (see Figure 3.2). For comparison, EDX results for the **IM5** (Figure 3.3) showed a gold percentage (52%). However, this refers to the gold content of a single target area on the surface of the monolith.

The percentage of gold in the carbon/gold composite monolith, **MI5,** was also calculated. Using this dynamic modification technique (manual injection, see Section 3.2.3.3), a considerably lower degree of surface coverage was achieved (equal to only 0.011 % w/w Au) (0.533 µM Au/g C) for a 5 µm templated monolith.

3.3.1.5. Measurement of gold particle size in the effluent modification solution for the preparation of the carbon/gold composite monolith RC5, by dynamic light scattering

As described in Section 3.2.3.2, the carbon monolith **RC5** was modified with gold by dynamic modification via re-circulation of 75 m*M* aqueous solution of tetrachlorauric acid through the column using a peristaltic pump. The aim of the following experiment was to measure the particle size of reduced gold particles in the modification solution coming out of the column during the modification procedure and consequently to know the particle size of the gold having been reduced on the surface of the carbon monolith as it passed through the column. The pale yellow effluent after modification was collected and analysed by the dynamic light scattering (DLS) technique using Malvern high performance particle sizer at 25 ^{o}C, typically in the sub-micron range (see details in Section 1.4.7, Chapter 1). The results of the measurement are available based either on intensity, volume or number.

The result obtained by cumulants analysis shown in Figure 3.11 gives three pieces of information. It gives a mean size (z-average diameter) of 396.1 nm, the polydispersity index (PdI) of 0.157 and gives a width of the distribution (PdI) of 68.45 nm. The PdI of gold micro-particles in solution was not close enough to zero which indicates a polydisperse suspension (distribution). The results are shown in Table 3.4. The graph representing the gold-micro-particles size distribution in solution after modification of the 5 μm templated carbon monolith is shown in Figure 3.11. The maximum on this graph corresponds to a particle size of 396.1 nm.

Table 3.4. The results of the gold micro-particle parameter measurements after modification of carbon monolithic column, **RC5**.

Sample	^{o}C	z-Average (d.nm)	100% Intensity	Width (nm)	PdI	Intercept
Gold(III) chloride after modification	25	396.1	100	68.45	0.157	0.926

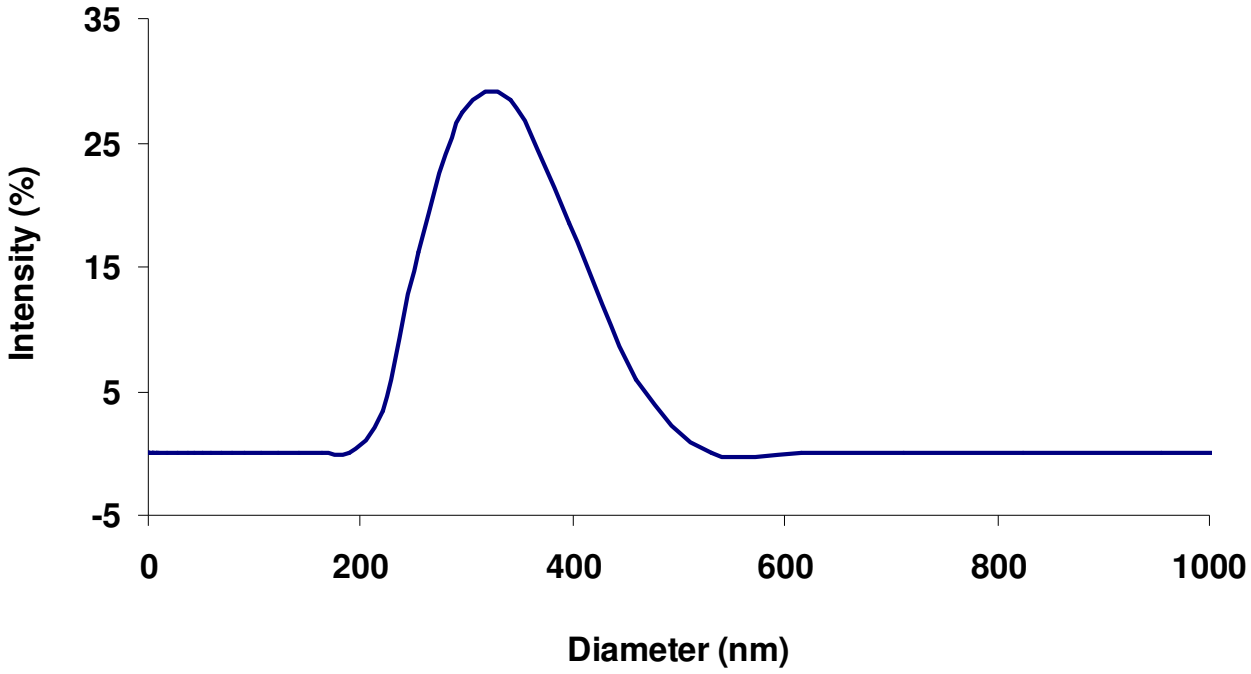

Figure 3.11. Particle size distribution within the tetrachlorauric acid aqueous solution following passage through carbon monolithic column, **RC5**.

The intensity autocorrelation curve is the measured data in a DLS experiment. All of the information regarding the size distribution of the ensemble collection of particles in the solution comes within the autocorrelation curve. The correlation of the signal takes a long time to decay as can be seen in the intensity correlogram of the 5 μm templated carbon/gold (Figure 3.12), which indicates the presence of large gold particles (~ 400 nm) in the effluent modification solution. The intensity correlogram shown in Figure 3.12 is typical from that reported in the literature [23].

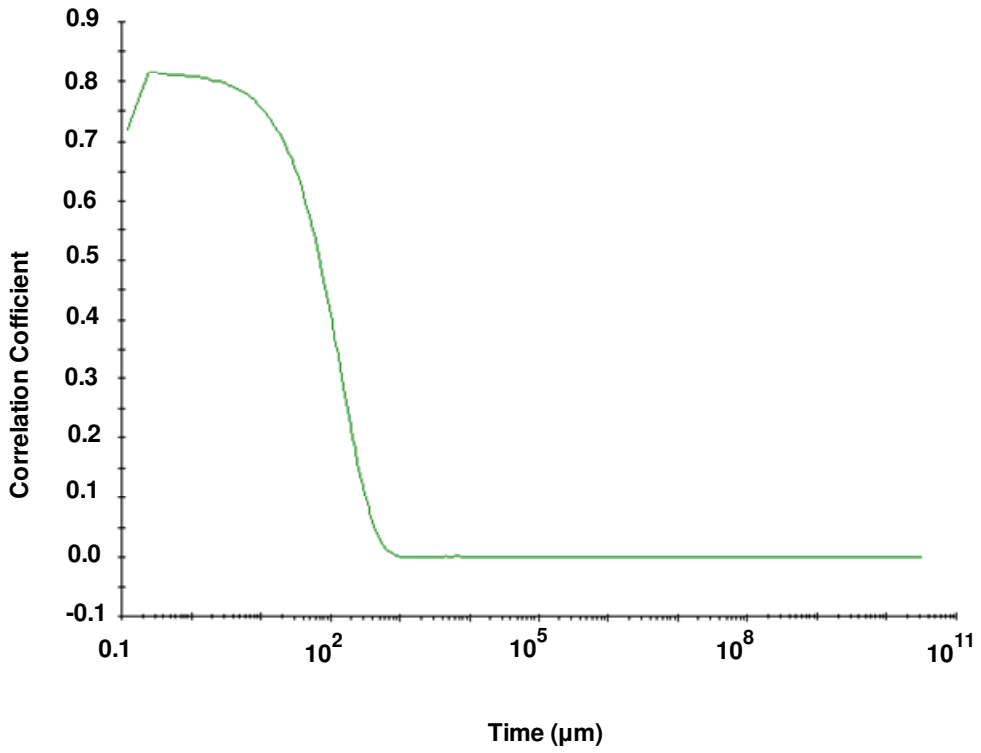

Figure 3. 12. Typical correlogram of gold containing large nano/micro-particles in aqueous solution (~ 400 nm) modified carbon monolithic column, **RC5**.

3.3.2. Dynamic coating of 6-mercaptohexanoic acid onto the surface of carbon/gold composite monoliths, IM5 and RC5

A layer of 6-mercaptohexanoic acid was immobilised onto the carbon/gold composite monolith surface using two different procedures, as described in Section 3.2.4. For the first procedure, **IM5** was immersed in a 10 m*M* aqueous solution of 6-mercaptohexanoic acid overnight, followed by drying for 24 h at room temperature. The second procedure involved re-circulating a 20 m*M* aqueous solution of 6-mercaptohexanoic acid through **RC5,** for 48 h.

The successful immobilisation of 6-mercaptohexanoic acid onto the gold particles was investigated using the resultant monolith as a stationary phase for ion exchange chromatography, to study the retention of organic cations (see Chapter 4).

Also, SEM images of **IM5**, (Figure 3.2 (b)) before, and (Figure 3.13) after the attachment of 6 mercaptohexanoic acid to the gold particles, were obtained (see Sections 3.2.3.4 and 3.2.4.1 for SEM conditions before and after the attachment, respectively).

The high resolution images obtained show the gold nano/micro-particles as various sized round-shaped particles on the surface of the carbon monolithic column as previously reported [15-16] and discussed in Section 3.3.1. An SEM image of the gold particles following 6-mercaptohexanoic acid modification is shown in Figure 3.13, which only shows that the modification with 6-mercaptohexanoic acid did not unintentionally cause all of the gold to be removed from carbon surface.

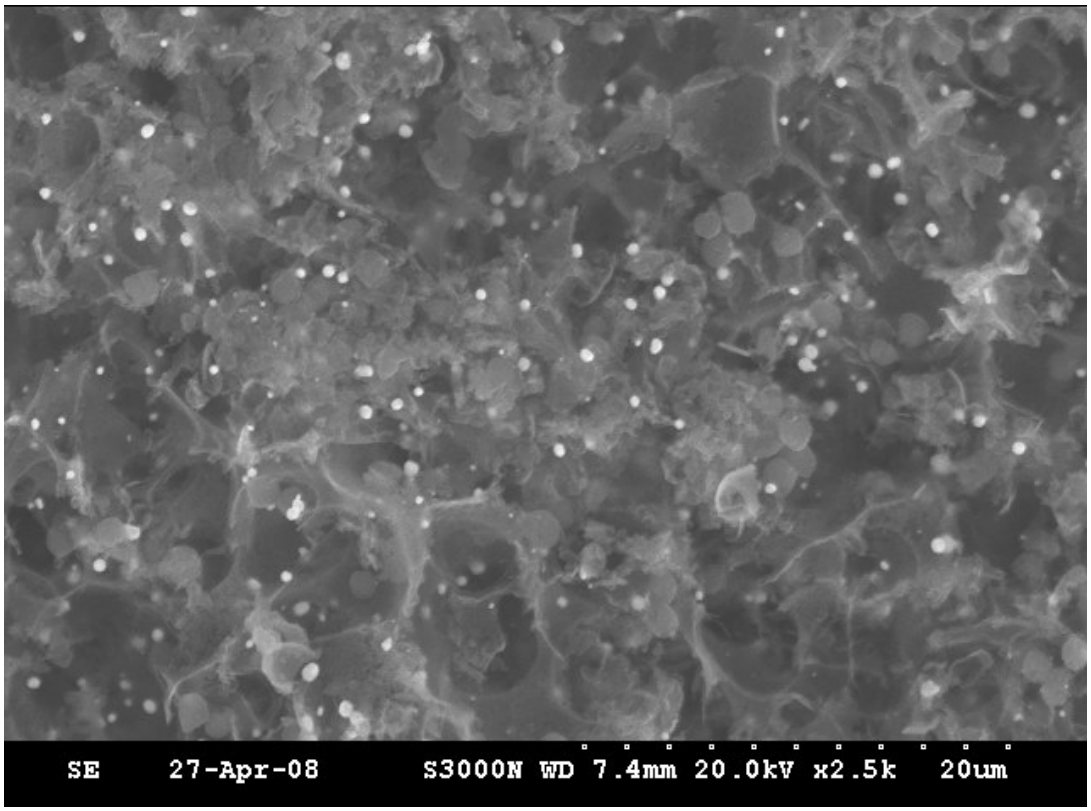

Figure 3.13. SEM image of the carbon/gold composite monolith, **IM5,** after the attachment of 6 mercaptohexanoic acid.

EDX analysis for **IM5,** and **RC5,** confirmed that the 6-mercaptohexanic acid was successfully immobilised onto the gold particles. The EDX spectra of **IM5,** (Figure 3.14) and **RC5,** (Figure 3.15) show the elemental presence of C, Au and S.

As mentioned earlier is Section 3.3.1.4, the modification procedure used to produce **IM5,** through immersion of the carbon monolith (5 µm pore diameter) in 100 m*M* tetrachloroauric acid proved superior in regard to the amount of gold nano/micro-particles modified carbon monolith. Similar results were obtained regarding the amount of 6-mercaptohexanoic acid attached to the gold particles, when **IM5** was immersed in an aqueous solution of 10 m*M* 6-mercaptohexanoic acid overnight, as described in Section 3.2.4. An EDX spectrum of **IM5,** (Figure 3.14) shows a strong sulphur peak after modification with 6-mercaptohexanoic acid, indicating that the number of acid molecules attached to the gold particles was higher compared to that of **RC5,** shown in Figure 3.15, produced by re-circulation of 20 m*M* 6-mercaptohexanoic acid through **RC5,** which shows a weak sulphur peak.

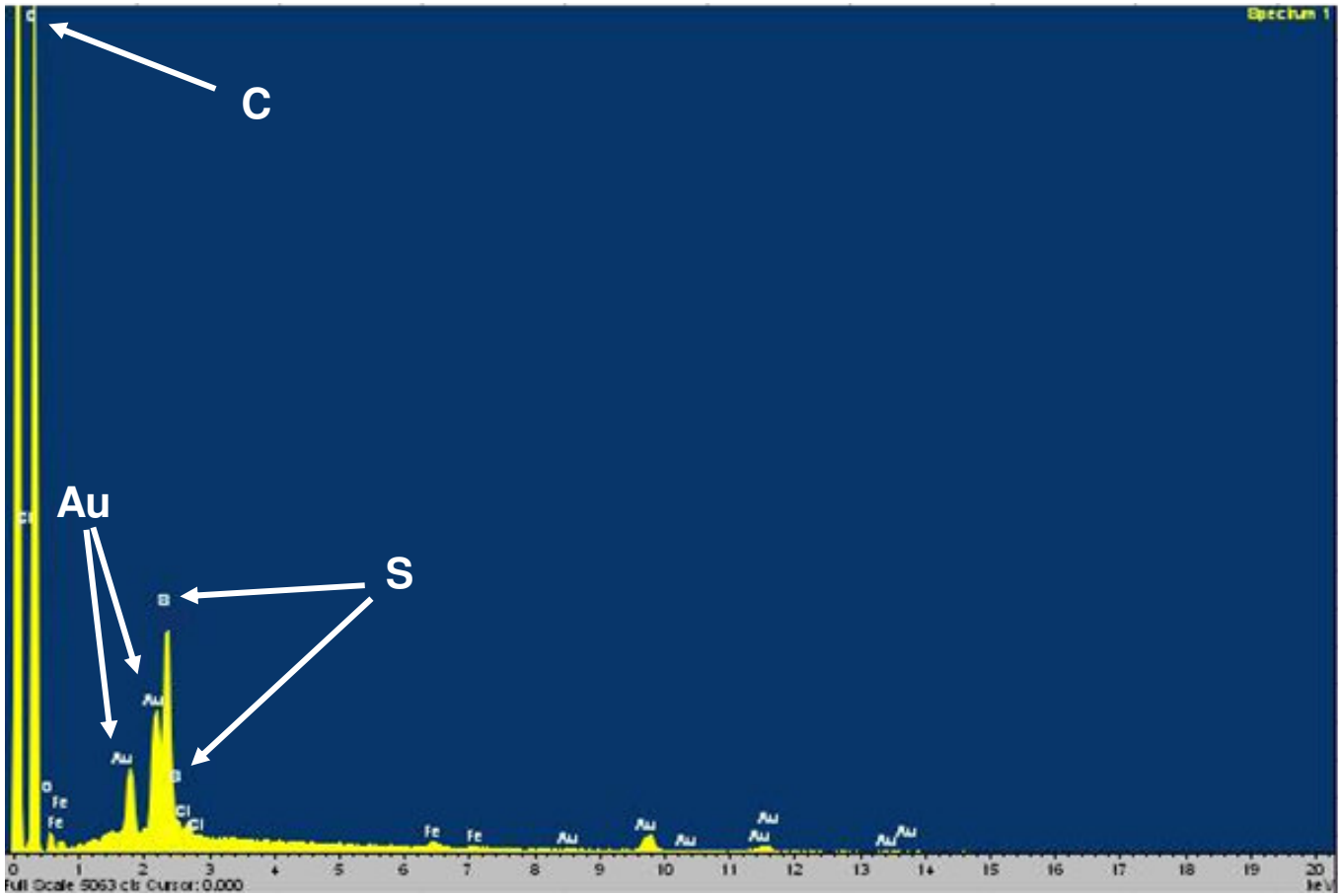

Figure 3.14. EDX spectrum of the carbon/gold composite monolith, **IM5,** after modification with 6 mercaptohexanoic acid.

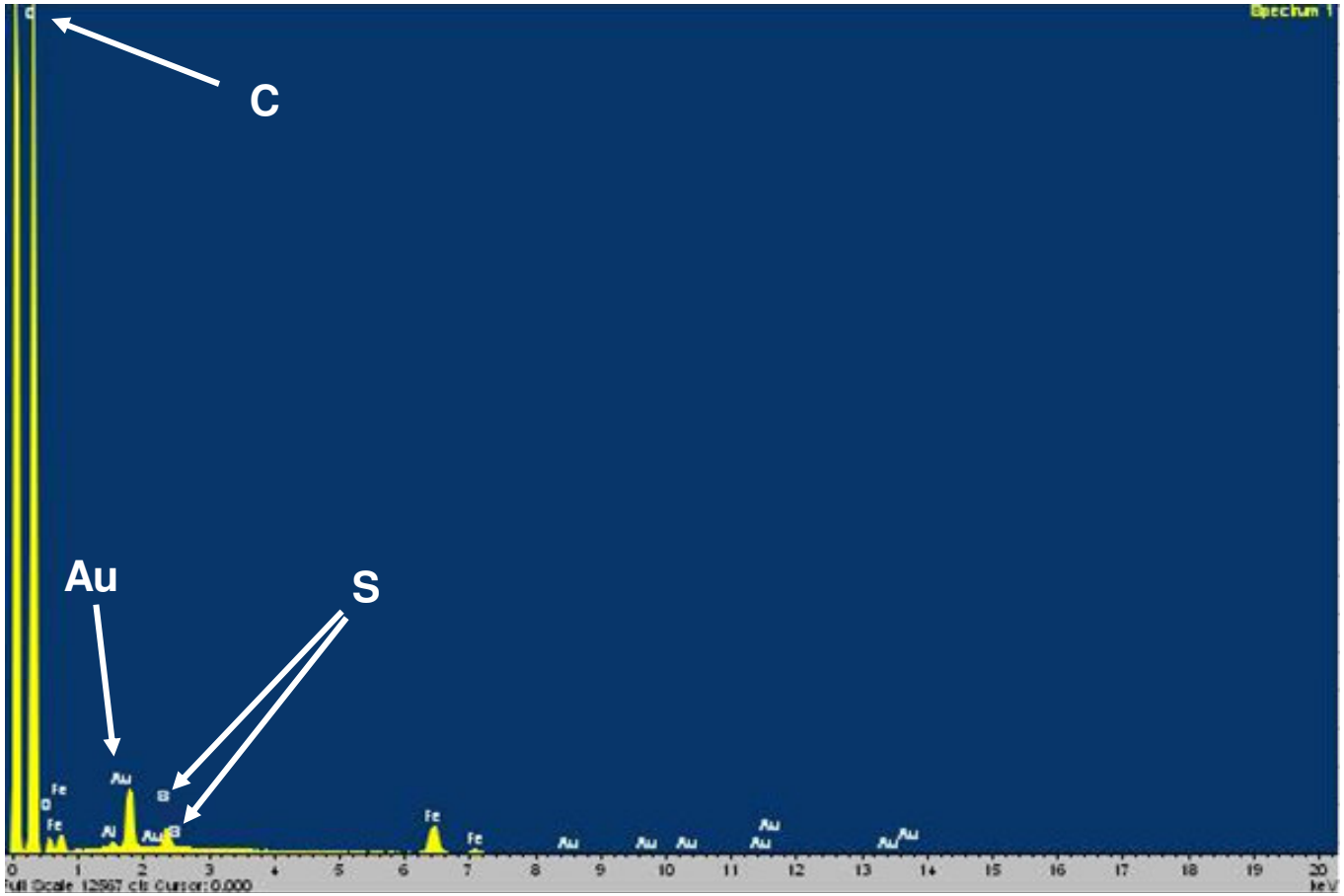

Figure 3.15. EDX spectrum of the carbon/gold composite monolith, **RC5,** after modification with 6 mercaptohexanoic acid.

The above results were confirmed by the EDX of **IM5** and **RC5,** after modification with 6 mercaptohexanoic acid shown in Table 3.5.

Table 3.5. The results of EDX for of **IM5** and **RC5,** modified with 6 mercaptohexanoic acid.

Element : Carbon ratio	**IM5**	**RC5**
Au : C	0.08 : 1	0.003 : 1
O : C	0.06 : 1	0.08 : 1
S : C	0.05 : 1	0.01 : 1
Fe : C	0.004 : 1	0.06 : 1

As shown in Table 3.5, from EDX data of monoliths **IM5** and **RC5,** a small ratio of gold and sulphur to carbon was recorded from the selected cross section of monolith **IM5**, but this is higher in comparison to that of gold and sulphur to carbon in the selected cross section of monolith **RC5,** indicating that the modification technique by immersion of carbon/gold composite monolith in 6-mercaptohexanoic acid was more successful.

Another indication that the modification technique by immersion of carbon/gold composite monolith in 6-mercaptohexanoic acid was successful rather than the re-circulating technique, was the ratio of gold to sulphur which was recorded (1.6 : 1) from the selected cross section of monolith **IM5** compared to the ratio of gold to sulphur was recorded (0.3 : 1) from the selected cross section of monolith **RC5** which is not reflect the actual amount of sulphur in the sample as it refers to the sulphur content of a single target area on the surface of the monolith not the whole sample. The entire amount of sulphur in the sample is expected to be less than the gold as the gold in the carbon/gold composite monolith, **IM5,** had a higher surface coverage (Figure 3.2 (b)), while the 6-meractohexanoic acid ligands attached partially to the gold particles surface.

A number of minor peaks in the EDX spectra (Figures 3.14 and 3.15) were attributed to residual metal iron, iron carbide (CH_4Fe_3) or (Fe_3C) rooted in the graphite strips and surface impurities. However, outer iron carbide may also remain on the graphite surface and cannot be removed by acid washing. Similar observations

were reported in the literature when Liang *et al.,* [30] prepared carbon monoliths, showing a small amount of residual iron particles and iron carbide embedded in the graphite strips indicated by minor peaks observed in the X-ray diffraction pattern.

Iron was more significantly visible on the surface of the selected cross section of monolith **RC5,** and this could be attributed to two reasons. The first reason is that during the pyrolysis of the carbon-silica rod used for the preparation of monolith **RC5**, the iron ions were reduced to iron atoms thereby catalysing the crystallisation of the glassy carbon and forming the graphite strips within the carbon matrix. As a result of a partial leaching of the iron metal and an incomplete crystallisation of the glassy carbon, the iron could be presented [30]. The second reason could be the shortness of the etching time of carbon-silica monolith with concentrated HF to remove the silica template and iron catalyst from the carbon-silica rod after the pyrolysis.

3.3.3. Direct modification of carbon monoliths, P1, P2, P5 and P10, with gold paint, and characterisation by SEM/EDX

Gold paint (organo-gold) containing 12 % gold and some organic components such as nitrobenzene and turpentine was investigated for the direct modification of the carbon monolithic surface. Modification of carbon monolithic rods (1, 2, 5 and 10 µm pore diameter), with gold paint (12 %) was carried out as described in Section 3.2.5. The resultant carbon monoliths **P1**, **P2**, **P5**and **P10**, were characterised using SEM and EDX. The carbon monolith (5 µm pore diameter) modified with gold paint, (**P5)** was also characterised by HR-SEM.

The EDX spectra of these samples shown in Figures 3.16 (b), 3.17 (b), 3.18 (b) and 3.19 (b), respectively. The elemental presence of C and Au was clearly seen in these four monolithic samples, respectively. Strong gold peaks indicated that the gold was successfully immobilised from the gold paint and aggregated on the surface of the carbon monolith. The EDX data for the analysis of **P1**, **P2**, **P5** and **P10** is shown in Table 3.6.

Table 3.6. The results of EDX for of **P1**, **P2**, **P5** and **P10**.

Element :Carbon ratio	**P1**	**P2**	**P5**	**P10**
Au : C	0.5 : 1	0.3 : 1	0.3 : 1	0.4 : 1
O : C	0.05 : 1	0.02 : 1	0.05 : 1	0.12 : 1
Fe : C				0.05 : 1
Al : C				0.01 : 1
Ag : C		0.02 : 1		

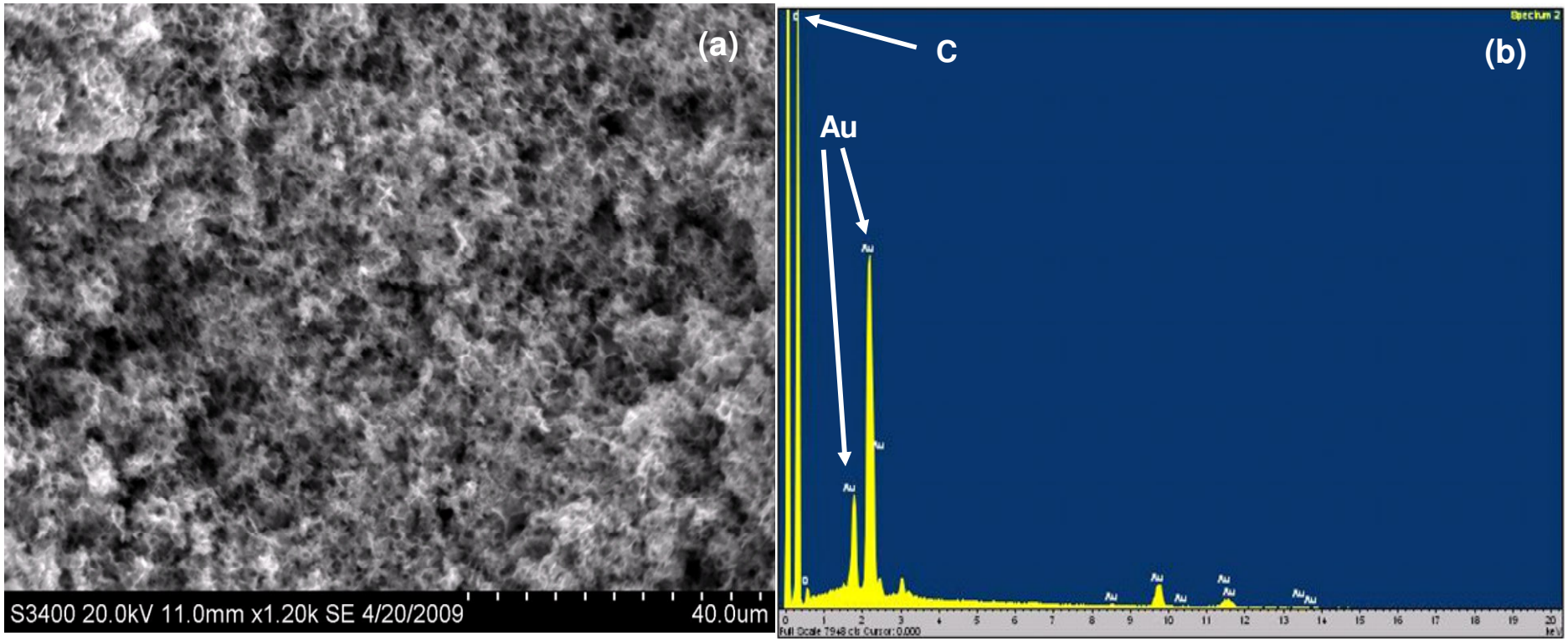

Figure 3.16. (a) SEM image, and (b) EDX spectrum of the carbon monolith (1 µm pore diameter) modified with gold paint, **P1**.

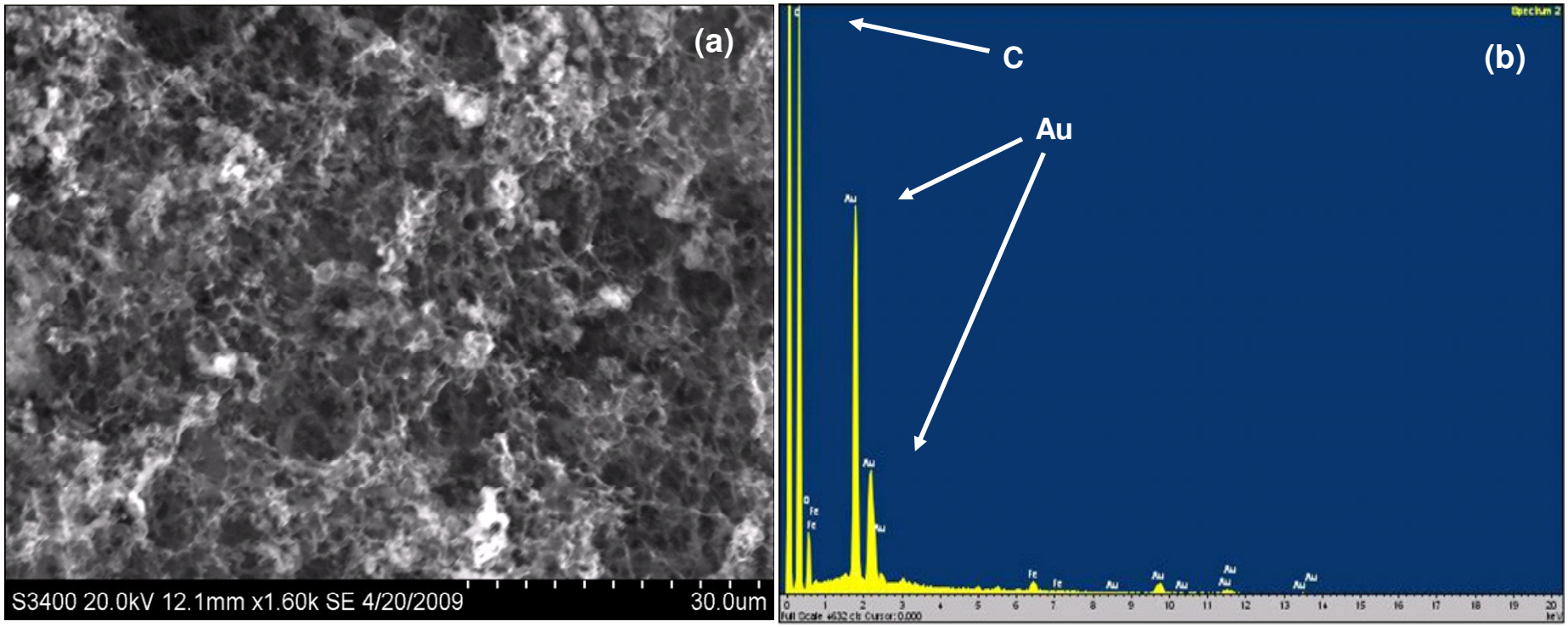

Figure 3.17. (a) SEM image, and (b) EDX spectrum of the carbon monolith (2 µm pore diameter) modified with gold paint, **P2**.

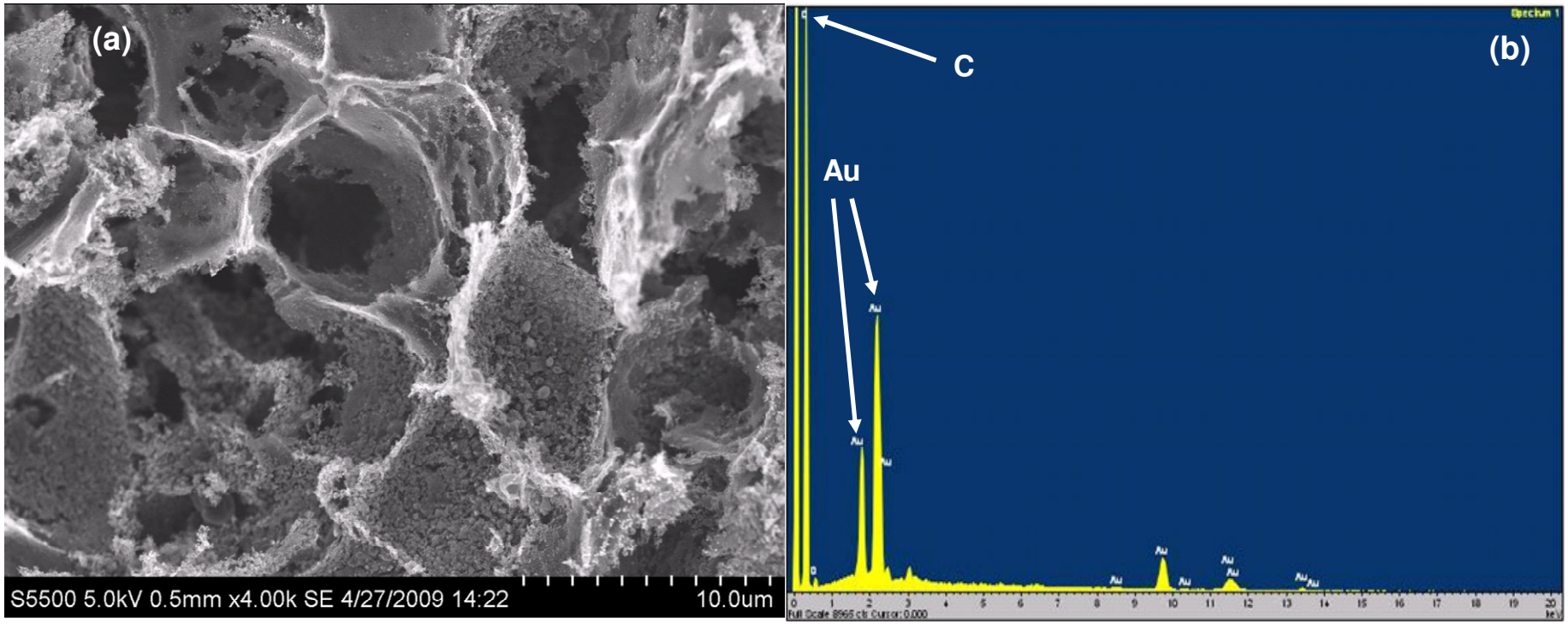

Figure 3.18. (a) HR-SEM image, and (b) EDX spectrum of the carbon monolith (5 µm pore diameter) modified with gold paint, **P5**.

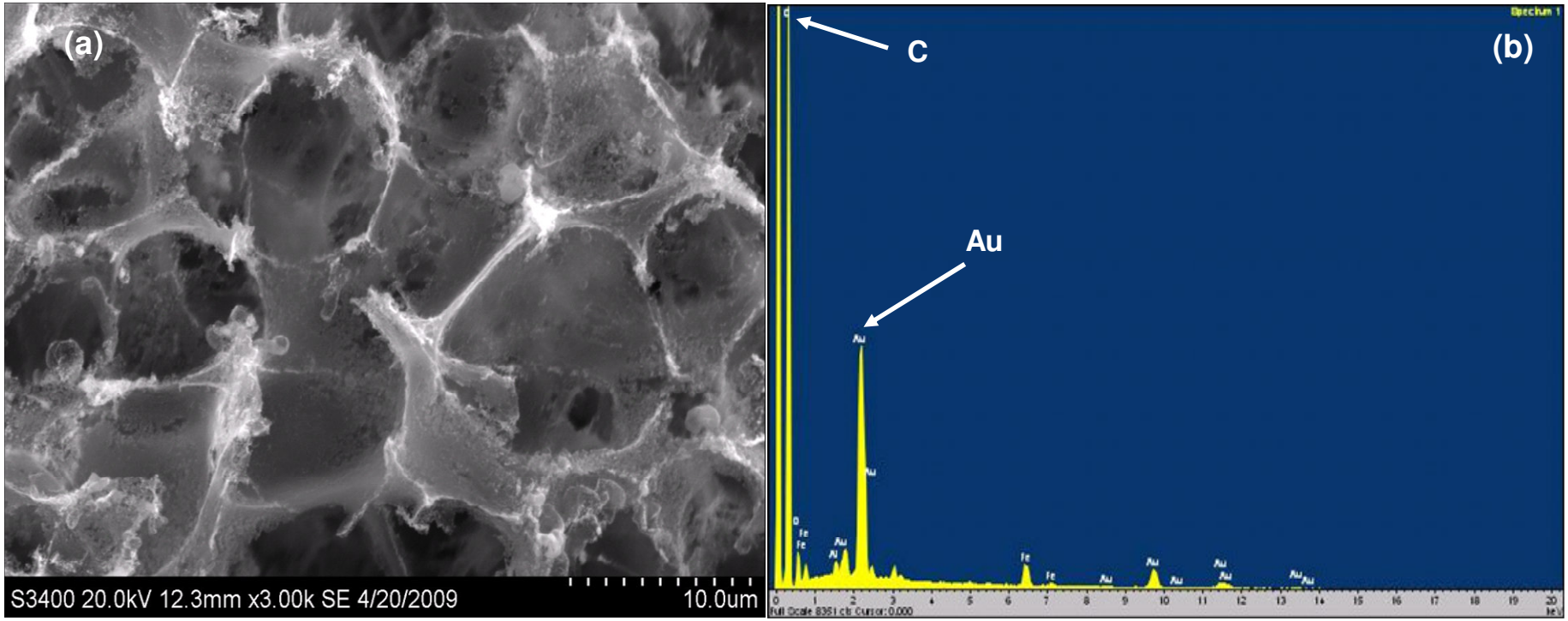

Figure 3.19. (a) SEM image, and (b) EDX spectrum of the carbon monolith (10 µm pore diameter) modified with gold paint, **P10**.

As shown in Table 3.6, a high ratio of (gold : carbon) was recorded for the selected cross sections of monoliths **P1**, **P2**, **P5** and **P10,** indicating that the modification procedure using gold paint was successful. The highest monolith in surface area gave the highest in % gold surface coverage.

A number of peaks such as silver in the EDX spectrum of monolith **P2** were visible, probably caused by surface contamination. Also, a weak iron peak in the EDX spectrum of monolith **P10**, (Figure 3.19) was attributed to residual iron particles and iron carbide. A minor amount of aluminium was detected in monolith **P10,** again as a surface contamination possibly caused by the furnace during the pyrolysis of the carbon monolith, as an alumina tube was being used in this furnace.

The colour of the 10% gold paint solution in trichloroethene was dark brown before modification, and did not change significantly after the modification, possibly due to the presence of the gold paint components such as nitrobenzene and turpentine.

Although, standard analysis using SEM did not show substantial gold particles present, examination of the samples at higher resolution (Figure 3.20) revealed a mixture of roughly spherical immobilised gold nano-particle present on the carbon surface. The average size of these particles was approximately 30 nm, with a size range of ~ 10 to 60 nm. Clearly, the use of the gold paint direct modification procedure results in a markedly different particle size distribution to that obtained using the previous methods described herein.

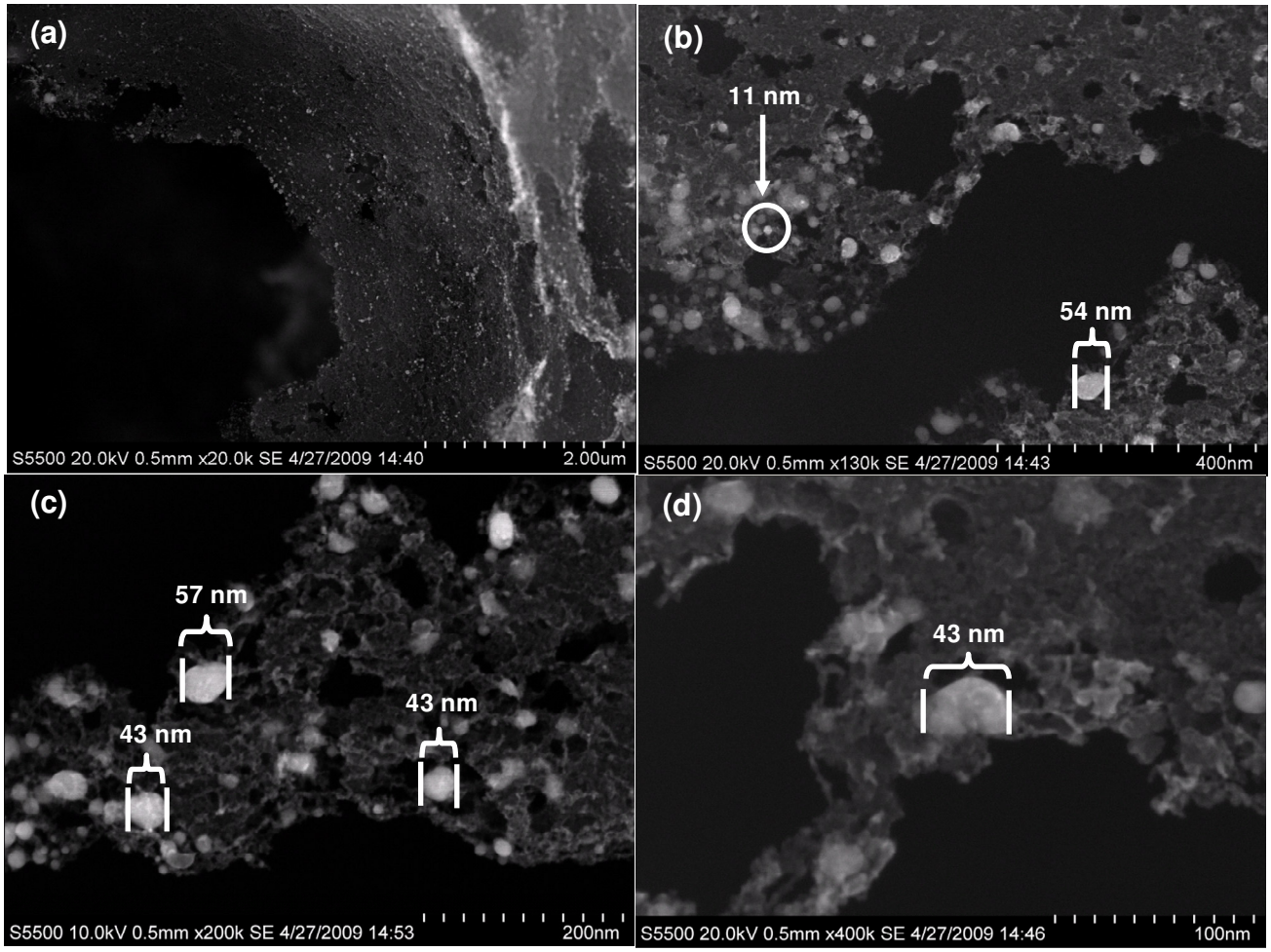

Figure 3.20. HR-SEM images of the carbon monolith (5 µm pore diameter) modified with gold paint, **P5,** at magnification of (a) 20 k, (b) 130 k, (c) 200 k and (d) 400 k.

3.3.4. Conductivity measurements of the carbon/gold composite monoliths

Gold/carbon composite monoliths are conductive materials and therefore excellent candidate for potential electrochemical and sensor applications. Electrical conductivity or specific conductivity of the glassy carbon monoliths was calculated and described earlier in Section 2.3.9, Chapter 2. Resistances of the carbon/gold composite monoliths were measured using a clamp voltmeter and the electrical conductivities were calculated to determine the ability of the monolith to conduct an electric current.

As mentioned in Section 2.3.9 (Chapter 2), *R* will be highly affected by the surface area of the carbon monolithic samples at certain length and radius. The highest surface area, the lowest resistance and therefore, the highest conductivity.

Comapared to the electrical conductivity of bare glassy carbon previously studied by Barykin *et al.*, [31] and calculated in Section 2.3.9, Chapter 2,

Table 3.7. Resistance measurements for the glassy carbon and modified carbon/gold composite monoliths, **IM5** and **P5**.

Carbon/gold composite monoliths	**Resistance (Ω)**	**Length (mm)**	**Rod Diameter (mm)**
Glassy carbon	0.18 (measured by Barykin *et al.,* [31].)	10	15.2
IM5	1.3	10	6
P5	2.1	10	5

Calculations of the electrical conductivity of 5 μm modified carbon/gold composite monoliths, **IM5** and **P5**, were carried out using the equations 2.3, 2.4 and 2.5 in Section 2.3.9, Chapter 2, as follows:

For the monolith, **IM5**:

$A = r^2 . \pi$

$A = (0.003)^2$ x 3.14

$A = 2.826$ x 10^{-5} m^2

$p = RA/L$

$p = 1.3\ (\Omega).\ 2.826$ x 10^{-5} $m^2/0.01$ m

$p = 3.6738$ x 10^{-3} Ωm

$\sigma = 1/p$

$\sigma = 1/3.6738$ x 10^{-3} Ωm

$\sigma = 272$ Sm^{-1}

For the monolith, **P5**:

$A = (0.0025)^2 \times 3.14$

$A = 1.9625 \times 10^{-5}\ m^2$

$p = 2.1\ (\Omega).\ 1.9625 \times 10^{-5}\ m^2/0.01\ m$

$p = 4.12125 \times 10^{-3}\ \Omega m$

$\sigma = 4.12125 \times 10^{-3}\ \Omega m$

$\sigma = 243\ Sm^{-1}$

The electrical conductivities of the 5 µm modified carbon/gold composite monoliths, **IM5** and **P5**, were 272 and 243 (S/m), respectively (Table 3.8.). These values were higher than that of unmodified carbon monoliths, (1 µm) 177, (2 µm) 169, (5 µm) 161 and (10 µm) 154 S/m (see Table 2.4, Chapter 2) as they were modified with gold particles, making the monolith more conductive.

Table 3.8. Conductivity measurements of the carbon monoliths, carbon/gold composite monoliths, glassy carbon, **IM5** and **P5**.

Carbon Materials	**Conductivity (S/m)**
5 µm (pore diameter) templated carbon monolithic rod	161
10 µm (pore diameter) templated carbon monolithic rod	154
Commercial glassy carbon electrode	306
IM5	272
P5	243

The carbon/gold composite monolithic rod showed is the highest conductivity compared to that of the carbon monolithic rod modified with gold paint containing 12 % gold. As mentioned in Section 2.3.9, (Chapter 2), the electric current density is the amount of flow passing through a unit area of the monolith so the highest surface area

sample, the more conductive and the carbon monolith modified with 100 % gold chloride has a larger surface area than that of carbon monolith modified with 12 % gold paint.

3.3.5. Modification of the carbon monoliths, with silver micro-particle, S10, and characterisation by SEM/EDX

Modification of carbon monolithic rods with silver was also investigated; as such results have been reported and mentioned earlier utilising glassy carbon electrodes [22]. The modification procedure was carried out by immersion of the carbon monolithic rod in an aqueous solution of silver nitrate overnight as described in Section 3.2.6. The modification involves a process of spontaneous reduction of Ag^{+} ions to Ag(0) on the surface of carbon monolith, then, the silver atoms were immobilised, aggregated and presented in its elemental state an inner and outer surface layers of the carbon monolith, where growth of silver micro-particles took place.

Examination of the resultant carbon/silver composite monolith, **S10,** by SEM (Figure 3.21) revealed a small round-silver micro-particles shape, indicating the homogenous distribution of the silver micro-particles aggregating on the surface of the carbon monolith and formed by a surface induced reduction.

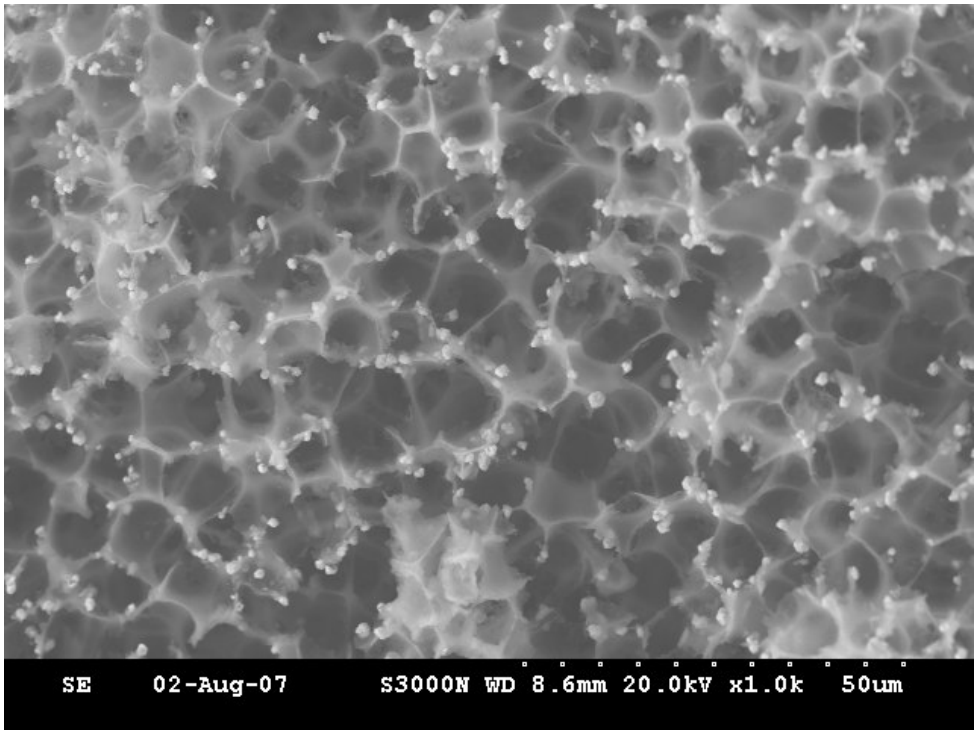

Figure 3.21. SEM image of the carbon/silver composite monolith, **S10**.

EDX analysis was carried out on the cross section of the carbon/silver composite monolith. An EDX spectrum of **S10,** (Figure 3.22) shows a strong silver peak after modification of the carbon monolithic rod, indicating that these particles were successfully and significantly immobilised on the surface of the carbon monolith, and the carbon monolithic surface itself was indeed acting as the reducing agent. The EDX spectrum (Figure 3.22) of **S10** shows the presence of C and Ag, only.

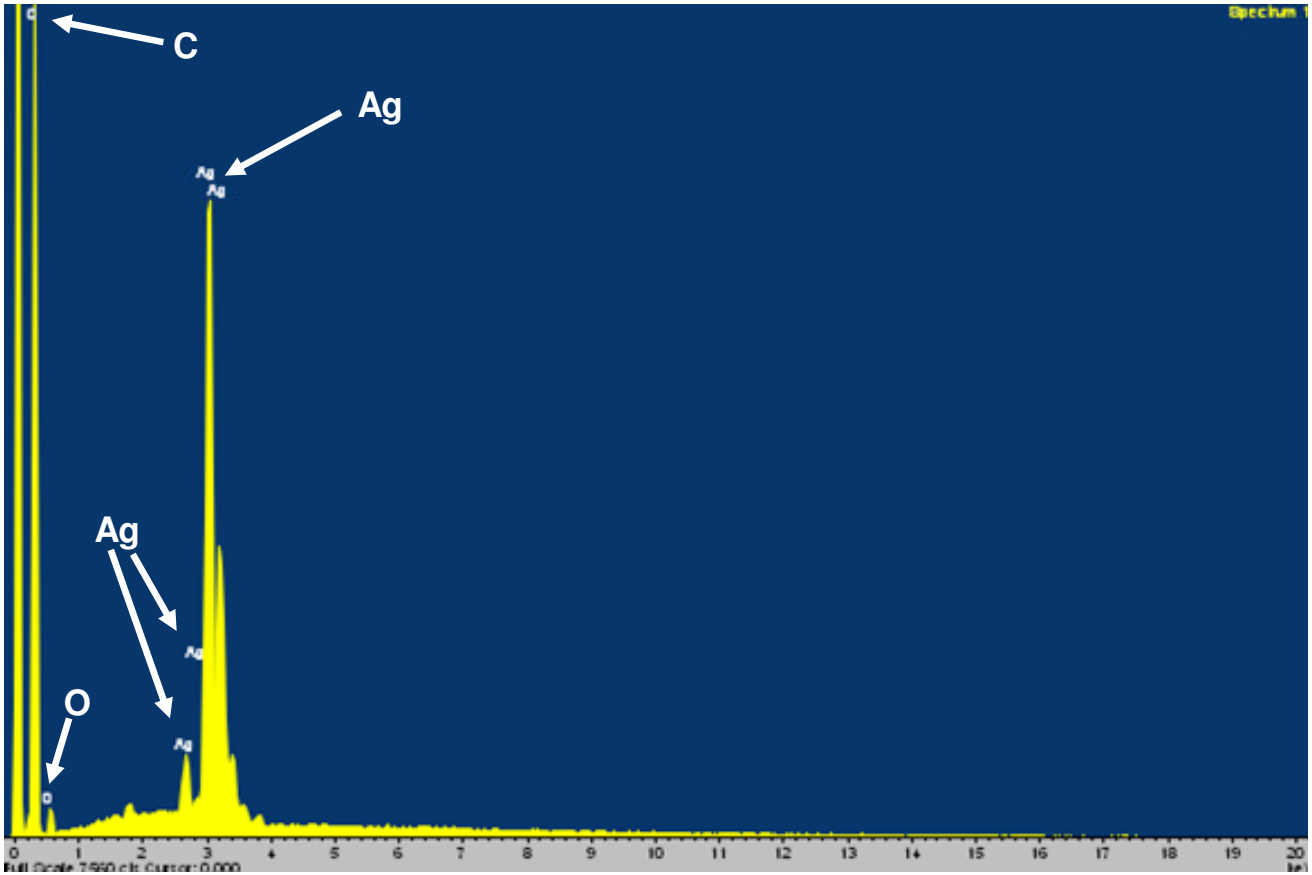

Figure 3.22. EDX spectrum of the carbon/silver composite monolith, **S10**.

The EDX data for the carbon/silver composite monolith, **S10,** is shown in Table 3.9.

Table 3.9. The results of EDX for the carbon/silver composite monolith, **S10**.

Element : Carbon ratio	**S10**
Ag : C	0.76 : 1
O : C	0.1 : 1

As shown in Table 3.9, a very high (silver : carbon) ratio and a small (oxygen : carbon) ratio were recorded from the selected cross section of monolith **S10**, indicating the successful modification procedure based on the simple immersion technique.

Also, for the determination of silver present on the surface of the carbon/silver composite monolith, the monolith was digested in concentrated HNO_3 and analysed using ICP-OES. It was shown that Ag content was 2.7 % w/w Ag (252 µM Ag/g C) for a 10 µm templated monolith.

3.3.6. Direct modification of the carbon monolith, with gold nano-particles (5 nm particle size), Au5, and characterisation by SEM/EDX

An attempt to directly modify a monolithic glassy carbon rod (5 µm pore diameter) using gold colloid suspension was performed. A carbon/gold nano-particles composite monolith, **Au5,** was attempted through immersion of the carbon monolithic rod for 24 h in gold colloid suspension **Au5,** as described in Section 3.2.7. The resultant monolithic rod was characterised using HR-SEM. The HR-SEM image (Figure 3.23) shows no sign of gold nano-particles adsorbed onto the monolith surface. The results showed clearly that for previous methods, the surface reduction process was critical for gold immobilization and that simple gold nano-particles adsorption did not take place.

The carbon monolith with its high surface area has a great capacitive charge, as indicated by the large background confirmed by CV analysis (see Future work chapter), as capacitance is proportional to surface area [32]. The structure, size and surface charge density of the carbon monolith are critical factors to determine the gold

nano-particles ability to attach to the monolithic surface. In previous modification procedures, Au^{3+} solution was used, so ions were reduced on the surface of carbon monolith and thus covalently bonded. Using gold nano-particles in suspension was not successful as the gold colloid (5 nm particle size) used contains ~ 0.01% tannic acid and ~ 0.04% sodium citrate. The colloid also contains 0.02% sodium azide as a preservative. The negatively-charged citrate ions were attached to the gold nano-particles, introducing the surface charge that repelled the particles and prevented them from aggregating on the surface of the carbon monolith.

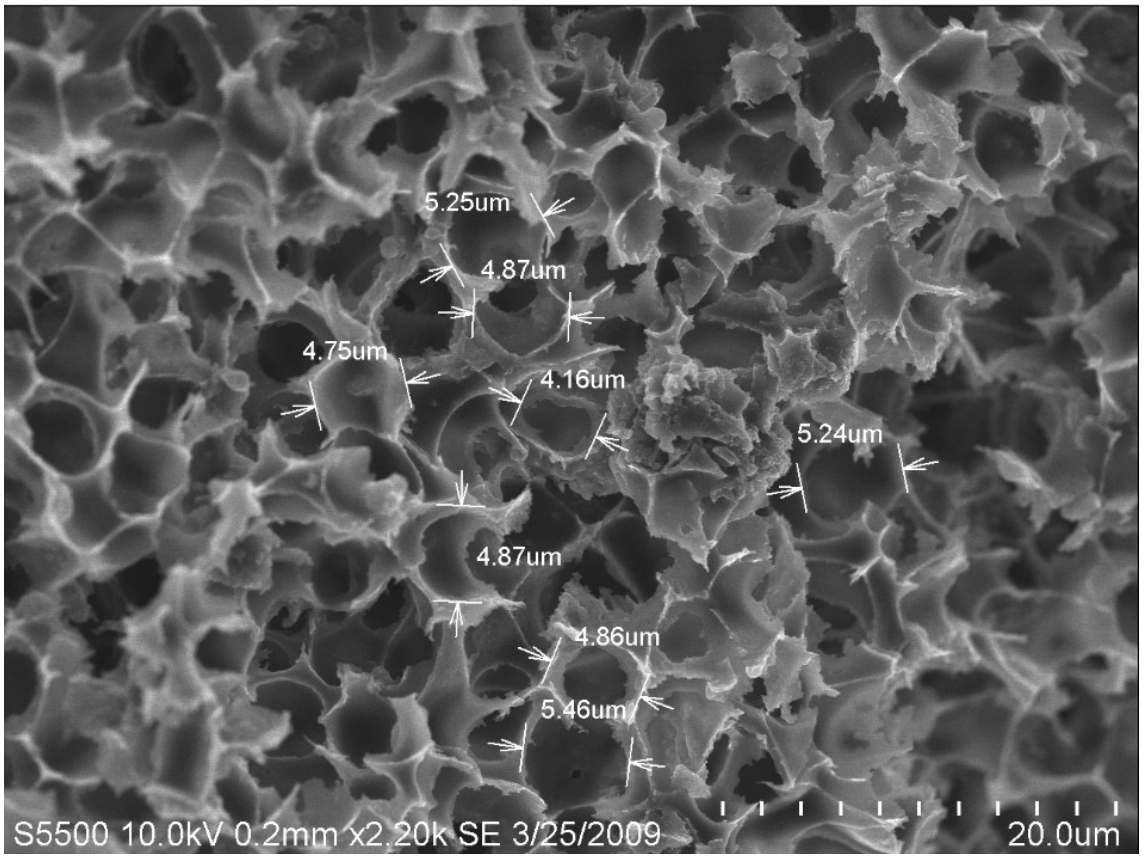

Figure 3.23. HR-SEM image of the carbon monolith (5 µm pore diameter) after the modification attempt with gold nano-particles (5 nm particle size).

The procedure was repeated again and the carbon monolith was immersed in the gold nano-particles colloid suspension for a longer period (48 h), followed by drying in the vacuum oven at 80 ^{o}C for 24 h. The same result was observed and no sign of gold nano-particles attached to the carbon monolithic surface was evident.

HR-SEM analysis with higher magnification (9 k (Figure 3.24 (a) and 18 k (Figure 3.24 (b)) could not detect the presence of gold nano-particles (5 nm particle size) on the carbon monolithic surface.

The resultant carbon monolithic rod was also characterised using EDX analysis (Figure 3.25), which confirmed that the gold nano-particles (5 nm particle size) did not attach to the carbon monolithic surface.

As shown in Table 3.10, no sign of gold was detected by EDX analysis from the selected cross section of monolith **Au5**.

Iron metal or its compounds may have an effect on the EDX analysis. Several minor peaks in the EDX spectrum (Figure 3.25) indicated that the monolithic carbon rod has a small amount of residual halogen, oxygen, iron particles and iron carbide. A high oxygen : carbon ratio was recorded possibly due to the large pore diameter (5 μm) of the monolith used. Also, tiny amounts of silica, iron and chlorine, possibly attributed to residual iron, silica particles and iron carbide, or incomplete etching time of silica particles by concentrated HF treatment. The halogen-, oxygen-containing groups on the graphite surface or at its edges could be reduced by heating the carbon rod to 1600 °C under a hydrogen stream. However, such temperature cannot be achieved and was above the limit of the furnace used for the pyrolysis of the carbon monoliths. Also, the residual iron particles were embedded in the graphite strips and the superficial iron carbide cannot be removed by acid washing and may remain on the graphite surface, causing these minor peaks in the EDX spectrum.

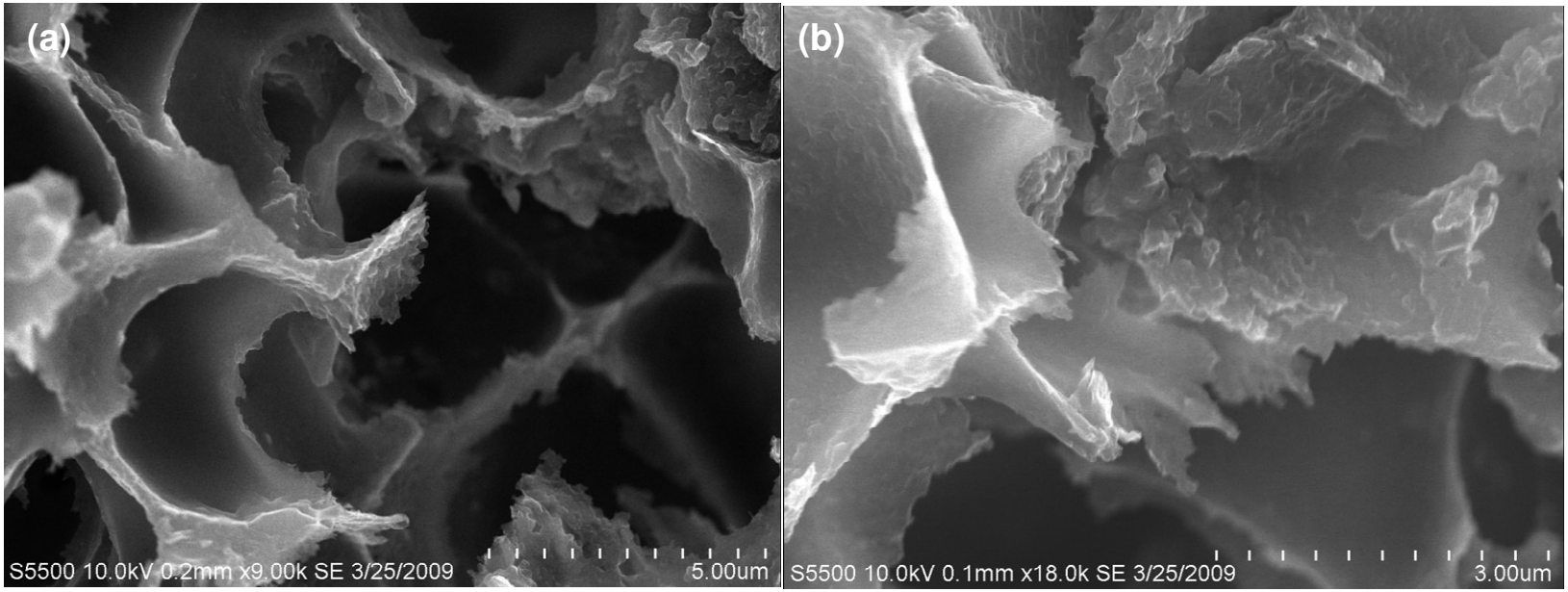

Figure 3.24. HR-SEM image of the meso-porous carbon monolith (5 µm pore diameter) following attempted modification with gold nano-particles (5 nm particle size), (a) at magnification 9 k. (b) at magnificati

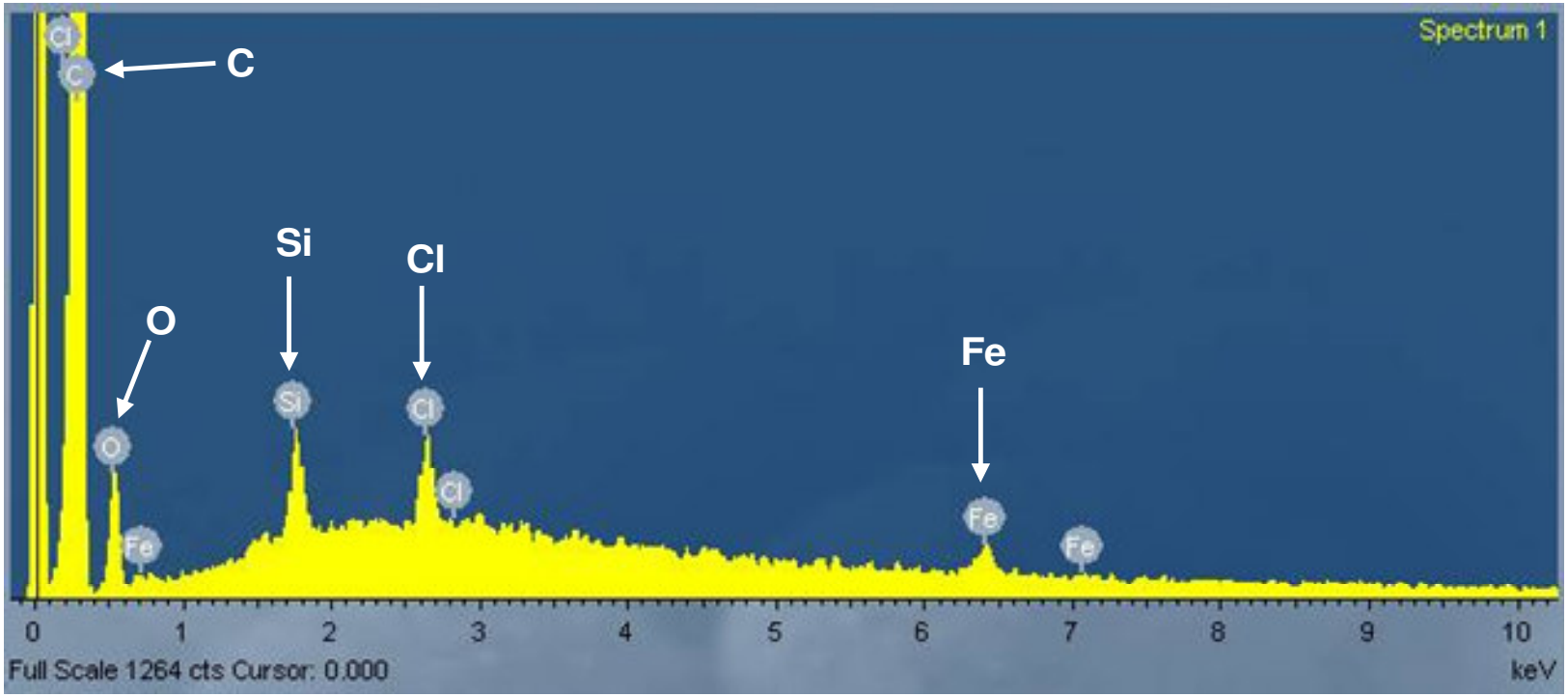

Figure 3.25. The results of EDX analysis of the carbon monolith (5 µm pore diameter) following attempted modification with gold nanoparticles (5 nm particle size) prepared by immersion in colloid gold suspension for 48 h.

The EDX data of the carbon monolith (5 µm pore diameter) modified with gold nano-particles (5 nm particle size) is shown in Table 3.10.

Table 3.10. The results of EDX for the carbon monolith (5 µm pore diameter) modified with gold nano-particles (5 nm particle size).

Element : Carbon ratio	**Au5**
Au : C	0 : 1
O : C	0.1 : 1
Si : C	0.01 : 1
Cl : C	0.01 : 1
Fe : C	0.01 : 1

Table 3.11 shows a metal:carbon ratio of the metal/carbon composite monoliths. The gold:carbon ratio of **IM5** prepared by immersion technique was slightly higher than that of **RC5** prepared by re-circulating technique. Also **IM5** showed significant gold content compared to that of **P1** to **P10** as the gold paint used for the formation of **P1 to P10** contains only 12 % gold compared with 100 % gold chloride was used for the formation of **IM5** and **RC5**. In addition, the gold:carbon ratio of **IM5** is significantly higher than that of silver:carbon ratio of **S10,** both prepared by immersion technique indicating that the reduction of the gold particles on the surface of the carbon monolith was higher than that of silver particles. Finally the gold:carbon ratio shows no gold as the reduction process did not take place as mentioned earlier in Section 3.3.6.

Table 3. 11. Element : Carbon ratio of the metal/carbon composite monoliths.

Metal/carbon composite monolith	Au:C	Ag:C
IM5	1.3 : 1	N/A
RC5	0.2 : 1	N/A
P1	0.5 : 1	N/A
P2	0.3 : 1	N/A
P5	0.3 : 1	N/A
P10	0.4 : 1	N/A
S10	N/A	0.76 : 1
Au5	0 : 1	N/A

3.3.6.1. The UV analysis of gold nano-particle colloid solution

The gold nano-particle suspensions (colloidal gold, 5 nm particle size) were scanned by UV before and after modifying the carbon monolith. The absorbance of the colloidal gold suspension was 1.028 at λ_{max} 520 nm (Figure 3.26 (a)). The effluent after modification was collected and analysed by UV as well. The absorbance of this suspension was 0.842 at λ_{max} 530 nm (Figure 3.26 (b)). Little change in absorption shows no sign of significant gold removal and the colour of the suspension after the modification remained the same, which indicates that adsorption of the gold nano-particles did not take place on the surface of the carbon monolith.

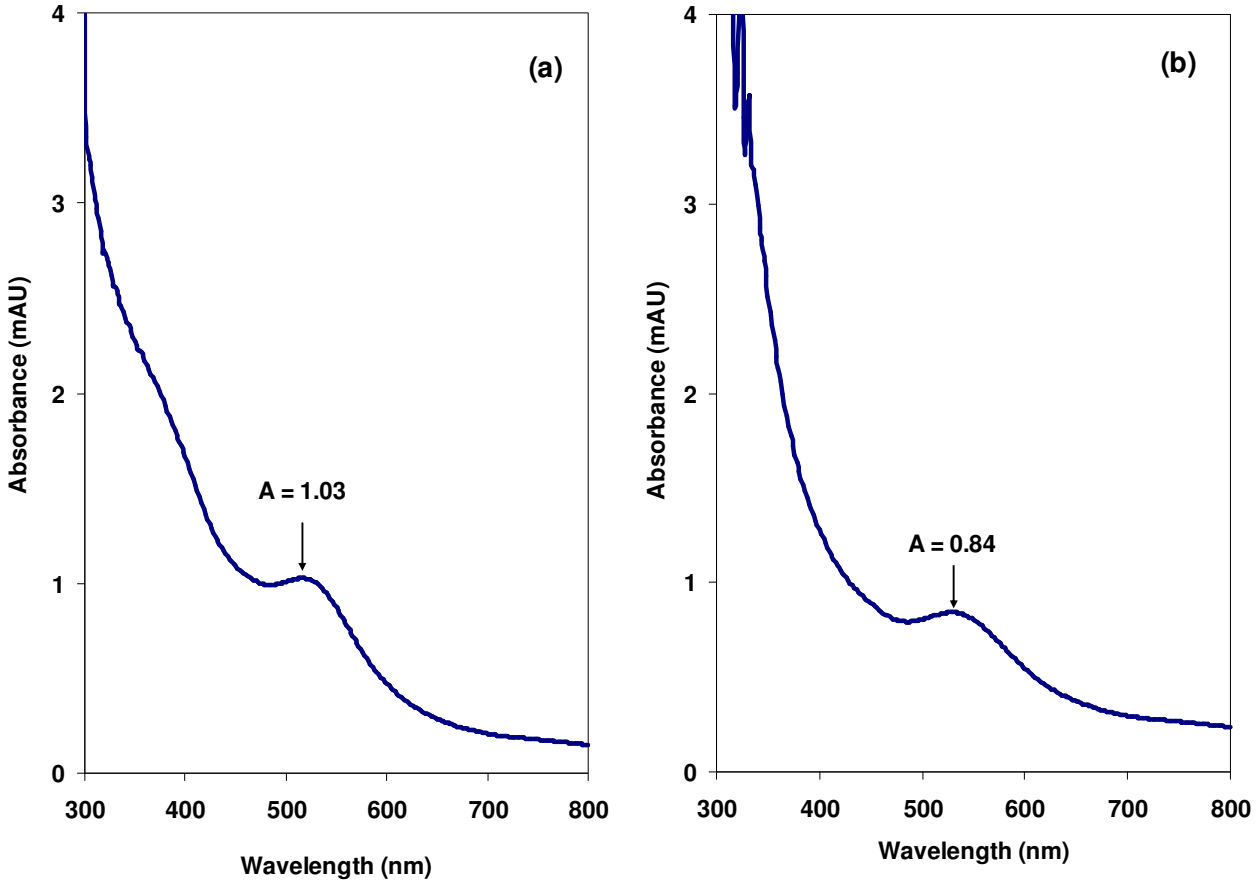

Figure 3.26. The UV spectra of the gold nano-particle colloid suspension (5 nm particle size) (a) before, and (b) after modifying the carbon monolithic rod (5 µm pore diameter).

3.4. Conclusions

Unique carbon/gold and carbon/silver composite monoliths were successfully prepared by different procedures and characterised using various techniques. The modification procedure by direct immersion technique was the best in regard to the amount of gold nano/micro-particles on the modified carbon monolith. Modification of the carbon/gold nano/micro-particles composite monolith with mercaptohexanoic acid was achieved and was later used for simple ion exchange characterisation (see Chapter 4). Conductivity of the prepared carbon/gold composite monoliths was tested. The electrical conductivities of the 5 μm modified carbon/gold composite monoliths, **IM5** and **P5**, were 272 and 243 (S/m), respectively, higher than that of unmodified carbon monoliths (5 μm) 161. These results showed that these composite materials can be potentially used as electrodes in electrochemistry. Silver particles effectively reduced on the surface of the 10 μm templated carbon monolith. The resultant carbon/silver composite monolith was characterised using SEM and EDX analysis for silver particles contents.

References

1. G. Hua, Y. Ma, Y. Guo, S. Shao, *Electrochim. Acta*, 53 (2008) 6610.
2. Q. Dai, X. Liu , J. Coutts, L. Austin, Q. Huo, *J Am Chem Soc.*,130(26) (2008) 8138..
3. D. D. Evanoff, G. Chumanov, *ChemPhysChem*, 6 (2005) 1221.
4. M. Haruta, *J. Nanopart. Res*., 5 (2003) 3.
5. M. C. Daniel, D. Astruc, *Chem. Rev.,* 104 (2004), 293.
6. D. Austruc, F. Lu, J. R. Aranzaes, *Angew. Chem. Int. Ed*., 44 (2005) 7852.
7. E. Katz, I. Willner, *Angew. Chem. Int. Ed*., 43 (2004), 6042.
8. J. H. Fendler, Editor, *Nanopart. and Nanostr. Films*, Wiley-VCH, Weinheim (1998).
9. J. Liu, R. Xu, A. E. Kaifer, *Langmuir*, 14 (1998) 7337.
10. N. A. F. Al-Rawashdeh, M. L. Sandrock, C. J. Seugling, C. Foss, *J. Phys. Chem., B,* 102 (1998) 361.
11. T. Vossmeyer, B. Guse, I. Besnard, R. E. Bauer, K. Mullen, A. Yasuda, *Adv. Mater.,* 14 (2002) 238.
12. M. Brust, J. Fink, D. Bethell, D. J. Schiffrin, C. Kiely, *J. Chem. Soc., Chem. Commun.,* (1995) 1655.
13. M. Brust, D. Bethell, C. Kiely, D. J. Schiffrin, *Langmuir,* 14 (1998) 5425.
14. A. C. Templeton, W. P. Wuelfing, R. W. Murray, *Acc. Chem. Res.,* 33 (2000) 27.
15. H. Yang, T. Lu, K. Xue, S. Sun, S. Chen, *J. Appl. Electrochem.*, 27 (1997) 428.
16. H. Yang, T. Lu, K. Xue, S. Sun, G. Lu, S. Chen, *J. Mol. Catal., A*, 144 (1999) 315.
17. B. Neiman, E. Grushka, O. Lev, *Anal. Chem.,* 73 (2001) 5220.
18. J. D. Sunderhaus, B. Steinbock, O. Steinbock, *Abstr. Pap. Am. Chem. Soc*. 2002, *223*, 360-PHYS Part 2.
19. P. Viberg, M. Jornten-Karlsson, P. Petersson, P. Spegel, S. Nilsson, *Anal. Chem.*, 74 (2002) 4595.
20. G. M. Gross, D. A. Nelson, J. W. Grate, R. E. Synovec, *Anal. Chem.*, 75 (2003) 4558.
21. G. M. Gross, J. W. Grate, R. E. Synovec*, J. Chromatogr., A,* 1029 (2004) 185.
22. A. Dekanski, J. Stevanovi, R. Stevanovi, V. M. Jovanovi, *Carbon*, 39 (2001) 1207.

23. http://www.malvern.com. Accessed 11 May, 2009.
24. Q. Huo, J. G. Worden, *J. Nano. Res.*, 9 (2007) 1013.
25. N. Marinkovic , A. Dekanski, Z. Lausevic, B. Vucurovic , M. Lausevic, J. Stevanovic, *Vacuum*, 40 (1990) 95.
26 A. Dekanski, N.S. Marinkovic, J. Stevanovic, V.M. Jovanovic, Z. Lausevic and M. Lausevic. *Vacuum*, 41 (1990) 1772.
27. M. Hostetler, J. Wingate, C. Zhong, J. Harris, R. Vachet, M. Clark, J. Londono, S. Green, J. Stokes, G. Wignall, G. Glish, M. Porter, N. Evans, R. Murray, *Langmuir,* 14 (1998) 17.
28. M. Brust, M. Walker, D. Bethell, D. J. Schiffrin, R. Whyman, *J. Chem. Soc., Chem. Commun.*, (1994) 801.
29. D. Walsh, L. Arcelli, T. Ikoma, J. Tanaka, S. Mann, *Nat. Mater.,* 2 (2003) 386.
30. C. Liang, S. Dai, G. Guiochon, *Anal. Chem*., 75 (2003) 4904.
31. B. M. Barykin, E. G. Spiridonov, A. S. Tarabanov, *Khim. Tverdogo Topliva (USSR)*, 2 (1967) 116.
32. Handbook of the electrochemistry, Cynthia G. Zoski, First edition, Elsvier publications, Oxford, UK, 2007.

CHAPTER FOUR

Chromatographic Evaluation of Porous Carbon Monolithic Columns

4.1. Introduction

Chromatographic columns packed with porous particle type silica, alumina, titania and zirconia particles are well studied and widely used [1]. Therefore, a number of studies devoted to the preparation of monoliths based on these materials have been published. Fewer attempts involving the preparation of monolithic columns based on different porous oxides, particularly aluminum oxide, titanium oxide, zirconium oxide, and also carbon have been reported [2-5]. However, the development of monolithic columns prepared using porous carbon has been attempted, with however only limited success, as these materials contained micro-pores, which provide low surface area and as a result show a poor LC performance [6].

Both Taguchi *et al.,* [7] and Liang *et al.,* [5] reported attempts to prepare and apply carbon monolithic columns to chromatographic separations. In both cases, the procedure, suggested by Knox [8] for the preparation of porous graphitised carbon particles for HPLC was used, and the prepared monoliths exhibited a hierarchical, fully interconnected porosity. The same approach was used by Chirica and Remcho for the preparation of polymeric monolithic columns [9]. In this procedure, high quality meso-porous silica particles for HPLC were impregnated with a carbon precursor that was pyrolysed under a neutral atmosphere. The silica was then dissolved in hydrofluoric acid and the carbon was graphitised at high temperature. Taguchi *et al.,* [7] used a silica monolith that he had prepared using the procedure described by Ishizuka *et al.,* [10] and impregnated it with furfuryl alcohol, which was then polymerised at 90 °C for 15 h and reimpregnated. The material was then carbonised at 800 °C for 5 h then immersed in a 9% HF solution for 6 h. The SEM images showed that the carbon monolith was a replica of the silica monolith. However, these monolithic carbons have a very high specific surface area (1115 m^2/g)

and pore volume (1.27 cm^3/g) made up of uniform meso-pores. They can be used in a wide range of applications such as the separation or adsorption of large molecules (i.e. immobilisation of enzymes).

Liang *et al.,* [5] used a different approach, in which 10 μm silica particles were suspended in water/ethanol mixture to which $FeCl_3$ and resorcinol were added, followed by formaldehyde. The solution polymerised into a solid rod that was dried, then aged and carbonised at 800 °C then at 1250 °C, after it was cooled and immersed in concentrated HF solution to dissolve silica beads and iron catalyst. The rod was clad in a heat-shrinkable Teflon tubing and glued into a stainless steel tube. It was shown that the average throughpore diameter was approximately 7.5 μm but the efficiency (*N*) was poor, with a minimum value of the height equivalent to the theoretical plate (HETP) of 72 μm. The carbon surface was found to be non-polar but it had a much higher energy than that of the C_{18} bonded particles. The surface of the carbon material was composed of micro-pores which have negative adsorption properties such as band broadening and tailing on chromatographic peaks and thus exhibited poor LC performance unless graphitised at ~ 2400 ^oC [5]. The oven needed for the graphitisation is an uncommon piece of equipment and, therefore, researchers have not yet been able to prepare a highly efficient carbon rod [5].

In this Chapter, the monolithic carbon-based columns previously produced in this study were evaluated chromatographically. The carbon rods were clad as monolithic columns for use in HPLC, using a variety of methods to ensure elimination of all column housing voids and to enable chromatographic evaluation. These columns were checked with a series of alkylbenzene and aromatic compounds under both normal-phase (NP) and reversed-phase (RP) conditions. Finally, surface modified carbon rods with gold nano/micro-particles, were also evaluated chromatographically for solute retention.

4.2. Experimental:

4.2.1. Chemicals

All solvents used including hexane, pentane, acetonitrile, methanol and isopropanol were HPLC grade and were obtained from Labscan (Dublin, Ireland). Toluene (99.9%), ethylbenzene (99.9+%), butylbenzene (99.9%), acetophenone, nitrobenzene, sulphuric acid (95-98 %), nitric acid (90%), benzoic acid (99.5%),

caffeine (99%), theophylline (99%), tetrachloroauric acid, imidazole (99%), resorcinol (99%) and histidine (99%) were obtained from Sigma-Aldrich (Gillingham, UK). Reagent water was obtained from a Millipore Milli-Q water purification unit (Millipore, Bedford, MA, USA) and was 18.2 MΩ. All chemicals were used as received from the manufacturers.

4.2.2. Instrumentation

For chromatographic characterisation of the carbon monolithic columns, LC was carried out on two systems. The first system was a SpectraSYSTEM HPLC system, comprising of a high pressure pump Model P4000, vacuum degasser Model SCM 1000, UV detector Model UV 2000 (AH Thermo Separations, San Jose, CA, USA) and a high pressure Rheodyne 7125 injector with a 20 µL sample loop (Rheodyne, Rohnert Park, CA, USA). For data acquisition, a Dell Optiplex GX-1 personal computer was used with ADC-16 High Resolution Data Logger, Pico Technology Limited (Cambridgeshire, UK). The second system was an Agilent 1200 series high performance liquid chromatograph, comprising of a vacuum degasser, quaternary pump, ALS autosampler, thermostatted column compartment and UV-Vis detector. Data analysis was performed using Agilent Chemstation software, version B.02.01 (Agilent Technologies, USA).

4.2.3. Chromatographic characterisation

Carbon monolithic columns were prepared with different pore size (1, 5 and 10 macro-pores), length 30 and 50 mm (for 5 µm pore size), 73 mm (for 1 µm pore size) and 75 mm (for 10 µm pore size) and cladding techniques (either using - shrinkable PTFE tubing or the rods were completely encased directly within epoxy resin of ~ 0.5 cm thickness). Carbon monolithic rods were then sealed into chromatographic columns and evaluated for flow through porosity and back-pressure profiles and retention selectivity for a range of test solutes. All columns were tested under either RP or NP conditions. The freshly made column was washed with a number of solvents at flow rate of 1 mL/min in the following order: water (2 h), methanol (2 h), isopropanol (2 h) and hexane (2 h). Bare carbon monolithic columns were tested for NP-HPLC through injections of 15-25 µL of model mixtures containing 1-100 µg/mL each of toluene, ethylbenzene, butylbenzene, acetophenone

and nitrobenzene in hexane, with hexane as the mobile phase delivered at 0.7-1 mL/min depending on column parameters, with UV detection performed between 254-270 nm.

The gold and 6-mercaptohexanoic acid modified carbon monoliths were washed by flushing Milli-Q water at 1 mL/min and tested for ion exchange capacity by injection of 10 µL of 1-500 µg/mL solutions of imidazole and resorcinol in 1 m*M* sodium acetate, with photometric detection at 211-280 nm. 1 m*M* sodium acetate/acetic acid buffer solution was used as the eluent at 1 mL/min flow-rate. The net pressure drop over the columns was approximately 21-24 bar.

4.3. Results and discussion

Column LC can provide important information on the quality and properties of the prepared carbon monoliths. Firstly, the right peak shape or elution profile of any retained solute will confirm the absence of cracks or significant internal cavities within the monolithic rod and reflect the uniformity of the porous structures. Secondly, the recording of backpressure at the top of the carbon monolith column provides information on the permeability of the material and the interconnectivity of the pores within the monolith. Low column backpressure allows for the use of high flow rates, thus, faster separation. Lastly, the evaluation of selectivity and retention of model substances can provide information on adsorption properties of the surface of the bare monoliths.

4.3.1. Templated porous carbon monolithic columns

4.3.1.1. Chromatographic evaluation of 5 µm templated carbon monolithic column

The porous glassy carbon monolithic rod with 5 µm macro-pore diameter, 7 nm nano-pore diameter and surface area of 85 m^2/g was clad with heat shrinkable Teflon, followed by glueing and packing into a 50 x 6.0 mm i.d. PEEK column (Figure 4.1) (see Section 2.2.3.3, Chapter 2).

Usually, hydrophobic analytes have strong adsorption on graphite under RP conditions, so, it was assumed a high concentration of a typical RP organic solvent would be required for their elution from the carbon monolithic columns in this work.

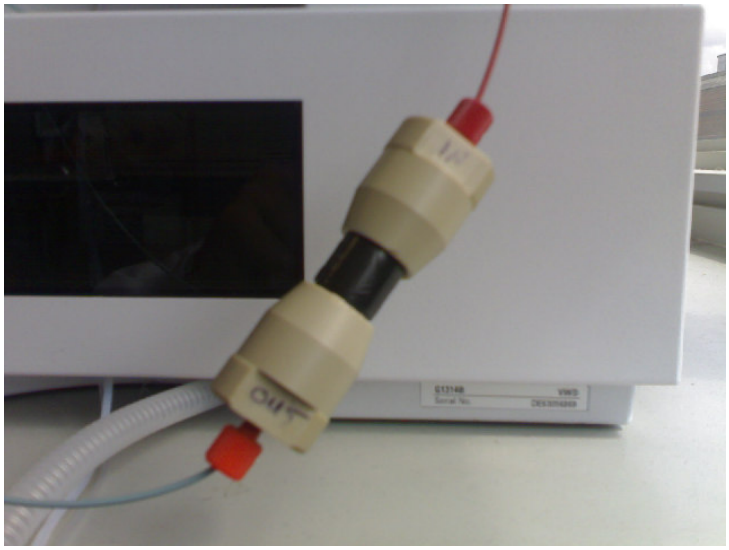

Figure 4.1. Typical 5 µm templated glassy carbon monolithic rod (50 x 6 mm i.d.) housed in PEEK tubing.

In RP-HPLC mode, pure methanol and acetonitrile were initially used, while in NP-HPLC mode, hexane and pentane were utilised as the mobile phases for evaluation of the adsorption properties of carbon monolithic columns. Chlorinated solvents were not used as the prepared columns were clad with heat shrinkable Teflon, which is chemically not stable in solvents such as dichloromethane or chloroform. Alkylbenzenes, such as toluene, ethylbenzene and butylbenzene and a number of polar aromatic compounds such as caffeine, theophylline, benzoic acid, acetophenone and nitrobenzene were selected as model compounds for the evaluation of the adsorption properties of carbon monolithic columns.

4.3.1.2. RP-HPLC on 5 µm templated carbon monolithic column

Toluene, ethylbenzene and butylbenzene were introduced in series onto the prepared column (glassy carbon monolith, 50 x 6 mm i.d., 5 µm pore size). Methanol (100%) was used as the mobile phase, the flow rate was 1 mL/min, UV detection was performed at 270 nm, and the column backpressure was 2 bar. The concentration of samples was 500 µg/mL.

However, no retention of these analytes was observed under these conditions and elution time for all alkylbenzenes studied was 0.47 min. corresponding to the void volume of 0.47 mL. Overlaid chromatograms are shown in Figure 4.2.

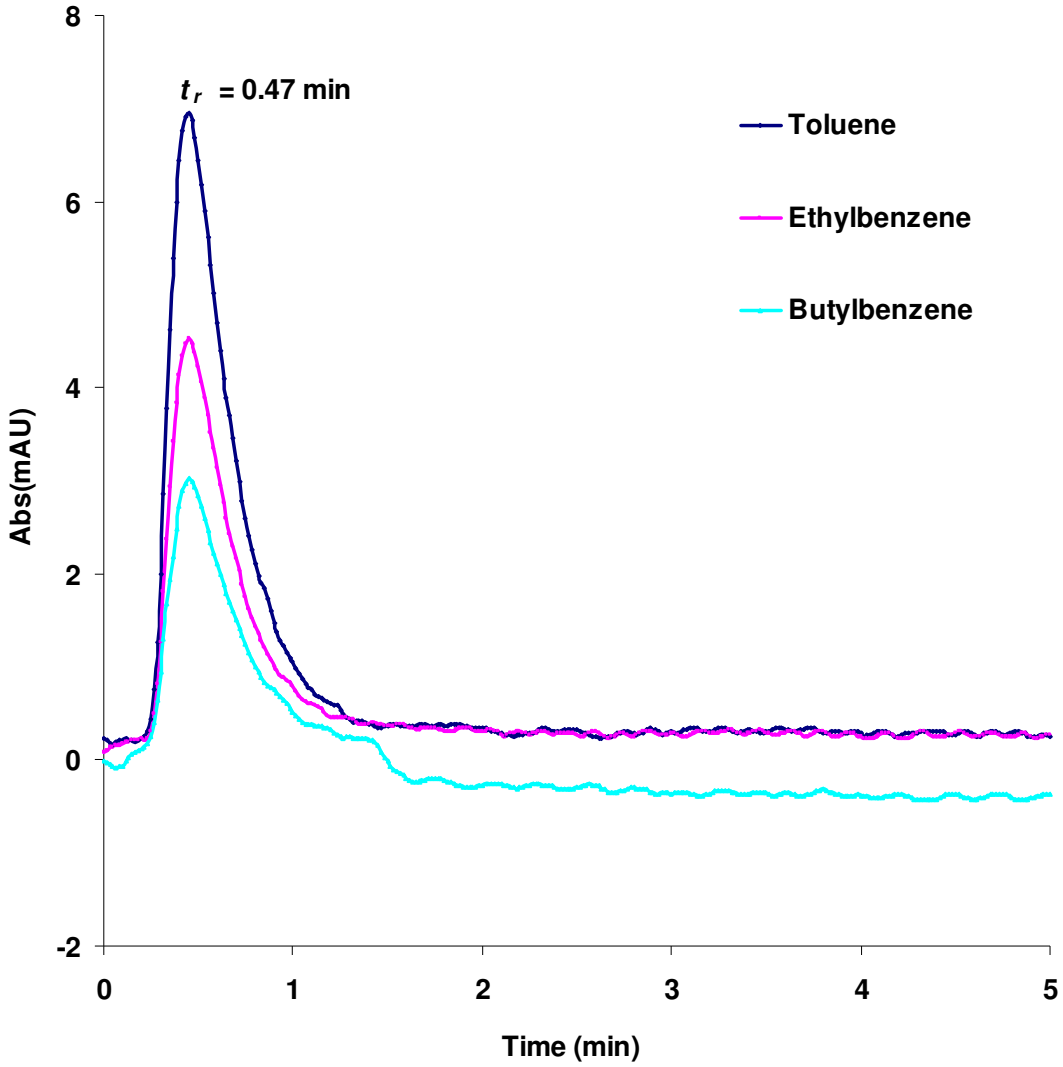

Figure 4.2. Overlaid chromatograms of toluene, ethylbenzene and butylbenzene (500 µg/mL standard concentration). Column: glassy carbon monolith 5 µm pore size (50 x 6 mm i.d.). Mobile phase: 100% methanol, flow rate: 1.0 mL/min and UV detection: 270 nm.

Using the same column and 100% acetonitrile as the mobile phase, the retention of toluene was studied, but still no significant retention was observed. The chromatogram is shown in Figure 4.3.

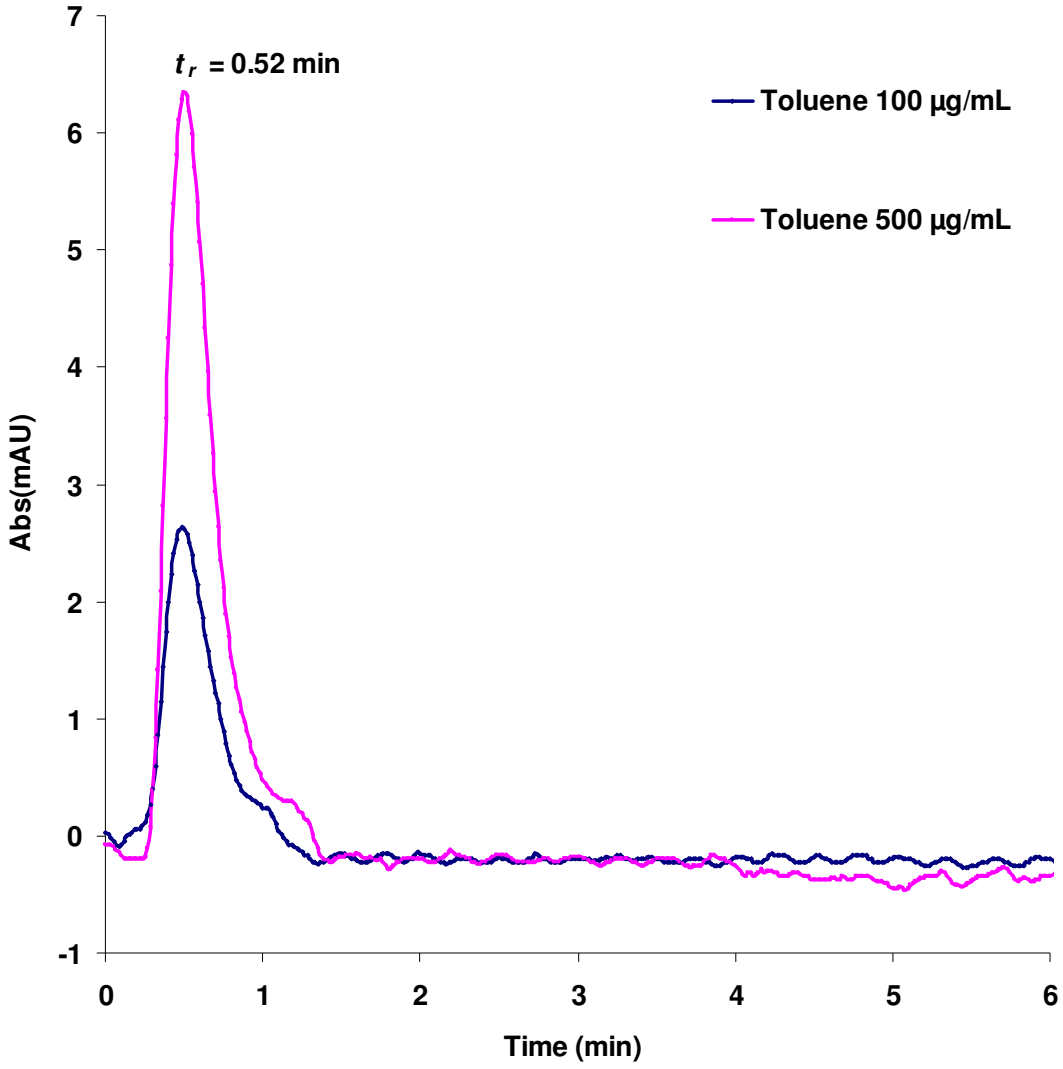

Figure 4.3. Chromatograms of toluene (500 µg/mL and 100 µg/mL standard concentration). Column: glassy carbon monolith, 5 µm pore size (50 x 6 mm i.d.). Mobile phase: 100% acetonitrile, flow rate: 1.0 mL/min and UV detection: 270 nm.

As mentioned earlier, high concentrations of organic solvents should be used for hydrophobic analytes on graphite as they exhibit strong adsorption. However, in this work on the predominantly glassy carbon surface, the tests showed the opposite and no retention or very poor retention were observed. Therefore, weaker mobile phases were used instead of 100% methanol and acetonitrile. Methanol-water mixtures were used, ranging from 100% down to 20%, and toluene injected onto the column (glassy carbon monolith, 50 x 6 mm i.d., 5 µm pore size). Flow rate was 1

mL/min, UV detection was performed at 270 nm, and the column backpressure was between 3-5 bar. The concentration of sample was 100 µg/mL.

However, once again no retention for this analyte was observed under any of the mobile phase conditions investigated. Therefore, RP-HPLC tests for hydrophobic molecules (alkylbenzenes) showed no retention on the glassy carbon monolithic column. The same was seen for hydrophilic molecules. For example, caffeine, theophylline and benzoic acid were also introduced onto the column in RP-mode using various concentrations of acetonitrile as a mobile phase, and no retention was observed. Thus, the prepared glassy carbon monolithic columns were not suitable as stationary phases in RP-HPLC mode. This was possibly due to the very low surface area and short dimensions of the monoliths and because of this they simply had insufficient surface hydrophobicity and capacity to show retention under RP conditions. A typical surface area of an alternative commercial silica RP monolith was calculated to be 300 m^2/g using Brunauer–Emmett–Teller (BET) method [11].

In addition, the IR spectrum of the carbon monolith indicated that the prepared glassy carbon monolithic columns may not be suitable as stationary phases in RP-HPLC mode. Figure 2.38, Chapter 2 showed clearly the presence of polar groups such as carbonyl and hydroxyl groups.

4.3.1.3. NP-HPLC on 5 µm templated carbon monolithic column

As it was shown that there was no retention for either polar or hydrophobic compounds in RP-mode, it was necessary to test the prepared column in NP-mode. Under NP-HPLC conditions the columns showed some retention for both polar and non-polar compounds. In NP chromatography, the mobile phase consists of a very nonpolar solvent like hexane or heptane, mixed with a slightly more polar solvent like isopropanol, ethyl acetate or chloroform. Retention increases as the amount of nonpolar solvent in the mobile phase increases. Chromatograms of toluene, ethylbenzene, butylbenzene (1 µg/mL) and alkylbenzene on the glassy carbon monolithic column (50 x 6 mm i.d., 5 µm pore diameter) are shown in Figures 4.4, 4.5, 4.6 and 4.7, respectively. Hexane was used as the mobile phase, the flow rate was 0.7 mL/min, UV detection was performed at 270 nm, and the column backpressure was 2 bar. Retention times were 2.10 min (toluene), 2.95 min (ethylbenzene), and 2.95 min (butylbenzene).

The retention time (t_r) of the analyte includes, the time the components remain in the actual mobile phase passing through the column and the time the analyte is retained on the stationary phase. Reduced retention time, $t`_r$ is the difference between the total retention time, t_r, and the hold-up time, t_0.
Reduced retention volume $V`_r$. is the difference between the analyte retention volume, V_r, and the void volume, V_o. The ratio of the reduced retention time to the hold-up time is an extensively used dimensionless parameter called retention factor, k, which is independent of the mobile phase, column dimension and flow rate, and allows the analyst to compare columns being used under different conditions.

To describe the selectivity of the glassy carbon monoliths for alkylbenzenes, the retention factor, k was calculated.

$$k = \frac{t_R - t_0}{t_0} \qquad \text{Eq. 4.1}$$

t_r and t_0 are easily obtained from a chromatogram. When an analytes retention factor is less than one, elution is so fast that accurate determination of the retention time is very difficult. High retention factors (greater than 20) mean that elution takes a very long time. Ideally, the retention factor for an analyte is between one and five.

Using equation 4.1, the retention factor, k and a number of other characteristics for toluene, ethylbenzene and butylbenzene were calculated and the results are shown in Table 4.1 and Figures 4.4 - 4.6. In this case the void time was recorded as 0.47 min as mentioned in Section 4.3.1.2.

Table 4.1. Retention, retention factor and efficiency data for a range of alkylbenzenes on 5 μm templated glassy carbon monolithic column (50 x 6 mm i.d.) using a hexane as the mobile phase.

Analyte	*Retention time (t_r) (min)*	*Retention factor (k)*	*Efficiency (N) (per meter)*	*Peak symmetry (A_s)*
Toluene	2.10	3.47	1740	3.8
Ethylbenzene	2.95	5.28	1580	3.13
Butylbenzene	2.95	5.28	3180	3.13

The results on the retention of n-alkylbenzenes (Table 4.1) show similar trends in retention with variation in the length of an alkyl substitute and with the number of substitutes within a molecule.

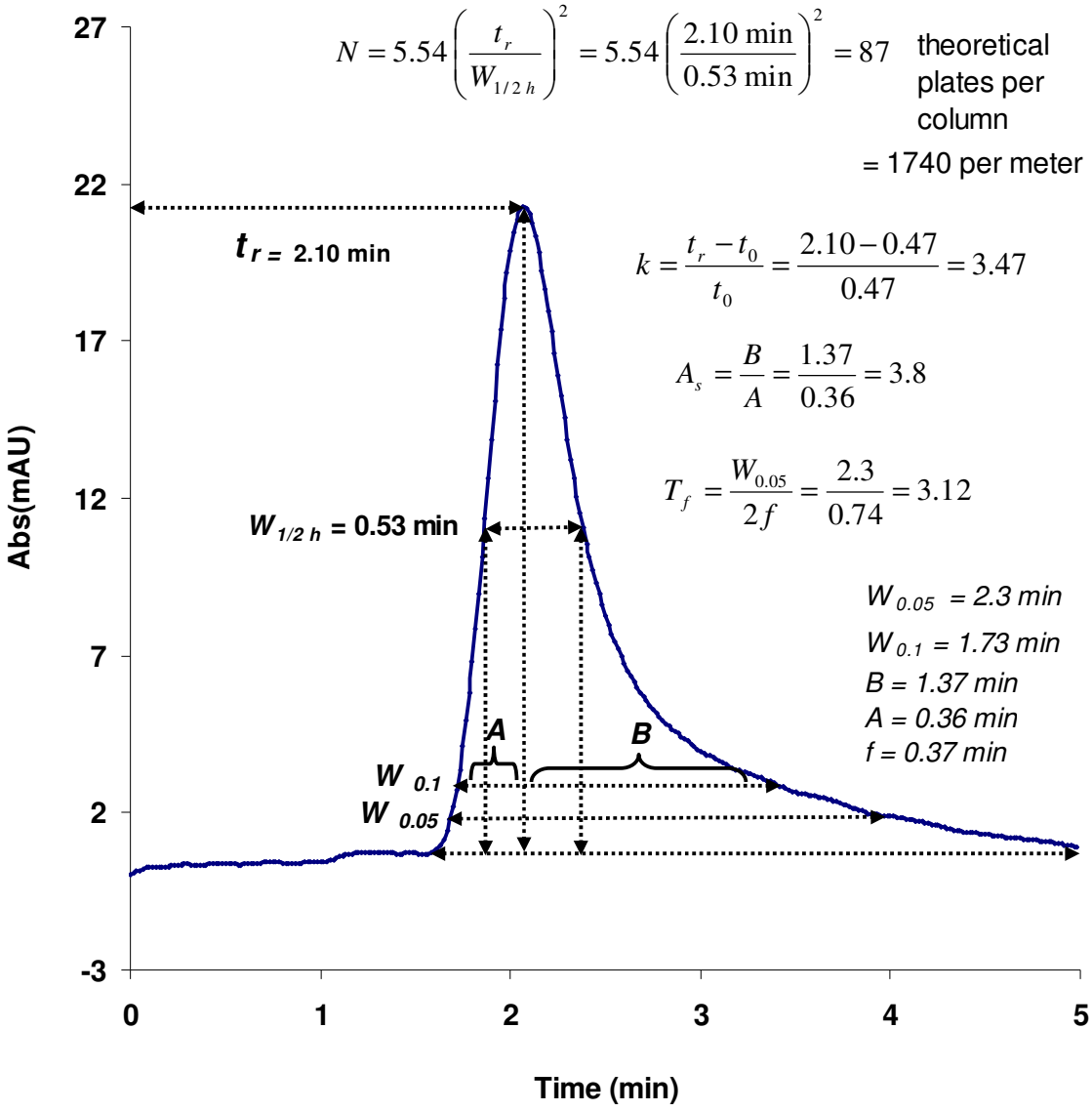

Figure 4.4. Chromatogram of a toluene (1 µg/mL standard concentration). Column: glassy carbon monolith 5 µm pore size. Mobile phase: hexane, flow rate: 0.7 mL/min and UV detection: 270 nm.

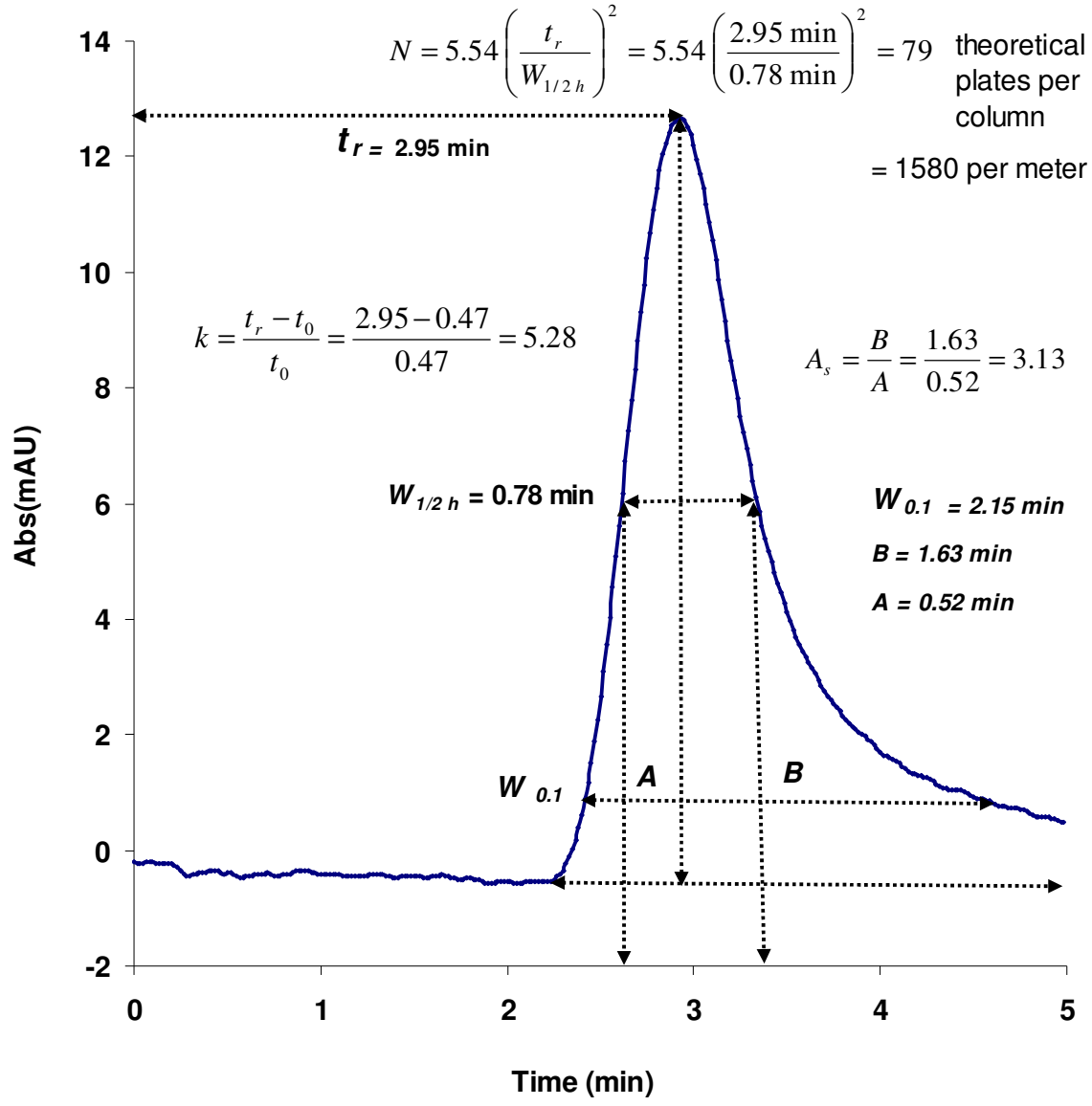

Figure 4.5. Chromatogram of an ethylbenzene (1 µg/mL standard concentration). Column: glassy carbon monolith, 5 µm pore size (50 x 6 mm i.d.). Mobile phase: hexane, flow rate: 0.7 mL/min and UV detection: 270 nm.

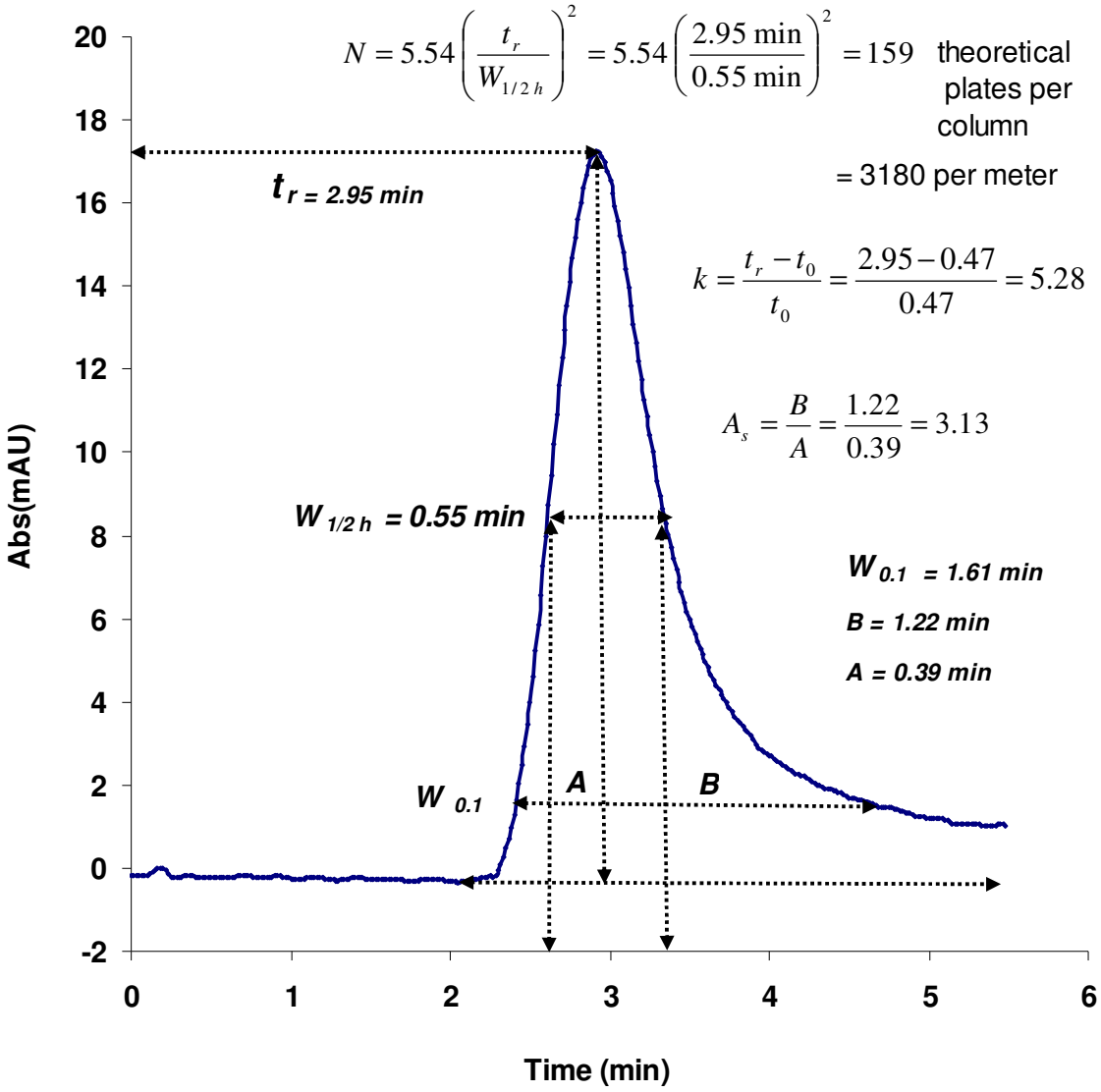

Figure 4.6. Chromatogram of a butylbenzene (1 µg/mL standard concentration). Column: glassy carbon monolith, 5 µm pore size (50 x 6 mm i.d.). Mobile phase: hexane, flow rate: 0.7 mL/min and UV detection: 270 nm.

However, no chromatographic separation was achieved after injecting the toluene, ethylbenzene and butylbenzene as a mixture, as shown in the chromatogram in Figure 4.7. This was probably due to the very limited surface area and capacity of the short monolithic phase. To obtain separations of the above solutes, based upon the observed limited differences in selectivity, a much longer/higher capacity monolithic column would appear to be required.

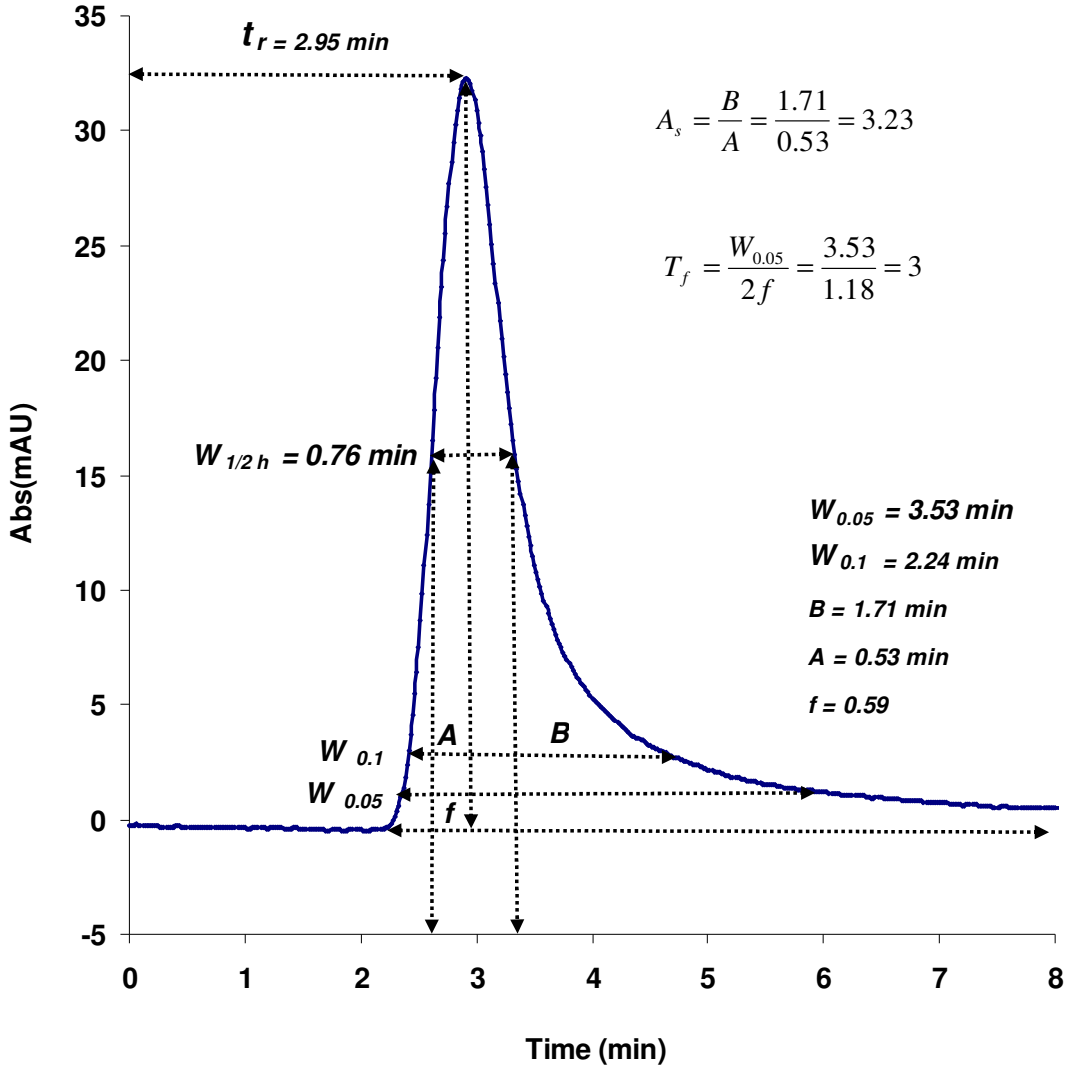

Figure 4.7. Chromatogram of a toluene-ethylbenzene-butylbenzene mixture (1 µg/mL standard concentration). Column: glassy carbon monolith, 5 µm pore size (50 x 6 mm i.d.). Mobile phase: hexane, flow rate: 0.7 mL/min and UV detection: 270 nm.

The results under NP conditions show a slight increase in retention with an increase in the alkyl length between toluene and ethylbenzene, and no retention difference was observed for ethylbenzene and butylbenzene (Figures 4.8 and 4.9). However, this difference in retention was not enough to provide sufficient peak resolution and thus good separation, and efficiency was still very low (Figures 4.4-4.7. Interestingly, the addition of toluene to the alkylbenzene standard mixture, resulted in its increased retention, with only a single peak eluting at 2.95 min. This

effect was shown to be reproducible although the cause of such an effect was not clear. The overlaid chromatograms of a toluene standard and an alkylbenzene mixture (toluene, ethylbenzene and butylbenzene) (1 µg/mL), and of toluene, ethylbenzene and butylbenzene (1 µg/mL), injected separately, on the 5 µm glassy carbon monolithic column (50 x 6 mm i.d.) are presented in Figures 4.8 and 4.9, respectively. Hexane was used as mobile phase, with a flow rate of 0.7 mL/min, and UV detection was performed at 270 nm.

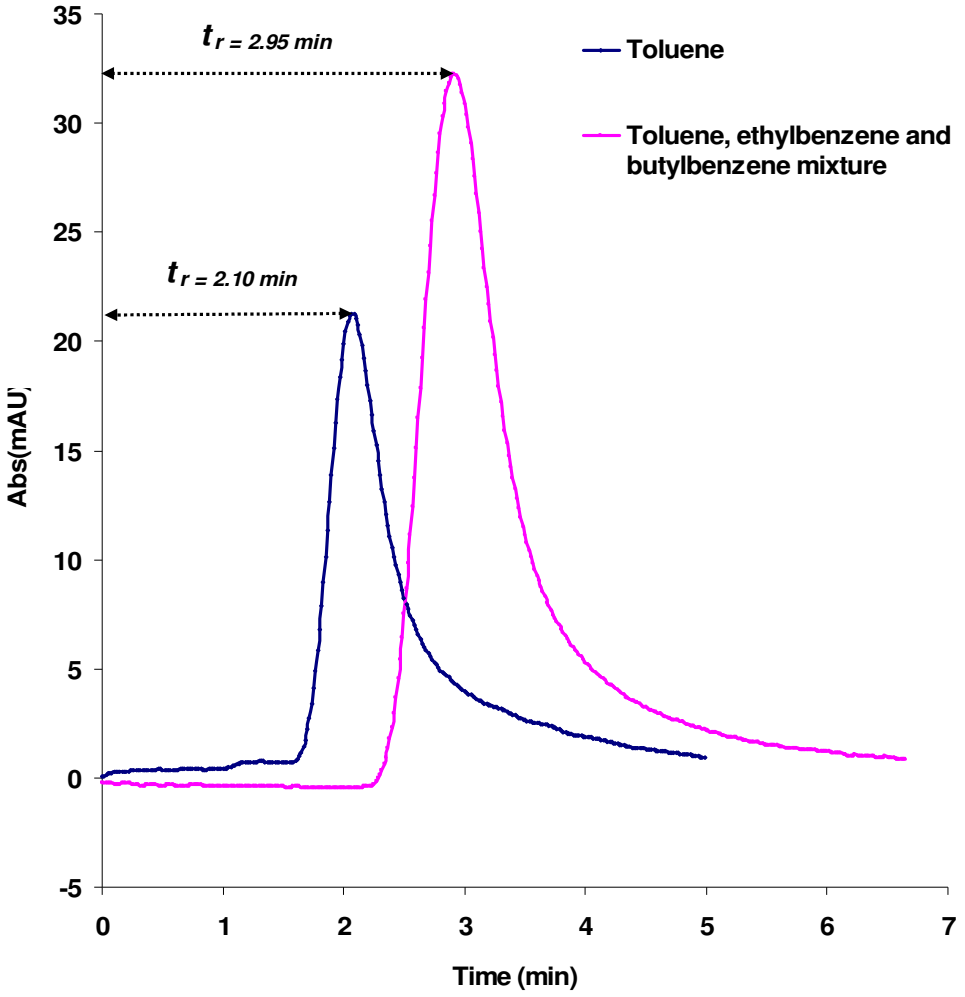

Figure 4.8. Overlaid chromatograms of toluene and alkylbenzenes mixture (1 µg/mL) in hexane on a 5 µm templated glassy carbon monolithic column (50 x 6 mm i.d.) using hexane as mobile phase, flow rate was 0.7 mL/min and UV detection was performed at 270 nm.

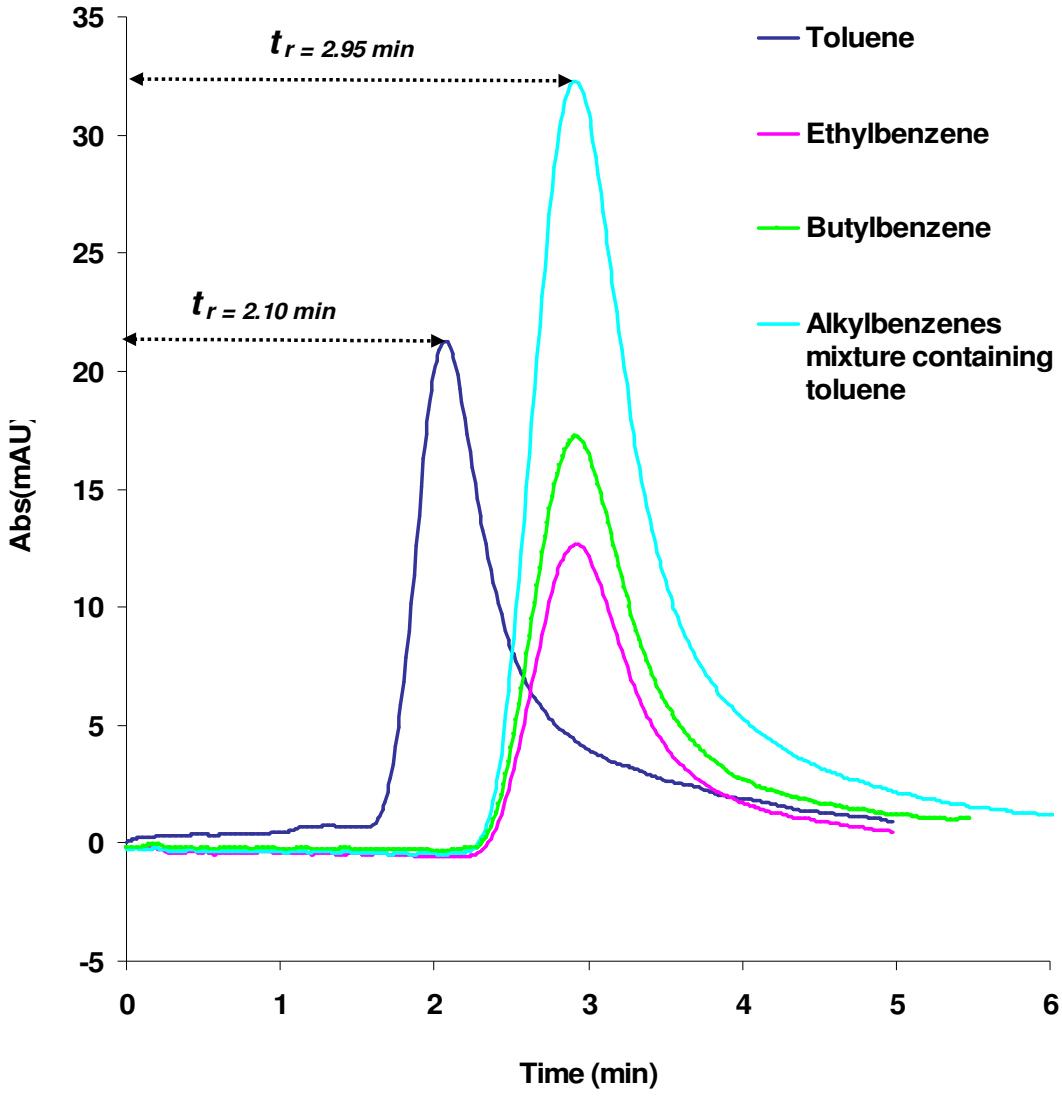

Figure 4.9. Overlaid chromatograms of alkylbenzenes (toluene, ethylbenzene and butylbenzene) (1 µg/mL) in hexane on a 5 µm templated glassy carbon monolithic column (50 x 6 mm i.d.) using hexane as mobile phase, flow rate was 0.7 mL/min and UV detection was performed at 270 nm.

Pentane as an alternative mobile phase (dielectric constant 1.8) was used instead of hexane in an attempt to increase the retention of alkylbenzenes and to increase the resolution. However, similar results were obtained and no separation was achieved, again suggesting that the reason for such low retention was the low surface area and short column length. The elution profile of the alkylbenzenes

mixture on the 5 µm glassy carbon monolithic column (50 x 6 mm i.d.) is shown in Figure 4.10.

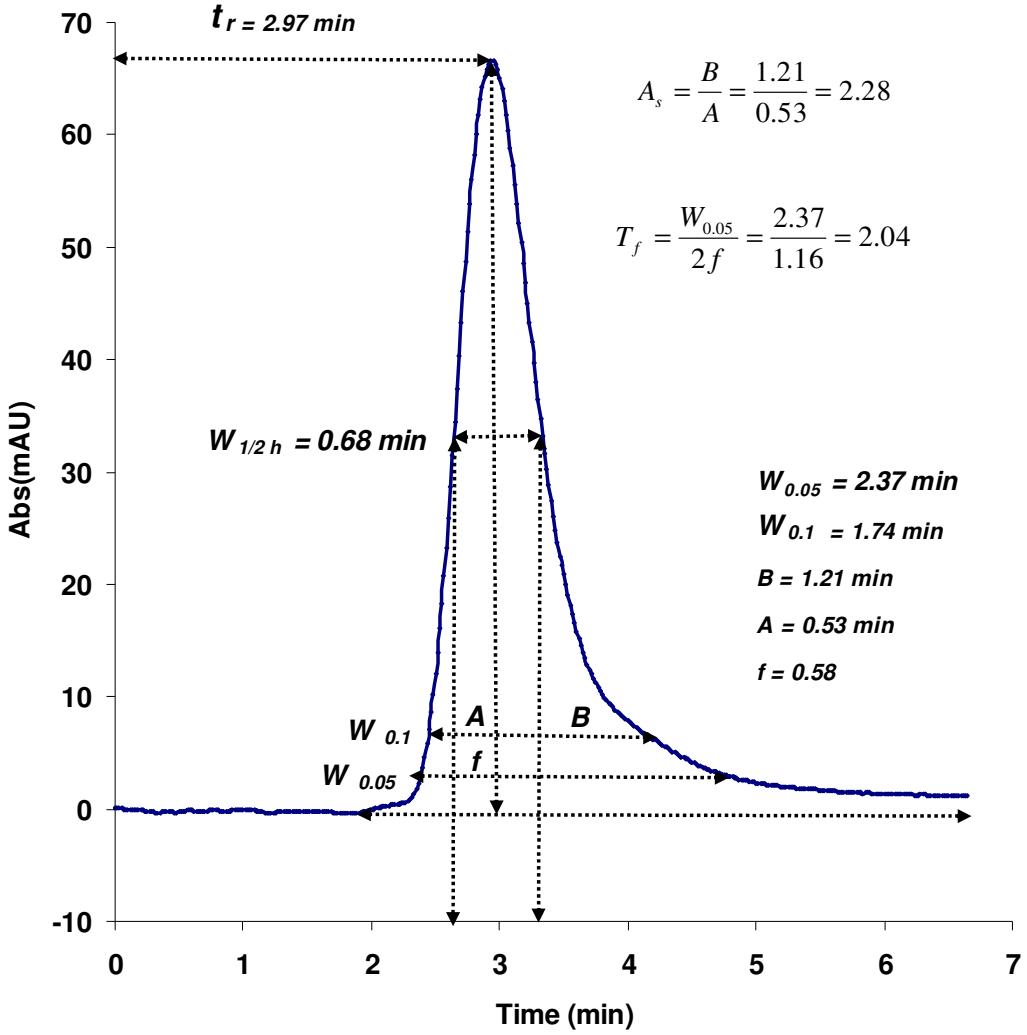

Figure 4.10. Elution profile of alkylbenzenes mixture (1 µg/mL) in pentane on a 5 µm templated glassy carbon monolithic column (50 x 6 mm i.d.) using pentane as mobile phase, flow rate was 0.7 mL/min and UV detection was performed at 270 nm.

Overlaid chromatograms of (1 µg/mL) individual toluene, ethylbenzene and butylbenzene standards on the 5 µm glassy carbon monolithic column (50 x 6 mm i.d.) are shown in Figure 4.11. Pentane was used as mobile phase, with a flow rate of 0.7 mL/min, UV detection was performed at 270 nm, and a column backpressure was

2 bar. Retention times of alkylbenzenes were 3.17 min, 3.20 min and 3.22 min, respectively.

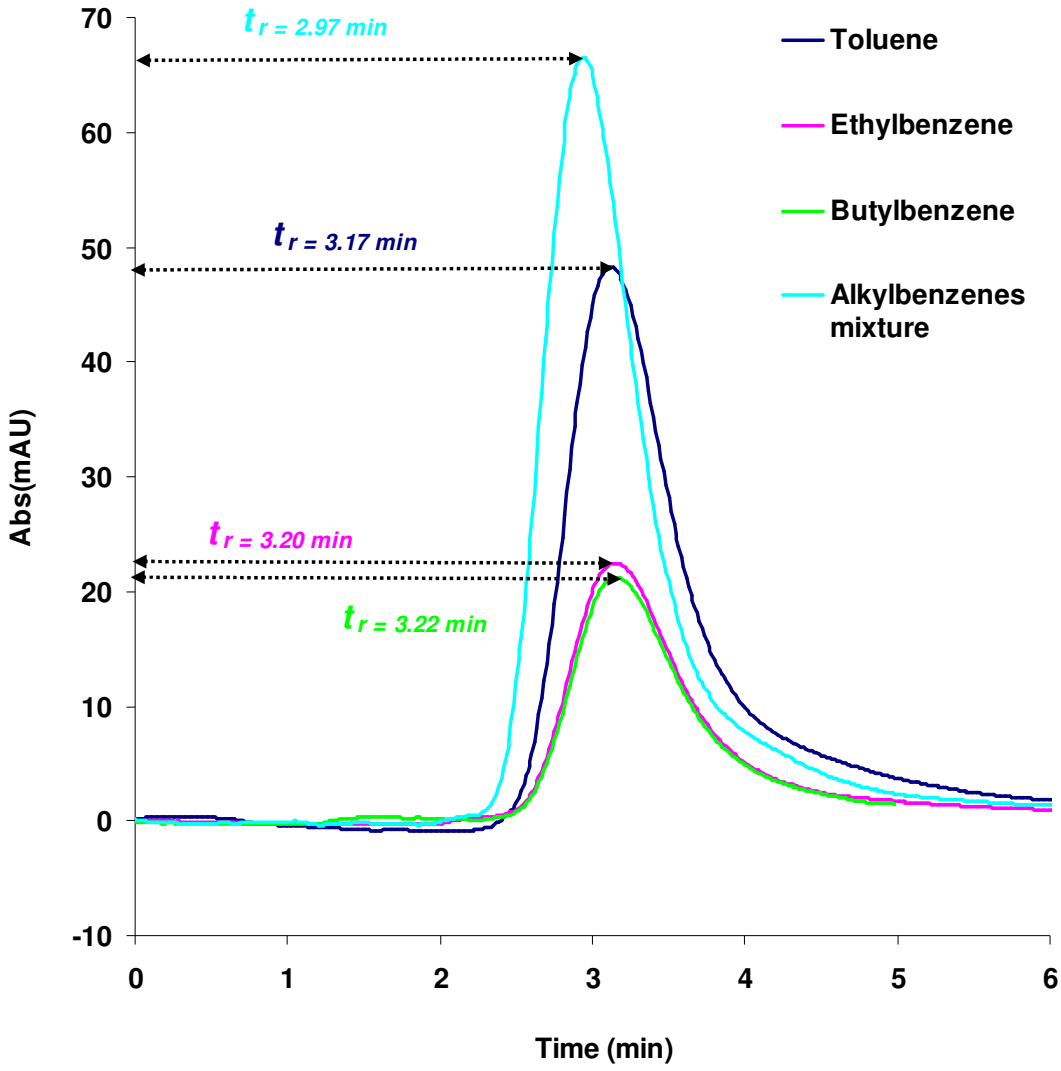

Figure 4.11. Overlaid chromatograms of individual alkylbenzene standards and alkylbenzenes mixture (1 µg/mL) in 100% pentane on a 5 µm templated glassy carbon monolithic column (50 x 6 mm i.d.).

4.3.1.4. Chromatographic evaluation of acid treated carbon monolithic column (5 μm pore diameter), using NP-HPLC

As it was mentioned in Section 4.3.1.3, non-polar compounds (alkylbenzenes) showed only slight retention on the 5 μm templated glassy carbon monolithic columns (50 x 6 mm i.d) under NP-HPLC conditions. Therefore, to try to improve the surface polarity, of the glassy carbon monolith, and thus attempt to increase retention of more polar solutes under NP conditions, similar 5 μm templated monolith (30 x 6 mm i.d.) (Figure 4.12) was conditioned with 0.5 *M* nitric acid for 3 h (see comprehensive surface study in Section 4.3.1.5). The monolith was subsequently flushed with water for 1 h followed by isopropanol for 1 h.

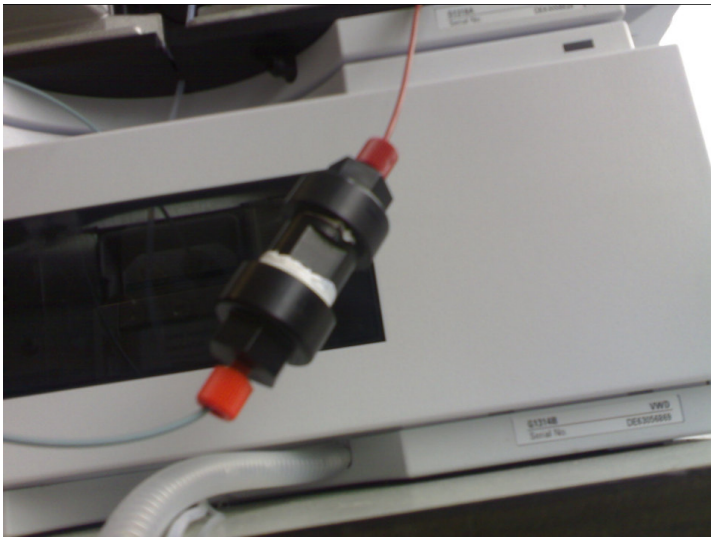

Figure 4.12. Typical 5 μm macro-porous carbon monolithic column (30 x 6 mm i.d).

Figure 4.13 shows the elution profile of butylbenzene using pentane as a mobile phase at a flow rate of 1 mL/min. Only very slight retention of butylbenzene was shown under these conditions, as the retention factor was only 1.05 (the retention time of 0.78 min while the time corresponding to void peak was 0.38 min).

However, partial separation of alkylbenzene could be achieved on the acid washed glassy carbon monolithic column (Figures 4.14 and 4.15). In NP chromatography, the most hydrophobic compounds elute first and the most polar compounds elute last and this is what was observed for the preliminary separation of a mixture of butylbenzene and acetophenone (100 μg/mL) on the short 30 x 6 mm i.d. acid conditioned column.

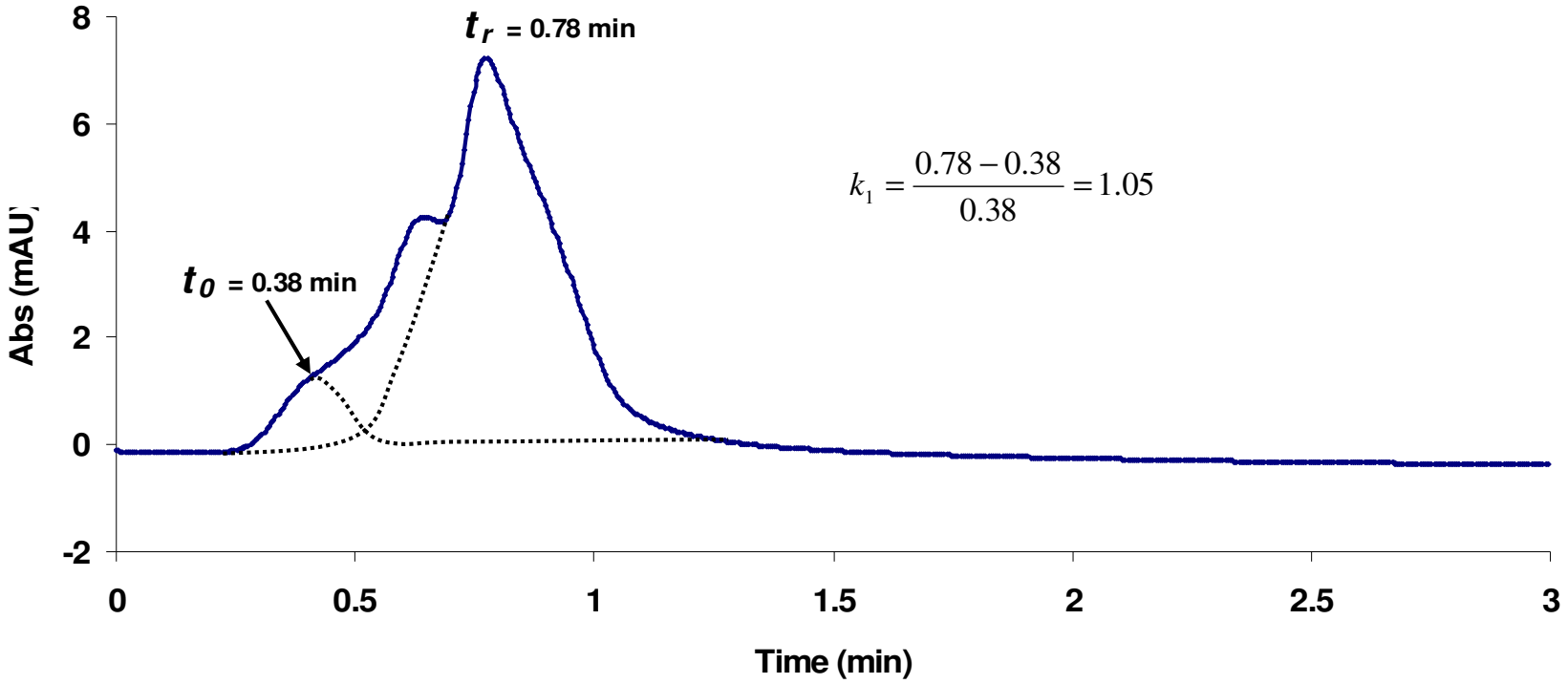

Figure 4.13. Chromatogram of butylbenzene (100 µg/mL) on a 5 µm templated acid washed glassy carbon monolithic column (30 x 6 mm i.d.) using 100% pentane as mobile phase, flow rate was 1 mL/min and UV detection was performed at 254 nm.

The mobile phase used was hexane, at a flow rate of 1 mL/min, with a backpressure of 8 bar, and UV detection was performed at 254 nm, with an injection volume of 15 µL (Figure 4.14).

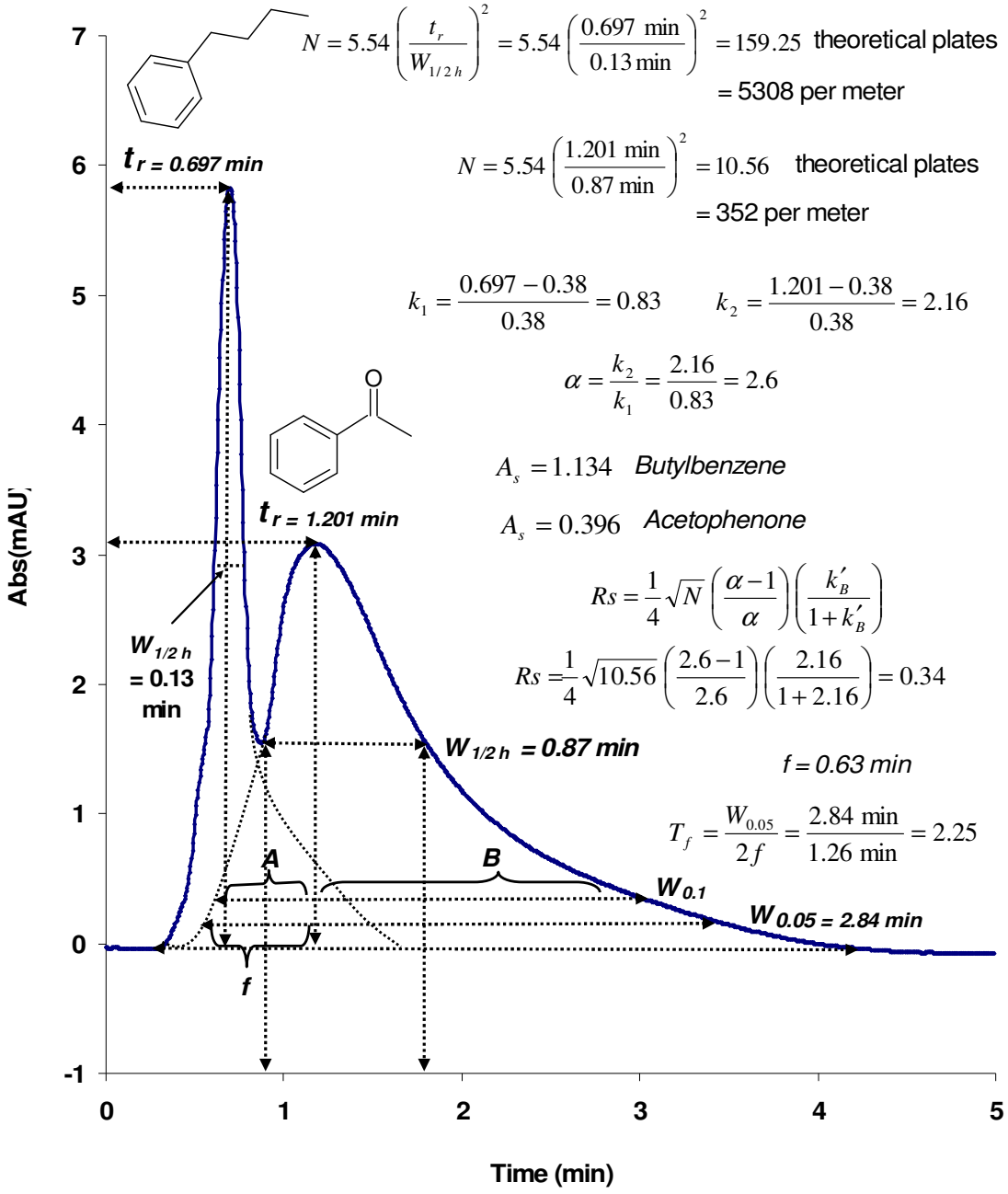

Figure 4.14. Partial separation of butylbenzene and acetophenone (100 µg/mL) in hexane on a 30 x 6 mm i.d. 5µm templated acid washed glassy carbon monolithic column using hexane as mobile phase, flow rate was 1 mL/min and UV detection was performed at 254 nm.

For acetophenone, *k* was calculated as 2.16, indicating that the analyte was significantly retained by the carbon monolith phase. The efficiency of 352 theoretical plates per meter was disappointing. The short length of the column (30 mm) is a significant reason behind the poor efficiency and it should also be noted that the 5 µm pore diameter of the carbon monolith was not small enough to result in a high efficiency column.

Table 4.2. Retention, efficiency, peak symmetry, resolution and selectivity data for butylbenzene and acetophenone on an acid washed templated glassy carbon monolithic column, (30 x 6 mm i.d.), 5 µm pore size.

Analyte	t_r (min)	*k*	*N (per meter)*	A_s (reported)	R_s	α
Butylbenzene	0.697	0.83	5308	1.134		
Acetophenone	1.201	2.16	352	0.396	0.34	2.6

Preliminary separations of mixtures of butylbenzene and nitrobenzene (100 µg/mL) on the above glassy carbon monolithic column (30 x 6 mm i.d.) were also carried out. The mobile phase was hexane, the flow rate was 1 mL/min, with a backpressure of 5 bar, and UV detection was performed at 254 nm, with an injection volume of 15 µL (Figure 4.15). For nitrobenzene, *k* was calculated as 3.28. This separation is shown as Figure 4.15.

Table 4.3. Retention, efficiency, peak symmetry, resolution and selectivity data for butylbenzene and nitrobenzene on a 5 µm templated acid washed glassy carbon monolithic column, 30 x 6 mm i.d.

Analyte	t_r (min)	*k*	*N (per meter)*	A_s (reported)	R_s	α
Butylbenzene	0.799	1.10	376	0.735		
Nitrobenzene	1.628	3.28	128	0.276	0.25	2.98

$$N_{(Butylbenzene)} = 5.54\left(\frac{0.799\ \text{min}}{0.56\ \text{min}}\right)^2 = 11.28$$ theoretical plates per column = 376 per meter

$$N_{(Nitrobenzene)} = 5.54\left(\frac{1.628\ \text{min}}{1.96\ \text{min}}\right)^2 = 3.83$$ theoretical plates per column = 128 per meter

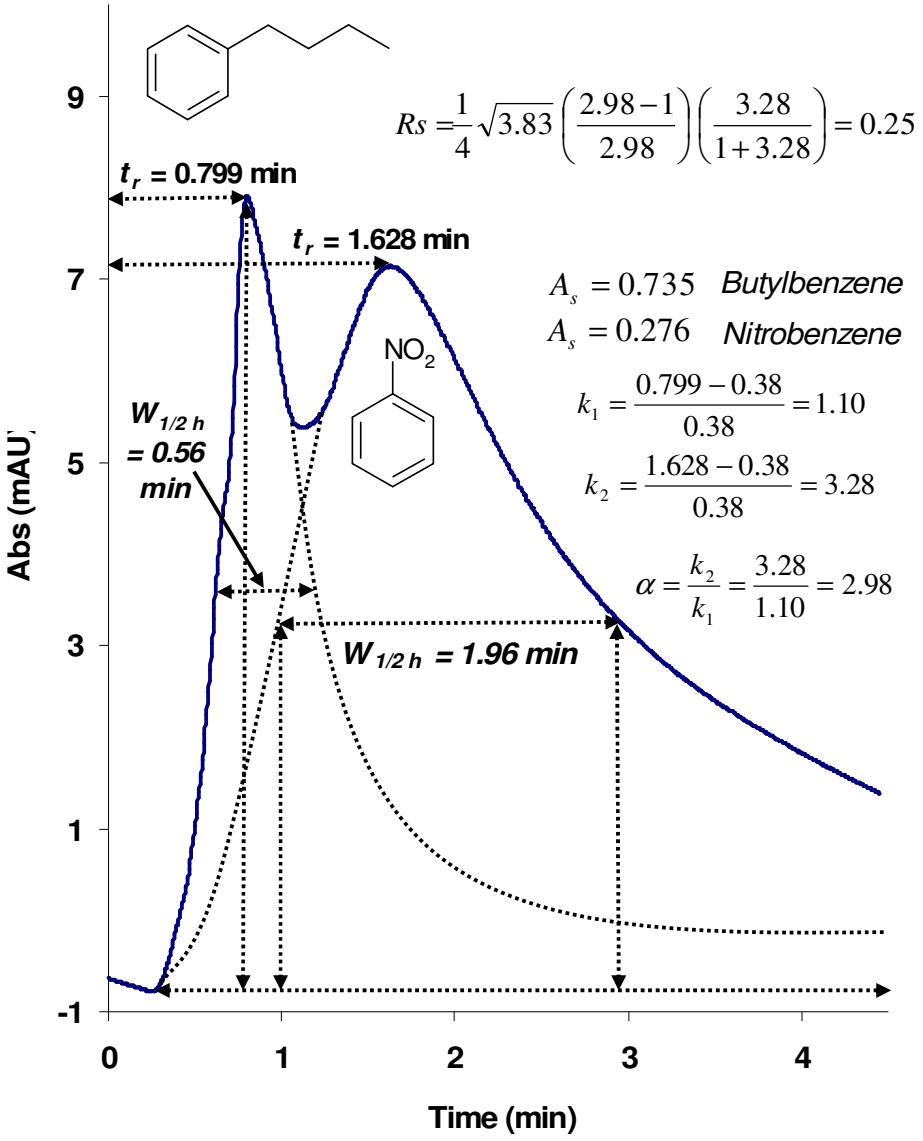

Figure 4.15. Partial separation of butylbenzene and nitrobenzene (100 µg/mL) in hexane on a 5µm templated acid washed glassy carbon monolithic column (30 x 6 mm i.d.) using hexane as the mobile phase, flow rate was 1 mL/min and UV detection was performed at 254 nm.

The greater retention exhibited for acetophenone and nitrobenzene suggests that the surface of the carbon monolithic column does indeed contain negatively charged and polar surface groups, and that retention under NP-HPLC conditions is likely to be due to the hydrogen bonds formed with such surface groups originating from oxygen and nitrogen containing impurities located on the surface [5]. This carbon monolithic column exhibited poor peak shape and strong tailing, which itself is likely to originate from strong interactions within micro-pores and with mineral and oxygen-containing surface impurities. The *k* for nitrobenzene is within the range of ideal retention factor for an analyte between (1-5) as mentioned in Section 4.3.1.4.

4.3.1.5. Study of the surface treatment of carbon monolithic columns on the NP retention of non-polar and polar solutes

Initial studies of carbon monolithic columns (Section 4.3.1.4) produced disappointing results and the column showed low efficiency in both RP and NP modes. Using a short (50 x 6 mm i.d.), 5 µm pore size glassy carbon monolithic phase, very weak retention of aromatic hydrocarbons including toluene, ethylbenzene and butylbenzene was noted in hexane. The glassy carbon monolithic phase exhibited slightly stronger retention for more polar molecules under NP LC conditions (see Figure 4.14). However, porous glassy carbon has previously been shown to be a strong RP adsorbent, showing strong retention for non-polar solutes [12]. The high purity of the glassy carbon itself would therefore appear to be critical in obtaining such retention.

The monolithic porous glassy carbon columns in the current work show some indications of NP retention. This suggests that there are polar groups such as carbonyl and aldehyde groups, present on the surface. Smith and Schaeffer [13] reported that a variety of oxygen-containing groups can be found using emission spectra in the decomposition products of carbon black attacked with electrons in a vacuum. Among these groups are – CHO, – OH**,** – COOH, and – C = O.

The ‘conditioning’ of the glassy carbon surface using mineral acids was investigated to increase retention of polar solutes by activating oxygen-containing groups on the surface of the carbon monolith. Nesterenko *et al.* [14] removed the graphite phase and improved the surface polarity by acid treatment of the sintered diamonds as a stationary phase in ion chromatography. The surface was conditioned

using 0.5 and 2 *M* solutions of sulphuric acid, as well as a 2 *M* solution of 50/50 sulphuric/nitric acid. Following each conditioning step, nitrobenzene and acetophenone were injected onto the column and retention was recorded. It was shown that retention factors for these analytes increased with each conditioning step, indicating an increase in the number of polar sites on the surface of the glassy carbon monolith (Table 4.4, Figure 4.16). The IR analysis indicated the presence of the polar sites on the surface of the carbon monolith (see Section 2.3.8., Chapter 2). The IR data for the carbon monolith is shown in Table 4.4.

Table 4.4. Functional groups present on the surface of the carbon monolith.

Functional group	**IR signal (cm^{-1})**
C=O	1700
C–O	1384
O–H	3428

The *k* for nitrobenzene was increased but the resulting peak was very broad, indicating very poor efficiency. No increase was observed for the non-polar butylbenzene, clearly demonstrating an NP retention mechanism was responsible for the observed retention selectivity.

Table 4.5. Retention factor values for test solutes on a 5 μm glassy carbon monolith (30 x 6 mm i.d.) following surface modification with mineral acids.

Monolith surface modification	**Retention factor, *k***			
	butylbenzene	% increase	nitrobenzene	% increase
No modification	0.29		1.39	
0.5 *M* H_2SO_4	0.32	10%	1.98	42%
2.0 *M* H_2SO_4	0.32	0%	3.92	98%
2.0 *M* HNO_3/H_2SO_4	0.33	3%	9.07	131%

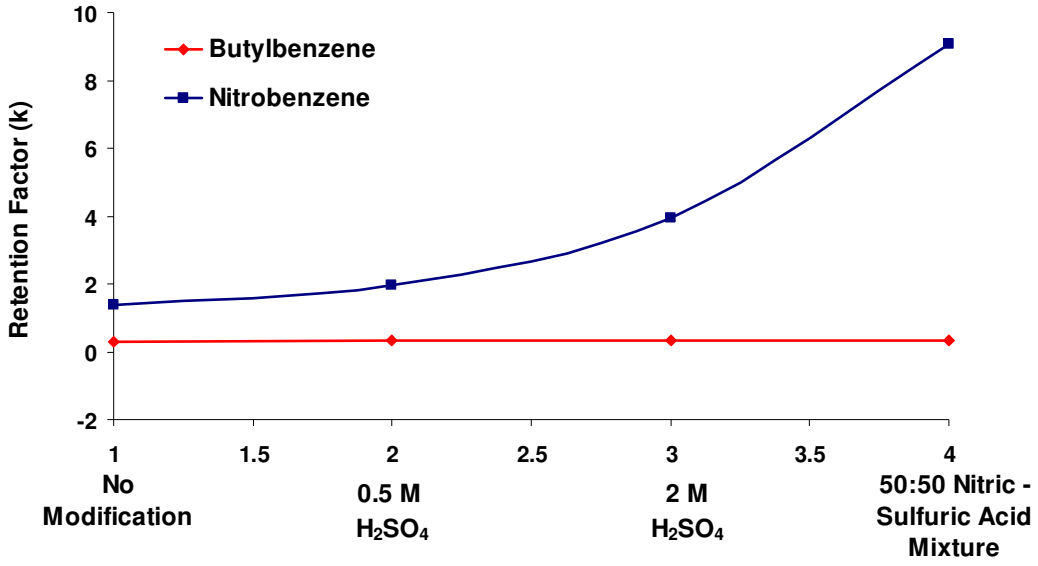

Figure 4.16. The dependence of *k* on surface treatment on a 5 µm templated glassy carbon monolithic column (30 x 6 mm i.d.) treated with mineral acids**.**

4.3.1.6. Increased monolith length and pore size effects

To study the effect of both the length of the carbon monolithic column and the pore size on the observed efficiency and comparing to the short column (30 x 6 mm i.d.) previously shown in Section 4.3.1.4, glassy carbon monolithic columns (1 and 10 µm pore size), dimensions 73 x 4 mm i.d. and 75 x 6 mm i.d., respectively, were prepared.

Preliminary NP-HPLC tests were carried out by injecting 50 µg/mL of butylbenzene, acetophenone and nitrobenzene individually, firstly onto the 10 µm templated monolithic column (Figure 4.17). Hexane was used as mobile phase, the flow rate was 1 mL/min, with a backpressure of 3 bar, UV detection was performed at 254 nm, and the injection volume was 15 µL. However, no retention was observed under these conditions (Figure 4.18).

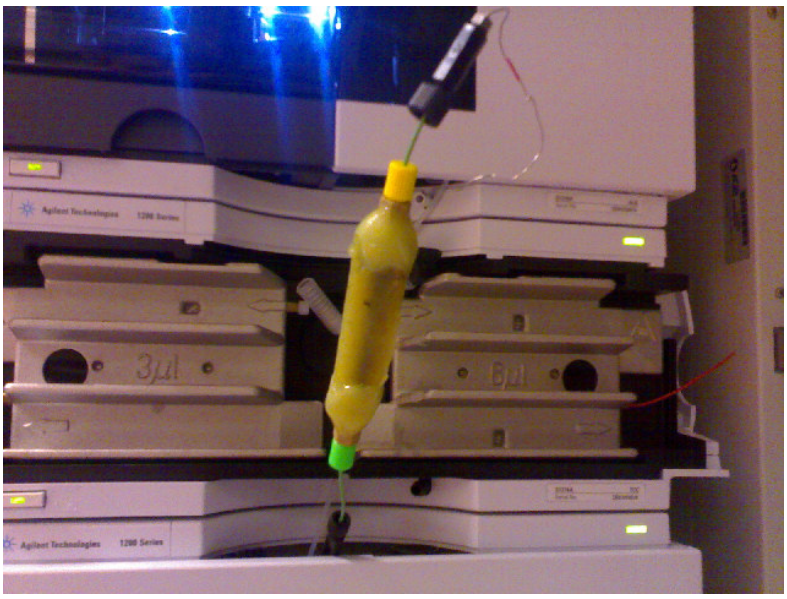

Figure 4.17. The typical image of the carbon monolithic column (1 µm pore diameter), 75 x 6 mm i.d encased within epoxy resin.

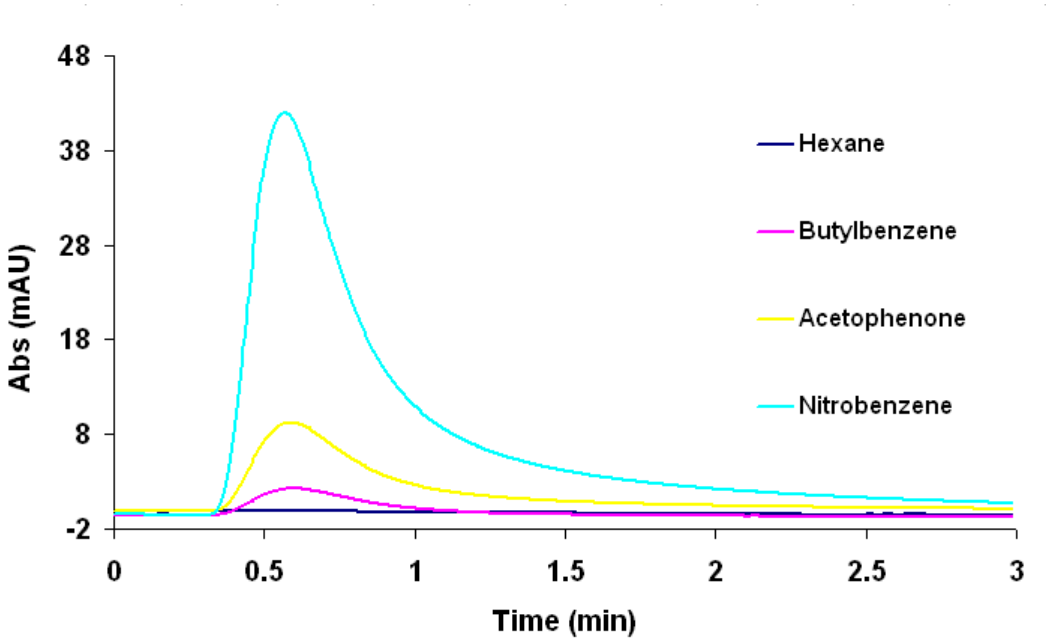

Figure 4.18. Overlaid chromatograms of 50 µg/mL of hexane, butylbenzene, acetophenone and nitrobenzene on a 10 µm templated glassy carbon monolithic column (75 x 6 mm i.d.) using hexane as mobile phase, flow rate of 1 mL/min and UV detection was performed at 254 nm.

Following this initial experiment, nitrobenzene (50 µg/mL) was injected onto the 10 µm monolithic column at various hexane:isopropanol mixture ratios. Different

ratios of hexane:isopropanol mixture (0-100 %) were investigated as the mobile phase, at a flow rate of 0.5 mL/min, giving a backpressure of 3-21 bar (as the isopropanol (IPA) ratio increased), with UV detection at 254 nm, and an injection volume of 15 µL. As shown from the overlaid chromatograms in Figure 4.19, the retention was slightly decreased as the ratio of IPA increased. Increasing the polarity of the eluent by increasing the IPA fraction, leads to strong interactions between nitrobenzene and IPA. As a result, the retention of the nitrobenzene was very slightly decreased, which is consistent with NP retention behaviour. The retention behaviour for nitrobenzene is shown in Table 4.6.

Table 4.6. Retention factor values for nitrobenzene on an encased glassy carbon monolithic column (10 µm pore size).

Hexane : IPA ratio	**Retention factor, *k***
100 : 0	0.21
80 : 20	0.21
60 : 40	0.19
40 : 60	0.15
20 : 80	0.08

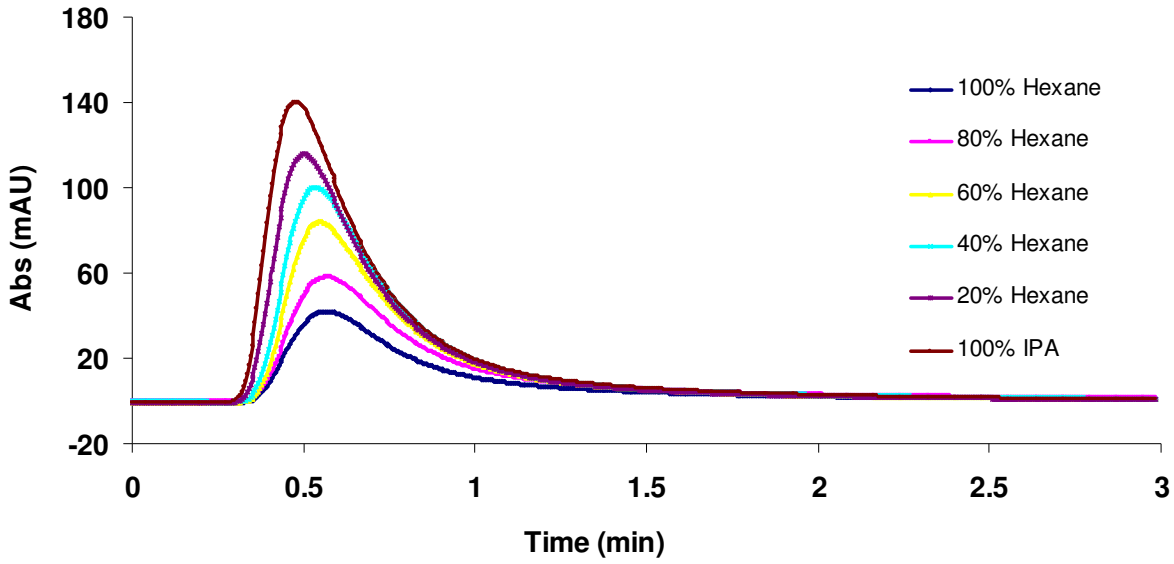

Figure 4.19. Overlaid chromatograms of nitrobenzene (50 µg/mL) on a 10 µm templated glassy carbon monolithic column (75 x 6 mm i.d.).

4.3.1.7. Acid Surface treatment of 10 µm templated carbon monolithic column.

The same experiment as detailed in Section 4.3.1.5 was performed on the 10 µm glassy carbon monolithic column (75 x 6 mm i.d.) to investigate the influence of acid treatment on the retention time, through increasing the polarity of the glassy carbon surface. The monolith surface was again treated with inorganic acids. An increase in retention time was observed after the treatment of the column with 50:50 sulphuric-nitric acid mixture. Nitrobenzene (50 µg/mL) was injected on the 10 µm glassy carbon monolithic column before the acid treatment and (100 µg/mL) was injected after the acid treatment, using hexane as the mobile phase, at a flow rate of 1 mL/min, generating backpressure of a 3-5 bar, with UV detection performed at 254 nm, and an injection volume of 15 µL. The retention time increased by 56%, from 0.55 to 0.86 min., after the column surface acid treatment. To determine the void peak, unretained butylbenzene (50 µg/mL) was injected onto the 10 µm monolithic column under the same conditions, giving an approximate void time of t_0 = 0.49 min. The k for nitrobenzene was increased from 0.12 before the treatment of the column with sulphuric-nitric acid mixture, to 0.76 after the treatment, a 6 fold increase, indicating the increased polarity of the carbon monolithic surface. Poor efficiency was obtained for this column, however it was increased from 200 theoretical plates per meter before the treatment of the column with sulphuric-nitric acid mixture to 240 theoretical plates per meter after the treatment, indicating that the polarity and therefore the capacity of the carbon monolithic surface was improved (Figure 4.20). However, the chromatographic peak of the nitrobenzene (100 µg/mL) injected on the column after the acid treatment showed a considerable deterioration in peak shape, indicating the acid conditioning of the monolithic column could have effected the physical pore structure of the monolith itself or damaged the column housing causing channels or voids.

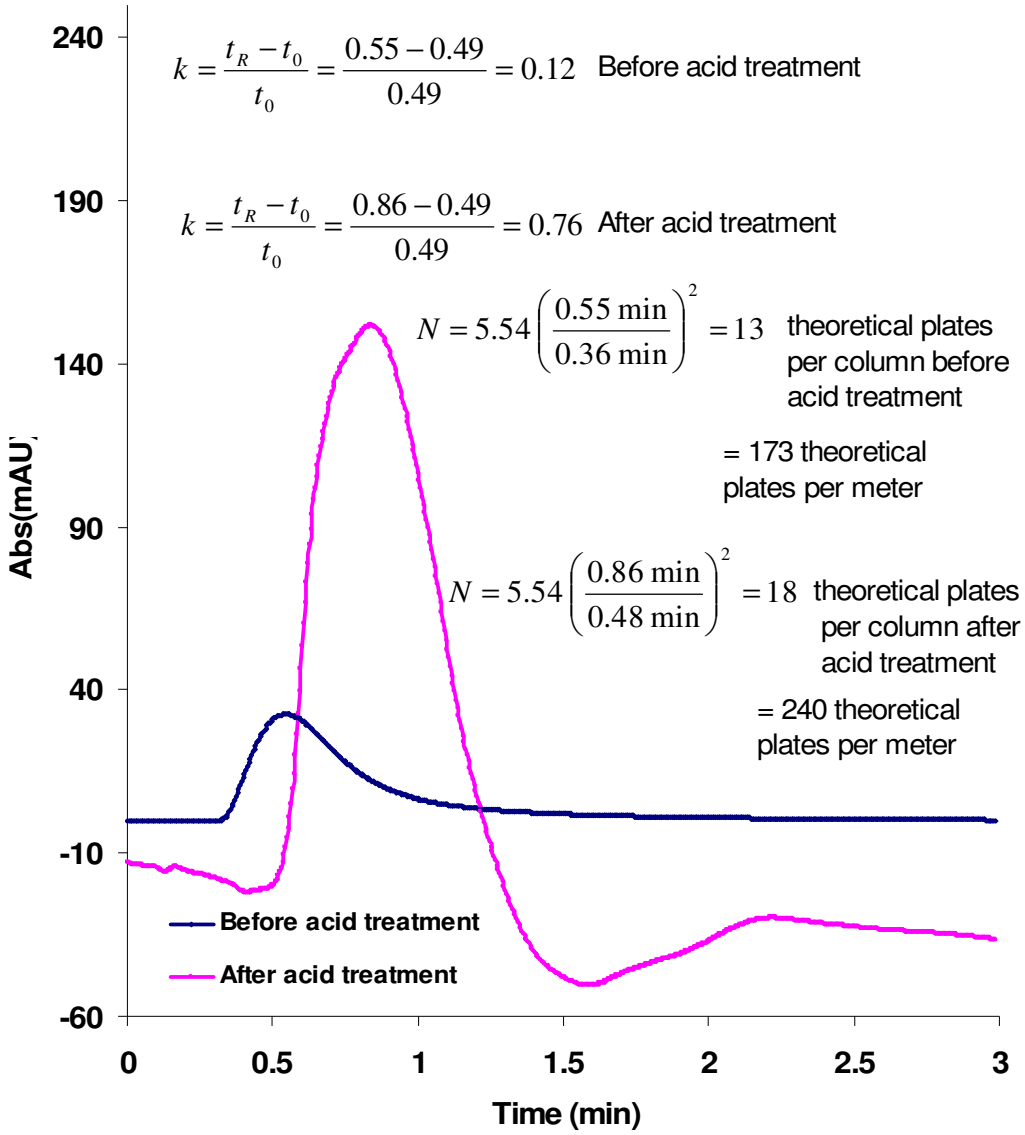

Figure 4.20. Chromatograms of nitrobenzene (50 µg/mL) before and (100 µg/mL) after acid treatment of the a 10 µm templated glassy carbon monolithic column (75 x 6 mm i.d.) with sulphuric and nitric acid. Mobile phase: hexane, flow rate of 1 mL/min and UV detection was performed at 254 nm.

4.3.1.8. Chromatographic evaluation of 1 µm templated carbon monolithic column by NP-HPLC

As shown in Section 4.3.1.4, poor efficiency was observed for the 5 µm templated carbon monolithic column, of 30 mm in length. In a final attempt to improve the retention and efficiency being observed, a lower pore diameter (1 µm) and longer (73 mm) column was used. In addition, the column i.d. was also reduced to 4 mm, down from the previously evaluated monoliths (6 mm i.d.).

The effect of the length and pore diameter of the carbon monolithic column on the efficiency was studied by injecting acetophenone (50 µg/mL) on the 1 µm (glue encased) carbon monolithic column (73 x 4 mm i.d.) under NP-HPLC conditions (Figure 4.21).

Figure 4.21. The typical image of the 1 µm templated carbon monolithic column (73 x 4 mm i.d.) encased within epoxy resin.

To determine the void peak, unretained butylbenzene (50 µg/mL) was injected on the 1 µm monolithic column giving an approximate void time of t_0 = 0.22 min. Hexane was used as the mobile phase, at a flow rate of 0.5 mL/min, generating a backpressure of 4 bar, with UV detection performed at 254 nm, and an injection volume of 15 µL.

Preliminary NP tests were carried out by injecting separately a butylbenzene (50 µg/mL) and acetophenone (50 µg/mL) onto the 1 µm monolithic column. Only

limited retention was observed in this initial test. The same limited retention was observed after injecting (50 µg/mL) of nitrobenzene on this column, under the same conditions. Overlaid chromatograms of butylbenzene and acetophenone are shown in Figure 4.22.

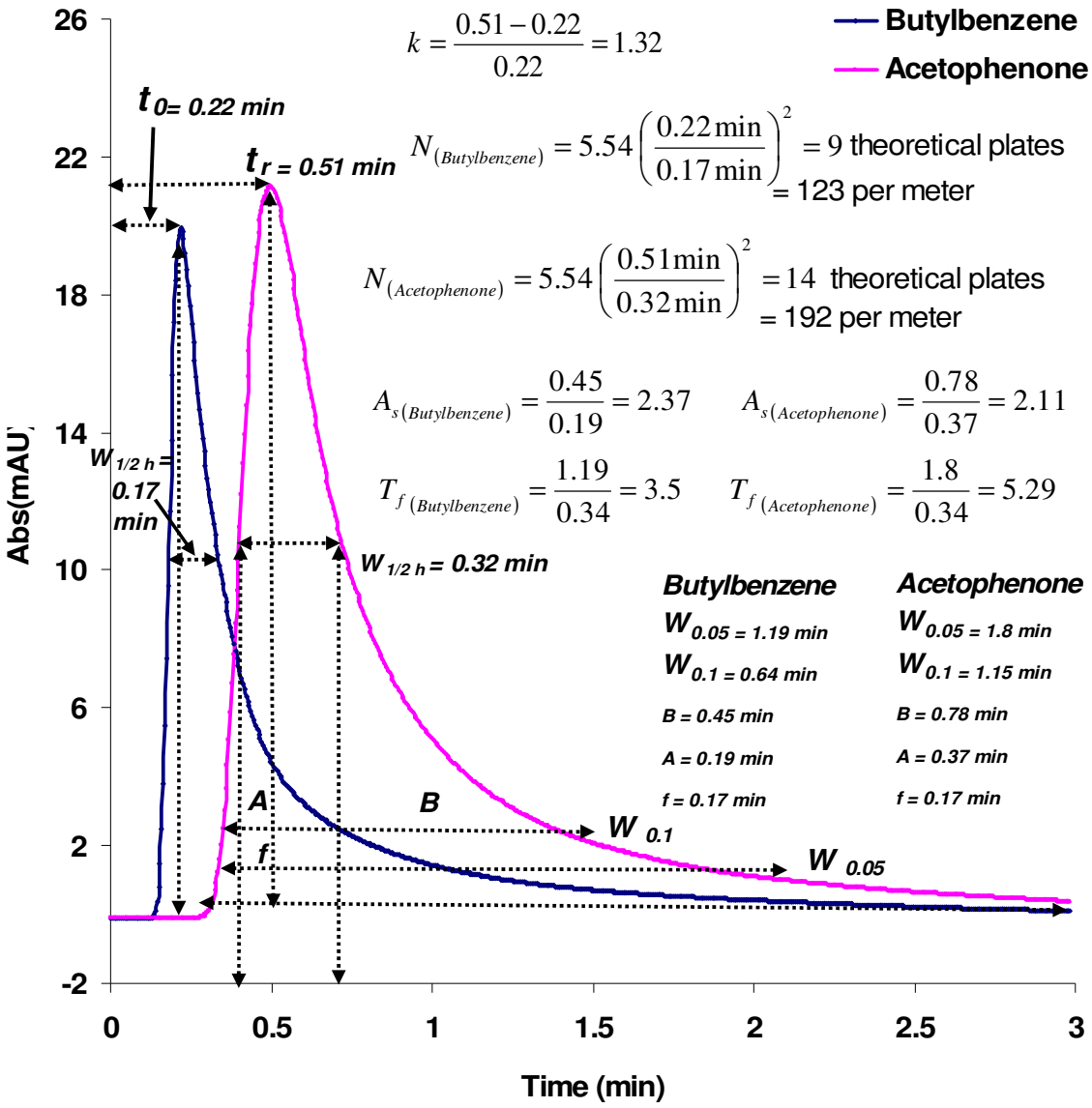

Figure 4.22. Chromatograms of butylbenzene (50 µg/mL) and acetophenone (50 µg/mL) on a 1 µm templated glassy carbon monolithic column (73 x 4 mm i.d.). Mobile phase: hexane, flow rate of 0.5 mL/min and UV detection was performed at 254 nm.

The tailing factor (T_f) is a useful parameter, which reflects the peak symmetry (A_s). When T_f = 1, it indicates a perfectly symmetrical peak and T_f greater than 2 indicates a tailing peak which is generally not acceptable due to difficulty in integrating the peak area accurately. The values of A_s and T_f are quite similar for most peaks having T_f values greater than 0.5 and smaller than 2. A_s is smaller than T_f for severely tailing peaks. However, the chromatogram for acetophenone in Figure 4.22 exhibited severe tailing, with T_f of 5.29 and poor column efficiency of only 192 theoretical plates per meter was observed.

Despite the obvious tailing and limited efficiency, acetophenone did interact with the carbon monolith stationary phase and took 0.51 min to be detected, giving a *k* of 1.32. This value was indeed promising and within the range of the ideal retention factor for an analyte which is between 1-5.

4.3.1.9. Acid surface treatment for 1 µm templated monolithic column

The same treatment as described in Section 4.3.1.5 was applied to the 1 µm glassy carbon monolithic column (73 x 4 mm i.d.) to investigate the affect of acid treatment on the observed selectivity. The monolith surface was treated with 50:50 sulphuric-nitric acid overnight. However, no changes in retention time or peak profile were observed after the acid mixture treatment (Figure 4.23), as indicated by injecting 50 µg/mL of acetophenone on the 1 µm glassy carbon monolithic column before and after treatment possibly due to the very low surface area of the monolith and because of this they simply had insufficient surface hydrophilicity and capacity to show retention under NP conditions on this specific column. As mentioned earlier in Section 4.3.1.2., a typical surface area of the silica monolith was calculated to be 300 m^2/g using Brunauer–Emmett–Teller (BET) method [11]. Hexane was used as the mobile phase, the flow rate was 0.5 mL/min, generating backpressure of 3 bar (4 bar after the acid mixture treatment), with UV detection was performed at 254 nm. Nitrobenzene was not injected and tested as no retention was observed by the acetophenone test before and after the acid treatment.

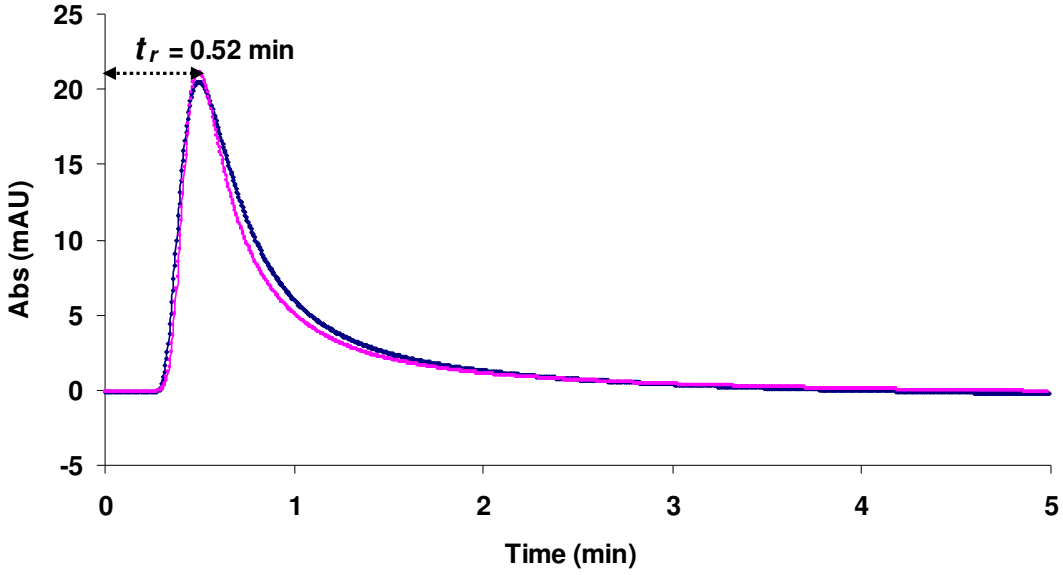

Figure 4.23. Elution profile of acetophenone (50 µg/mL) on a 1 µm templated glassy carbon monolithic column (73 x 4 mm i.d.) before and after acid treatment. Mobile phase: hexane, flow rate was 0.5 mL/min and UV detection was performed at 254 nm.

4.3.2. Modified porous carbon monolithic columns

4.3.2.1. Gold nano/micro-particles modified carbon monolithic column.

As discussed in Chapter 3, a glassy carbon monolithic rod (5 µm pore diameter, 30 x 6 mm i.d.) was modified with gold nano/micro-particles, obtained by self-assembly in solution followed by surface induced reduction at functional group sites at the surface. The modified carbon monolith was examined and characterised by SEM/EDX (see Section 3.3.1.1 and Figures 3.2 and 3.3, Chapter 3). Modification of the carbon/gold composite monolith with 6-mercaptohexanoic acid was carried out as described in Section 3.3.2, Chapter 3.

The rod was then clad with heat shrinkable PTFE followed by glueing and fitting into a PEEK column (see Section 2.2.3.3, Chapter 2).

4.3.2.2. Backpressure measurements on the carbon/gold composite monolithic column modified with 6-mercaptohexanoic acid

Efficient separations and rapid analysis can be achieved at relatively low backpressures using monolithic columns prepared from organic and silica monomers [15]. As the backpressures for monolithic columns are typically low, they can be used at higher flow rates or multiple columns can be joined together to improve plate counts and peak resolution. Thus, Tolstikov *et al.,* [16] used a 90 cm long monolithic column for the analysis of the metabolome of *Arabidopsis thaliana* and Bones *et al.,* [17] used a 1 meter coupled monolithic column for the separation of ten proteins, generating only 140 bar column backpressure.

It is clear that monolithic columns prepared from carbon can also offer low backpressures typical of common silica and polymer monolithic columns. The carbon/gold composite monolithic rod (5 μm pore diameter, 30 x 6 mm i.d) modified with 6-mercaptohexanoic acid was encased within heat shrinkable Teflon tubing and further encased within a PEEK column housing, and sealed using Araldite epoxy glue. The resulting column was tested for flow through backpressures using a variety of solvents (Figure 4.24). The backpressure on the freshly prepared 5 μm templated carbon/gold composite monolithic column was investigated using the following solvents at 0.5 to 3.0 mL/min: pentane, methanol, water, acetonitrile and isopropanol. The highest backpressure at flow rate of 3 mL/min was recorded (~ 160 bar) using isopropanol as the solvent with the highest viscosity (1.96 CP at 25 °C), and the lowest backpressure was recorded (~ 30 bar) using pentane as a solvent with the lowest viscosity (0.240 CP at 20 °C). In general, this column provided a relatively low backpressure, typical of common monolithic columns suitable for chromatographic application.

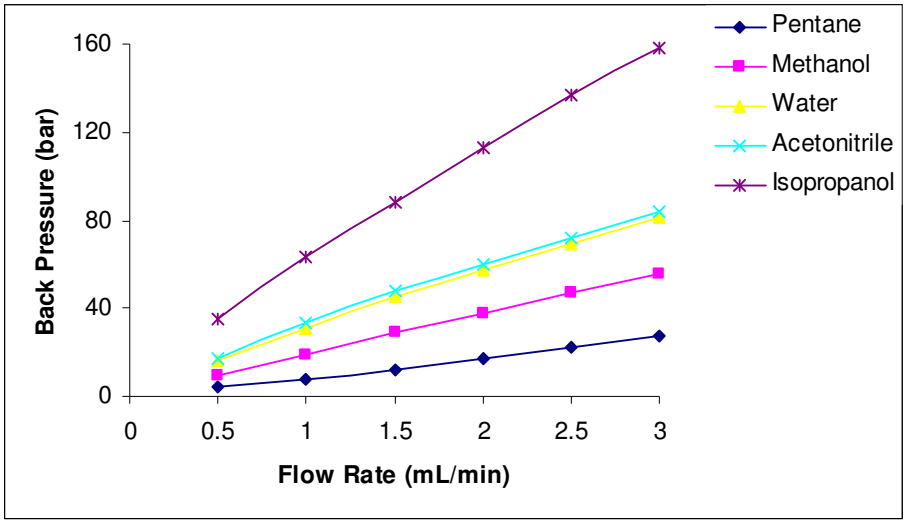

Figure 4.24. The dependence of backpressure of the carbon/gold composite monolithic column (5 µm pore diameter) on flow rate in various solvents.

4.3.2.3. Chromatographic evaluation of the carbon/gold composite monolithic column modified with 6-mercaptohexanoic acid

The modified column was tested chromatographically, using imidazole (1 µg/mL) (pKa = 7) as a standard solute, with a 1 m*M* acetate buffer (pH 3.96) eluent, a flow rate of 1 mL/min, generating a system backpressure of 24 bar, with UV detection performed at 280 nm, and an injection volume of 10 µL. Figure 4.25 shows the retention of the imidazole cation on the short 30 mm long gold particle modified 5 µm templated glassy carbon monolith.

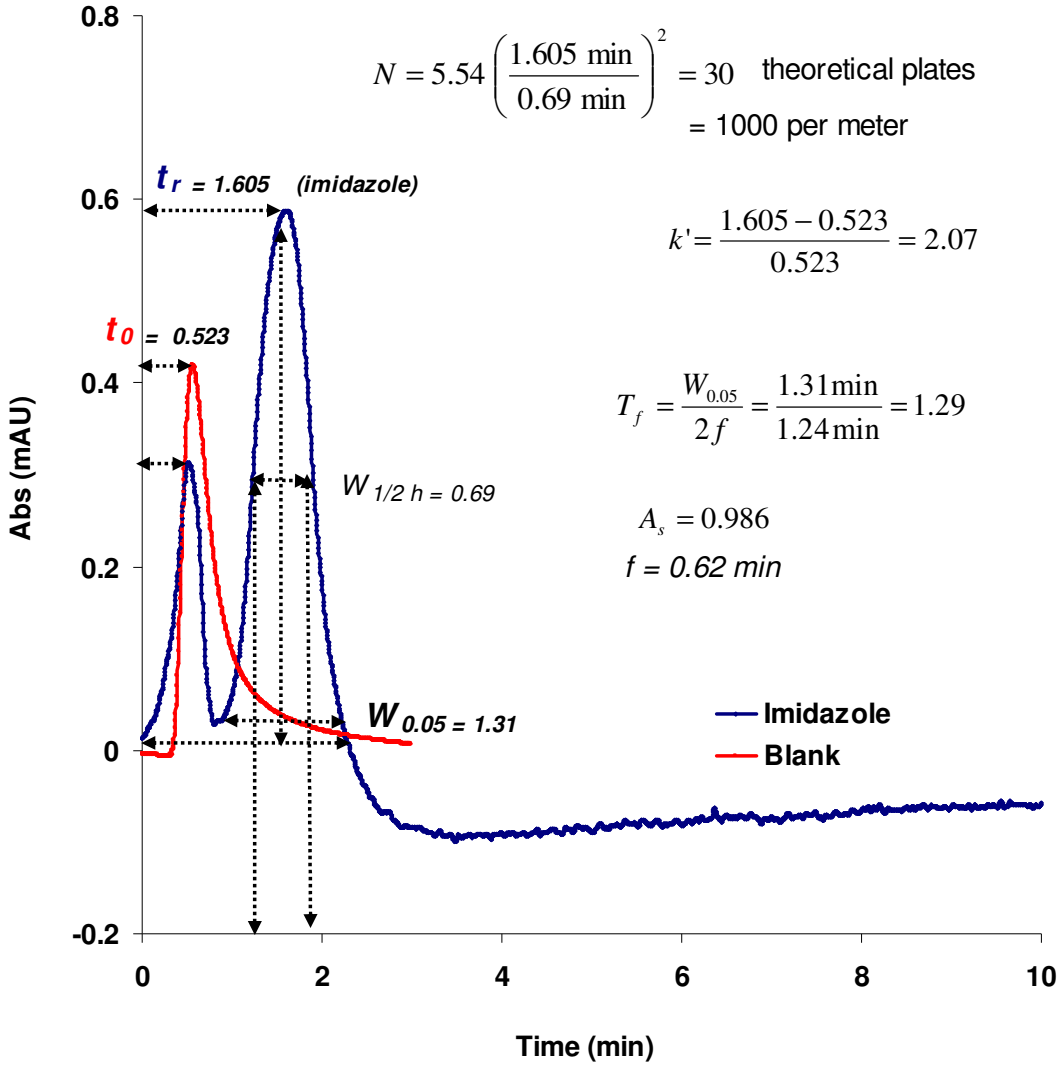

Figure 4.25. Retention of imidazole (1 µg/mL) (prepared in 1 m*M* acetate buffer) on a gold-mercaptohexanoic acid modified 5 µm templated glassy carbon monolithic column (30 x 6 mm i.d). Mobile phase: 1 m*M* acetate buffer, flow rate was 1 mL/min and UV detection was performed at 280 nm.

The resultant chromatogram showed significant retention of the organic cation on the weak cation exchange modified monolithic column. Although efficiency was limited on the short column, the retention achieved (k = 2.07) and the acceptable peak shape demonstrated the modified monoliths did exhibit chromatographic potential which could be further optimised.

4.3.2.4. 1 µm templated carbon monolithic column modified with gold nano/micro-particles

A 1 µm templated glassy carbon monolith (73 x 4 mm i.d.) was clad within an epoxy resin column and subsequently modified with gold through pumping 100 m*M* chlorauric acid (pH 1.8) through the carbon monolithic column overnight. Further modification with 6-mercaptohexanoic acid was carried out as described in Section 3.2.4, Chapter 3, to convert the surface of modified monolith to a weak cationic exchanger. Using this dynamic modification technique a considerably lower degree of surface coverage was achieved (equal to only 0.011 % w/w Au for a 5 µm templated monolith) (see Section 3.3.1.4, Chapter 3). Using the above moderately modified 1 µm templated column, the relative retention of neutral resorcinol and cationic imidazole was investigated.

A preliminary ion-exchange test was carried out by injecting 50 µg/mL of imidazole on the 1 µm monolithic column. 1 m*M* of acetate buffer (pH 5.71) was used as the eluent, at a flow rate of 1 mL/min, generating a backpressure of 24 bar, with UV detection at 280 nm, and an injection volume of 10 µL. Compared to the 5 µm templated glassy carbon monolith (30 x 6 mm i.d.) previously tested with imidazole giving a retention time at 1.605 min (see previous Section 4.3.2.3), and under the conditions above, no retention was detected by the 1 µm templated gold/mercaptohexanoic acid modified glassy carbon monolith (73 x 4 mm i.d.) (Figure 4.26), possibly due to a reduced concentration of functional groups present on the surface of both columns, or poor coverage of 6-mercaptohexanoic acid, and thus different chromatographic behaviour.

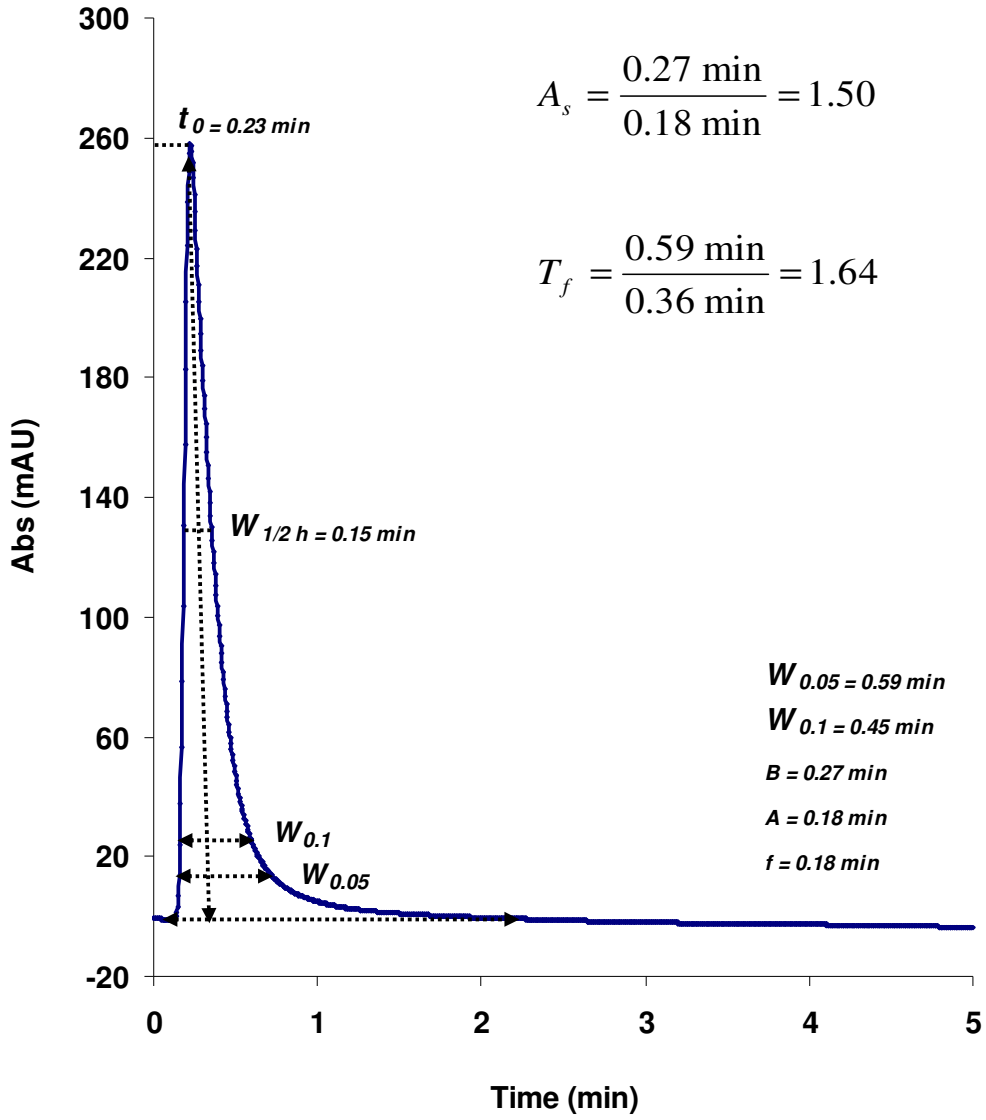

Figure 4.26. Chromatogram of imidazole (50 µg/mL) on a gold-mercaptohexanoic acid modified 1 µm templated glassy carbon monolithic column (73 x 4 mm i.d.) using 1 m*M* of acetate buffer (pH 5.71) as the eluent, flow rate was 1 mL/min and UV detection was performed at 280 nm.

Another organic cation, histidine, was also tested under the same conditions. However, once again, no retention was detected (Figure 4.27) possibly for the same reasons mentioned above.

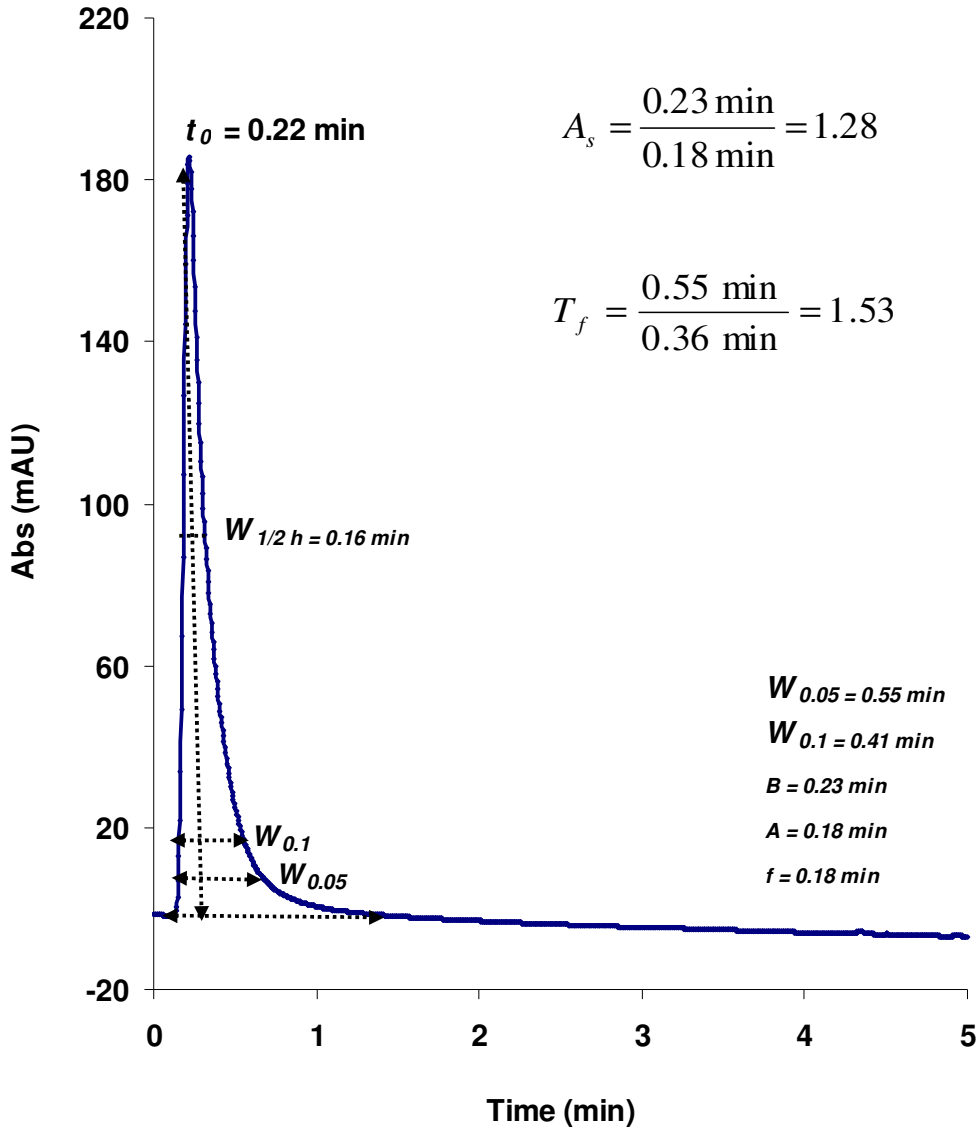

Figure 4.27. Chromatogram of histidine (50 µg/mL) on a gold-mercaptohexanoic acid modified 1 µm templated glassy carbon monolithic column (73 x 4 mm i.d.) using 1 m*M* of acetate buffer (pH 5.71) as the eluent, flow rate was 1 mL/min and UV detection was performed at 280 nm.

However, two observations can be made from the previous two chromatograms. Firstly, the peak profile is greatly improved, with a significantly reduced band width and acceptable peak tailing factor. Secondly, the column void volume, which is equal to 0.22 mL, is significantly lower than the larger pore for diameter columns.

4.3.2.5. The effect of the column temperature on the retention

The use of the columns at high temperatures leads to a decrease in the viscosity of the mobile phase and consequently the column backpressure and usually affects the retention (k), efficiency (N) and selectivity (α). For monolithic columns, both retention and separation has been shown to be considerably affected by temperature in previous studies on silica based monoliths [18].

In ion exchange-chromatography, temperature has been shown to significantly increase retention under certain conditions [19]. Therefore, the effect of column temperature on the retention of imidazole on the 1 µm templated modified carbon monolithic column (73 x 4 mm i.d.) with gold and 6-mercaptohexanoic acid was studied. 1 m*M* of acetate buffer (pH 5.71) was used as the eluent, at a flow rate of 1 mL/min, with UV detection performed at 211 nm, and an injection volume of 10 µL. Retention was recorded at 0.23-0.26 min between 15-40 °C and then increased gradually as the temperature increased above 40 ^{o}C (Table 4.7). The graphs showing the influence of temperature on retention and corresponding chromatograms are shown in Figures 4.28 and 4.29.

Table 4.7. The dependence of retention on temperature for imidazole on the weak cation exchange modified monolith

Temperature (^{o}C)	Retention time (t_r)/min
15	0.23
20	0.23
25	0.23
30	0.24
35	0.24
40	0.26
45	0.52
50	0.57
55	0.60
60	0.60

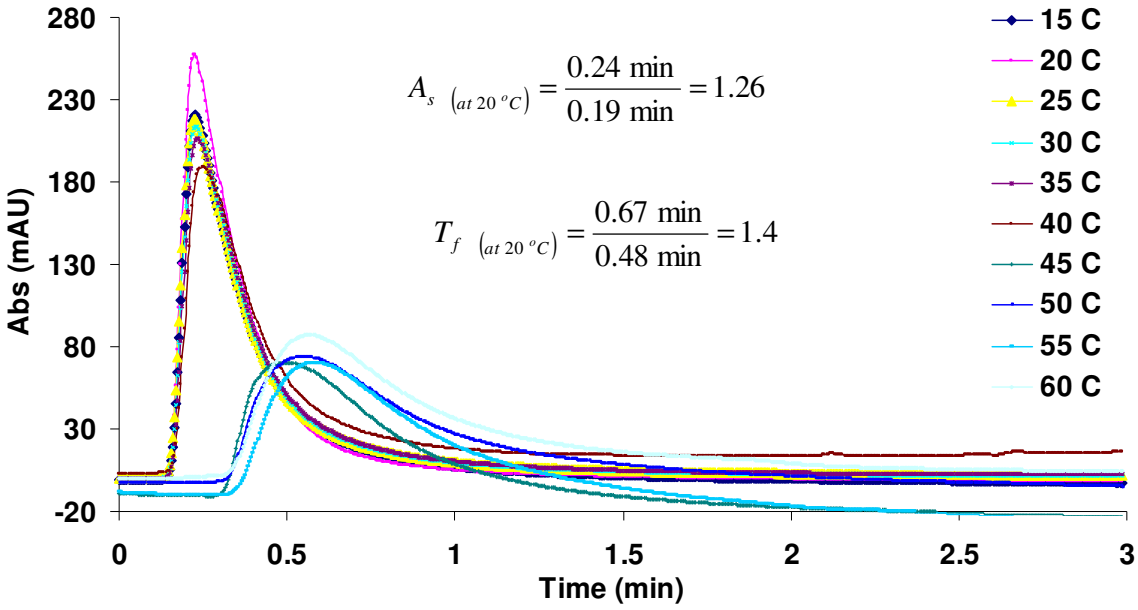

Figure 4.28. Chromatograms showing the influence of temperature on retention of imidazole. Column: gold-mercaptohexanoic acid modified 1 µm templated glassy carbon monolithic column (73 x 4 mm i.d.) over 15 to 60 ^{o}C using a 1 m*M* acetate buffer (pH 5.71) as the eluent, flow rate was 1 mL/min and UV detection was performed at 211 nm.

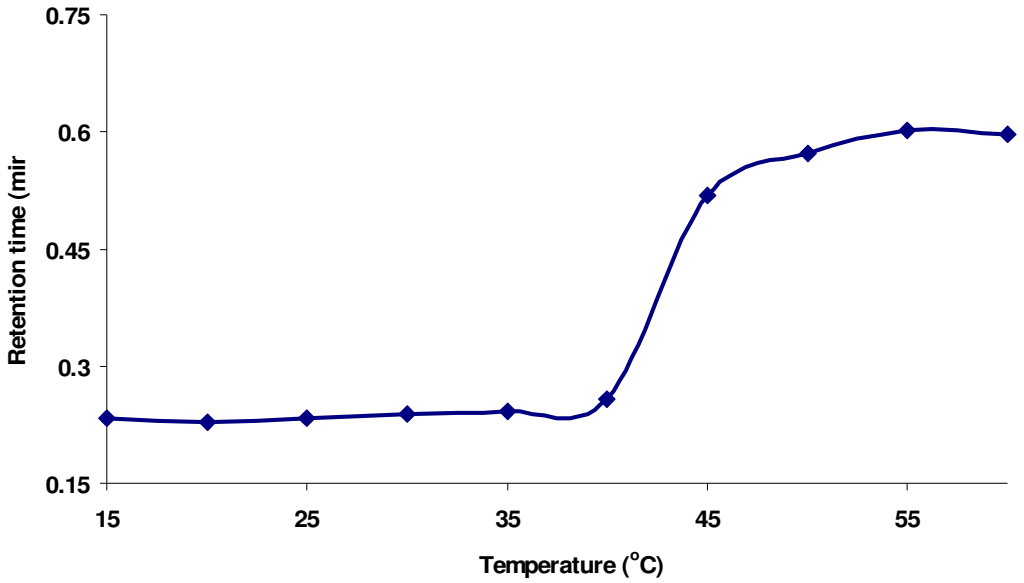

Figure 4.29. The retention dependence on column temperature for imidazole on a gold-mercaptohexanoic acid modified 1 μm templated glassy carbon monolithic column (73 x 4 mm i.d.).

The efficiency was also calculated under each temperature condition. The best efficiency was achieved (205 theoretical plates) using a column temperature of 20 °C. (Table 4.8, Figure 4.30).

Table 4.8. The dependence of efficiency on temperature for imidazole on a mercaptohexanoic acid modified gold/carbon monolith.

Temperature (°C)	Efficiency (*N*) per meter
15	111
20	205
25	111
30	109
35	109
40	128
45	111
50	95
55	114
60	105

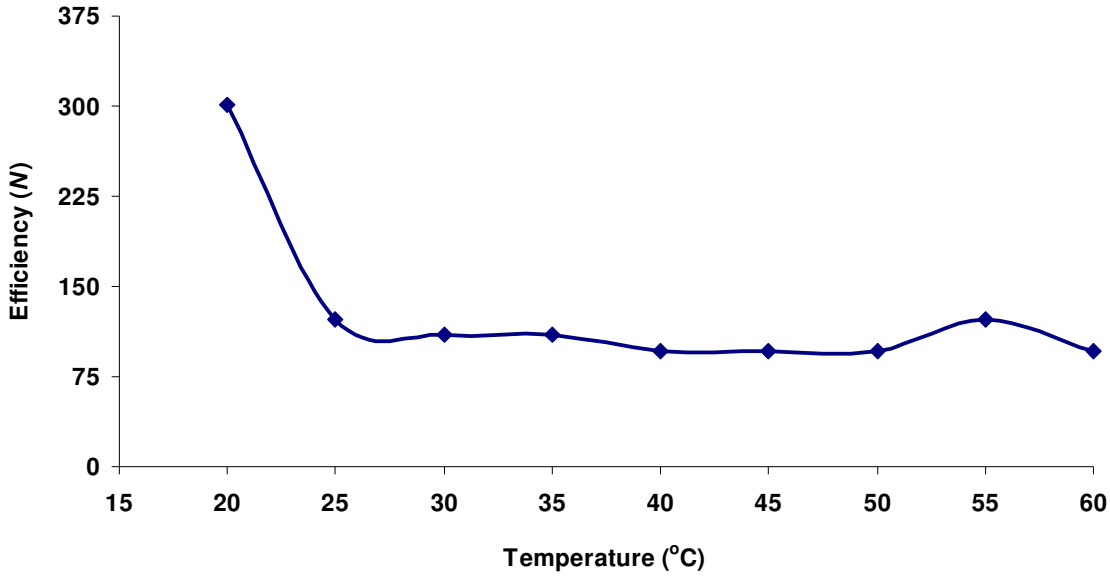

Figure 4.30. The efficiency (*N*) dependence on column temperature for imidazole on a gold-mercaptohexanoic acid modified 10 μm templated glassy carbon monolithic column (73 x 4 mm i.d.).

To verify the previous changes in retention where indeed due to ion exchange, a neutral solute was injected and tested under the same conditions with a neutral solute no increased retention was shown. A strange sudden change was occurred between 40 and 45 ^{o}C possibly due to the strong interactions of imidazole with the residual halogen, oxygen, iron particles, iron carbide [5] and carbonyl and hydroxyl functional groups present on the surface of the carbon monolith as mentioned in Section 3.3.1.1., Chapter 3. Such interactions did not take place below 45 ^{o}C makes the imidazole retains and stayed longer as the temperature increased. Resorcinol (100 μg/mL) was injected onto the column at temperatures of between 30 and 60 ^{o}C. Under all of these conditions no retention was detected (Figure 4.31), and no increase observed.

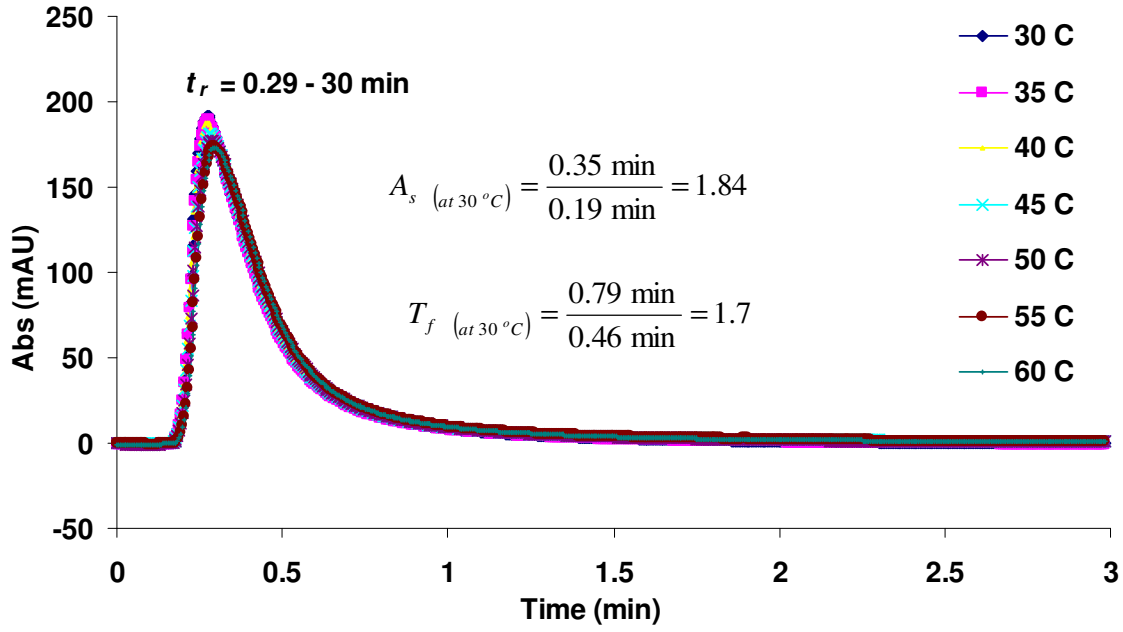

Figure 4.31. Elution profile for resorcinol on a carbon/gold composite monolith (1 µm pore size) modified with 6-mercaprohexanoic acid mercaptohexanoic acid using a 1 m*M* acetate buffer (pH 5.71) as the eluent, flow rate was 1 mL/min and UV detection was performed at 211 nm.

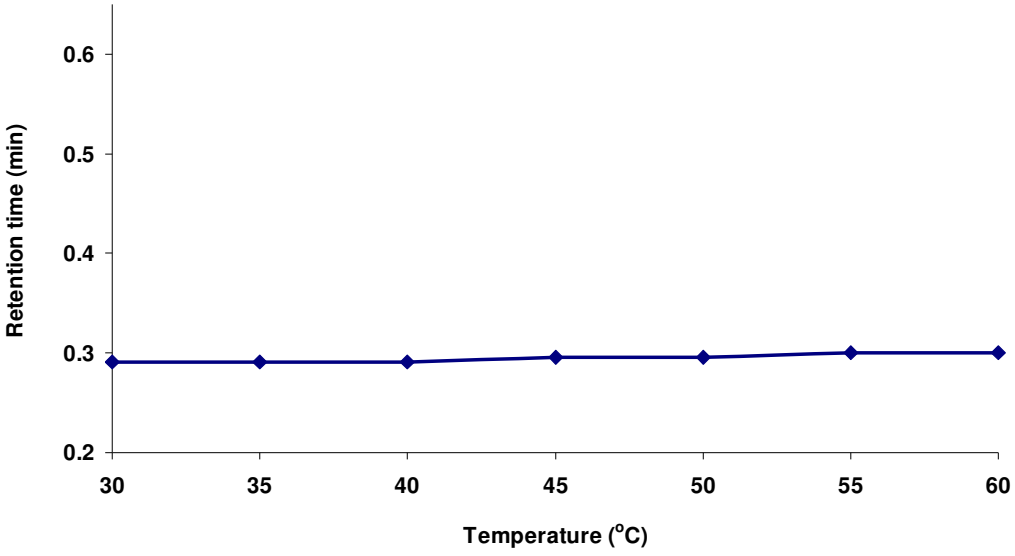

Figure 4.32. The retention dependence on column temperature for resorcinol on a gold-mercaptohexanoic acid modified 1 µm templated glassy carbon monolithic column (73 x 4 mm i.d.).

As shown in Figures 4.28 and 4.31, the 1 µm templated monolith exhibited a significantly reduced void volume compared to the 5 µm templated monolith. Given the relative total volumes of the two monolithic rods, namely 0.849 cm^3 for the short 5 µm templated monolith compared to 0.917 cm^3 for the longer 1 µm templated rod, the observed void volumes correspond to a large difference in both column density and overall porosity, equivalent to ~ 25% total porosity for the 1 µm rod compared to ~ 70% for the 5 µm templated material. This reflects the low surface area of the 5 µm material noted in Table 4.9.

Table 4.9. Surface area and pore volume measurements of the carbon monoliths after pyrolysis.

Macro-pore (µm)	Monolith surface area (m^2/g)	Monolith pore volume (cm^3/g)
1	178	0.23
2	154	0.23
5	85	0.095
10	125	0.32

As shown in Table 4.9, the surface area and pore volume of the carbon monolith (5 µm pore diameter) were lower than expected and lower than the monolith (10 µm pore diameter). They may be due to the non-homogeneous and non-uniform size of silica particles (5 µm particle size) used for the preparation of the original 5 µm templated silica-polymer mix, resulting in the potential presence of internal voids and larger than expected overall porosity.

Chromatographically, this difference is reflected in the observed peak shapes shown in Figures 4.14, 4.28 and 4.31 (Table 4.10), where the 1 µm templated rod exhibited a considerable improvement in both peak width and symmetry, although a reduced overall ion exchange capability (Figures 4.28 and 4.31).

Table 4.10. The dependence of A_s and T_f on pore diameter of 1 and 5 µm carbon monolithic columns

Chromatographic parameter	Butylbenzene-acetophenone mixture on 5 µm templated monolithic column (Figure 4.14)	Imidazole on 1 µm templated monolithic column (Figure 4.28)	Resorcinol on 1 µm templated monolithic column (Figure 4.31)
A_s	0.396	1.26	1.84
T_f	2.25	1.4	1.7

The effect of temperature upon retention was investigated to confirm the dominance of ion exchange in the retention mechanism on the modified monoliths. Despite low capacity the effect upon retention of imidazole compared to the resorcinol was significant, with no temperature effect upon retention or change in peak shape noted between 30 ^{o}C and 60 ^{o}C for the neutral solute, but a significant increase in retention was observed for the imidazole.

This effect was also seen with 1 µm and 10 µm templated gold-mercaptohexanoic acid modified monoliths, with the reproducibility of peak shapes for both retained and unretained species following multiple temperature variations confirming thermal stability of both the surface modification and the carbon rod cladding itself (Figure 4.31 shows 7 overlaid chromatograms spanning the temperature range 30 to 60 ^{o}C).

The results show clearly that the potential for higher capacity modified monoliths exits through immobilise the immersion based modification approach on the monoliths of higher surface area and greater density, namely the 1 and 10 µm templated materials.

4.3.2.6. The effect of the column temperature on the retention of imidazole on 10 µm modified carbon monolithic column

The effect of the column temperature on the retention of imidazole on a 10 µm (glue encased) carbon monolithic column (75 x 6 mm i.d.) modified with gold

and 6-mercaptohexanoic acid was also studied and the results of the study were similar of that for the 1 µm carbon monolithic column (73 x 4 mm i.d.) (see Section 4.3.2.5).

Imidazole (100 µg/mL) was injected onto this column at various temperatures. 1 m*M* of acetate buffer (pH 5.71) was used as the eluent, at a flow rate of 1 mL/min, with UV detection performed at 211 nm, and an injection volume of 10 µL. Retention was recorded at 0.39 min between 20-30 °C and then again started to increase gradually as the temperature was increased (Table 4.11). The glue encased column was however in this instance not stable and started leaking over 60 ^{o}C as the epoxy glue became unstable above this temperature.

Another clear change was observed between 30 and 35 ^{o}C, a lower temperature than on the 10 µm modified carbon monolithic column. The decomposition of the thiol carboxylic acid could be another reason behind these changes in the retention times, however, this is not expected as the retention times at various temperatures were reproducible and this would not take place if the thiol were decomposed.

The graphs showing the influence of temperature on retention and corresponding chromatograms are shown in Figures 4.33 and 4.34.

Table 4.11. The dependence of retention on temperature for imidazole on the weak cation exchange modified monolith

Temperature (^{o}C)	Retention time (t_r)/min
20	0.39
25	0.39
30	0.39
35	0.54
40	0.61
45	0.75
50	0.88
55	0.95
60	1.13

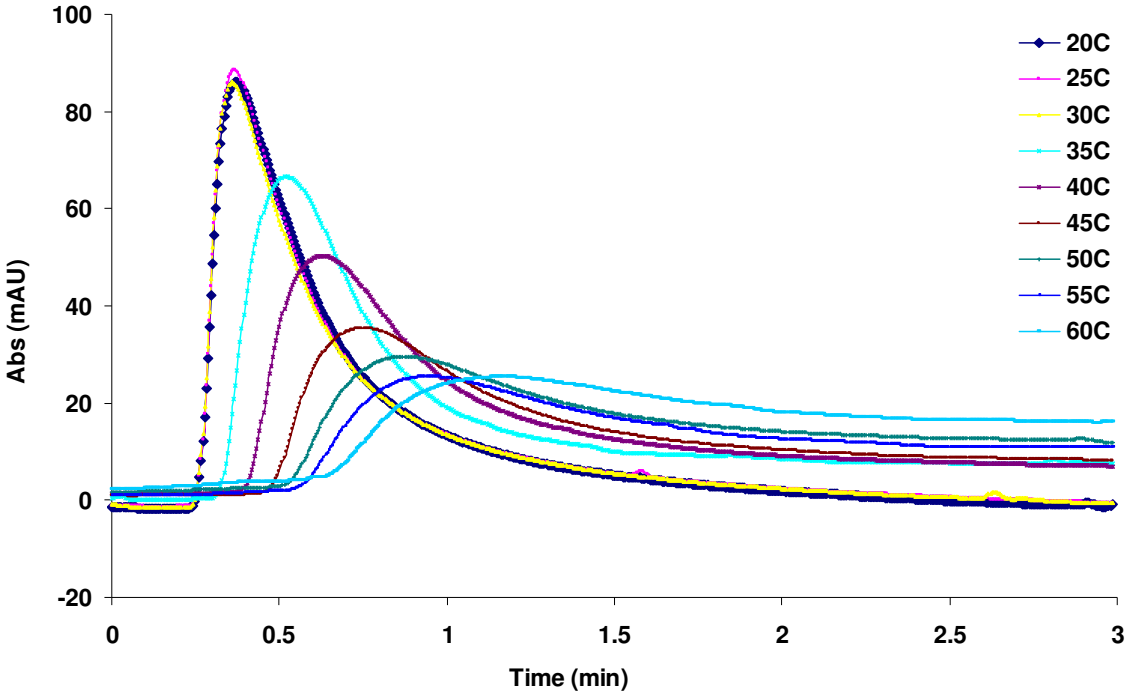

Figure 4.33. The increase of retention of imidazole on a gold-mercaptohexanoic acid modified 10 µm templated glassy carbon monolithic column (75 x 6 mm i.d.) over 20 to 60 ^{o}C using a 1 m*M* acetate buffer (pH 5.71) as the eluent.

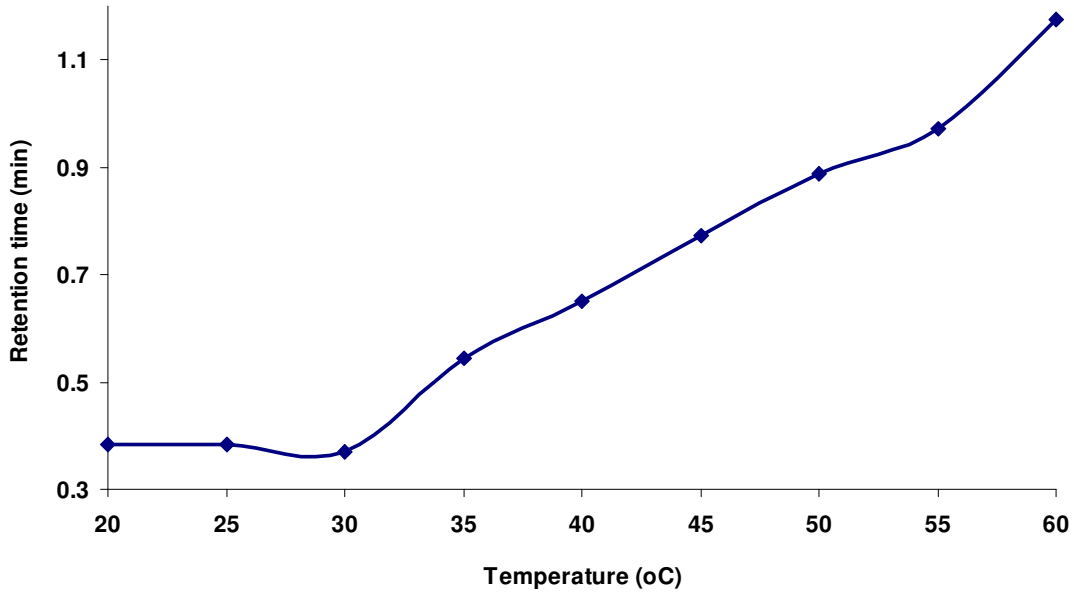

Figure 4.34. The retention dependence on column temperature of of imidazole on a gold-mercaptohexanoic acid modified 10 µm templated glassy carbon monolithic column (75 x 6 mm i.d.).

Again, resorcinol (100 µg/mL) was also injected onto this column at various temperatures under the same conditions. No change retention was detected and no increase observed at temperatures between 20-60 °C (Figure 4.35).

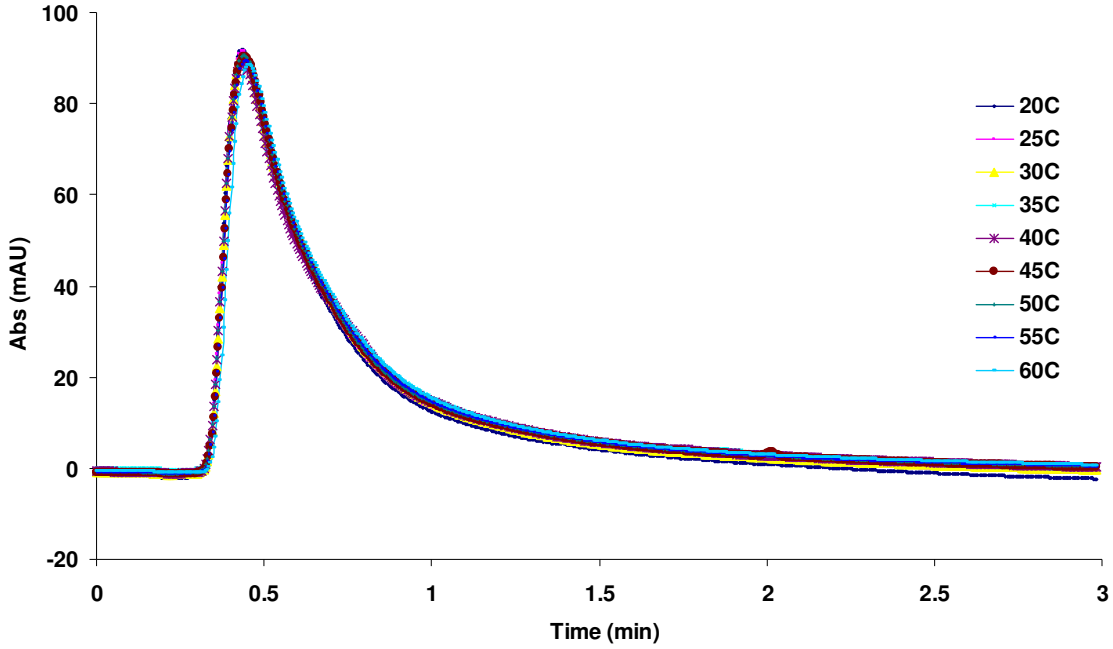

Figure 4.35. Elution profile for resorcinol on a carbon/gold composite monolith (10 µm pore size) modified with 6-mercaprohexanoic acid mercaptohexanoic acid using 1 m*M* of acetate buffer (pH 5.71) as the eluent, flow rate was 1 mL/min and UV detection was performed at 211 nm.

In general, retention time in both RP and NP chromatography is decreased with increased temperature [20], however the opposite was observed when imidazole was injected into both 1 µm and 10 µm modified monolithic columns due to a clear ion exchange retention mechanism. These experiments showed that significant changes in temperature greatly affected retention times of imidazole.

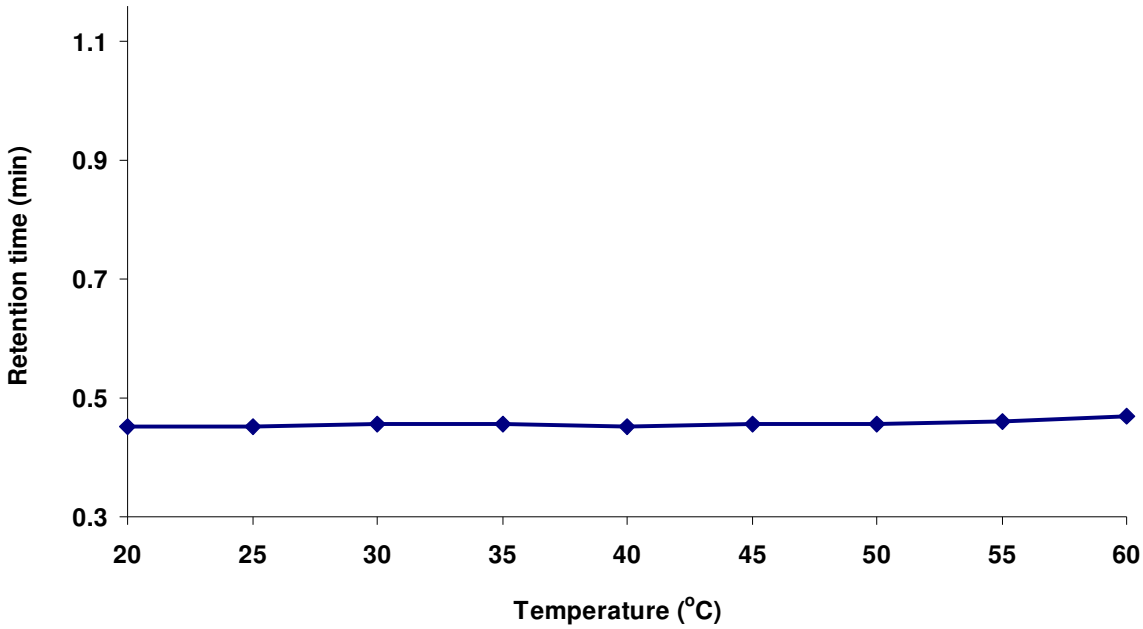

Figure 4.36. The retention dependence on column temperature for resorcinol on a gold-mercaptohexanoic acid modified 10 μm templated glassy carbon monolithic column (75 x 6 mm i.d.).

4.4. Conclusions

In-house prepared carbon monolithic columns were tested for potential chromatographic applications. The obtained columns were studied in both NP and RP modes, with modified monolithic columns evaluated for ion exchange capacity.

The separation ability of the carbon monolithic columns was studied for multicomponent mixtures of aromatic compounds, such as alkylbenzenes. Unfortunately, it was impossible to separate alkylbenzenes, as only limited selectivity and resolution was observed, which can be due to the very low surface area of the carbon monoliths produced.

The column was studied under NP conditions for the separation of polar compounds such as nitrobenzene and acetophenone. Under these conditions limited retention was observed. In order to increase retention, the surface of monolith was treated with acids in order to provide more functional sites. Following such treatment, it was shown that the retention of analytes of interest increase indicating the increase

of surface polarity of the monolith, though it's worth nothing that the efficiency of the columns were still far too low, for high performance chromatographic separation.

However, the surface immobilisation of gold nano/micro-particles and modification with mercaptohexanoic acid allowed some promising retention in ion exchange chromatography. The observed retention of organic cations on the higher capacity modified monoliths obtained through the immersion procedures did provide some scope for further improvement in both retention and efficiency in further studies.

References

1. M. Grun, A. A. Kurganov, S. Schacht, F. Schuth, K. K. Unger, *J. Chromatogr., A*, 740 (1996) 1.
2. J. Randon, S. Huguet, A. Piram, G. Puy, C. Demesmay, J. L. Rocca, *J. Chromatogr., A*, 1109 (2006) 19.
3. D. C. Hoth, J. G. Rivera, L. A. Colon, *J. Chromatogr., A*, 1079 (2005) 392.
4. V. Zizkovsky, R. Kucera, J. Klimes, J. Dohnal, *J. Chromatogr., A*, 1189 (2008) 83.
5. C. Liang, S. Dai, G. Guiochon, *Anal. Chem.*, 75 (2003) 4904.
6. J. H. Knox, M. T. Gilbert, U.K. Patent 2,035,282, 1978.
7. A. Taguchi, J. H. Smatt, M. Linden, *Adv. Mater.*, 15 (2003) 1209.
8. J. H. Knox, B. Kaur, G. R. Millward, *J. Chromatogr.*, 352 (1986) 3.
9. G. S. Chirica, V. T. Remcho, *J. Chromatogr., A*, 924 (2001) 223.
10. N. Ishizuka, H. Minakuchi, K. Nakanishi, N. Soga, N. Tanaka, *J. Chromatogr., A*, 797 (1998) 133.
11. R. Mallik, D. S. Hage, *J Pharm Biomed Anal.*, 46 (2009) 820.
12. M. T. Gilbert, J. H. Knox, B. Kaur, *Chromatographia,* 16 (1982) 138.
13. W. R. Smith, W. D Schaeffer, *Proc. Second Rubber Technol. Conj., London,* (1948) 403.
14. P. N. Nesterenko, O. N. Fedyanina, Y. V. Volgin, P. Jones, *J. Chromatogr. A*, 1155 (2007) 2.
15. L. Rieux, H. Niederlander, E. Verpoorte, R. Bischoff, *J. Sep. Sci.,* 28 (2005) 1628.
16. V. V. Tolstikov, A. Lommen, K. Nakanishi, N. Tanaka, O. Fiehn, *Anal. Chem.,* 75 (2003) 6737.
17. J. Bones, C. Duffy, M. Macka, B. Paull, *Analyst*, 133 (2008) 180.
18. M. Lammerhofer, F. Svec, J. M. J. Frechet, *Anal. Chem.*, 72 (2000) 4623.
19. W. Bashir, B. Paull, *Analyst*, 128 (2003) 335.
20. E. Landberg, A. Lundblad, P. Pahlsson, *J. Chromatogr., A*, 814 (1998) 97.

FUTURE WORK CHAPTER

Electrochemical Properties of Porous Glassy Carbon Monolithic Electrodes

Current and future applications of carbon monolithic materials include both chromatographic and electrochemical uses.

Here a preliminary study into the use of the glassy carbon monolith as an electrode for electrochemical analysis is presented as a foundation short study for future further development.

5.1. Introduction

Use of porous carbon monolith materials had been preliminarily explored for a number of applications, due to their unique surface area properties and porosity characteristics. These applications include, use as columns for chromatography, catalyst supports, various adsorbents, hydrogen-storage, etc. Carbon and carbon/gold composite monoliths have the advantage of being conductive materials and therefore have also been investigated as electrode materials for electrochemical analysis. Electrochemical studies indicated that the meso/macro-porous carbon monoliths with high surface area and large porosity had good electrochemical double-layer capacitance properties and provided very efficient energy storage devices [1-2].

As an application for a lithium-ion battery anode, Wang *et al.,* [3] prepared a monolithic, three-dimensionally ordered macro-porous/meso-porous carbon/tin (IV) oxide nano-composite. Using an infiltration-hydrolysis process, tin (IV) oxide nanocrystals were loaded into the mesopores of the carbon monolith while maintaining connections between macro-pores. In comparison with glassy carbon electrodes similarly templated without the tin oxide component, the composite electrode exhibited greater reversible capacity.

Using an electrostatic layer-by-layer method, Zhang *et al.*, [4] prepared uniform multiwalled carbon nanotubes on glassy carbon electrodes, based on electrostatic interaction of the negatively charged carbon nanotubes and positively

charged poly(diallyldimethylammonium chloride). For O_2 reduction in alkaline media, the layer-by-layer assembled multiwalled carbon nanotube films showed significant electrocatalytic activity.

Metal nano/micro-particles have been widely used in electroanalysis. Chemical modification of electrodes containing specific chemical groups on the surface has shown some advantages over conventional electrode substrates, such as improving the response time and selectivity of the modified electrodes [5-8]. Chemical modification of electrodes with high surface area was carried out by electro-deposition of transition metals on graphitic substrates [9]. Modification with nickel, cobalt, platinum and gold species onto the surfaces of glassy carbon has been used for improving the electrochemical detection of carbohydrates, alcohols and sulfite [10-13]. Casellaa *et al.,* [14] prepared a gold-modified glassy carbon electrode (Au-CME) by depositing gold on the surface of a glassy carbon electrode. The electro-oxidation of the carbohydrate sample took place on the AuOH sites. A 1.5-3% signal loss over 8 h was observed with the gold modified glassy carbon electrode response for the carbohydrates investigated under flow injection and anion-exchange LC conditions. SEM and cyclic voltammetry (CV) were used to examine the surface morphology and electrochemical properties of the Au-CME [14].

Recently, for the electrochemical determination of nitrite in a real sample of wastewater, Yanping *et al.,* [15] successfully modified a glassy carbon surface with gold nano-particles, and characterised them with HR-SEM and CV, showing the gold nano-particles attached effectively onto the glassy carbon surface.

In this Chapter, unique porous glassy carbon monolithic electrodes (PGCME) and gold modified porous glassy carbon monolithic electrodes (Au/PGCME) were evaluated for electrochemical characteristics. The large BET surface area and the large pore volume of meso/macro-porous carbon was expected to support electrolyte transfer in the pore system and increase the carbon–electrolyte interfacial area. PGCME and Au/PGCME were electrochemically investigated using CV.

5.2. Experimental

5.2.1. Reagents and materials

Potassium chloride and potassium ferricyanide (III) were obtained from Sigma-Aldrich (Gillingham, UK)**.** Araldite epoxy glue was obtained from Bostik

Findley Limited (Stafford, UK). Water was obtained from a Millipore Milli-Q water purification unit (Millipore, Bedford, MA, USA) and was 18.2 MΩ. Class A volumetric pipettes and flasks were used to prepare solutions.

5.2.2. Instrumentation

The electrochemical experiments were carried out using a CH Instruments model 660 electrochemical workstation and a three-electrode cell. All potentials quoted are with respect to a Ag/AgCl reference electrode (in 3.0 *M* KCl). Voltammograms were collected on a Data Translation DT-2805/5716 A/D board (Data Translation, Marlboro, MA, USA), which was controlled using WinView software (Superlogics, Inc., Newton, MA, USA) on a 486DX/66 interfaced to the EC-225. The data acquisition rate was controlled by Winview at 20 Hz.

5.2.3. Electrochemical characterisation

PGCME and Au/PGCME were characterised by CV in a solution containing 10 m*M* $K_3Fe(CN)_6$ and 2 *M* KCl between -0.2 and +1.1 V. The scan rates used for the above characterisations were between 20–100 mV/s.

5.2.4. Electrochemical Cell

A three electrode system consisting of either a PGCME or Au/PGCME working electrode, Ag/AgCl reference electrode and a platinum-mesh counter electrode were immersed in a small glass vial through holes drilled into a threaded plastic cap. Prior to the experiment, the working electrode was polished with a small amount of 0.3 and 0.05-micron alumina powder on a felt polishing pad (CH Instruments) and rinsed thoroughly with distilled water to remove alumina adhered to the electrode surface. A magnetic stir bar was placed in the solution whenever repeated voltammograms of a particular solution were required.

5.2.5. Procedure

5.2.5.1. Cyclic voltammetry

Cyclic voltammetry on PGCME and Au/PGCME was performed. The electrodes were connected to the potentiostat. The stock solution (ferricyanide

solution along with the supporting electrolyte potassium chloride) and the three electrodes were placed in the electrochemical cell and a cyclic voltammogram was obtained at each scan rate between 20 – 100 mV/s, with each subsequent scan rate being increased by 20 mV/s.

5.2.5.2. Preparation of Au/PGCME

For the synthetic procedure for the production of the carbon monolithic materials see Chapters 2 and 3. Silver wire was attached to the carbon and gold/carbon composite monoliths using Araldite epoxy glue (Figure 5.1 b) to enable its use as an electrode. The silver wire was wrapped around the section of carbon monolith several times in a coiled fashion to ensure complete and robust electrical contact.

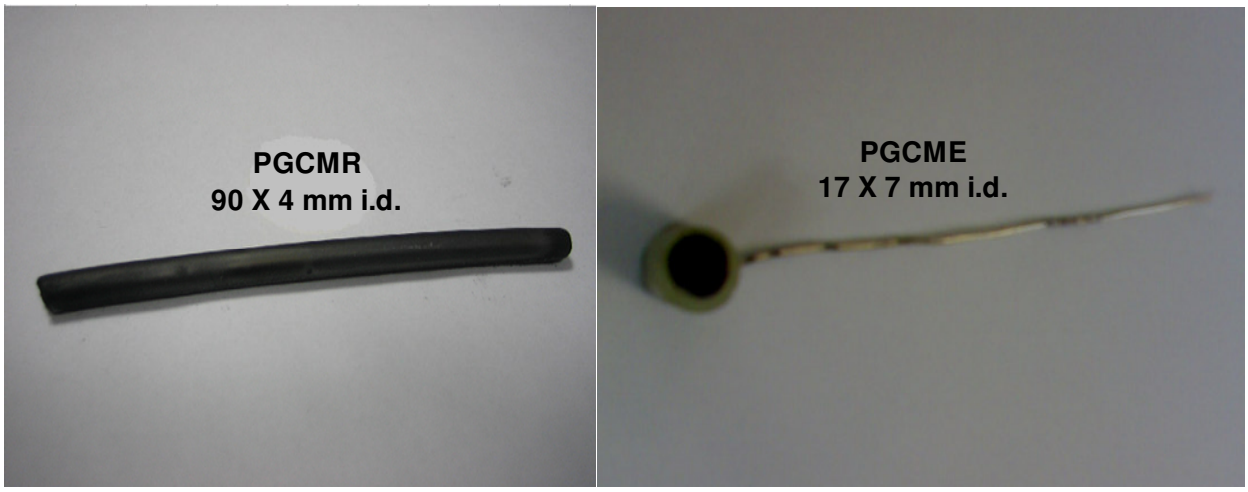

Figure 5.1. (a) Typical PGC monolithic rod, (b) Typical PGCME electrode.

5.3. Results and discussion

5.3.1. Cyclic voltammetry of commercial glassy carbon electrode

Cyclic voltammetry is a type of potentiodynamic electrochemical measurement. Figure 5.2 shows a typical cyclic voltammogram of 10 m*M* $Fe(CN)_6$ on a 1mm commercial glassy carbon electrode in PEEK at a scan rate of 20 mV/s.

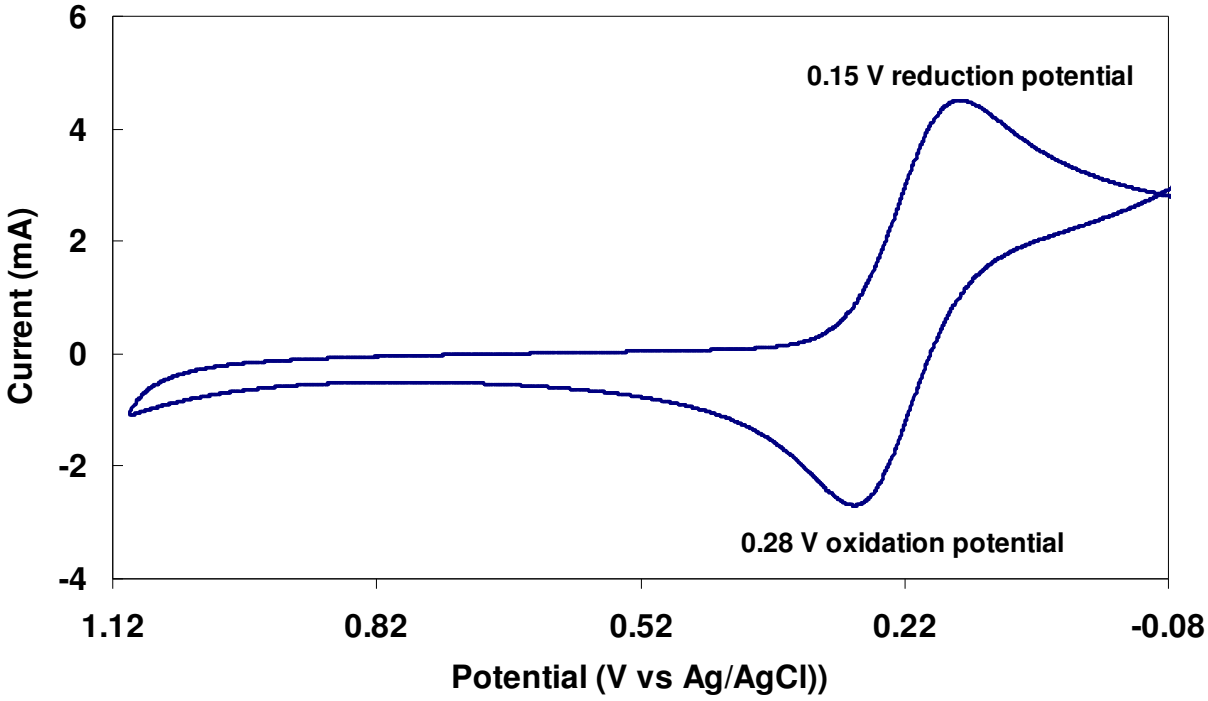

Figure 5.2. Cyclic voltammogram of 10 m*M* $Fe(CN)_6^{3-}$ on a commercial 1 mm glassy carbon in PEEK. Scan rate: 20 mV/s.

5.3.2. Electrocatalytic reduction of ferricyanide on PGCME

As mentioned, PGCME and Au/PGCME were synthesised according to the procedures described in Sections 2.2.3 and 3.2.3.1, Chapters 2 and 3, respectively. Both electrodes were characterised using various techniques. Surface morphologies were examined by SEM, surface area and the pore volume by BET, porosity by mercury porosimetry and the shrinkage during pyrolysis by dilatometry (see Sections 2.2.2 and 3.2.2, Chapters 2 and 3, respectively).

The unique porous structure, the large surface area and the large pore volume of the macro-porous carbon was expected to favour electrolyte transfer in the pore system and increase the carbon–electrolyte interfacial area. Therefore, here we examined the potential of the macro-porous monolithic carbon as an electrode for electrochemical analysis. Cyclic voltammograms were carried out in 1-2 *M* KCl in a half-cell setup configuration at room temperature. A platinum mesh electrode and a

saturated Ag/AgCl electrode served as the counter electrode and reference electrode, respectively.

In a recent study by Yanping *et al.,* [15] it was reported that no faradaic current was observed for a bare glassy carbon electrode in a phosphate buffer, as shown in Figure 5.3, while for gold modified glassy carbon electrode, a small anodic wave at 1.10 V and a significant cathodic wave at 0.40 V corresponding to the characteristic peaks of gold were observed, further confirming the attachment of gold nano-particles on the glassy carbon surfaces (see Figure 5.3 (right)).

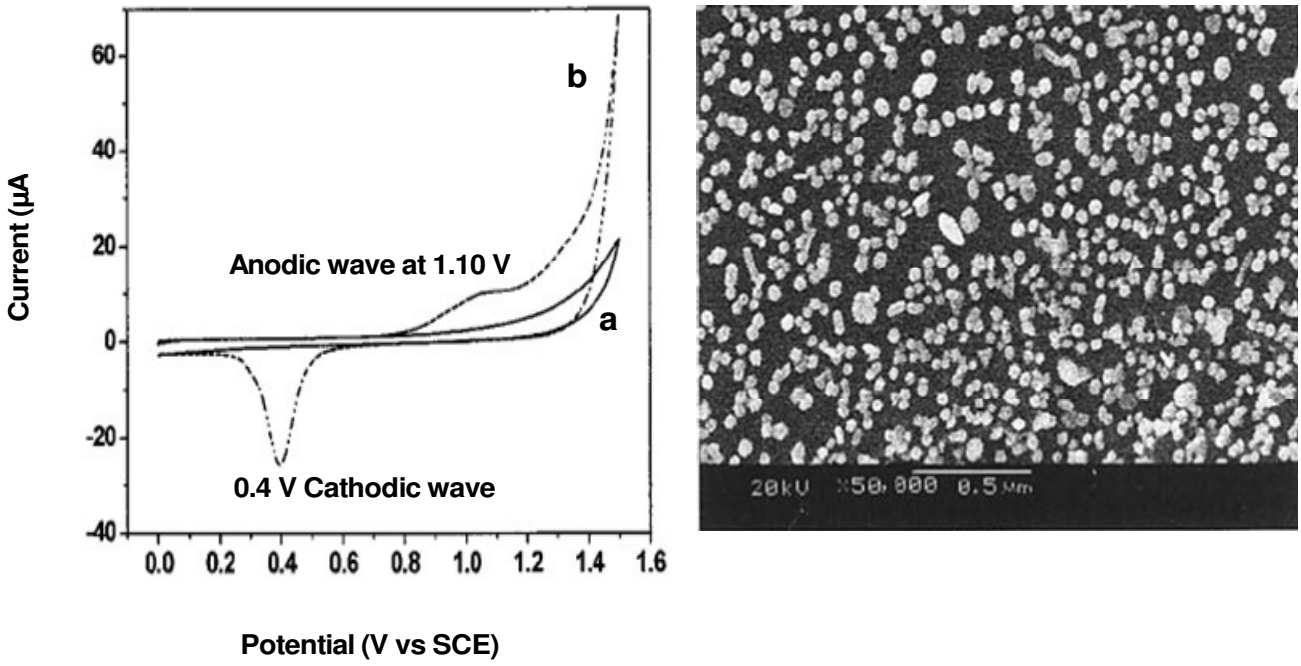

Figure 5.3. (Left) Cyclic voltammograms on a (a) bare glassy carbon electrode and (b) on an Au/glassy carbon electrode, in 0.1 *M* phosphate buffer solution at at 100 mV/s. (Right) HR-SEM image of the Au/GCE surface. Reproduced from [15].

Similar results were obtained in this work, on a bare 5 or 10 µm templated PGCME in 1 *M* KCl at a scan rate of 20 mV/s, where no redox peaks or anodic or cathodic waves were observed, as shown in Figure 5.4. Cyclic voltammograms using the 5 µm modified PGCME (Figure 5.4) showed big slopes indicative of high resistance (~ 30 Ω).

Following the above experiments, cyclic voltammograms in the presence of ferricyanide on the 10 µm templated PGCME at scan rate 20 mV/s were carried out.

These scans showed clear oxidation and reduction potentials at 0.51 V and 0.01 V *vs* Ag/AgCl reference electrode, respectively (Figure 5.5).

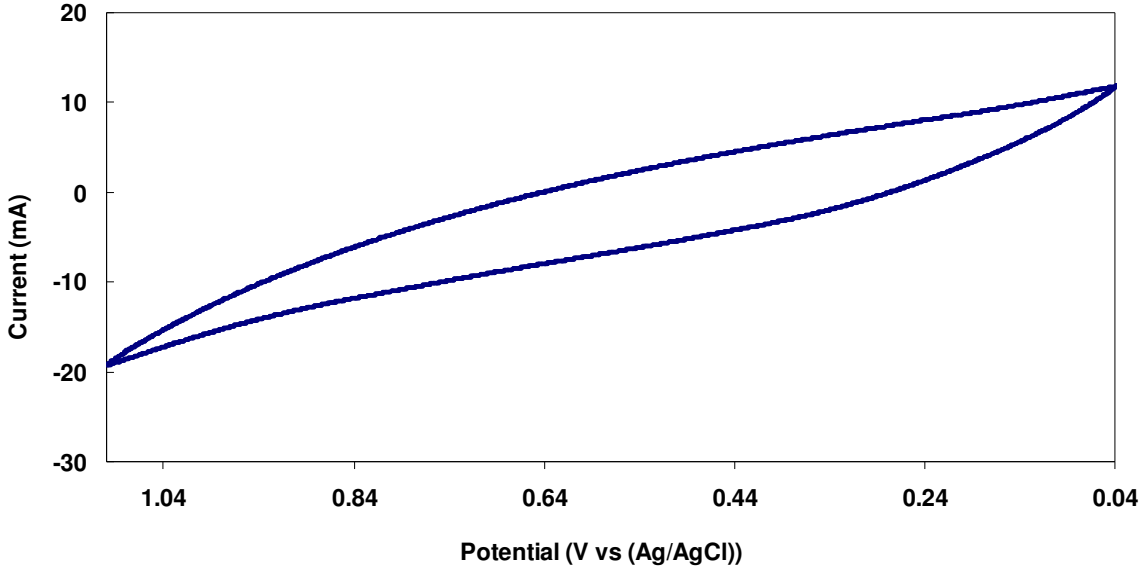

Figure 5.4. Cyclic voltammogram on a bare 5 µm templated PGCME in 1 *M* KCl, at scan rate of 20 mV/s.

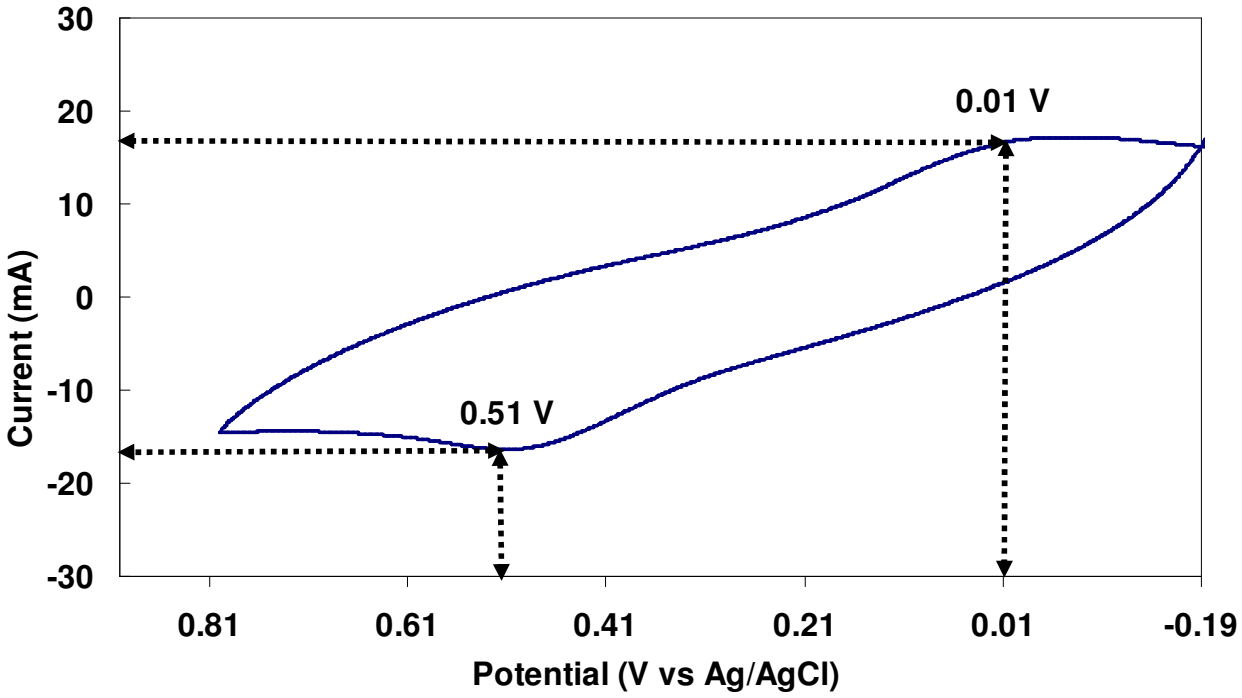

Figure 5.5. Cyclic voltammetry on a 10 µm templated PGCME in the presence of ferricyanide (1 *M* KCl), at a scan rate of 20 mV/s.

Cyclic voltammograms obtained on the 10 µm templated PGCME (Figure 5.5) were typical of that from standard bare glassy carbon electrodes as reported by Maruyama *et al.*, [16] with a large background indicating the greater capacitive charge of the glassy carbon.

Cyclic voltammograms obtained in the presence of ferricyanide on a 5 µm templated PGCME (scan rate 20 mV/s) (Figure 5.6) showed very similar responses to that shown above on the 10 µm templated PGCME, under the same conditions. Figure 5.6 shows oxidation and reduction potentials at 0.45 V and 0.04 V *vs* Ag/AgCl reference electrode, respectively.

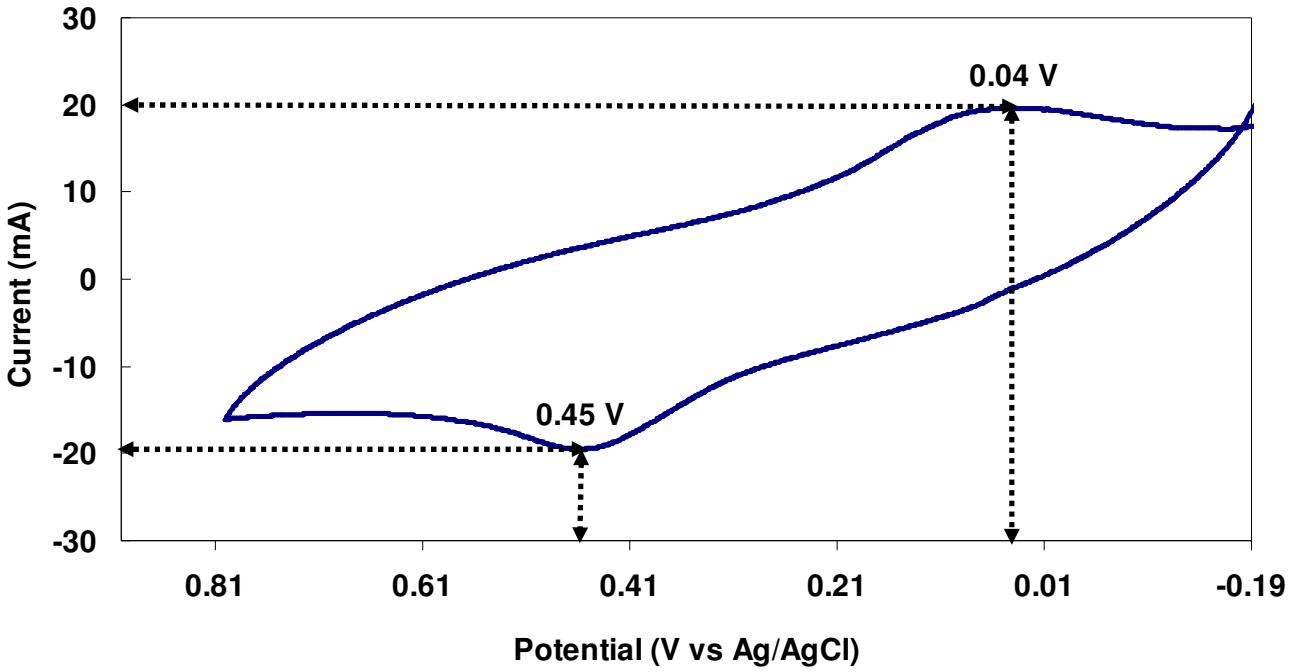

Figure 5.6. Cyclic voltammetry on a 5 µm templated PGCME in the presence of ferricyanide (1 *M* KCl), at a scan rate of 20 mV/s.

The background of the PGCME (Figure 5.6) is much greater than that of the commercial glassy carbon electrode (Figure 5.2), this indicates that at the PGCME there is a greater capacitive charge. Capacitance is proportional to surface area so this is one possible explanation for the large background [17]. However, the magnitude of the current on the PGCME was approximately 15 mA greater than that on the commercial glassy carbon electrode (4 mA) indicating the larger resistance, lower conductivity and a greater capacitive performance.

5.3.3. Characterisation of Au/PGCME by SEM/EDX

As mentioned in Section 4.3.2.1., Chapter 4, the glassy carbon monolithic rod was modified with gold nano/micro-particles by self-assembly in solution following spontaneous induced reduction upon functional groups at the surface. Initial modification of rods was carried out by simple immersion of the monolithic rods in 100 m*M* tetrachloroauric acid (see Section 3.2.3.1, Chapter 3). Initial experiments showed the density of the surface of the carbon monolith immobilised gold particles, **IM5** was proportional to immersion time. Thus, the longer the immersion time of the carbon monolithic rod in the tetrachloroauric acid solution, the higher density of gold particles on the surface.

The SEM image of the surface of the Au/PGCME used here is shown in Figure 5.7, confirming the substantial attachment of gold nano/micro-particles to the surface of the PGCME via the immersion method. The SEM conditions were as following: accelerating voltage was 20 keV, working distance was 6.7 mm and magnification was 2.5 k. Nano/micro-particles were observed with diameters of between 50–150 nm, showing a high degree of surface coverage.

As mentioned in Section 3.3.1.1, Chapter 3, EDX analysis was also performed on cross sections of the carbon/gold composite monoliths. A corresponding EDX spectrum of a section of the carbon/gold composite 5 μm templated monolith sample used to prepare the Au/PGCME (Figure 5.8) shows clearly the elemental presence of C and Au only.

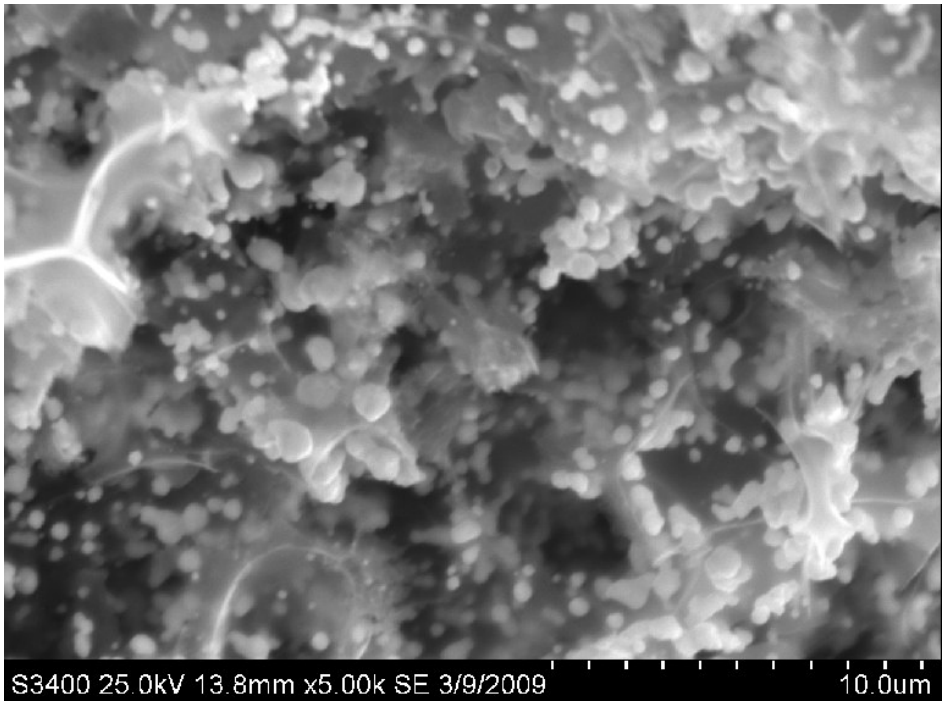

Figure 5.7. SEM image of the surface of the Au/PGCME.

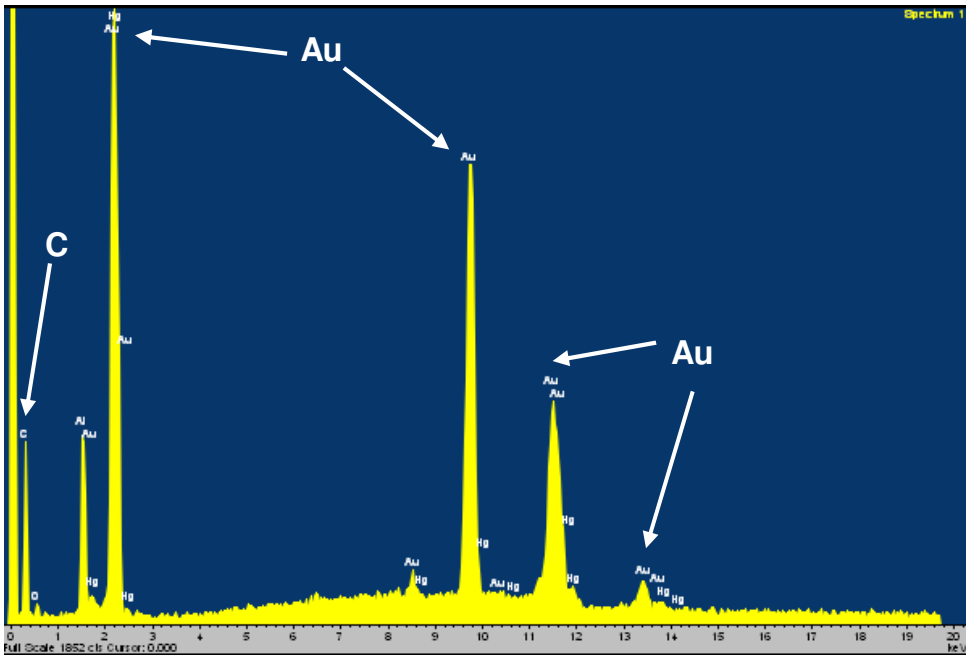

Figure 5.8. EDX spectrum of the surface of the Au/PGCME.

5.3.4. Electrocatalytic oxidation of ferricyanide on Au/PGCME

In order to evaluate the electrocatalytic activity of attached gold nano/micro-particles toward the oxidation of ferricyanide, CV on an Au/PGCME was performed in 1 *M* KCl at room temperature. A platinum mesh electrode and a saturated Ag/AgCl electrode served as the counter electrode and reference electrode, respectively.

Yanping *et al.,* [15] investigated the oxidation of nitrite on a bare glassy carbon electrode and a gold nano-particle modified glassy carbon electrode. No redox peaks were observed on the Au/glassy carbon electrode in the absence of nitrite, while with the addition of 1×10^{-4} *M* NO_2^-, a significant oxidation peak for NO_2^- appeared at 0.77 V *vs*. saturated calomel reference electrode (SCE), as shown in Figure 5.9. Compared with the results obtained on the bare glassy carbon electrode, the potential was shifted negatively by about 150 mV with the Au/GCE, accompanied with an enhancement of 0.8 μA in peak current [15].

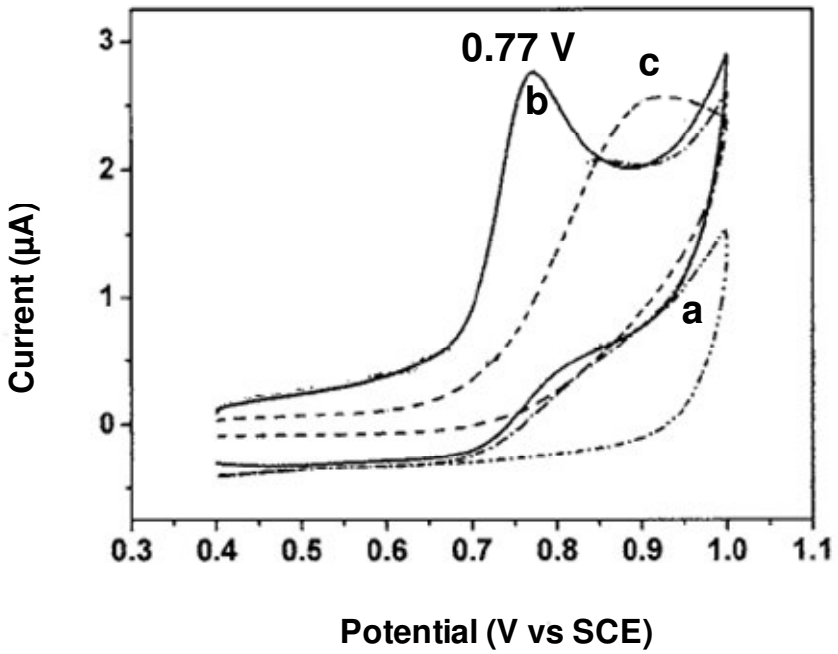

Figure 5.9. Cyclic voltammograms of (a) Au/glassy carbon electrode in the absence and (b) in the presence of of nitrite ions. (c) bare glassy carbon electrode in the presence of 1×10^{-4} *M* NO_2^- in 0.2 *M* acetate buffer solution at 100 mV/s. Reproduced from [15].

In this study, CV on a 5 µm modified Au/PGCME in the absence of any redox active species in 1 *M* KCl, at a scan rate of 20 mV/s showed no clear redox peaks or anodic or cathodic waves (Figure 5.10) possibly due to the presence of the contaminants on the surface of the electrode [18]. It is a big resistance (~ 50 Ω) expected from the cyclic voltammogram of the 5 µm modified Au/PGCME (Figure 5.10).

Figure 5.11 shows the repeat experiment this time in the presence of 10 m*M* ferricyanide on the 5 µm modified Au/PGCME in 1 *M* KCl, at a scan rate of 20 mV/s. Also in this study, the figures of potential increasing to the left and the oxidation potential is always the most positive. Compared with the unmodified PGCME in the presence of ferricyanide, which resulted in a reduction potential at 0.04 V and a significant oxidation potential at 0.45 V (Figure 5.6), the response with the Au/PGCME, showed a larger reduction potential at 0.105 V and a smaller oxidation potential at 0.18 V. Also detected was a second smaller oxidation potential at 0.391 V, corresponding to the characteristic peak of gold, as reported previously by Yanping *et al.*, [15]. The cyclic voltammograms from the 5 µm modified Au/PGCME (Figure 5.11) confirmed the attachment of gold nano/micro-particles on the surface of PGCME, compared with that of the 5 µm unmodified PGCME (Figure 5.6).

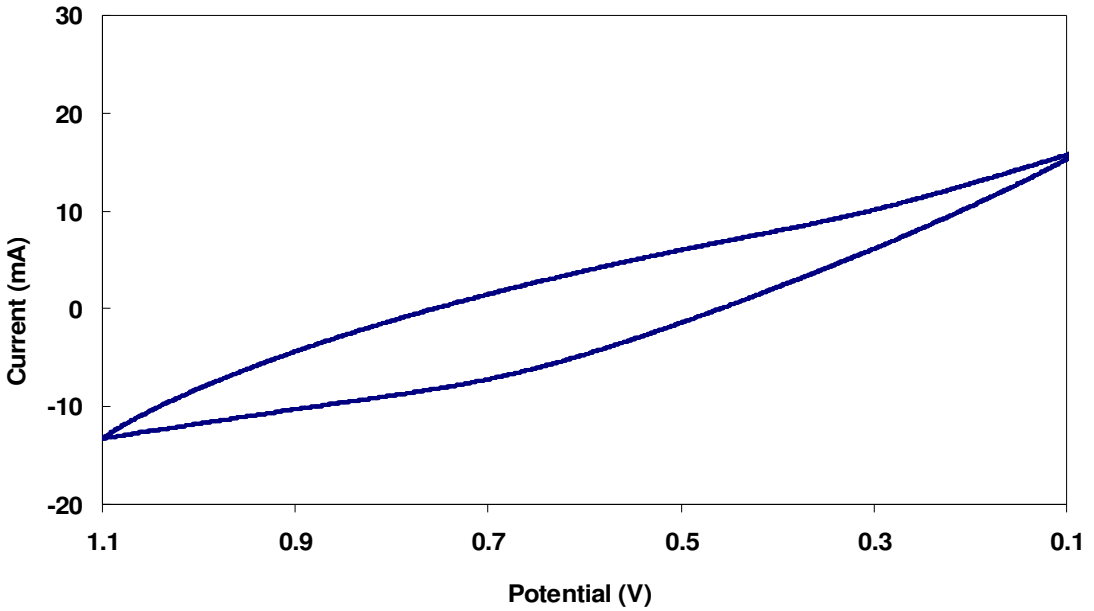

Figure 5.10. Cyclic voltammogram of 5 µm modified Au/PGCME in the absence of ferricyanide (1 M KCl), at 20 mV/s.

Ferricyanide on the Au/PGCME produced a sharper reduction peak, with an almost 1 mA decreases in peak current, with the oxidation potential shifted negatively by approximately 270 mV (Figure 5.11), compared with the unmodified PGCME (Figure 5.6). These results show that the gold nano/micro-particles do exhibit some encouraging catalytic activity toward the reduction of ferricyanide.

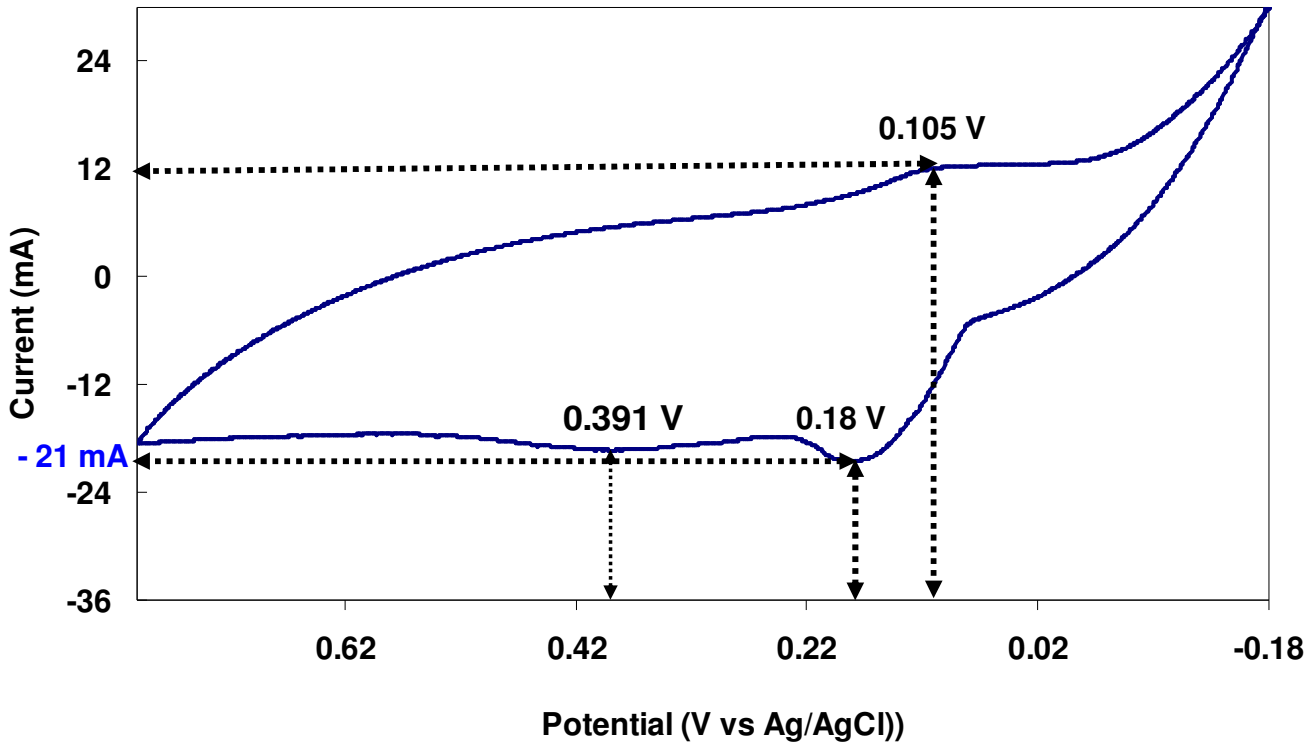

Figure 5.11. Cyclic voltammetry on a 5 µm templated Au/PGCME, in the presence of ferricyanide (1 *M* KCl), at a scan rate of 20 mV/s.

Furthermore, the stability of the Au/PGCME was investigated by storing the electrode at room temperature for 7 days. The current response for a solution of ferricyanide was the same after 7 days, indicating that this modified electrode displays good long-term stability and precision.

5.4. Conclusions

Unique PGCME and Au/PGCME electrodes have been successfully prepared for electrochemical applications. Electrochemical measurements obtained on the anodised (5 and 10 µm) PGCME and (5 µm) Au/PGCME showed a more stable and reproducible response relative to the standard glassy carbon electrode. The electrode was investigated using CV following electrochemically induced surface oxidation and generated oxygen-containing surface functional groups to improve hydrophilicity. Cyclic voltammetry was investigated using a solution containing potassium ferricyanide and KCl between -0.2 and +1.1 V. The scan rate used for the above characterisations was between 20–100 mV/s. Some evidence of the catalytic activity of the gold modified glassy carbon monolithic electrode could be seen.

References

1. Y. Zhao, M.-B. Zheng, J.-M. Cao, X.-F. Ke, J.-S. Liu, Y.-P. Chen, J. Tao, *Mater. Lett*., 62 (2008) 548.
2. V. Ruiz, C. Blanco, R. Santamaria, J.M. Ramos-Fernandez, M. Martinez-Escandell, A. Sepulveda-Escribano, F. Rodrıiguez-Reinoso, *Carbon*, 47 (2009) 195.
3. Z. Wang , M. A. Fierke, A. Stein, *J. Electrochem. Soc*., 155 (2008) A658.
4. M. Zhang, Y. Yan, K. Gong, L. Mao, Z. Guo, Y. Chen, *Langmuir*, 20 (2004**)** 8781.
5. E. Wang, A. Liu, *J. Electroanal. Chem.,* 319 (1991) 217.
6. R. P. Baldwin, K. N. Thomsen, *Talanta,* 38 (1991) 1.
7. Y. Ikariyama, W. R. Heineman, *Anal. Chem.,* 58 (1986) 1803.
8. T. Ohsaka, T. Okajima, N. Oyama, *J. Electroanal. Chem.,*215 (1986) 191.
9. E. J. M. O'Sullivan, E. J. Calvo, in *Electrode Kinetics: Reactions,* ed. Compton, R. G., Elsevier, Oxford, 27 (1987) Ch. 3.
10. I. G. Casella, E. Desimoni, A. M. Salvi, *Anal. Chim. Acta,* 248 (1991) 117.
11. T. R. I. Cataldi, I. G. Casella, E. Desimoni, T. Rotunno, *Anal. Chim. Acta,* 270 (1992) 161.
12. I. G. Casella, T. R. I. Cataldi, A. M. Salvi, E. Desimoni, *Anal. Chem.,* 65 (1993) 3143.
13. I. G. Casella, R. Marchese, *Anal. Chim. Acta,* 311 (1995) 199.
14. I.G. Casellaa, A. Destradis, E. Desimonib, *Analyst*, 121 (1996) 249.
15. C. U. Yanping, Y. A. Changzhu, Z. E. Wei, O. Y. Munetaka, P. U. Wenhong, Z. H. Jingdong, *Anal. Sci.*, 23 (2007) 1421.
16. J. Maruyama, I. Abe, *Electrochim. Acta,* 46 (2001) 3381.
17. Handbook of the electrochemistry, Cynthia G. Zoski, First edition, Elsvier publications, Oxford, UK, 2007.
18. C. Liang, S. Dai, G. Guiochon, *Anal. Chem*., 75 (2003) 4904.

General conclusions and future work

Carbon monolithic rods (1-10 μm pore diameter) were prepared by polymerisation of a phenolic resin formed upon a silica template, followed by pyrolysis, and removal of the silica template using HF treatment. Unique metallically modified carbon monoliths, were also successfully prepared by modification the resultant carbon monoliths with gold and silver particles.

Various techniques, such as SEM/EDX, BET, dilatometry, mercury porosimetry, DTA/TGA, DMA, conductivity and backpressure determination were used to characterise prepared porous monolithic rods. It was shown that the total surface area of the carbon monoliths were 178 m^2/g (1 μm), 154 m^2/g (2 μm), 85 m^2/g (5 μm) and 125 m^2/g (10 μm) and each monolith exhibited high porosity. Mercury porosimetry was used to determine the pore size distribution of the carbon monoliths. The flow through pores after pyrolysis and removal of the silica template found to be reduced in diameter due to shrinkage during pyrolysis.

Carbon monolithic columns were tested for potential chromatographic applications in both reversed-phase and normal phase modes for the attempted separation of polar and non-polar compounds. Unfortunately, separation of alkylbenzenes was not successful and it was not possible to achieve an efficient separation of butylbenzene-acetophenone and butylbenzene-nitrobenzene mixtures, as only limited resolution and efficiency was obtained, which was likely due to the low surface area of carbon monolith.

For functionalised gold/carbon composite monoliths, modified with gold nano/microparticles and further with 6-mercaptohexanoic acid, EDX analysis showed a strong sulphur peak indicating that the modification technique of carbon/gold composite monolith with 6-mercaptohexanoic acid was successful. These modified monolithic columns were evaluated for ion exchange capacity for the separation of some organic cations and showed that although some cation exchange capacity was demonstrated, the efficiency of the columns was still low, unsuitable for high performance chromatographic separations.

For electrochemical application, the electrical conductivity of the carbon monoliths was measured. As the conductivity is inversely proportional to the particle size, thus, the carbon monolith with smallest pore diameter showed the highest conductivity and with the largest pore diameter showed the lowest. Using cyclic voltammetry for further electrochemical evaluation, the electrochemical measurements obtained on the unique porous glassy carbon monolithic electrode and gold modified porous glassy carbon monolithic electrode (5-10 μm pore size) showed a more stable and reproducible response relative to the standard glassy carbon electrode. Both electrodes showed oxidation and reduction potentials *vs* Ag/AgCl reference electrode.

The preparation of efficient porous monolithic carbon columns still posses significant challenges for various reasons. Despite this study optimising and demonstrating the synthetic process, the resultant rods had insufficient surface area capacity to be suited to high performance separations. Although not utilised within this study, clearly the use of higher temperature treatment for the production of fully graphitised monolithic rods may improve the surface area and capacity of the produced rods.

Also, the carbon monolith columns produced within this study were only evaluated for liquid chromatographic based separations. However, potential exists for their application in alternative modes of separation science, such as gas chromatography. Time restraints in the current study meant such evaluation was not possible but previous early studies show glassy carbon substrates can have possible application under gas chromatographic conditions.

Finally, more electrochemical applications and evaluation is required beyond the preliminary evaluation carried out in this work. Such work is currently being explored through collaborative ongoing projects.